Journal of Mechanics of Materials and Structures

Volume 7, No. 7 September 2012

msp

JOURNAL OF MECHANICS OF MATERIALS AND STRUCTURES

jomms.net

Founded by Charles R. Steele and Marie-Louise Steele

See http://jomms.net for submission guidelines.

JoMMS (ISSN 1559-3959) is published in 10 issues a year. The subscription price for 2012 is US $555/year for the electronic version, and $735/year (+$60 shipping outside the US) for print and electronic. Subscriptions, requests for back issues, and changes of address should be sent to Mathematical Sciences Publishers, Department of Mathematics, University of California, Berkeley, CA 94720–3840.

JoMMS peer-review and production is managed by EditFLOW® from Mathematical Sciences Publishers.

PUBLISHED BY
mathematical sciences publishers
http://msp.org/

A NON-PROFIT CORPORATION

Typeset in LaTeX

JOURNAL OF MECHANICS OF MATERIALS AND STRUCTURES
Vol. 7, No. 7, 2012
dx.doi.org/10.2140/jomms.2012.7.613

MOLECULAR DYNAMICS-BASED CONTINUUM MODELS FOR THE LINEAR ELASTICITY OF NANOFILMS AND NANOWIRES WITH ANISOTROPIC SURFACE EFFECTS

WONBAE KIM, SEUNG YUN RHEE AND MAENGHYO CHO

A continuum-based sequential multiscale model is presented for application to nanofilms and nanowires with anisotropic surfaces. The surface effect is accounted for via the inclusion of surface energy due to surface stress and surface strain in the internal energy. For anisotropic surfaces such as a <110> surface, a linear surface elasticity model is used instead of the isotropic surface elasticity model proposed by Gurtin and Murdoch. A molecular dynamics simulation is performed in order to calculate initial surface stress and surface elastic tensor. Equilibrium strain and size-dependent elasticity are estimated by the proposed continuum model.

1. Introduction

As more and more nanoscaled structures such as nanofilms and nanowires are fabricated, it is becoming more important to understand the mechanical characteristics of nanostructures. It is well known that the mechanical properties of a nanosized structure significantly differ from those of bulk materials because of the surface effect. Therefore, although the surface effect is negligible in macroscale studies, it is crucial for a nanosized structure analysis to account for the influence of the surface effect [Miller and Shenoy 2000; Zhou and Huang 2004; Diao et al. 2004; Liang et al. 2005; Guo and Zhao 2005; Sun and Zhang 2005; Dingreville et al. 2005; Wang et al. 2008; He and Lilley 2008; Zhang et al. 2008; Dingreville et al. 2008; Park 2009; Kim and Cho 2010].

An atom on a free surface of a crystal structure has a different coordination number (i.e. the number of nearest neighbors) from an atom in the bulk material. For this reason, solid crystal surfaces contain excess surface energy and residual surface stress. The surface stress significantly affects the equilibrium state and elastic properties of a nanostructure [Wolf 1991; Cammarata and Sieradzki 1989; Streitz et al. 1994]. Streitz et al. [1994] introduced a surface stress model and calculated the equilibrium biaxial strain and biaxial modulus for an axis-symmetric thin film. Miller and Shenoy [2000] estimated the effective stiffnesses of nanosized structures using atomistic calculations. Recently, Dingreville et al. [2008] proposed a semi-analytical method for quantifying the size-dependent elasticity of nanostructures, and Kim and Cho [2010] computed equilibrium strain and size-dependent elasticity using a surface relaxation model and a new surface stress model.

As one of the continuum approaches, Gurtin and Murdoch [1975; 1978] introduced a surface elasticity model for isotropic surfaces using initial surface stress and surface Lamé constants. A plate theory based on Kirchhoff and Mindlin plate theories, which included the surface effect by using Gurtin and

Keywords: surface effects, sequential multiscale model, finite element method, nanofilm, nanowire, size-dependent elasticity, molecular dynamics simulation.

Murdoch's surface model, was proposed by Lim and He [2004] and Lu et al. [2006]. Recently, Cho et al. [2009] proposed a continuum-based bridging model for a nanofilm using the surface elasticity model by Gurtin and Murdoch [1975; 1978]. Cho et al. [2009] suggested a sequential multiscale method in order to determine initial surface stress and surface Lamé constants using a matching method based on a molecular dynamics (MD) simulation. As an extension of this multiscale model, a finite element analysis including thermomechanical properties was carried out by Choi et al. [2010a].

With the exception of {111} surfaces, FCC crystal surfaces are not isotropic; for example, a {100} surface and a {110} surface of an FCC single crystal are orthotropic. Therefore, the surface elasticity model developed by Gurtin and Murdoch cannot be universally applied to single crystal surfaces. Choi et al. [2010b] modified Gurtin and Murdoch's model, adding an additional parameter to two surface Lamé constants for the analysis of a nanofilm resonator with a {100} surface. However, this modified surface elasticity is not applicable to a {110} surface. Although there is need for a multiscale continuum model that can be applied to general nanostructures, no single model can handle all anisotropic surfaces.

This paper presents a new continuum-based sequential multiscale model for nanofilms and nanowires with anisotropic surfaces. This model utilizes a linear surface elastic model, which is represented in terms of initial surface stress and surface elastic tensor, instead of relying on Gurtin and Murdoch's surface model. The surface parameters, initial surface stress and surface elastic tensor, are determined by applying a matching technique to the results from an MD simulation.

2. Multiscale continuum model including surface effect

2.1. ***Multiscale continuum model for a nanofilm.*** Mindlin plate theory is adopted for the proposed model. For a nanofilm with top (Ω^+) and bottom (Ω^-) surfaces, as shown in Figure 1, the displacement field based on Mindlin plate theory is defined as

$$\begin{aligned} u_\alpha &= u_\alpha^0 + x_3\psi_\alpha, \\ u_3 &= u_3^0 = w, \end{aligned} \tag{1}$$

where u_α^0 and u_3^0 denote in-plane and out-of-plane displacements defined in the mid-plane of the thin film, respectively, ψ_α is the rotational degree of freedom, and the subscript α represents in-plane directions 1

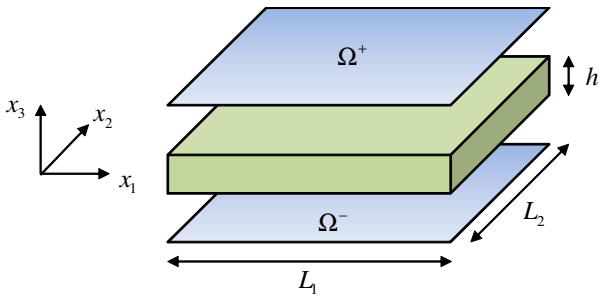

Figure 1. Schematic diagram of a nanofilm with top and bottom surfaces.

and 2. Using this displacement field, the strain-displacement relationship, $\epsilon_{ij} = (u_{i,j} + u_{j,i})/2$, yields

$$\begin{aligned} \epsilon_{\alpha\beta} &= \tfrac{1}{2}[u^0_{\alpha,\beta} + u^0_{\beta,\alpha} + x_3(\psi_{\alpha,\beta} + \psi_{\beta,\alpha})], \\ \epsilon_{3\alpha} &= \tfrac{1}{2}[w_{,\alpha} + \psi_\alpha], \end{aligned} \tag{2}$$

where $u^0_{\alpha,3} = 0$ because $u^0_\alpha = u^0_\alpha(x_1, x_2)$. The in-plane components of the strain tensor are

$$\begin{aligned} \epsilon_{11} &= u^0_{1,1} + x_3\psi_{1,1}, \\ \epsilon_{22} &= u^0_{2,2} + x_3\psi_{2,2}, \\ 2\epsilon_{12} &= (u^0_{1,2} + u^0_{2,1}) + x_3(\psi_{1,2} + \psi_{2,1}), \end{aligned} \tag{3}$$

and the transverse shear components of the strain tensor are

$$\begin{aligned} 2\epsilon_{31} &= w_{,1} + \psi_1, \\ 2\epsilon_{32} &= w_{,2} + \psi_2. \end{aligned} \tag{4}$$

The displacements on the upper and lower surfaces are described as

$$\begin{aligned} u^{s\pm}_\alpha &= u^0_\alpha \pm \tfrac{h}{2}\psi_\alpha, \\ u^{s\pm}_3 &= w, \end{aligned} \tag{5}$$

where $s+$ and $s-$ denote the upper and lower surfaces, respectively, and h is the film thickness. The strain field on a surface can be written as

$$\begin{aligned} \epsilon^{s\pm}_{11} &= u^0_{1,1} \pm \tfrac{h}{2}\psi_{1,1}, \\ \epsilon^{s\pm}_{22} &= u^0_{2,2} \pm \tfrac{h}{2}\psi_{2,2}, \\ 2\epsilon^{s\pm}_{12} &= (u^0_{1,2} + u^0_{2,1}) \pm \tfrac{h}{2}(\psi_{1,2} + \psi_{2,1}). \end{aligned} \tag{6}$$

The virtual work principle states that the internal virtual work is equal to the external virtual work, i.e. $\delta U = \delta W_E$. The external virtual work δW_E can be written as

$$\delta W_E = \int_\Omega p_\alpha \delta u^0_\alpha + p_3 \delta w \, dA, \tag{7}$$

where p_α and p_3 are the in-plane and out-of-plane force per unit area, respectively. The internal virtual work consists of bulk energy and surface energy ($\delta U = \delta U_{\text{bulk}} + \delta U_{\text{surf}}$). The bulk energy can be written in terms of displacements and resultant forces, as follows:

$$\begin{aligned} \delta U_{\text{bulk}} &= \int_v \sigma_{\alpha\beta}\delta\epsilon_{\alpha\beta} \, dv + \int_v \sigma_{3\alpha}\delta\gamma_{3\alpha} \, dv \\ &= \int_\Omega N_{\alpha\beta}\delta u^0_{\alpha,\beta} + M_{\alpha\beta}\delta\psi_{\alpha,\beta} \, dA + \int_\Omega Q_\alpha(\delta w_{,\alpha} + \delta\psi_\alpha) \, dA, \end{aligned} \tag{8}$$

where $\sigma_{\alpha\beta}$ and $\epsilon_{\alpha\beta}$ are in-plane stress and strain components, respectively; $\sigma_{3\alpha}$ and $\gamma_{3\alpha}$ are transverse shear stress and strain components, respectively; and $N_{\alpha\beta}$, $M_{\alpha\beta}$, and Q_α are force stress resultants,

moment resultants, and shear stress resultants, respectively. These last three variables are defined by

$$N_{\alpha\beta} = \int_{-h/2}^{h/2} \sigma_{\alpha\beta}\, dx_3, \quad M_{\alpha\beta} = \int_{-h/2}^{h/2} \sigma_{\alpha\beta} x_3\, dx_3, \quad Q_\alpha = \int_{-h/2}^{h/2} \sigma_{3\alpha}\, dx_3. \tag{9}$$

The surface energy due to surface stress is composed of both top and bottom surface energies:

$$\delta U_{\text{surf}} = \int_{\Omega^\pm} \tau_{\alpha\beta}^{\pm} \delta \epsilon_{\alpha\beta}^{s\pm}\, dA = \int_{\Omega^\pm} \tau_{\alpha\beta}^{\pm} \delta (u_{\alpha,\beta}^0 \pm \tfrac{h}{2}\psi_{\alpha,\beta})\, dA, \tag{10}$$

where Ω^+ and Ω^- represent the top and bottom surfaces, respectively; $\tau_{\alpha\beta}^{s\pm}$ is a surface stress component; and $\epsilon_{\alpha\beta}^{s\pm}$ is a surface strain component. Using (8) and (10), the internal virtual work yields

$$\begin{aligned} \delta U &= \delta U_{\text{bulk}} + \delta U_{\text{surf}} \\ &= \int_\Omega (N_{\alpha\beta} + \tau_{\alpha\beta}^+ + \tau_{\alpha\beta}^-) \delta u_{\alpha,\beta}^0\, dA + \int_\Omega \big(M_{\alpha\beta} + \tfrac{h}{2}(\tau_{\alpha\beta}^+ - \tau_{\alpha\beta}^-)\big) \delta\psi_{\alpha,\beta}\, dA + \int_\Omega Q_\alpha (\delta w_{,\alpha} + \delta\psi_\alpha)\, dA. \end{aligned} \tag{11}$$

The linear elastic constitutive equation, $\sigma_{ij} = C_{ijkl}\epsilon_{kl}$, is utilized for the bulk material, and the following relationship is used to determine the surface constitutive relationship:

$$\tau_{\alpha\beta}^{\pm} = \tau_{\alpha\beta}^0 + T_{\alpha\beta\kappa\lambda} \epsilon_{\kappa\lambda}^{s\pm}, \tag{12}$$

where $\tau_{\alpha\beta}^0$ is the initial surface stress component at zero strain and $T_{\alpha\beta\kappa\lambda}$ is the surface elastic tensor component. This linear surface constitutive equation can be used for any anisotropic surface, whereas Gurtin and Murdoch's surface elasticity can be applied only to isotropic surfaces.

Finite element implementation for a nanofilm. When implementing a finite element analysis for a nanofilm, an isoparametric 4-node element is used. The nodal displacement is defined as

$$\boldsymbol{d} = \big[(u_1, u_2, w, \psi_1, \psi_2)_1, \ldots, (u_1, u_2, w, \psi_1, \psi_2)_n\big]^T,$$

and the displacement field is interpolated within nodal values.

$$u_\alpha^0 = \sum_{i=1}^n N_i (u_\alpha)_i, \quad w = \sum_{i=1}^n N_i w_i, \quad \psi_\alpha = \sum_{i=1}^n N_i (\psi_\alpha)_i, \tag{13}$$

where N_i is the i-th interpolation function and n is the number of nodes per element. Using these nodal displacements, the strain field can be rewritten as

$$\begin{Bmatrix} \epsilon_{11} \\ \epsilon_{22} \\ 2\epsilon_{12} \end{Bmatrix} = \begin{Bmatrix} u_{1,1}^0 \\ u_{2,2}^0 \\ u_{1,2}^0 + u_{2,1}^0 \end{Bmatrix} + x_3 \begin{Bmatrix} \psi_{1,1} \\ \psi_{2,2} \\ \psi_{1,2} + \psi_{2,1} \end{Bmatrix} = \boldsymbol{B}_m \boldsymbol{d} + x_3 \boldsymbol{B}_b \boldsymbol{d}, \tag{14}$$

$$\begin{Bmatrix} 2\epsilon_{31} \\ 2\epsilon_{32} \end{Bmatrix} = \begin{Bmatrix} w_{,1} + \psi_1 \\ w_{,2} + \psi_2 \end{Bmatrix} = \boldsymbol{B}_s \boldsymbol{d}, \tag{15}$$

where matrices $\boldsymbol{B}_m$, $\boldsymbol{B}_b$, and $\boldsymbol{B}_s$ represent the relationships between nodal displacement and membrane, bending, and transverse shear strains, as follows:

$$\begin{aligned}
\boldsymbol{B}_m\boldsymbol{d} &= [\boldsymbol{B}_m^{(1)}, \boldsymbol{B}_m^{(2)}, \ldots, \boldsymbol{B}_m^{(n)}]\boldsymbol{d} = \begin{Bmatrix} u^0_{1,1} \\ u^0_{2,2} \\ u^0_{1,2} + u^0_{2,1} \end{Bmatrix}, \\
\boldsymbol{B}_b\boldsymbol{d} &= [\boldsymbol{B}_b^{(1)}, \boldsymbol{B}_b^{(2)}, \ldots, \boldsymbol{B}_b^{(n)}]\boldsymbol{d} = \begin{Bmatrix} \psi_{1,1} \\ \psi_{2,2} \\ \psi_{1,2} + \psi_{2,1} \end{Bmatrix}, \\
\boldsymbol{B}_s\boldsymbol{d} &= [\boldsymbol{B}_s^{(1)}, \boldsymbol{B}_s^{(2)}, \ldots, \boldsymbol{B}_s^{(n)}]\boldsymbol{d} = \begin{Bmatrix} w_{,1} + \psi_1 \\ w_{,2} + \psi_2 \end{Bmatrix},
\end{aligned} \tag{16}$$

and

$$\boldsymbol{B}_m^{(i)} = \begin{bmatrix} N_{i,x} & 0 & 0 & 0 & 0 \\ 0 & N_{i,y} & 0 & 0 & 0 \\ N_{i,y} & N_{i,x} & 0 & 0 & 0 \end{bmatrix}, \quad \boldsymbol{B}_b^{(i)} = \begin{bmatrix} 0 & 0 & 0 & N_{i,x} & 0 \\ 0 & 0 & 0 & 0 & N_{i,y} \\ 0 & 0 & 0 & N_{i,y} & N_{i,x} \end{bmatrix}, \quad \boldsymbol{B}_s^{(i)} = \begin{bmatrix} 0 & 0 & N_{i,x} & N_i & 0 \\ 0 & 0 & N_{i,y} & 0 & N_i \end{bmatrix}. \tag{17}$$

The constitutive equations of in-plane and transverse shear parts are

$$\begin{Bmatrix} \sigma_{11} \\ \sigma_{22} \\ \sigma_{12} \end{Bmatrix} = [\boldsymbol{Q}] \begin{Bmatrix} \epsilon_{11} \\ \epsilon_{22} \\ 2\epsilon_{12} \end{Bmatrix}, \tag{18}$$

$$\begin{Bmatrix} \sigma_{31} \\ \sigma_{32} \end{Bmatrix} = [\boldsymbol{C}_G] \begin{Bmatrix} 2\epsilon_{31} \\ 2\epsilon_{32} \end{Bmatrix}, \tag{19}$$

where $[\boldsymbol{Q}]$ is the 3×3 matrix representing the plane-stress constitutive relationship. $[\boldsymbol{Q}]$ is defined in terms of the submatrices of $[\boldsymbol{C}]$, namely

$$\boldsymbol{C}_{aa} = \begin{bmatrix} C_{11} & C_{12} & C_{16} \\ C_{12} & C_{22} & C_{26} \\ C_{16} & C_{26} & C_{66} \end{bmatrix}, \quad \boldsymbol{C}_{ab} = \begin{bmatrix} C_{13} & C_{14} & C_{15} \\ C_{23} & C_{24} & C_{25} \\ C_{63} & C_{64} & C_{65} \end{bmatrix}, \quad \boldsymbol{C}_{bb} = \begin{bmatrix} C_{33} & C_{34} & C_{35} \\ C_{43} & C_{44} & C_{45} \\ C_{35} & C_{45} & C_{55} \end{bmatrix}, \tag{20}$$

via the formula

$$[\boldsymbol{Q}] = \boldsymbol{C}_{aa} - \boldsymbol{C}_{ab}\boldsymbol{C}_{bb}^{-1}\boldsymbol{C}_{ab}^T.$$

The components C_{ij} of the matrix $[\boldsymbol{C}]$ are the elastic constants written in Voigt form. Further, in (19), we have set

$$[\boldsymbol{C}_G] = \begin{bmatrix} C_{55} & C_{45} \\ C_{45} & C_{44} \end{bmatrix}, \tag{21}$$

The internal virtual work due to force stress resultants is

$$\begin{aligned}\delta U_{\text{bulk}}^{N_{\alpha\beta}} &= \int_\Omega N_{\alpha\beta}\delta u^0_{\alpha,\beta}\,dA \\ &= \delta \boldsymbol{d}^T\left[\int_\Omega \boldsymbol{B}_m^T\left(\int_{-h/2}^{h/2}[\boldsymbol{Q}](\boldsymbol{B}_m + x_3\boldsymbol{B}_b)\,dx_3\right)dA\right]\boldsymbol{d} \\ &= \delta \boldsymbol{d}^T\left[\int_\Omega \boldsymbol{B}_m^T[\boldsymbol{A}]\boldsymbol{B}_m + \boldsymbol{B}_m^T[\boldsymbol{B}]\boldsymbol{B}_b\,dA\right]\boldsymbol{d},\end{aligned} \tag{22}$$

where

$$[\boldsymbol{A}] = \int_{-h/2}^{h/2}[\boldsymbol{Q}]\,dx_3, \quad [\boldsymbol{B}] = \int_{-h/2}^{h/2}[\boldsymbol{Q}]x_3\,dx_3. \tag{23}$$

Similarly, the internal virtual work terms due to moment resultants and shear stress resultants are

$$\begin{aligned}\delta U_{\text{bulk}}^{M_{\alpha\beta}} &= \int_\Omega M_{\alpha\beta}\delta\psi_{\alpha,\beta}\,dA \\ &= \delta \boldsymbol{d}^T\left[\int_\Omega\left(\int_{-h/2}^{h/2}x_3\boldsymbol{B}_b^T[\boldsymbol{Q}](\boldsymbol{B}_m + x_3\boldsymbol{B}_b)\,dx_3\right)dA\right]\boldsymbol{d} \\ &= \delta \boldsymbol{d}^T\left[\int_\Omega \boldsymbol{B}_b^T[\boldsymbol{B}]\boldsymbol{B}_m + \boldsymbol{B}_b^T[\boldsymbol{D}]\boldsymbol{B}_b\,dA\right]\boldsymbol{d},\end{aligned} \tag{24}$$

$$\begin{aligned}\delta U_{\text{bulk}}^{Q_\alpha} &= \int_\Omega Q_\alpha(\delta w_{,\alpha} + \delta\psi_\alpha)\,dA \\ &= \delta \boldsymbol{d}^T\left[\int_\Omega k\boldsymbol{B}_s^T\left(\int_{-h/2}^{h/2}[\boldsymbol{C}_G]\boldsymbol{B}_s\,dx_3\right)dA\right]\boldsymbol{d} \\ &= \delta \boldsymbol{d}^T\left[\int_\Omega k\boldsymbol{B}_s^T[\boldsymbol{G}]\boldsymbol{B}_s\,dA\right]\boldsymbol{d},\end{aligned} \tag{25}$$

where

$$[\boldsymbol{D}] = \int_{-h/2}^{h/2}[\boldsymbol{Q}]x_3^2\,dx_3, \quad [\boldsymbol{G}] = \int_{-h/2}^{h/2}[\boldsymbol{C}_G]\,dx_3 \tag{26}$$

and k is the shear correction factor. Using (22), (24), and (25), the bulk internal energy can be written in the matrix form as

$$\begin{aligned}\delta U_{\text{bulk}} &= \delta U_{\text{bulk}}^{N_{\alpha\beta}} + \delta U_{\text{bulk}}^{M_{\alpha\beta}} + \delta U_{\text{bulk}}^{Q_\alpha} \\ &= \delta \boldsymbol{d}^T\left[\int_\Omega \boldsymbol{B}_m^T[\boldsymbol{A}]\boldsymbol{B}_m + \boldsymbol{B}_b^T[\boldsymbol{D}]\boldsymbol{B}_b\,dA\right]\boldsymbol{d} + \delta \boldsymbol{d}^T\left[\int_\Omega k\boldsymbol{B}_s^T[\boldsymbol{G}]\boldsymbol{B}_s\,dA\right]\boldsymbol{d} \\ &\qquad + \delta \boldsymbol{d}^T\left[\int_\Omega \boldsymbol{B}_m^T[\boldsymbol{B}]\boldsymbol{B}_b + \boldsymbol{B}_b^T[\boldsymbol{B}]\boldsymbol{B}_m\,dA\right]\boldsymbol{d}.\end{aligned} \tag{27}$$

Both top and bottom surface energies are considered when determining the internal virtual work due to surface energy. The surface stress term is divided into two components. The first component is

determined by the initial surface stress at zero strain, and the second component by the surface elastic tensor. Thus,

$$\delta U_{\text{surf}} = \int_{\Omega^{\pm}} \tau^0_{\alpha\beta}\delta\big(u^0_{\alpha,\beta} \pm \tfrac{h}{2}\psi_{\alpha,\beta}\big)\,dA + \int_{\Omega^{\pm}} T_{\alpha\beta\kappa\lambda}\big(u^0_{\kappa,\lambda} \pm \tfrac{h}{2}\psi_{\kappa,\lambda}\big)\delta\big(u^0_{\alpha,\beta} \pm \tfrac{h}{2}\psi_{\alpha,\beta}\big)\,dA. \tag{28}$$

In terms of nodal displacement, the surface strain field is defined as

$$\begin{Bmatrix} \epsilon^{s\pm}_{11} \\ \epsilon^{s\pm}_{22} \\ 2\epsilon^{s\pm}_{12} \end{Bmatrix} = \boldsymbol{B}_{\tau\pm}\boldsymbol{d} = \big[\boldsymbol{B}^{(1)}_{\tau\pm}, \boldsymbol{B}^{(2)}_{\tau\pm}, \ldots, \boldsymbol{B}^{(n)}_{\tau\pm}\big]\boldsymbol{d}, \tag{29}$$

with

$$\boldsymbol{B}^{(i)}_{\tau\pm} = \begin{bmatrix} N_{i,x} & 0 & 0 & \big(\pm\frac{h}{2}\big)N_{i,x} & 0 \\ 0 & N_{i,y} & 0 & 0 & \big(\pm\frac{h}{2}\big)N_{i,y} \\ N_{i,y} & N_{i,x} & 0 & \big(\pm\frac{h}{2}\big)N_{i,y} & \big(\pm\frac{h}{2}\big)N_{i,x} \end{bmatrix}; \tag{30}$$

$\boldsymbol{B}_{\tau\pm}$ is the matrix that represents the relationship between surface strain and nodal displacement. The internal virtual work due to the surface energy can be written in the following discrete form:

$$\begin{aligned}\delta U_{\text{surf}} = \delta\boldsymbol{d}^T \int_{\Omega^+} \boldsymbol{B}^T_{\tau+}\{\tau^0\}\,dA + \delta\boldsymbol{d}^T \int_{\Omega^-} \boldsymbol{B}^T_{\tau-}\{\tau^0\}\,dA \\ + \delta\boldsymbol{d}^T\bigg[\int_{\Omega^+} \boldsymbol{B}^T_{\tau+}[\boldsymbol{T}]\boldsymbol{B}_{\tau+}\,dA\bigg]\boldsymbol{d} + \delta\boldsymbol{d}^T\bigg[\int_{\Omega^-} \boldsymbol{B}^T_{\tau-}[\boldsymbol{T}]\boldsymbol{B}_{\tau-}\,dA\bigg]\boldsymbol{d},\end{aligned} \tag{31}$$

where $\{\tau^0\}$, the initial surface stress vector, and $[\boldsymbol{T}]$, the surface elastic tensor, are defined by

$$\{\tau^0\} = \begin{Bmatrix} \tau^0_{11} \\ \tau^0_{22} \\ \tau^0_{12} \end{Bmatrix}, \quad [\boldsymbol{T}] = \begin{bmatrix} T_{1111} & T_{1122} & T_{1112} \\ T_{2211} & T_{2222} & T_{2212} \\ T_{1211} & T_{1222} & T_{1212} \end{bmatrix}. \tag{32}$$

If the material and surface orientations of both the top (Ω^+) and bottom (Ω^-) surfaces are the same, (31) can be rewritten in terms of $\boldsymbol{B}_m$ and $\boldsymbol{B}_b$ from (17), as follows:

$$\delta U_{\text{surf}} = \delta\boldsymbol{d}^T\bigg[\int_{\Omega} 2\boldsymbol{B}^T_m\{\tau^0\}\,dA\bigg] + \delta\boldsymbol{d}^T\bigg[\int_{\Omega} 2\boldsymbol{B}^T_m[\boldsymbol{T}]\boldsymbol{B}_m\,dA\bigg]\boldsymbol{d} + \delta\boldsymbol{d}^T\bigg[\int_{\Omega} \tfrac{h^2}{2}\boldsymbol{B}^T_b[\boldsymbol{T}]\boldsymbol{B}_b\,dA\bigg]\boldsymbol{d}. \tag{33}$$

Combining (27) and (33) yields the following equation for internal virtual work, assuming the same surface type on both top and bottom surfaces:

$$\begin{aligned}\delta U = \delta\boldsymbol{d}^T\bigg[\int_{\Omega} \boldsymbol{B}^T_m[\boldsymbol{A}']\boldsymbol{B}_m + \boldsymbol{B}^T_b[\boldsymbol{D}']\boldsymbol{B}_b\,dA\bigg]\boldsymbol{d} + \delta\boldsymbol{d}^T\bigg[\int_{\Omega} k\boldsymbol{B}^T_s[\boldsymbol{G}]\boldsymbol{B}_s\,dA\bigg]\boldsymbol{d} \\ + \delta\boldsymbol{d}^T\bigg[\int_{\Omega} \boldsymbol{B}^T_m[\boldsymbol{B}]\boldsymbol{B}_b + \boldsymbol{B}^T_b[\boldsymbol{B}]\boldsymbol{B}_m\,dA\bigg]\boldsymbol{d} + \delta\boldsymbol{d}^T\bigg[\int_{\Omega} 2\boldsymbol{B}^T_m\{\tau^0\}\,dA\bigg],\end{aligned} \tag{34}$$

where

$$[\boldsymbol{A}'] = [\boldsymbol{A}] + 2[\boldsymbol{T}] = h[\boldsymbol{Q}] + 2[\boldsymbol{T}] \quad \text{and} \quad [\boldsymbol{D}'] = [\boldsymbol{D}] + \tfrac{1}{2}h^2[\boldsymbol{T}] = \tfrac{1}{12}h^3[\boldsymbol{Q}] + \tfrac{1}{2}h^2[\boldsymbol{T}] \tag{35}$$

are respectively the effective membrane and effective bending rigidities.

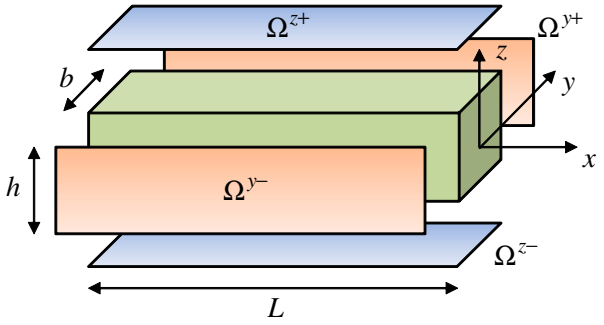

Figure 2. Schematic diagram of a rectangular nanowire with four surfaces.

2.2. ***Multiscale continuum model for a nanowire.*** To develop a model for a nanowire, a simple beam model with a rectangular cross-section is considered. This model accounts for both bending and shear deformations, but not for torsional effect. In Figure 2, x is the axial direction, and y and z represent two perpendicular directions of the rectangular cross-section. Under the assumptions set forth by Timoshenko beam theory, the following displacement field is used:

$$\begin{aligned} u_x &= u_x^0 + y\psi_y + z\psi_z, \\ u_y &= u_y^0 = v, \\ u_z &= u_z^0 = w, \end{aligned} \tag{36}$$

The strain field is defined as

$$\begin{aligned} \epsilon_{xx} &= u_{x,x}^0 + y\psi_{y,x} + z\psi_{z,x}, \\ \gamma_{xy} &= v_{,x} + \psi_y, \\ \gamma_{xz} &= w_{,x} + \psi_z. \end{aligned} \tag{37}$$

The displacements on the y-surface are given as

$$\begin{aligned} u_x^{y\pm} &= u_x^0 \pm \tfrac{b}{2}\psi_y + z\psi_z, \\ u_y^{y\pm} &= v, \\ u_z^{y\pm} &= w, \end{aligned} \tag{38}$$

where $y+$ and $y-$ represent the top and bottom surfaces normal to the y-direction, and b is the beam width along the y-direction. Similarly, the displacement on the z-surface can be written as follows:

$$\begin{aligned} u_x^{z\pm} &= u_x^0 + y\psi_y \pm \tfrac{h}{2}\psi_z, \\ u_y^{z\pm} &= v, \\ u_z^{z\pm} &= w, \end{aligned} \tag{39}$$

where $z+$ and $z-$ represent the top and bottom surfaces normal to the z-direction, and h is the beam thickness along the z-direction.

According to the virtual work principle, the internal virtual work is equal to the external virtual work. The external virtual work is defined as

$$\delta W_E = \int_L p_x \delta u_x^0 + p_y \delta v + p_z \delta w \, dx, \tag{40}$$

where p_x, p_y, and p_z are external forces in the x, y, and z directions, respectively. The internal virtual work includes both bulk and surface energy components. The internal virtual work of the bulk component can be written as

$$\begin{aligned}
\delta U_{\text{bulk}} &= \int_V \sigma_{ij} \delta \epsilon_{ij} \, dV \\
&= \int_V \sigma_{xx} \delta \epsilon_{xx} \, dV + \int_V \sigma_{xy} \delta \gamma_{xy} \, dV + \int_V \sigma_{xz} \delta \gamma_{xz} \, dV \\
&= \int_L E_x A u_{x,x}^0 \delta u_{x,x}^0 + E_x I_{yy} \psi_{y,x} \delta \psi_{y,x} + E_x I_{zz} \psi_{z,x} \delta \psi_{z,x} \, dx \\
&\qquad + \int_L kG_{66} A(\psi_y + v_{,x}) \delta(\psi_y + v_{,x}) \, dx + \int_L kG_{55} A(\psi_z + w_{,x}) \delta(\psi_z + w_{,x}) \, dx,
\end{aligned} \tag{41}$$

where E_x is the Young's modulus, k is the shear correction factor, A is the cross-sectional area, and I_{yy} and I_{zz} comprise the second moment of area, defined as

$$I_{yy} = \int_A y^2 \, dA, \quad I_{zz} = \int_A z^2 \, dA. \tag{42}$$

In the multiscale continuum model for a nanofilm, there are only two surfaces, top and bottom, whereas a nanowire with a rectangular cross-section has four surfaces: two in the y-direction (Ω^{y+} and Ω^{y-}) and two in the z-direction (Ω^{z+} and Ω^{z-}). The internal virtual work of these four surfaces is calculated as

$$\begin{aligned}
\delta U_{\text{surf}} &= \int_{\Omega^{y\pm}} (\tau_{xx}^{y\pm} \delta \epsilon_{xx}^{y\pm} + \tau_{xz}^{y\pm} \delta \gamma_{xz}^{y\pm}) \, d\Omega^{y\pm} + \int_{\Omega^{z\pm}} (\tau_{xx}^{z\pm} \delta \epsilon_{xx}^{z\pm} + \tau_{xy}^{z\pm} \delta \gamma_{xy}^{z\pm}) \, d\Omega^{z\pm} \\
&= \int_{\Omega^{y\pm}} \tau_{xx}^{y\pm} \delta (u_{x,x}^0 \pm \tfrac{b}{2} \psi_{y,x} + z \psi_{z.x}) + \tau_{xz}^{y\pm} \delta (\psi_z + w_{,x}) \, d\Omega^{y\pm} \\
&\quad + \int_{\Omega^{z\pm}} \tau_{xx}^{z\pm} \delta (u_{x,x}^0 + y \psi_{y,x} \pm \tfrac{h}{2} \psi_{z,x}) + \tau_{xy}^{z\pm} \delta (\psi_y + v_{,x}) \, d\Omega^{z\pm},
\end{aligned} \tag{43}$$

where Ω is the surface domain, $\tau_{\alpha\beta}$ is the surface stress, and superscript $y\pm$ and $z\pm$ represent the y-surface and z-surface, respectively. Using linear surface elasticity, defined as

$$\tau_{\alpha\beta}^s = \tau_{\alpha\beta}^{s0} + T_{\alpha\beta\kappa\lambda}^s \epsilon_{\kappa\lambda}^{s\pm},$$

the surface internal virtual work can be divided into two parts: the initial surface stress $\delta U_{\text{surf}}^{(\tau)}$ and the surface elastic tensor $\delta U_{\text{surf}}^{(T)}$:

$$\delta U_{\text{surf}} = \delta U_{\text{surf}}^{(\tau)} + \delta U_{\text{surf}}^{(T)}. \tag{44}$$

Their values are

$$\delta U_{\text{surf}}^{(\tau)} = \int_{\Omega^{y\pm}} \tau_{xx}^{y0}\delta\big(u_{x,x}^0 \pm \tfrac{b}{2}\psi_{y,x} + z\psi_{z,x}\big) + \tau_{xz}^{y0}\delta(\psi_z + w_{,x})\,d\Omega^{y\pm} + \int_{\Omega^{z\pm}} \tau_{xx}^{z0}\delta\big(u_{x,x}^0 + y\psi_{y,x} \pm \tfrac{h}{2}\psi_{z,x}\big) + \tau_{xy}^{z0}\delta(\psi_y + v_{,x})\,d\Omega^{z\pm} \tag{45}$$

and

$$\begin{aligned}\delta U_{\text{surf}}^{(T)} = {} & \int_{\Omega^{y\pm}} T_{1111}^{y}\big(u_{x,x}^0 \pm \tfrac{b}{2}\psi_{y,x} + z\psi_{z,x}\big)\delta\big(u_{x,x}^0 \pm \tfrac{b}{2}\psi_{y,x} + z\psi_{z,x}\big)\,d\Omega^{y\pm} \\ & + \int_{\Omega^{y\pm}} T_{1212}^{y}(\psi_z + w_{,x})\delta(\psi_z + w_{,x})\,d\Omega^{y\pm} \\ & + \int_{\Omega^{z\pm}} T_{1111}^{z}\big(u_{x,x}^0 + y\psi_{y,x} \pm \tfrac{h}{2}\psi_{z,x}\big)\delta\big(u_{x,x}^0 + y\psi_{y,x} \pm \tfrac{h}{2}\psi_{z,x}\big)\,d\Omega^{z\pm} \\ & + \int_{\Omega^{z\pm}} T_{1212}^{z}(\psi_y + v_{,x})\delta(\psi_y + v_{,x})\,d\Omega^{z\pm}.\end{aligned} \tag{46}$$

Assuming that both the top and bottom surfaces in the y-direction are of the same type ($\Omega^{y+} = \Omega^{y-}$) and that both surfaces in the z-direction are also the same ($\Omega^{z+} = \Omega^{z-}$), the initial surface stress component of the internal virtual work in (45) yields

$$\delta U_{\text{surf}}^{(\tau)} = \int_{\Omega^{y}} 2\tau_{xx}^{y0}\delta(u_{x,x}^0 + z\psi_{z,x}) + 2\tau_{xz}^{y0}\delta(\psi_z + w_{,x})\,d\Omega^{y} + \int_{\Omega^{z}} 2\tau_{xx}^{z0}\delta(u_{x,x}^0 + y\psi_{y,x}) + 2\tau_{xy}^{z0}\delta(\psi_y + v_{,x})\,d\Omega^{z}, \tag{47}$$

and hence

$$\delta U_{\text{surf}}^{(\tau)} = \int_L 2h\tau_{xx}^{y0}\delta u_{x,x}^0 + 2h\tau_{xz}^{y0}\delta(\psi_z + w_{,x})\,dx + \int_L 2b\tau_{xx}^{z0}\delta u_{x,x}^0 + 2b\tau_{xy}^{z0}\delta(\psi_y + v_{,x})\,dx. \tag{48}$$

The surface elastic tensor portion of the internal virtual work in (46) can be rewritten as

$$\begin{aligned}\delta U_{\text{surf}}^{(T)} = {} & \int_{\Omega^{y}} 2T_{1111}^{y}(u_{x,x}^0 + z\psi_{z,x})\delta(u_{x,x}^0 + z\psi_{z,x}) + 2T_{1111}^{y}\big(\tfrac{b}{2}\psi_{y,x}\big)\delta\big(\tfrac{b}{2}\psi_{y,x}\big)\,d\Omega^{y} \\ & + \int_{\Omega^{y}} 2T_{1212}^{y}(\psi_z + w_{,x})\delta(\psi_z + w_{,x})\,d\Omega^{y} \\ & + \int_{\Omega^{z}} 2T_{1111}^{z}(u_{x,x}^0 + y\psi_{y,x})\delta(u_{x,x}^0 + y\psi_{y,x}) + 2T_{1111}^{z}\big(\tfrac{h}{2}\psi_{z,x}\big)\delta\big(\tfrac{h}{2}\psi_{z,x}\big)\,d\Omega^{z} \\ & + \int_{\Omega^{z}} 2T_{1212}^{z}(\psi_y + v_{,x})\delta(\psi_y + v_{,x})\,d\Omega^{z},\end{aligned} \tag{49}$$

and hence

$$\begin{aligned}\delta U_{\text{surf}}^{(T)} = &\int_L 2hT_{1111}^{y}(u_{x,x}^0)\delta(u_{x,x}^0)\,dx \\ &+ \int_L \tfrac{1}{6}h^3T_{1111}^{y}(\psi_{z,x})\delta(\psi_{z,x}) + \tfrac{1}{2}hb^2T_{1111}^{y}(\psi_{y,x})\delta(\psi_{y,x})\,dx \\ &+ \int_L 2hT_{1212}^{y}(\psi_z + w_{,x})\delta(\psi_z + w_{,x})\,dx \\ &+ \int_L 2bT_{1111}^{z}(u_{x,x}^0)\delta(u_{x,x}^0)\,dx \\ &+ \int_L \tfrac{1}{6}b^3T_{1111}^{z}(\psi_{y,x})\delta(\psi_{y,x}) + \tfrac{1}{2}bh^2T_{1111}^{z}(\psi_{z,x})\delta(\psi_{z,x})\,dx \\ &+ \int_L 2bT_{1212}^{z}(\psi_y + v_{,x})\delta(\psi_y + v_{,x})\,dx. \end{aligned} \tag{50}$$

Finite element implementation for a nanowire. The displacement field of a nanowire can be interpolated using an interpolation function N_i and the nodal displacement

$$\boldsymbol{d} = \left[(u_x^0, v, w, \psi_y, \psi_z)_1, \ldots, (u_x^0, v, w, \psi_y, \psi_z)_n\right]^T,$$

so that

$$u_x^0 = \sum_{i=1}^{n} N_i u_{xi}^0, \quad v = \sum_{i=1}^{n} N_i v_i, \quad w = \sum_{i=1}^{n} N_i w_i, \quad \psi_y = \sum_{i=1}^{n} N_i \psi_{yi}, \quad \psi_z = \sum_{i=1}^{n} N_i \psi_{zi}, \tag{51}$$

where n is the number of nodes per element. Using these nodal displacements, the membrane aspect of the bulk internal virtual work can be rewritten as

$$\delta U_{\text{bulk}}^{\text{mem}} = \int_L E_x A u_{x,x}^0 \delta u_{x,x}^0\,dx = \delta \boldsymbol{d}^T \left[\int_L \boldsymbol{B}_m^T[\boldsymbol{A}]\boldsymbol{B}_m\,dx\right]\boldsymbol{d}, \tag{52}$$

where

$$[\boldsymbol{A}] = [E_x A], \tag{53}$$

$$\{u_{x,x}^0\} = \boldsymbol{B}_m \boldsymbol{d} = [\boldsymbol{B}_m^{(1)}, \boldsymbol{B}_m^{(2)}, \ldots, \boldsymbol{B}_m^{(n)}]\boldsymbol{d}, \tag{54}$$

$$\boldsymbol{B}_m^{(i)} = \begin{bmatrix} N_{i,x} & 0 & 0 & 0 & 0 \end{bmatrix}. \tag{55}$$

The bending component of the internal virtual work is defined as

$$\begin{aligned}\delta U_{\text{bulk}}^{\text{bend}} &= \int_L E_x I_{yy}\psi_{y,x}\delta\psi_{y,x} + E_x I_{zz}\psi_{z,x}\delta\psi_{z,x}\,dx \\ &= \delta \boldsymbol{d}^T\left[\int_L \boldsymbol{B}_b^T[\boldsymbol{D}]\boldsymbol{B}_b\,dx\right]\boldsymbol{d}, \end{aligned} \tag{56}$$

where

$$[\boldsymbol{D}] = \begin{bmatrix} E_x I_{yy} & 0 \\ 0 & E_x I_{zz} \end{bmatrix}, \tag{57}$$

$$\begin{Bmatrix} \psi_{y,x} \\ \psi_{z,x} \end{Bmatrix} = \boldsymbol{B}_b \boldsymbol{d} = [\boldsymbol{B}_b^{(1)}, \boldsymbol{B}_b^{(2)}, \ldots, \boldsymbol{B}_b^{(n)}]\boldsymbol{d}, \tag{58}$$

$$\boldsymbol{B}_b^{(i)} = \begin{bmatrix} 0 & 0 & 0 & N_{i,x} & 0 \\ 0 & 0 & 0 & 0 & N_{i,x} \end{bmatrix}. \tag{59}$$

The transverse shear component of the virtual work is

$$\begin{aligned} \delta U_{\text{bulk}}^{\text{shear}} &= \int_L kG_{66}A(\psi_y + v_{,x})\delta(\psi_y + v_{,x})\,dx + \int_L kG_{55}A(\psi_z + w_{,x})\delta(\psi_z + w_{,x})\,dx \\ &= \delta \boldsymbol{d}^T \left[\int_L k \boldsymbol{B}_s^T [\boldsymbol{G}] \boldsymbol{B}_s \, dx \right] \boldsymbol{d}, \end{aligned} \tag{60}$$

where

$$[\boldsymbol{G}] = \begin{bmatrix} G_{66} & 0 \\ 0 & G_{55} \end{bmatrix}, \tag{61}$$

$$\begin{Bmatrix} v_{,x} + \psi_y \\ w_{,x} + \psi_z \end{Bmatrix} = \boldsymbol{B}_s \boldsymbol{d} = [\boldsymbol{B}_s^{(1)}, \boldsymbol{B}_s^{(2)}, \ldots, \boldsymbol{B}_s^{(n)}]\boldsymbol{d}, \tag{62}$$

$$\boldsymbol{B}_s^{(i)} = \begin{bmatrix} 0 & N_{i,x} & 0 & N_i & 0 \\ 0 & 0 & N_{i,x} & 0 & N_i \end{bmatrix}. \tag{63}$$

The internal virtual work of the bulk component can be obtained with a summation of Equations (52), (56), and (60):

$$\delta U_{\text{bulk}} = \delta \boldsymbol{d}^T \left[\int_L \boldsymbol{B}_m^T [\boldsymbol{A}] \boldsymbol{B}_m + \boldsymbol{B}_b^T [\boldsymbol{D}] \boldsymbol{B}_b + k \boldsymbol{B}_s^T [\boldsymbol{G}] \boldsymbol{B}_s \, dx \right] \boldsymbol{d}. \tag{64}$$

As for surface internal virtual work, the initial surface stress component of the internal virtual work in (48) can be written in the following discrete form:

$$\delta U_{\text{surf}}^{(\tau)} = \int_L \begin{Bmatrix} u_{x,x}^0 \\ \psi_y + v_{,x} \\ \psi_z + w_{,x} \end{Bmatrix}^T \begin{Bmatrix} 2h\tau_{xx}^{y0} + 2b\tau_{xx}^{z0} \\ 2b\tau_{xy}^{z0} \\ 2h\tau_{xz}^{y0} \end{Bmatrix} dx = \delta \boldsymbol{d}^T \left[\int_L \boldsymbol{B}_\tau^T \{\tau^0\} \, dx \right], \tag{65}$$

where

$$\{\tau^0\} = \begin{Bmatrix} 2h\tau_{xx}^{y0} + 2b\tau_{xx}^{z0} \\ 2b\tau_{xy}^{z0} \\ 2h\tau_{xz}^{y0} \end{Bmatrix}, \tag{66}$$

$$\begin{Bmatrix} u_{x,x}^0 \\ \psi_y + v_{,x} \\ \psi_z + w_{,x} \end{Bmatrix} = \boldsymbol{B}_\tau \boldsymbol{d} = [\boldsymbol{B}_\tau^{(1)}, \boldsymbol{B}_\tau^{(2)}, \ldots, \boldsymbol{B}_\tau^{(n)}]\boldsymbol{d}, \tag{67}$$

and

$$\boldsymbol{B}_{\tau}^{(i)} = \begin{bmatrix} N_{i,x} & 0 & 0 & 0 & 0 \\ 0 & N_{i,x} & 0 & N_i & 0 \\ 0 & 0 & N_{i,x} & 0 & N_i \end{bmatrix}. \tag{68}$$

The surface elastic tensor component of the internal virtual work in (50) can be expressed in the following discrete form, under the assumption that $\Omega^{y+} = \Omega^{y-}$ and $\Omega^{z+} = \Omega^{z-}$:

$$\begin{aligned} \delta U_{\text{surf}}^{(T)} &= \int_L (2hT_{1111}^{y} + 2bT_{1111}^{z})(u_{x,x}^{0})\delta(u_{x,x}^{0})\,dx \\ &\quad + \int_L \left(\tfrac{1}{6}h^3 T_{1111}^{y} + \tfrac{1}{2}bh^2 T_{1111}^{z}\right)(\psi_{z,x})\delta(\psi_{z,x})\,dx \\ &\quad + \int_L \left(\tfrac{1}{6}b^3 T_{1111}^{z} + \tfrac{1}{2}hb^2 T_{1111}^{z}\right)(\psi_{y,x})\delta(\psi_{y,x})\,dx \\ &\quad + \int_L 2hT_{1212}^{y}(\psi_z + w_{,x})\delta(\psi_z + w_{,x})\,dx \\ &\quad + \int_L 2bT_{1212}^{z}(\psi_y + v_{,x})\delta(\psi_y + v_{,x})\,dx \\ &= \delta \boldsymbol{d}^T \left[\int_L \boldsymbol{B}_m^T[\boldsymbol{T}_m]\boldsymbol{B}_m + \boldsymbol{B}_b^T[\boldsymbol{T}_b]\boldsymbol{B}_b + \boldsymbol{B}_s^T[\boldsymbol{T}_s]\boldsymbol{B}_s\,dx \right] \boldsymbol{d}, \end{aligned} \tag{69}$$

where

$$\begin{aligned} [\boldsymbol{T}_m] &= [2hT_{1111}^{y} + 2bT_{1111}^{z}], \\ [\boldsymbol{T}_b] &= \begin{bmatrix} \frac{1}{2}b^2 hT_{1111}^{y} + \frac{1}{6}b^3 T_{1111}^{z} & 0 \\ 0 & \frac{1}{6}h^3 T_{1111}^{y} + \frac{1}{2}bh^2 T_{1111}^{z} \end{bmatrix}, \\ [\boldsymbol{T}_s] &= \begin{bmatrix} 2bT_{1212}^{z} & 0 \\ 0 & 2hT_{1212}^{y} \end{bmatrix}, \end{aligned} \tag{70}$$

and

$$\begin{aligned} \{u_{x,x}^{0}\} &= \boldsymbol{B}_m \boldsymbol{d} = [\boldsymbol{B}_m^{(1)}, \boldsymbol{B}_m^{(2)}, \ldots, \boldsymbol{B}_m^{(n)}]\boldsymbol{d}, \\ \begin{Bmatrix} \psi_{y,x} \\ \psi_{z,x} \end{Bmatrix} &= \boldsymbol{B}_b \boldsymbol{d} = [\boldsymbol{B}_b^{(1)}, \boldsymbol{B}_b^{(2)}, \ldots, \boldsymbol{B}_b^{(n)}]\boldsymbol{d}, \\ \begin{Bmatrix} v_{,x} + \psi_y \\ w_{,x} + \psi_z \end{Bmatrix} &= \boldsymbol{B}_s \boldsymbol{d} = [\boldsymbol{B}_s^{(1)}, \boldsymbol{B}_s^{(2)}, \ldots, \boldsymbol{B}_s^{(n)}]\boldsymbol{d}, \end{aligned} \tag{71}$$

with

$$\begin{aligned} \boldsymbol{B}_m^{(i)} &= \begin{bmatrix} N_{i,x} & 0 & 0 & 0 & 0 \end{bmatrix}, \\ \boldsymbol{B}_b^{(i)} &= \begin{bmatrix} 0 & 0 & 0 & N_{i,x} & 0 \\ 0 & 0 & 0 & 0 & N_{i,x} \end{bmatrix}, \\ \boldsymbol{B}_s^{(i)} &= \begin{bmatrix} 0 & N_{i,x} & 0 & N_i & 0 \\ 0 & 0 & N_{i,x} & 0 & N_i \end{bmatrix}. \end{aligned} \tag{72}$$

From (65) and (69), the matrix form of the surface internal virtual work can be written as

$$\delta U_{\text{surf}} = \delta \boldsymbol{d}^T \left[\int_L \boldsymbol{B}_m^T [\boldsymbol{T}_m] \boldsymbol{B}_m + \boldsymbol{B}_b^T [\boldsymbol{T}_b] \boldsymbol{B}_b + \boldsymbol{B}_s^T [\boldsymbol{T}_s] \boldsymbol{B}_s \, dx \right] \boldsymbol{d} + \delta \boldsymbol{d}^T \left[\int_L \boldsymbol{B}_\tau^T \{\tau^0\} \, dx \right]. \tag{73}$$

Consequently, the following matrix form of the internal virtual work is obtained for a nanowire with a rectangular cross-section:

$$\delta U = \delta \boldsymbol{d}^T \left[\int_L \boldsymbol{B}_m^T [\boldsymbol{A}'] \boldsymbol{B}_m + \boldsymbol{B}_b^T [\boldsymbol{D}'] \boldsymbol{B}_b + k \boldsymbol{B}_s^T [\boldsymbol{G}'] \boldsymbol{B}_s \, dx \right] \boldsymbol{d} + \delta \boldsymbol{d}^T \left[\int_L \boldsymbol{B}_\tau^T \{\tau^0\} \, dx \right], \tag{74}$$

where

$$[\boldsymbol{A}'] = \left[\boldsymbol{A} \left(E_1 + \frac{2}{b} T^y_{1111} + \frac{2}{h} T^z_{1111} \right) \right], \tag{75}$$

$$[\boldsymbol{D}'] = \begin{bmatrix} I_{yy} \left(E_1 + \dfrac{6}{b} T^y_{1111} + \dfrac{2}{h} T^z_{1111} \right) & 0 \\ 0 & I_{zz} \left(E_1 + \dfrac{2}{b} T^y_{1111} + \dfrac{6}{h} T^z_{1111} \right) \end{bmatrix}, \tag{76}$$

$$[\boldsymbol{G}'] = \begin{bmatrix} A \left(G_{66} + \dfrac{2}{h} T^z_{1212} \right) & 0 \\ 0 & A \left(G_{55} + \dfrac{2}{b} T^y_{1212} \right) \end{bmatrix}. \tag{77}$$

3. Elastic modulus and surface elastic tensor

In this study, an MD simulation is performed to calculate the elastic properties of bulk material. FCC single crystal copper is used as a test material. The LAMMPS software (http://lammps.sandia.gov) [Plimpton 1995] and the embedded atom method (EAM) [Daw and Baskes 1984; Foiles et al. 1986] are utilized for the MD simulation. Four nanofilms and three nanowires of different crystallographic orientations are investigated: {100}/<100>, {100}/<110>, {111}/<110>, and {110}/<100> nanofilms, and <100>/{100}, <100>/{110}, and <110>/{100} nanowires.

3.1. ***Elastic modulus of the bulk material.*** In order to calculate the elastic constants of single-crystal copper, a $4 \times 4 \times 4$ unit cell with periodic boundary conditions (PBCs) [Rapaport 2004] is utilized. When a periodic boundary condition is applied, a particle that moves to the right will reappear on the left, as shown in Figure 3(c). PBCs are applied to all directions in the bulk simulation. For initial relaxation, the MD simulations are performed under an isothermal-isobaric ensemble (where NPT represents a constant number of atoms, constant pressure, and a constant temperature) at 0.1 K for 200 picoseconds. After that, the simulation box is deformed slowly, via a 0.01% applied strain in the 1-direction, under the canonical ensemble (where NVT denotes a constant number of atoms, constant volume, and constant temperature) over a span of 50 picoseconds, as shown in Figure 3(a). Next, a 50-picosecond MD simulation is performed to get the average values of the virial stresses, which are defined as

$$\sigma^v_{ij} = \frac{1}{V_0} \sum_\alpha \left[-m^\alpha v_i^\alpha v_i^\beta + \frac{1}{2} \sum_{\beta=1}^{N} (R_i^\beta - R_i^\alpha) F_j^{\alpha\beta} \right], \tag{78}$$

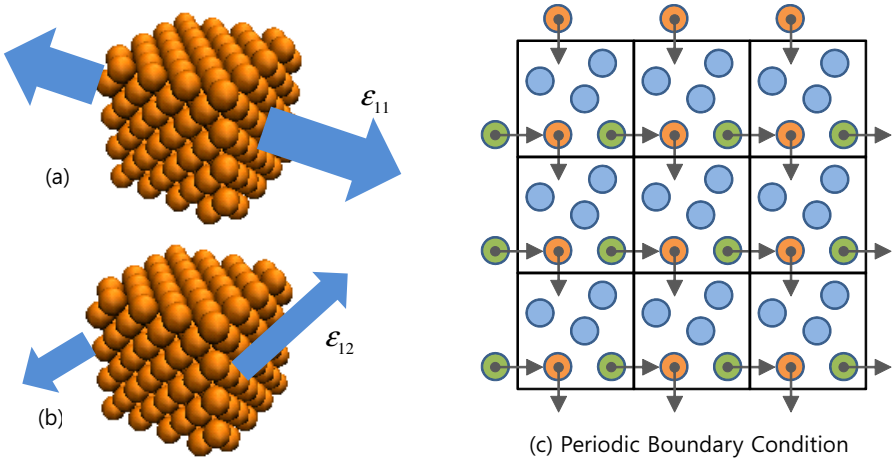

Figure 3. Molecular dynamics simulation for the calculation of elastic constants: (a) depiction of normal strain; (b) depiction of shear strain; (c) schematic of periodic boundary condition.

where σ_{ij}^v is a component of virial stress, V_0 is the volume of the simulation box, m^α is the mass, v_i^α is the i-directional velocity component, R_i^α is the i-directional position of atom α, and $F_j^{\alpha\beta}$ is the j-directional interatomic force between atoms α and β [Subramaniyan and Sun 2008]. The same procedure is performed under shear deformation for a shear component (see Figure 3(b)). As a result of these simulations, the material constants C_{11}, C_{12}, and C_{44} are calculated using the linear constitutive relationship $\sigma_i^v = C_{ij}\epsilon_j$:

$$\begin{aligned} \sigma_1^v &= C_{11}\hat{\epsilon}_1, \\ \sigma_2^v &= C_{12}\hat{\epsilon}_1, \\ \sigma_4^v &= C_{44}\hat{\epsilon}_4, \end{aligned} \tag{79}$$

where σ_i^v, C_{ij}, and $\hat{\epsilon}_i$ are virial stress, elastic constant, and applied strain in Voigt notation, respectively. The elastic constants of the bulk material are listed in Voigt form in Table 1. The elastic constants of the {100}/<100> direction are obtained from the MD simulation, and those of the other directions are calculated via coordinate transformations based on the C_{11}, C_{12}, and C_{44} values of the {100}/<100> direction.

The {100}/<100> nanofilm features {100} surfaces on the top and bottom. The two in-plane axes of the surface exist in the <100> direction. In this case, the film's material properties have cubic symmetry. The Young's modulus value of the {100}/<100> nanofilm is 61.5 GPa, and its Poisson's ratio is 0.43.

The surface type of the {100}/<110> nanofilm is also {100}, but its two in-plane axes are oriented in the <110> direction. The values of Young's moduli in the in-plane direction (E_1 and E_2) are 126.0 GPa, and the Poisson's ratios are $\nu_{12} = -0.18$ and $\nu_{13} = 0.87$.

Being isotropic, the {111} surface has uniform material properties in all in-plane directions. However, the {111} nanofilm has nonzero values for C_{14}, C_{24}, and C_{56} ($C_{14} = -C_{24} = 25.9$ GPa and $C_{56} =$

	{100}/<100>	{100}/<110>	{111}/<110>	{110}/<100>
C_{11}	167.3	222.1	222.1	167.3
C_{22}	167.3	222.1	222.1	222.1
C_{33}	167.3	167.3	240.4	222.1
C_{12}	124.2	69.3	105.9	124.2
C_{13}	124.2	124.2	87.6	124.2
C_{23}	124.2	124.2	87.6	69.3
C_{44}	76.4	76.4	39.9	21.6
C_{55}	76.4	76.4	39.9	76.4
C_{66}	76.4	21.6	58.1	76.4

Table 1. Elastic constants of bulk copper film (in GPa).

25.9 GPa). These variables equal zero for all other orthotropic surfaces. The Young's modulus of the in-plane direction (E_1) is 126.0 GPa, and its Poisson's ratio is $\nu_{12} = 0.52$.

Unlike {100} and {111} surfaces, the {110} surface is not axis-symmetric. The {110}/<100> surface has two different in-plane axis orientations: <100> for the 1-direction and <110> for the 2-direction. The Young's moduli of these two orientations are $E_1 = 61.5$ GPa and $E_2 = E_3 = 126.0$ GPa, respectively, and their Poisson's ratios are $\nu_{12} = 0.43$ and $\nu_{21} = 0.87$.

As for copper nanowires, the Young's moduli of both <100>/{100} and <100>/{110} nanowires are 61.5 GPa, and the Young's modulus of a <110>/{100} nanowire is 126.0 GPa.

3.2. ***Size-dependent elasticity and surface elastic tensor of copper nanofilms.*** For a nanoscaled thin film, mechanical properties such as Young's modulus and Poisson's ratio vary depending on the film thickness. An MD simulation is performed to evaluate the size-dependent elastic properties of copper nanofilms. Four types of MD model are used for the calculation of effective moduli, simulating nanofilms with {100}/<100>, {100}/<110>, {111}/<110>, and {110}/<100> surfaces.

For the MD nanofilm simulations, periodic boundary conditions (PBCs) are applied in both the 1- and 2-directions. A free boundary condition is applied in the direction of the nanofilm thickness. As in the bulk case, relaxation and deformation processes are performed, and a two-dimensional constitutive equation is used. The initial lattice spacing of nanofilms is set by the lattice constant of the bulk material. The NPT ensemble is utilized in the first step of the MD simulation to get an equilibrium configuration. The equilibrium strain of a nanofilm is then obtained from this equilibrium configuration. After that, the virial stress under a given applied strain is calculated using the NVT ensemble.

The effective membrane stiffness tensor, $[\boldsymbol{A}']$, in (35) can be obtained from the relationship between the applied strain and the virial stress, which is calculated using the results of the MD simulation.

$$\frac{1}{N_{\text{layer}}} \sum_{k=1}^{N_{\text{layer}}} \begin{Bmatrix} \sigma_{11}^{v} \\ \sigma_{22}^{v} \\ \sigma_{12}^{v} \end{Bmatrix}^{(k)} = \frac{1}{h}[\boldsymbol{A}'] \begin{Bmatrix} \hat{\epsilon}_{11} \\ \hat{\epsilon}_{22} \\ 2\hat{\epsilon}_{12} \end{Bmatrix}, \tag{80}$$

where $\sigma_{\alpha\beta}^{v(k)}$ is the virial stress of atoms in the k-th layer, $\hat{\epsilon}_{\alpha\beta}$ is the applied strain, N_{layer} is the number of layers, and h is the film thickness.

	{100}/<100>	{100}/<110>	{111}/<110>	{110}/<100>
T_{1111}	9.8084	13.7315	9.4804	−15.0566
T_{2222}	9.8084	13.7315	9.4804	−2.2873
T_{1122}	25.5585	5.3080	4.1747	−5.1194
T_{1212}	10.9082	−5.4126	2.6531	−1.0701

Table 2. Calculated surface elastic tensor of nanofilms using the one-point matching method (in N/m).

Considering the symmetry, the total number of unknowns in the 3×3 matrix $[\boldsymbol{A}']$ is six. However, the number of unknowns of a {100}/<100> film reduces to four, i.e. A'_{11}, A'_{12}, A'_{13}, and A'_{33}, because of the film's in-plane axis symmetry. Three of these components, A'_{11}, A'_{12}, and A'_{13}, can be determined using stress-strain equations obtained from the MD simulation with an applied strain of $\hat{\epsilon}_{\alpha\beta} = \lfloor 0.01\%, 0, 0 \rfloor^T$. The component A'_{33} is determined from the MD simulation with an applied strain of $\hat{\epsilon}_{\alpha\beta} = \lfloor 0, 0, 0.01\% \rfloor^T$.

The $[\boldsymbol{A}']$ matrices for {100}/<110> and {111}/<110> films are determined in the same way. Three MD simulations are performed for the {110}/<100> film, in order to collect sufficient data to calculate the components of matrix $[\boldsymbol{A}']$. An additional applied strain, $\hat{\epsilon}_{\alpha\beta} = \lfloor 0, 0.01\%, 0 \rfloor^T$, is utilized to determine the A'_{12}, A'_{22}, and A'_{32} values of the {110}/<100> nanofilm.

The surface elastic tensor $T_{\alpha\beta\kappa\lambda}$, a component of $[\boldsymbol{T}]$, can be calculated from (35) by applying a one-point matching technique to the results from the MD simulation. In this calculation, the matrix $[\boldsymbol{Q}]$ in (35), which represents the two-dimensional constitutive relationship under the plane-stress condition, is determined from the bulk elastic constants given in (20).

The surface elastic tensor matrix $[\boldsymbol{T}]$ is a symmetric matrix with the components listed in Table 2. The missing components in Table 2 are zeros ($T_{1112} = T_{2212} = 0$). According to the matching method, the MD simulations use 3.1 nm-thick {100}/<100> and {100}/<110> nanofilms and 5.2 nm and 4.2 nm-thick {111}/<110> and {110}/<100> nanofilms, respectively.

Figures 4 and 5 show size-dependent Young's moduli normalized by bulk material data. The results for {100}/<100>, {100}/<110>, and {111}/<110> nanofilms are shown in Figure 4. The in-plane axes of the {110}/<100> nanofilm have two different orientations: <100> and <110>. The relative moduli are denoted as E1 and E2, as shown in Figure 5. Size-dependent shear moduli normalized by bulk material data are shown in Figure 6. The lines are the results of the proposed continuum model and the marks represent the results of an MD simulation.

3.3. ***Size-dependent elasticity and surface elastic tensor of copper nanowires.*** When studying the size-dependent elasticity of a nanowire, three types of copper nanowires were considered: <100>/{100}, <100>/{110}, and <110>/{100}. Every nanowire has a rectangular cross-section and four surfaces. The <100>/{100} nanowire has four {100} surfaces, two in the y-direction and two in the z-direction, and the <100>/{110} nanowire has four {110} surfaces. The <110>/{100} nanowire has two {100} surfaces in the y-direction and two {110} surfaces in the z-direction.

The elastic modulus of a nanowire is influenced by the surface elastic tensor of the y- and z-surfaces, as described by (75). The surface elastic tensor of a nanowire is determined by applying the matching technique to the results of the MD simulation. In the cases involving <100>/{100} and <100>/{110}

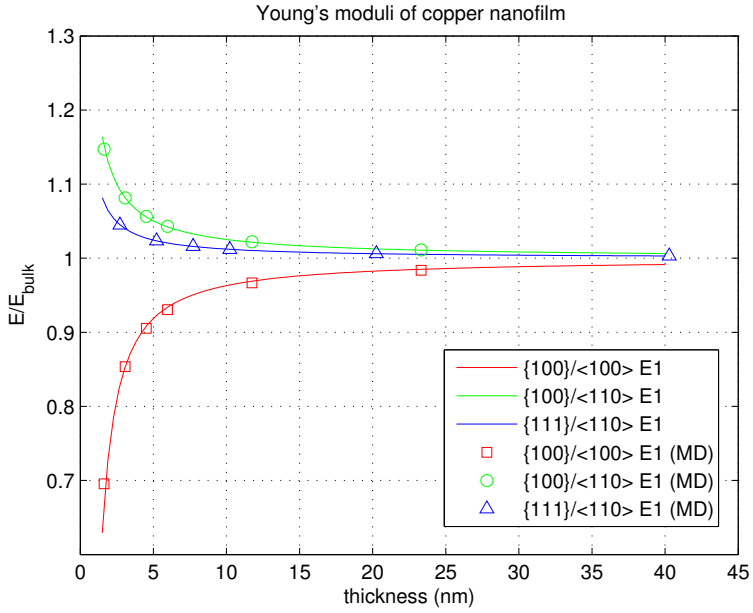

Figure 4. Size-dependent Young's moduli of {100}/<100>, {100}/<110>, {111}/<110> copper nanofilms.

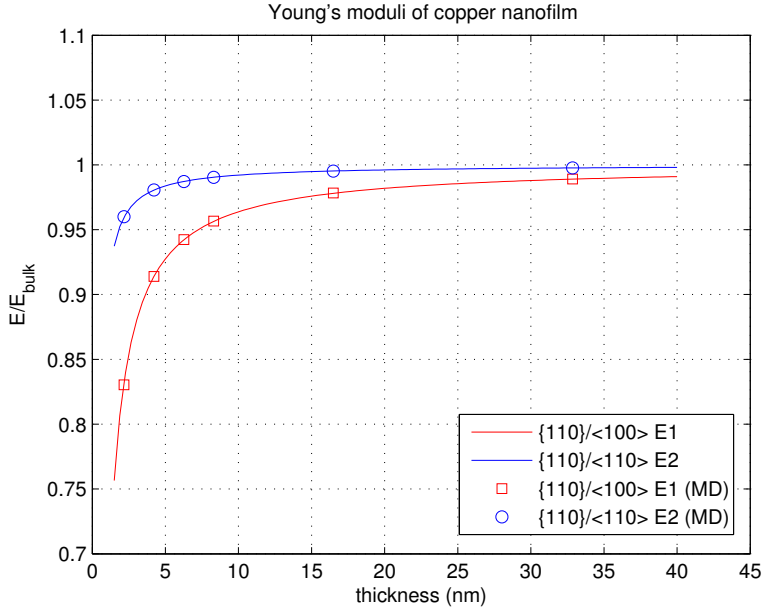

Figure 5. Size-dependent Young's moduli of a {110}/<100> copper nanofilm.

nanowires, only one MD simulation is needed for one-point matching because the surfaces in the y- and z-directions are identical. However, the <110>/{100} nanowire needs two MD simulations, one for the surface in the y-direction and one for the surface in the z-direction.

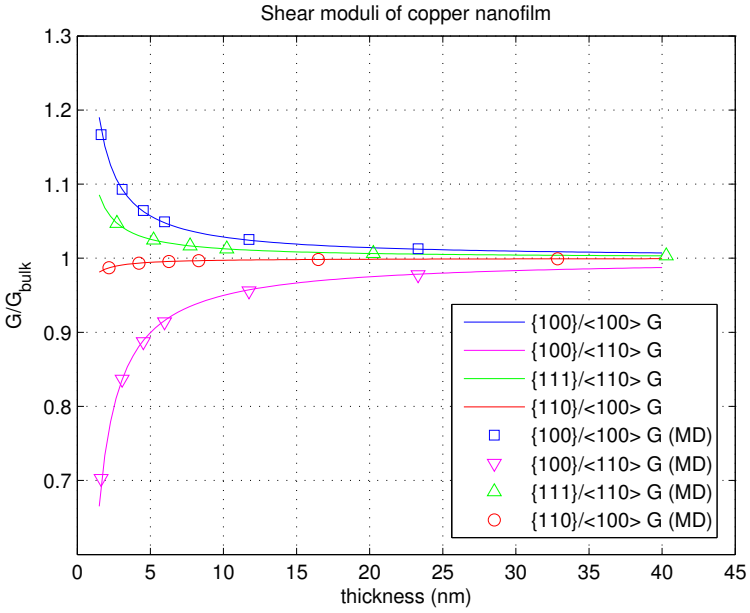

Figure 6. Size-dependent shear moduli of {100}/<100>, {100}/<110>, {111}/<110>, and {110}/<100> nanofilms.

	<100>/{100}	<100>/{110}	<110>/{100}
T^{y}_{1111}	−10.7613	−11.3434	27.3160
T^{z}_{1111}	−10.7613	−11.3434	−9.9535

Table 3. Surface elastic tensor of nanowires calculated by the matching method (in N/m).

In the matching method, the dimension $b = h = 4.5$ nm is used for the <100>/{100} nanowire, and $b = h = 6.3$ nm is set for the <100>/{110} nanowire. For the <110>/{100} nanowire, the width is set to $b = 4.5$ nm in the first simulation and $b = 8.9$ nm in the second simulation, and the thickness for both simulations is fixed at $h = 6.3$ nm.

The calculated surface elastic tensors for copper nanowires are listed in Table 3. As shown in Figure 7, the Young's moduli evaluated by the proposed continuum-based model (see the lines in the figure) have good agreement with the results of the MD simulation (see the marks in the figure). The "thickness" in Figure 7 represents the width, b, of a nanowire. In the z-direction, $h = b$ for <100>/{100} and <100>/{110} nanowires, and $h = \sqrt{2}(b - a/4)$ for the <110>/{100} nanowire, where a is the lattice constant of FCC single crystal copper.

3.4. ***Numerical examples of beam vibration.*** As an example of a surface effect on a nanofilm, the natural frequencies of clamped beams are investigated using the finite element method. The mesh configuration and vibration modes of the clamped beam are shown in Figure 8. The length and width of the beams are fixed at 300 nm and 30 nm, respectively, and the thickness varies from 3 nm to 12 nm. Isoparametric 4-noded plate elements are used in the finite element analysis, and a selective reduced

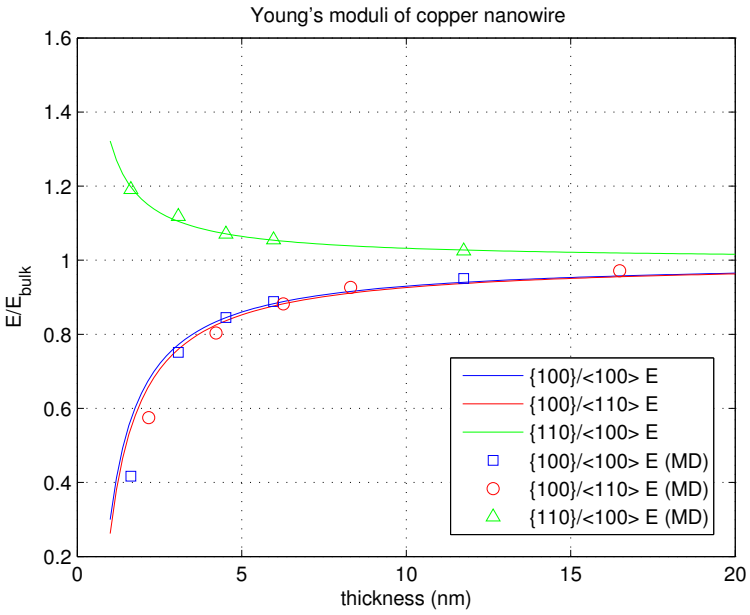

Figure 7. Size-dependent Young's moduli of <100>/{100}, <100>/{110}, <110>/{100} copper nanowires.

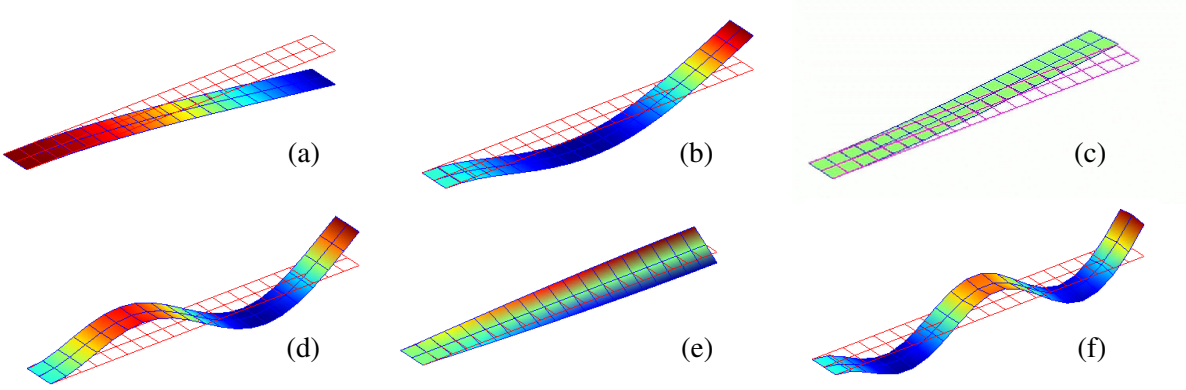

Figure 8. Mesh configuration and vibration modes of a clamped beam: (a) first mode, (b) second mode, (c) third mode, (d) fourth mode, (e) fifth mode without surface effect, (f) fifth mode with surface effect.

integration scheme is applied in order to avoid numerical transverse shear locking. Four-point Gaussian integration is used for the membrane and bending component, and two-point Gaussian integration is used for the transverse shear component: 2×1 for γ_{12} and 1×2 for γ_{13}. The shear correction factor k in (34) is set to $\frac{5}{6}$ in the finite element analysis. The natural frequencies of clamped beams, obtained through finite element analysis, are listed in Table 4.

The natural frequencies with surface effect are smaller than those without surface effect in all test cases. The surface effect increases as the thickness decreases. When the thickness is 3 nm, the natural

Thickness	Natural frequency (MHz)		
(nm)	w/o surf.	w/ surf.	(%)
3	14.4	10.0	69.4%
4.5	21.6	18.4	84.9%
6	28.8	26.0	90.1%
12	57.4	55.0	95.9%

Table 4. Natural frequencies of clamped beams without and with surface effect. The length and the width of the beams are 300 nm and 30 nm, respectively.

Thickness	Length	Natural frequency (GHz)		
(nm)	(nm)	w/o surf.	w/ surf.	MD sim.
1.6	11.7	4.95 (4.99)	1.85 (1.86)	2.55
3.1	23.3	2.37 (2.39)	1.75 (1.77)	1.77
4.5	34.9	1.55 (1.57)	1.29 (1.31)	1.26
6.0	46.5	1.15 (1.17)	1.00 (1.02)	1.01
11.7	92.7	0.56 (0.59)	0.52 (0.54)	0.50

Table 5. Natural frequencies of a {100}/<100> nanowire with one clamped edge. The width is equal to the thickness, and the length is about eight times the thickness. Numbers in parentheses indicate the analytic solution calculated using (81).

frequency with surface effect is 69% of the natural frequency without surface effect. Figure 8 shows the vibration modes of a clamped beam with 3 nm thickness. From first to fourth vibration modes, test cases without and with surface effects yield the same results, as shown in Figure 8(a) to 8(d). However, the fifth vibration mode with surface effect (see Figure 8(f)) is different from the fifth vibration mode without surface effect (see Figure 8(e)).

Another example of beam vibration is solved using beam finite element analysis. Two-node beam elements are used, and a selective reduced integral scheme is applied to avoid shear locking. Two-point Gaussian integration is used for the bending component and one-point Gaussian integration for transverse shear component. The shear correction factor k in (74) is set to $\frac{5}{6}$ in the finite element analysis. The natural frequencies of <100>/{100} nanowires with different thicknesses are obtained via FEM and MD simulation and listed in Table 5. The width of each nanowire is fixed to be equal to the thickness, and the length is eight times the thickness.

The natural frequencies of the clamped beams can be calculated analytically by the following equation [Weaver et al. 1990]:

$$f = \frac{1}{2\pi}\left(\frac{1.875}{L}\right)^2 \sqrt{\frac{EI}{\rho A}}, \tag{81}$$

where L is the length, A is the cross-sectional area, ρ is the density, E is the Young's modulus, and I is the second moment of area. In order to consider surface effect, the effective bending rigidity of a nanowire in (76) is used in the analysis.

The FEM results and analytical solutions show good agreement in all cases, both with and without surface effect. The results with surface effect also agree very well with MD results, except when the thickness is 1.6 nm. The main cause of this exception is that the estimated effective bending rigidity drops rapidly when the thickness of a nanowire reaches 1.6 nm.

4. Equilibrium strain and surface stress

The lattice spacing of a relaxed nanofilm is different from that of bulk material, due to the surface stress on the top and bottom surfaces. A similar phenomenon can occur with nanowires. The equilibrium strain in the relaxed state can be calculated using initial surface stress and surface elastic tensor. In addition, if the equilibrium strain of a nanofilm is known, the surface stress can be calculated from the equilibrium strain through a matching technique. In this section, surface stress is calculated using equilibrium strain as measured by the MD simulation.

4.1. ***Surface stress of copper nanofilms.*** Assume that the surface types of top and bottom surfaces are the same and that there is no external force on the film. The relationship between equilibrium strain ϵ^* and surface stress can be derived from (34), as follows:

$$\delta U = \delta \boldsymbol{d}^T \boldsymbol{B}_m^T ([\boldsymbol{A}'] \boldsymbol{B}_m \boldsymbol{d} + 2\{\tau^0\}) = 0, \tag{82}$$

$$[\boldsymbol{A}'] \begin{Bmatrix} \epsilon_{11}^* \\ \epsilon_{22}^* \\ 2\epsilon_{12}^* \end{Bmatrix} + 2 \begin{Bmatrix} \tau_{11}^0 \\ \tau_{22}^0 \\ \tau_{12}^0 \end{Bmatrix} = 0, \tag{83}$$

where $[\boldsymbol{A}'] = h[\boldsymbol{Q}] + 2[\boldsymbol{T}]$.

To obtain the equilibrium strain of a nanofilm, an MD simulation was performed using an NPT ensemble at a temperature of 0.1 K. The thickness of the MD model was set to 3.1 nm for the {100}/<100> and {100}/<110> nanofilms and 5.2 nm for the {111}/<110> nanofilm. The {110}/<100> nanofilm was 4.2 nm thick. The initial surface stress in Table 6 was calculated by applying the one-point matching method to the equilibrium strain obtained via an MD simulation. The shear component, τ_{12}^0, which is not shown in Table 6, is zero for all the tested surfaces.

The equilibrium strain of a copper nanofilm as a function of thickness is shown in Figure 9 and 10. The lines represent the results of the proposed continuum-based model, and the marks show the results of an MD simulation. The results for {100}/<100>, {100}/<110>, and {111}/<110> nanofilms are illustrated in Figure 9. Lines e1 and e2, denoted in Figure 10, are the equilibrium strains in the <100> and <110> directions, respectively, of the {110}/<100> nanofilm.

	{100}/<100>	{100}/<110>	{111}/<110>	{110}/<100>
τ_{11}^0	1.5034	1.3806	0.8717	1.1149
τ_{22}^0	1.5034	1.3806	0.8717	0.9993

Table 6. Initial surface stress of nanofilms, calculated by the one-point matching method (in N/m).

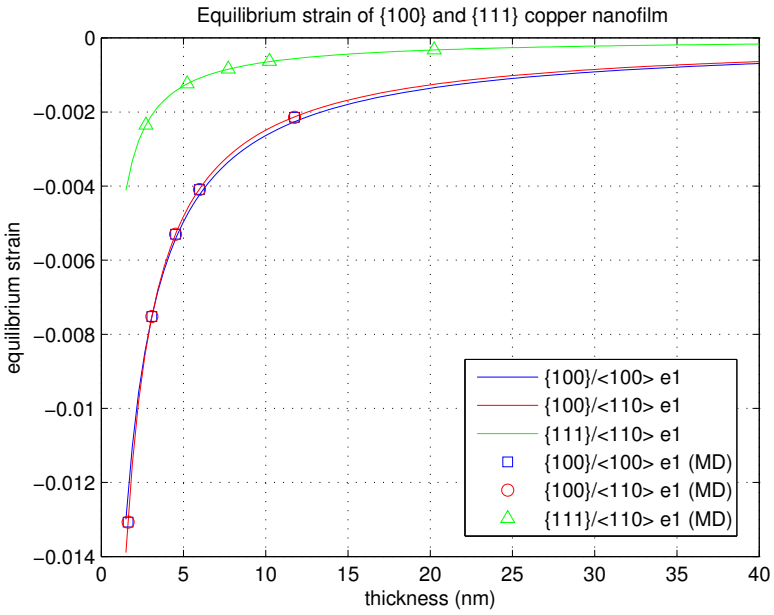

Figure 9. Equilibrium strain of {100}/<100>, {100}/<110>, and {111}/<110> copper nanofilms.

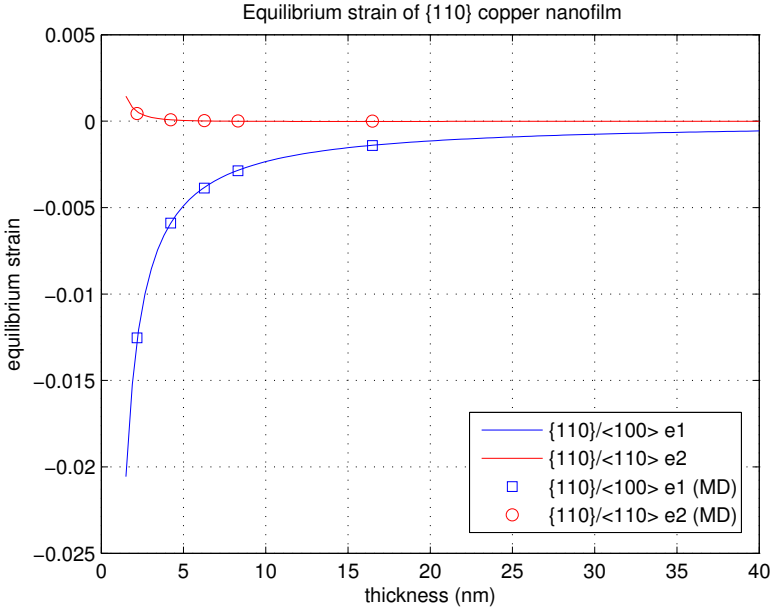

Figure 10. Equilibrium strain of a {110}/<100> copper nanofilm.

4.2. ***Surface stress of copper nanowires.*** The initial surface stress of a nanowire can be calculated using equilibrium strain in a manner analogous to the case of a nanofilm. The relationship between equilibrium strain and surface stress is given as follows:

	<100>/{100}	<100>/{110}	<110>/{100}
τ_{xx}^{y0}	0.6984	0.7047	1.5670
τ_{xx}^{z0}	0.6984	0.7047	−0.0178

Table 7. Initial surface stress of nanowires calculated by a matching method (in N/m).

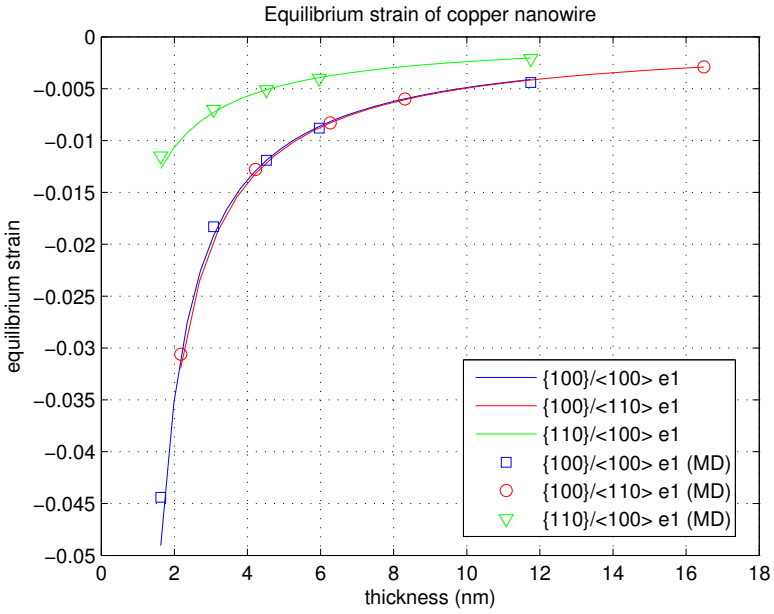

Figure 11. Equilibrium strain of <100>/{100}, <100>/{110}, and <110>/{100} copper nanowires.

$$[bh(E_1 + \tfrac{2}{b}T_{1111}^{y} + \tfrac{2}{h}T_{1111}^{z})]\{\epsilon_x^*\} + \{2h\tau_{xx}^{y0} + 2b\tau_{xx}^{z0}\} = 0, \tag{84}$$

where ϵ_x^* is the equilibrium strain of a nanowire, τ_{xx}^{y0} and τ_{xx}^{z0} are initial surface stress components of the y- and z-surfaces, and b and h are the width and thickness of a nanowire, respectively.

The equilibrium strains present in <100>/{100}, <100>/{110}, and <110>/{100} nanowires were obtained by an MD simulation. The cross-sectional dimensions of the MD models are $b = h = 4.5$ nm for the <100>/{100} nanowire and $b = h = 6.3$ nm for the <100>/{110} nanowire. For the <110>/{100} nanowire, an MD simulation was carried out twice with two different widths, $b = 4.5$ nm and $b = 8.9$ nm, and a constant thickness of $h = 6.3$ nm. The initial surface stress, calculated from the equilibrium strain, is listed in Table 7.

The equilibrium strain of a nanowire can be calculated from the initial surface stress using (84). These results are shown in Figure 11. The calculated equilibrium strains represented by lines in the figure have good agreement with the mark data obtained by MD simulation.

5. Conclusion

Multiscale continuum models and corresponding finite elements were developed for both nanofilms and nanowires subject to an anisotropic surface effect. In order to consider the anisotropic surface effect,

linear surface elasticity was used instead of the isotropic surface elasticity proposed by Gurtin and Murdoch. This linear surface elasticity was represented by initial surface stress and surface elastic tensor.

The surface elastic tensor of a nanofilm was calculated via the one-point matching method and an MD simulation. The initial surface stress was estimated using the equilibrium strain, which in turn was computed via MD simulation. Four different orthotropic nanofilms were considered as numerical examples, with {100}/<100>, {100}/<110>, {111}/<110>, and {110}/<100> surfaces. The size-dependent elastic modulus and equilibrium strain values calculated by the proposed continuum model were in good agreement with the results of the MD simulation. However, there were slight discrepancies between these surface parameters (initial surface stress and surface elastic tensor) as calculated by the matching technique and their corresponding reference values [Shenoy 2005; Dingreville and Qu 2007]. This is because the presented surface parameters include the hyperelastic effect of the bulk material as well as the surface effect itself.

For a nanowire, surface parameters were estimated using either the one-point or two-point matching method. <100>/{100}, <100>/{110}, and <110>/{100} nanowires with rectangular cross-sections were considered as numerical examples. In the calculation of surface parameters, only one MD simulation was used for the <100>/{100} and <100>/{110} nanowires, whereas two MD simulations were performed for the <110>/{100} nanowire because it had different surfaces in the y- and z-directions. The results from the continuum-based model and the MD simulation correlated very well.

In this paper, only rectangular cross-sectional nanowires were considered. If the shape of a cross-section is not rectangular, the surface component of the internal virtual work will change. Since a nanowire with a circular cross-section presents a special case, it might not always be feasible to apply the approach described in this paper. However, in most cases, this approach will work because a crystalline nanowire tends to have a multifaceted cross-section rather than a circular shape. Moreover, a nanowire could undergo surface reconstruction and could have various surfaces which are not low-index surfaces. If a nanowire has a surface different from those mentioned in this paper, initial surface stress and surface stress tensor will change. However, initial surface stress and surface stress tensor can still be evaluated using the MD-based matching method proposed in this paper. Therefore, the proposed model can be applied to nanowires with various kinds of surfaces.

The proposed multiscale continuum model could prove useful in the development of a finite element method including surface effect, and it is expected to be a good design tool for nanoscale structures in which the surface effect is dominant.

Acknowledgments

This research was supported by the World Class University (WCU) program (R31-2008-000-10083-0) and a National Research Foundation of Korea grant (No. 2012R1A3A2048841) funded by the Korea government (MEST).

References

[Cammarata and Sieradzki 1989] R. C. Cammarata and K. Sieradzki, "Effects of surface stress on the elastic moduli of thin films and superlattices", *Phys. Rev. Lett.* **62** (1989), 2005–2008.

[Cho et al. 2009] M. Cho, J. Choi, and W. Kim, "Continuum-based bridging model of nanoscale thin film considering surface effects", *Jap. J. Appl. Phys.* **48** (2009), 020219.

[Choi et al. 2010a] J. Choi, M. Cho, and W. Kim, "Multiscale analysis of nano-scale thin film considering surface effects: thermomechanical properties", *J. Mech. Mat. Struct.* **5** (2010), 161–183.

[Choi et al. 2010b] J. Choi, M. Cho, and W. Kim, "Surface effects on the dynamic behavior of nano-sized thin film resonator", *Appl. Phys. Lett.* **97** (2010), 171901.

[Daw and Baskes 1984] M. S. Daw and M. I. Baskes, "Embedded-atom method: derivation and application to impurities, surfaces, and other defects in metals", *Phys. Rev. B* **29** (1984), 6443–6453.

[Diao et al. 2004] J. Diao, K. Gall, and M. L. Dunn, "Atomistic simulation of the structure and elastic properties of gold nanowires", *J. Mech. Phys. Solids* **52** (2004), 1935–2186.

[Dingreville and Qu 2007] R. Dingreville and J. Qu, "A semi-analytical method to compute surface elastic properties", *Acta Mater.* **55** (2007), 141–147.

[Dingreville et al. 2005] R. Dingreville, J. Qu, and M. Cherkaoui, "Surface free energy and its effect on the elastic behavior of nano-sized particles, wires and films", *J. Mech. Phys. Solids* **53** (2005), 1827–1854.

[Dingreville et al. 2008] R. Dingreville, A. J. Kulkarni, M. Zhou, and J. Qu, "A semi-analytical method for quantifying the size-dependent elasticity of nanostructures", *Modelling Simul. Mater. Sci. Eng.* **16** (2008), 025002.

[Foiles et al. 1986] S. M. Foiles, M. I. Baskes, and M. S. Daw, "Embedded-atom method functions for the fcc metals Cu, Ag, Au, Ni, Pd, Pt, and their alloys", *Phys. Rev. B* **33** (1986), 7983–7991.

[Guo and Zhao 2005] J.-G. Guo and Y.-P. Zhao, "The size-dependent elastic properties of nanofilms with surface effects", *J. Appl. Phys.* **98** (2005), 074306.

[Gurtin and Murdoch 1975] M. E. Gurtin and A. I. Murdoch, "A continuum theory of elastic material surfaces", *Arch. Rat. Mech. Anal.* **57** (1975), 291–323.

[Gurtin and Murdoch 1978] M. E. Gurtin and A. I. Murdoch, "Surface stress in solids", *Int. J. Solid Struct.* **14** (1978), 431–440.

[He and Lilley 2008] J. He and C. M. Lilley, "Surface stress effect on bending resonance of nanowires with different boundary conditions", *Appl. Phys. Lett.* **93** (2008), 263108.

[Kim and Cho 2010] W. Kim and M. Cho, "Surface effect on the self-equilibrium state and size-dependent elasticity of FCC thin films", *Modelling Simul. Mater. Sci. Eng.* **18** (2010), 085006.

[Liang et al. 2005] H. Liang, M. Upmanyu, and H. Huang, "Size-dependent elasticity of nanowires: nonlinear effects", *Phys. Rev. B* **71** (2005), 241403.

[Lim and He 2004] C. W. Lim and L. H. He, "Size-dependent nonlinear response of thin elastic films with nano-scale thickness", *Int. J. Mech. Sci.* **46** (2004), 1715–1726.

[Lu et al. 2006] P. Lu, L. H. He, H. P. Lee, and C. Lu, "Thin plate theory including surface effects", *Int. J. Solid Struct.* **43** (2006), 4631–4647.

[Miller and Shenoy 2000] R. E. Miller and V. B. Shenoy, "Size-dependent elastic properties of nanosized structural elements", *Nanotechnology* **11** (2000), 139–147.

[Park 2009] H. S. Park, "Quantifying the size-dependent effect of the residual surface stress on the resonant frequencies of silicon nanowires if finite deformation kinematics are considered", *Nanotechnology* **20** (2009), 115701.

[Plimpton 1995] S. J. Plimpton, "Fast parallel algorithms for short-range molecular dynamics", *J. Comput. Phys.* **117** (1995), 1–19.

[Rapaport 2004] D. C. Rapaport, *The art of molecular dynamics simulation*, pp. 15–17, Cambridge University Press, 2004.

[Shenoy 2005] V. B. Shenoy, "Atomistic calculations of elastic properties of metallic fcc crystal surfaces", *Phys. Rev. B* **71** (2005), 094104.

[Streitz et al. 1994] F. H. Streitz, R. C. Cammarata, and K. Sieradzki, "Surface-stress effects on elastic properties, I: thin metal films", *Phys. Rev. B* **49** (1994), 10699–10706.

[Subramaniyan and Sun 2008] A. K. Subramaniyan and C. T. Sun, "Continuum interpretation of virial stress in molecular simulations", *Int. J. Solids Struct.* **45** (2008), 4340–4346.

[Sun and Zhang 2005] C. T. Sun and H. Zhang, "Size-dependent elastic moduli of platelike nanomaterials", *J. Appl. Phys.* **93** (2005), 1212–1218.

[Wang et al. 2008] J. Wang, Q.-A. Huang, and H. Yu, "Size and temperature dependence of Young's modulus of a silicon nano-plate", *J. Phys. D: Appl. Phys.* **41** (2008), 165406.

[Weaver et al. 1990] W. Weaver, Jr., S. P. Timoshenko, and D. H. Young, *Vibration problems in engineering*, 5th ed., pp. 416–432, John Wiley & Sons, 1990.

[Wolf 1991] D. Wolf, "Surface-stress-induced structure and elastic behavior of thin films", *Appl. Phys. Lett.* **58** (1991), 2081–2083.

[Zhang et al. 2008] T.-Y. Zhang, M. Luo, and W. K. Chan, "Size-dependent surface stress, surface stiffness, and Young's modulus of hexagonal prism [111] beta-SiC nanowires", *J. Appl. Phys.* **103** (2008), 104308.

[Zhou and Huang 2004] L. G. Zhou and H. Huang, "Are surfaces elastically softer or stiffer?", *Appl. Phys. Lett.* **84** (2004), 1940–1942.

Received 9 Jun 2011. Revised 1 Jun 2012. Accepted 18 Jun 2012.

WONBAE KIM: wbkim@snu.ac.kr
Division of WCU Multiscale Mechanical Design, School of Mechanical and Aerospace Engineering, Seoul National University, Seoul 151-744, South Korea

SEUNG YUN RHEE: syrhee8@snu.ac.kr
Aircraft Certification Team, Aerospace Safety and Certification Center, Korea Aerospace Research Institute, 169-84 Gwahangno, Yuseong-gu, Daejeon 305-806, South Korea

MAENGHYO CHO: mhcho@snu.ac.kr
Division of WCU Multiscale Mechanical Design, School of Mechanical and Aerospace Engineering, Seoul National University, Seoul 151-744, South Korea
http://ssnd.snu.ac.kr/members/professor.html

JOURNAL OF MECHANICS OF MATERIALS AND STRUCTURES
Vol. 7, No. 7, 2012
dx.doi.org/10.2140/jomms.2012.7.641

CHARACTERIZATION OF HUMAN SKIN THROUGH SKIN EXPANSION

DJENANE C. PAMPLONA AND CLAUDIO R. CARVALHO

This study characterized human skin of the lower leg and scalp during the surgical process of skin expansion. To our knowledge, this is the first study in this field, which has provided results that considerably improve our understanding of human skin. A detailed *in vivo* analysis was carried out involving four different patients that allowed for observation during the relaxation process. A comparison between the *in vivo* and numerical finite elements model of the expansion was used to identify the material elastic parameters of the skin. After a comprehensive search of constitutive equations for describing skin, Delfino's constitutive equation was chosen to model the *in vivo* results. We considered skin as an isotropic, homogeneous, hyperelastic, and incompressible membrane. The parameters of Delfino's exponential function obtained for the first skin stretch process were $a = 40.0\,\text{KPa}$ and $b = 20.2$. As skin is extended, such as with expanders or in other procedures that tighten the skin, the collagen fibers are also extended and cause stiffening in the skin, which results in it being more and more resistant to expansion or further stretching. We observed this phenomenon as an increase in parameters a and b as subsequent expansions continued. The results of this study allow for the quantification of stiffening of the skin after several stretches, when the skin becomes more and more inelastic. These results are very encouraging and provide insight into our understanding of the behavior of stretched skin and maybe other biological tissues, as swollen artery and veins.

A list of symbols can be found on page 653.

1. Introduction

Skin expansion is a physiological process that is defined as the ability of human skin to increase its surface area in response to stress or deformation. Skin expanders are silicone bags of different shapes and sizes that are implanted under the skin. Since the skin presents creep or relaxation, the resulting stress decreases after an imposed deformation over a specific period of time. The physiology of skin expansion not only considers stretching of the skin, but also the relaxation process used to obtain an extra flap of skin that possesses the needed characteristics. For example, skin expansion is used to reconstruct burned areas and breasts after mastectomy and to hide scars. Expansion is usually conducted near the location where the skin is required in order to provide skin of the same color, texture, sensation, and structure as the one to be removed.

Starting in 1982, several studies have improved the expansion process using self-inflation, continuous tissue, or controlled expansion [Austad and Rose 1982; Schmidt et al. 1991; Duffy and Shuter 1994]. Other studies have explored concepts and complications of the surgical process, and numerous analyses have been conducted on skin expansion from a medical point-of-view. In contrast, few studies have

Keywords: characterization of human skin, finite elements, skin expansion, biomembranes, constitutive equation.

explored the bioengineering process of expansion. In order to model reconstructive plastic surgeries numerically and achieve a better understanding of the process, it is critical to determine the mechanical properties of skin *in vivo*, and several recent studies have been performed with this goal in mind. The most frequently used techniques are indentation and suction of the skin, and some studies have used Young's modulus to establish the stiffness of the skin [Diridollou et al. 2000; Zahouani et al. 2009; Pailler-Mattei et al. 2009]. In addition, more recent studies have characterized the nonlinear mechanical behavior of human skin under indentation and suction processes [Hendriks et al. 2003; Delalleau et al. 2006; 2008; Geerligs et al. 2011; Lim et al. 2008].

To date, only one study has used a numerical model for skin under expansion [Socci et al. 2007], which assessed the stresses and strains of skin from inflation of an expander. This study only considered an axially symmetric configuration, in which a flat circular flap of a thin membrane (the skin) is expanded by a spherical balloon. In that study, a phenomenological approach was used to represent the growth of the skin after expansion.

The analysis of membranes under large deformation is usually based on the pioneering work of Green and Adkins in nonlinear elasticity [Green and Adkins 1970]. Several theoretical and numerical studies have been published in this field, but the total number of studies that have used this approach is rather low compared to theoretical and numerical approaches [Alexander 1971; Pamplona et al. 2006; 2001; Pamplona and Bevilacqua 1992; Gonçalves et al. 2009; 2008].

In this study, the skin was considered a hyperelastic membrane, and in order to execute the numerical analysis, finite membrane elements were used, since membrane structures are load adaptive and change their geometry to accommodate external loads with minimum variation in stress levels, and as the skin wrinkles in-plane compression. Our aim was to develop a method for characterizing the nonlinear mechanical behavior of skin under expansion using a numerical and *in vivo* technique. A consistent constitutive equation for the skin may allow for preoperative planning and optimal filling parameters in terms of both the volume of fluid expansion and duration between fills. Currently pain and observed tightness are the main guides to filling.

The study presented here aimed to model the human skin over successive skin expansions in order to obtain different parameters for the characterization of stretched skin over time. To accomplish this goal, a detailed *in vivo* analysis was carried out and at least four expansions were monitored for each patient, obtaining similar data for the same methodology done in animals [Beauchene et al. 1989]. During each expansion, at least five measurements were taken related to the volume inserted and the pressure inside the skin expander. These data provided enough information to characterize the skin at each stage of the stretching process, and the entire process provided more than 100 *in vivo* calculations of volume$\times$pressure. To obtain a constitutive equation that could describe the measured skin, several well-known constitutive relationships were analyzed using several previously described methods [Ogden 2003; Holzapfel et al. 2000; Delfino et al. 1997]. Since the pressure inside the skin expander dropped to zero between expansions, the skin was also considered viscoelastic. Skin growth was not considered although an overview on the mechanobiology underlying skin growth sustains that tensile stress applied to skin appears to stimulate skin growth [Silver et al. 2003]. Researchers recently are looking for a model to describe the growth of the skin under tensile stress, establishing computational models for stretch-induced skin growth under expansion [Buganza Tepole et al. 2011] and also patient-specific finite element simulation of skin growth in situ [Zöllner et al. 2012].

2. Methodology

The first step for expanding skin during surgery was to implant a skin expander directly underneath the skin and subcutaneous tissue. The surgeon outlined the shape and size of the skin expander on the skin and then made an incision on one side of the outline. The pocket that will contain the expander is then made by separating the subcutaneous tissue by obeying the contour of the drawing, and therefore delimiting the flap of skin to be expanded. Through this incision, the surgeon inserted the skin expander under the skin together with a valve that is connected to the expander. After the incision is closed, a saline solution, which should be approximately 10% of the nominal volume of the skin expander, V_{exp}, was injected into the skin expander by inserting a needle into the implanted valve. At this stage the pressure inside the expander was not measured, and this step was designated as A. Fifteen days after the surgery, the expansion was initiated, which guarantees cicatrization. Each week, a specified volume of saline solution was inserted inside the expander, which was dependent on the size of the expander. As the solution was inserted, the skin expands due to the increased pressure inside the expander and results in some pain for the patient; however, due to viscoelastic properties, the skin relaxes over time, which diminishes the pressure inside the expander and consequently the pain of the patient. After one week, no measurable pressure exists inside the expander. The major disadvantage of this process is the need for two surgeries, where one is used to implant the expander and the other is used to remove the expander and repair the skin defect. This research was done on patients that needed, for medical reasons, skin expansion, thus the selection of patients for this analysis did not consider the age of the patient or region of the body to be expanded, though these can prove to be important factors, specially the relation with the original skin laxity of the anatomic region.

In addition, expansion over elastic foundations, such as the abdomen or fatty tissue, was not considered since these locations would compromise the results of the numerical model.

3. *In vivo* analysis

This study was conducted on four patients, and all patients signed an informed consent. Of those, two patients had skin expansions performed in the scalp and the other two in the lower leg. In order to identify the behavior of the skin from successive skin expansions, it was necessary to measure the pressure inside the skin expander before, during, and after injection of saline solution for each expansion. For this purpose, an apparatus was developed that provided a pressure sensor coupled to the syringe used to perform the injection of liquid (see figure). The apparatus was coupled to a plastic Y tube, where one upper region of the Y tube (b) was attached to the syringe with the saline solution to be injected, and the other upper region of the tube (c) was coupled to the apparatus developed to measure the pressure. In addition, the lower side of the Y tube (a) was attached to the needle used to inject the saline solution into the valve of the skin expander. The initial thickness of the skin, H, of each patient and region was determined by the surgeon after performing the surgery.

(a) needle; (b) syringe; (c) apparatus.

During each skin expansion, the surgeon paused after each 5 or 10 ml of liquid was injected to measure the pressure inside of the expander, which provided both volume and pressure data points.

The measurements were continued in this manner until the final volume of the expansion was reached. The curves relating volume to the pressure of each skin expansion allowed for characterization of the skin for that expansion. During the week following each expansion, the viscoelastic properties of the skin allowed for relaxation to occur and for the pressure inside the expander to reach zero.

Only the final pressure and volume reached in each expansion are shown in the following tables, although to achieve the final pressure each expansion was carefully measured. For these analyses, V_{i-1} represented the initial volume and V_i represented the final volume of the i-th expansion. The letter A designated the initial insertion of fluid during the surgery, and the letter B indicated that the pressure for that particular expansion could not be measured for various reasons (e.g., the patient arriving late or at times when the measurements could not be performed).

Since the skin expanders for the patients have different shapes, dimensions, and nominal volumes, V_{exp}, the variable V_i^* was used to relate to the final pressure of that expansion, P_i. The ratio between V_{exp} and the final volume V_i inside the expander at the end of each expansion, i, is denoted by

$$V_i^* = \frac{V_i}{V_{\text{exp}}} \tag{3-1}$$

It is important to note that although the volume injected into the expander could be the same in each step, this volume is a smaller percentage of the total volume already injected into the expander, which is

$$V_i^{**} = \frac{V_i - V_{i-1}}{V_{i-1}} \tag{3-2}$$

3.1. ***Results of skin expansion in the scalp.*** Two patients were analyzed for expansion of the skin in the scalp, both with initial skin thickness $H = 0.5$ cm. Patient 1 was a 33-year-old female who had light brown skin, weighed 53 kg, and was 1.60 m in height. A rectangular skin expander ($V_{\text{exp}} = 400$ ml) was used on this patient. Patient 2 was a 12-year-old female with white skin, weighed 35 kg, and was 1.50 m in height. A lunar crescent-shaped expander ($V_{\text{exp}} = 300$ ml) was used on this patient.

Since the pressure inside the expander was measured after every 5 or 10 ml of liquid was injected, at least 4 parameters of the inside pressure related to the injected volume were determined for each skin expansion (i) obtained. Tables 1 and 2 show only the final results of the maximum pressure reached at the end of each weekly expansion (i).

(i)	V_{i-1} (ml)	V_i (ml)	$V_i - V_{i-1}$ (ml)	V_i^*	V_i^{**}	P_i(kPa)
A	0	80	x	x	x	x
1	0	110	30	0.28	0.38	29.50
2	110	140	30	0.35	0.27	28.20
B	140	380	x	x	x	x
3	380	425	45	1.06	0.12	26.10
4	425	465	40	1.16	0.09	26.80
5	465	500	35	1.25	0.08	26.00
6	500	538	38	1.35	0.08	25.20

Table 1. Patient 1 with a rectangular expander ($V_{\text{exp}} = 400$ ml) inserted under the scalp.

(i)	V_{i-1} (ml)	V_i (ml)	$V_i - V_{i-1}$ (ml)	V_i^*	V_i^{**}	P_i(kPa)
A	0	214	x	x	x	x
1	214	254	40	0.85	0.19	26.00
2	254	298	44	0.99	0.17	25.10
3	298	338	40	1.13	0.13	23.90
4	338	376	38	1.25	0.11	21.90

Table 2. Patient 2 with a crescent expander (V_{exp} = 300 ml) inserted under the scalp.

The data indicated that a maximum pressure achieved during each skin expansion was of the same magnitude and ranged between 22–29 kPa. This maximum pressure was limited by the discomfort or pain felt by the patient, important information to the doctor performing the procedure.

3.2. ***Results of skin expansion in the lower leg.*** Two patients were analyzed for expansion of skin on the lower leg, both with initial skin thickness $H = 0.8$ cm. Patient 3 was a 10-year-old female with light brown skin, weighed 45 kg, and had a height of 1.50 m. A rectangular expander (V_{exp} = 250 ml) was used on this patient. Patient 4 was an 18-year-old female with white skin, weighed 70 kg, and had a height of 1.80 m. A rectangular expander (V_{exp} = 400 ml) was also used on this patient. Since the pressure inside the expander was measured after every 5 or 10 ml of liquid was injected, at least 4 parameters of the inside pressure related to the injected volume were determined for each skin expansion (i). Tables 3 and 4 show the final results of the maximum pressure obtained at the end of each weekly expansion (i).

As seen in Tables 3 and 4, the results showed that the maximum pressure achieved during each skin expansion of the lower leg ranged from 9–19 kPa, which was lower than that obtained on the scalp. The

(i)	V_{i-1} (ml)	V_i (ml)	$V_i - V_{i-1}$ (ml)	V_i^*	V_i^{**}	P_i(kPa)
A	0	157	x	x	x	x
1	157	187	30	0.75	0.19	12.63
2	187	232	45	0.99	0.24	13.00
3	232	272	40	1.09	0.17	10.50
4	272	302	30	1.21	0.11	9.00

Table 3. Patient 3 with a rectangular expander (V_{exp} = 250 ml) inserted in the lower leg.

(i)	V_{i-1} (ml)	V_i (ml)	$V_i - V_{i-1}$ (ml)	V_i^*	V_i^{**}	P_i(kPa)
A	0	120	x	x	x	x
1	120	160	40	0.40	0.33	17.20
2	160	200	40	0.50	0.25	18.90
3	200	240	40	0.60	0.20	x
4	240	280	40	0.70	0.17	12.90
5	280	320	40	0.80	0.14	12.60

Table 4. Patient 4 with a rectangular expander (V_{exp} = 400 ml) inserted in the lower leg.

maximum pressure was also limited by the discomfort or pain that the patient felt, since discomfort was accentuated in the skin of the lower leg.

In addition, we also observed that the amount of pressure needed to fill the expander diminished as it was filled for both the scalp and skin of the lower leg, despite the injected volume being the same at each step. This could be related to Laplace's law often cited by surgeons, mostly related to aneurismal growth. In addition, this volume was a smaller percentage of the volume already present inside the expander, V_i^{**}.

4. Numerical analysis

To characterize the skin during expansion, it is necessary to model the procedure numerically, which can be accomplished using the commercial finite element software ABAQUS (version 6.8) together with the commercial program MATLAB. The goal was to identify an elastic constitutive equation that can characterize the skin of the scalp and lower leg during each expansion. However, the parameters of the constitutive equation for each region and expansion are not the same, since the collagen fibers of the stretched skin offer more resistance to expansion over the course of the expansion, as observed in [Lim et al. 2008].

To perform the numerical analysis, the finite element mesh used linear hybrid membrane quadrilateral or triangular finite elements (M3D4 or M3D3), depending on the geometry, when the initial thickness, H, was provided by the surgeon. The control of the volume inserted into the skin expander is essential for modeling this medical procedure, and it can only be done in ABAQUS by using the combination of membrane and fluid finite elements. In the fluid elements, the pressure is applied to one unique node, which is called the reference of cavity node. This pressure simulates the injection of fluid into the skin expander. The middle surface is the reference point for both the membrane and fluid elements. In the numerical analysis, the final geometry of one expansion is used as the initial geometry for the next expansion where the stress and pressure are equal to zero, since the pressure inside goes to zero within a week due to the relaxation of the skin. Because the expansions are successive, the thickness of the modeled skin changes at the end of each expansion, but not uniformly. Modeling a different thickness for every membrane element is impossible, since finite elements of the membrane were used and require a constant thickness continuum. Therefore, the mean thickness of all elements obtained in the previous expansion was used for all subsequent expansions together with the previous geometry. The ABAQUS code has a command to obtain the thickness of each finite element after it is deformed at the end of each expansion. With a maximum stretch of the skin, it is possible to determine the amount of skin provided by the skin expansion. The maximum principal stress reached at each expansion is an important data point, since this is associated with the discomfort or pain of the patient during the expansion. The results are presented in the following figures and tables. The boundary was considered simply connected and free to rotate. This boundary condition was chosen after careful observation of the expanded skin to ensure that the skin at the boundary did not exhibit peeling.

Skin is considered homogenous and hyperelastic, though it possesses properties that are much more complex. For example, skin exhibits viscoelastic behavior, which was demonstrated by the decrease in pressure of the expander to zero within one week after the expansion. The contact between the skin and the expander was not considered in the numerical model. This type of material is characterized through the Strain Energy Density, W, which is written as a function of the strain invariants I_1, I_2, and I_3. There

are several strain energy densities with those characteristics, including Mooney-Rivlin, Neo-Hookean, Ogden, Polynomial, Fung's, Delfino's exponential function, and Ogden [2003]. After assessing these equations as a description of the *in vivo* results numerically, Delfino's exponential function was chosen, since it provided the best fit for these data. This equation was initially proposed to describe a human artery under several loads and is represented

$$W = \frac{a}{b}\left\{\exp\left[\frac{b}{2}(I_1 - 3)\right] - 1\right\}, \tag{4-1}$$

where a and b are parameters of the material and I_1 is the first strain invariant, defined in terms of the principal stretches λ_i by

$$I_1 = \lambda_1^2 + \lambda_2^2 + \lambda_3^2 \tag{4-2}$$

For incompressible materials, such as biological tissues, the third invariant $I_3 = 1$ is used, given that the ratio between the initial thickness, H, and final thickness, t, of each expansion is equal to the product of the principal stretches:

$$\lambda_3 = \frac{t}{H} = \frac{1}{\lambda_1 \lambda_2} \tag{4-3}$$

To analyze the numerical results for parameters a and b, two variables are used: the ratio V_i^*, and the ratio between the initial thickness, H, and final medium thickness, t.

4.1. *Numerical results for the scalp.*

Patient 1. A mesh of 126 quadrilateral finite membrane elements, M3D4, was used on the rectangular skin expander of Patient 1, for which the dimensions were 13.6 cm×5.5 cm and V_{exp} = 400 ml.

For each expansion, a curve relating the inserted volume and the pressure inside the expander was calculated, which identifies the parameters that best describe the skin at each specific expansion. The Newton Raphson method was used to fit the numerical and *in vivo* results. Figure 1 shows the numerical and *in vivo* curves for the sixth expansion of the first patient with the fitting parameters a = 1.79 MPa and b = 120.5 of Delfino's exponential function. The data indicate that the maximum difference between the

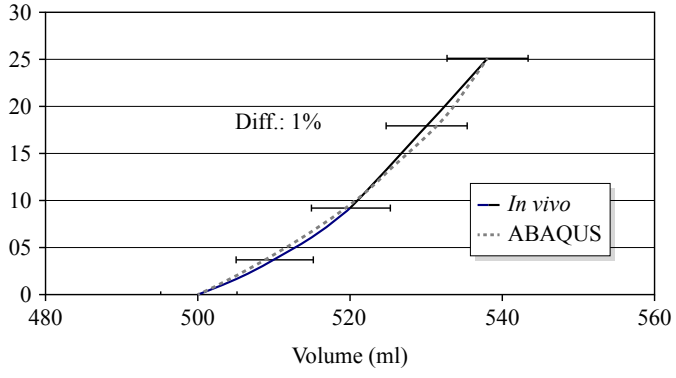

Figure 1. The relationship between the measured pressure (kPa) and inserted volume (ml) for the *in vivo* and numerical data of the sixth expansion of patient 1 using parameters a = 1.79 MPa and b = 120.5.

(i)	V_{i-1} ml	V_i ml	V_i^*	P_i kPa	$\lambda_{\max}$ added	$\sigma_{\max}$ kPa	t cm	H/t	a MPa	b
A	0	80	x	x	x	x	x		x	x
1	80	110	0.28	29.50	1.50	241.52	0.33	1.52	0.21	31.5
2	110	140	0.35	28.20	1.66	257.93	0.29	1.72	0.22	33.4
B	140	380	x	x	x	x	x	x	x	x
3	380	425	1.06	26.10	3.15	501.88	0.16	3.16	0.99	51.3
4	425	465	1.16	26.80	3.34	604.67	0.15	3.33	1.30	75.2
5	465	500	1.25	26.00	3.51	642.14	0.14	3.57	1.46	134.5
6	500	538	1.35	25.20	3.65	679.23	0.13	3.85	1.79	120.5

Table 5. Results of expansion for Patient 1. For expansion (i): V_{i-1} = initial volume; V_i = final volume; $V_i^* = V_i / V_{\text{exp}}$; t = final thickness.

numerical and *in vivo* results was 1%. The calculation of a volume versus pressure curve was calculated for each patient at every expansion point, which allows for the characterization of skin at each stage of the stretch.

Using the numerical analysis described, it is possible to fit the results of the numerical and *in vivo* analysis of the first expansion with the parameters $a = 0.21$ MPa and $b = 31.5$ of Delfino's exponential function. Figure 2 shows the principal stresses that occur during several stages of the expansion. Table 5 shows parameters a and b of Delfinos's function obtained from all the expansions of this patient. Parameter a changed from 0.21 MPa to 1.79 MPa and parameter b changed from 31.5 to 120.5. In addition, the initial thickness of 0.5 cm decreased to a final thickness of 0.13 cm, and the final thickness was expected to be smaller than the initial thickness, since the mean value of the thickness was used as the expansions progressed. Moreover, the maximum total stretch, $\lambda_{\max}$, reached 3.65 and the maximum principal stress, $\sigma_{\max}$, reached 679.6 kPa in Patient 1.

Patient 2. A mesh of 161 triangular finite membrane elements, M3D3, was used on the crescent skin expander for Patient 2, with dimensions of 10.1 cm×5.6 cm and $V_{\text{exp}} = 300$ ml. Using the numerical analysis described, we fit the results of the numerical and *in vivo* analysis from expansion one using the parameters $a = 0.64$ MPa and $b = 42.6$ of Delfino's exponential function. We found that parameter a changed from 0.64 MPa to 1.50 MPa and parameter b changed from 42.6 to 65.6 (Table 6). The initial

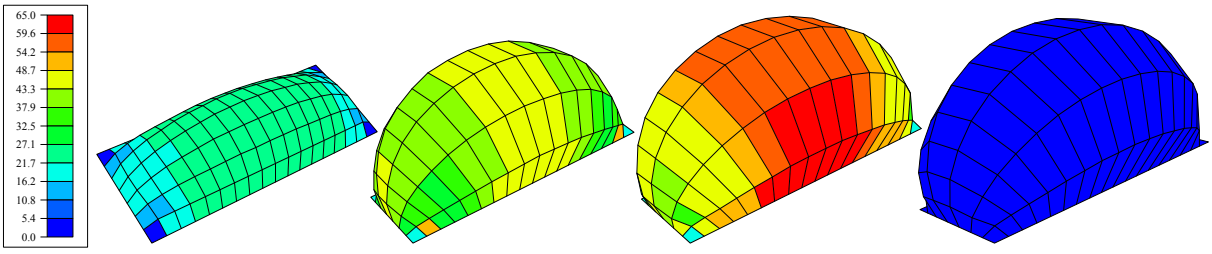

Figure 2. Finite element results for the principal stresses for patient 1 ($V_{\text{exp}} = 400$ ml) with, 126 quadrilateral finite membrane elements, M3D4: (a) 80–110 ml; (b) 380–425 ml; (c) 500–538 ml; (d) 500–538 ml after 7 days.

(i)	V_{i-1} ml	V_i ml	V_i^*	P_i kPa	$\lambda_{\max}$ added	$\sigma_{\max}$ MPa	t cm	H/t	a MPa	b
A	0	214	x	x	x	x	x		x	x
1	214	254	0.85	26.00	3.92	1,17	0.10	5.00	0.64	42.6
2	254	298	0.99	25.10	4.24	1,25	0.09	5.56	0.49	48.2
3	298	338	1.13	23.90	4.49	1,08	0.08	6.25	1.01	49.8
4	338	376	1.25	21.90	4.72	1,06	0.07	7.14	1.50	65.6

Table 6. Results of the parameters assessed for Patient 2.

thickness of 0.5 cm decreased to a final thickness of 0.07 cm, since the final value should be even smaller because we used the mean value for the thickness as the expansions progressed. The maximum stretch, $\lambda_{\max}$, reached 4.72 and the maximum principal stress, $\sigma_{\max}$, reached 1.06 MPa in Patient 2.

The data indicated that a principal stress, $\sigma_{\max}$, achieved during each skin expansion ranged between 679.6–1,060 kPa. This maximum stress is related with the pressure inside the skin expander, limited by the discomfort or pain felt by the patient.

4.2. *Numerical results for the skin of the lower leg.*

Patient 3. A mesh of 104 quadrilateral finite membrane elements, M3D4, was used on the rectangular skin expander of Patient 3, Figure 3, for which the dimensions were 9.6 cm×5.9 cm and $V_{\text{exp}} = 250$ ml. Using the numerical analysis described, we fit the results of the numerical and *in vivo* analysis and found that parameter a changed from 0.04 MPa to 0.30 MPa and parameter b changed from 22.0 to 45.0 (Table 7). The initial thickness of 0.80 cm decreased to a final thickness of 0.18 cm after expansion. The maximum stretch, $\lambda_{\max}$, reached 3.00 and the maximum principal stress, $\sigma_{\max}$, was 131.90 kPa in Patient 3.

Patient 4. A mesh of 126 quadrilateral finite membrane elements (M3D4) was used on the rectangular skin expander of Patient 4, for which the dimensions were 13.6 cm×5.5 cm and $V_{\text{exp}} = 400$ ml. Using the numerical analysis described, it was possible to fit the results of the numerical and *in vivo* analyses together. Table 8 shows parameters a and b for Delfino's exponential function for this patient. Parameter

Figure 3. Final expansion of patient 3; as the skin is expanded, the thickness of both dermis and epidermis decreases.

(i)	V_{i-1} ml	V_i ml	V_i^*	P_i kPa	$\lambda_{\max}$ added	$\sigma_{\max}$ kPa	t cm	H/t	a MPa	b
A	0	157	x	x	x	x	x	x	x	x
1	157	187	0.75	2.63	2.38	27.70	0.27	2.96	0.04	22.00
2	187	232	0.93	13.00	2.64	143.80	0.23	3.48	0.08	32.80
3	232	272	1.09	10.50	2.86	136.10	0.20	4.00	0.16	32.90
4	272	302	1.21	9.00	3.00	131.90	0.18	4.44	0.30	45.00

Table 7. Results for parameters assessed in Patient 3.

(i)	V_{i-1} ml	V_i ml	V_i^*	P_i kPa	$\lambda_{\max}$ added	$\sigma_{\max}$ kPa	t cm	H/t	a MPa	b
A	0	120	x	x	x	x	x	x	x	x
1	120	160	0.40	17.20	1.86	94.30	0.47	1.70	0.10	12.90
2	160	200	0.50	18.90	2.09	128.40	0.41	1.95	0.09	27.20
B	200	240	x	x	x	x	x	x	x	x
3	240	280	0.70	12.90	2.50	114.50	0.34	2.35	0.13	36.50
4	280	320	0.80	12.60	2.70	123.70	0.31	2.58	0.17	44.20

Table 8. Results for parameters assessed for Patient 4.

a changed from 0.10 MPa to 0.17 MPa, and parameter b changes from 12.9 to 44.2 from expansion 1 to 4, respectively. In addition, the initial thickness of 0.8 cm decreased to a final thickness of 0.31 cm. The maximum stretch, $\lambda_{\max}$, reached 2.7 and the maximum principal stress, $\sigma_{\max}$, was 123.4 kPa.

As seen in Tables 7 and 8, the results showed that a principal stress, $\sigma_{\max}$, achieved during each skin expansion of the lower leg was of the same magnitude and ranged between 144–128 kPa, which was lower than that obtained on the scalp.

4.3. ***Comparison between the scalp and skin of the lower leg related to V*.*** We next assessed the change in parameters a and b in relation to volume V^* as the skin was expanded. To obtain the change in the elastic parameters a and b of Delfino's exponential function for the scalp and the skin of the lower leg, the following procedure was used. Figure 4 shows the relationship between V_i^* and parameters a and b, obtained from Tables 5, 6, 7, and 8 for each skin expansion i.

The pressures measured *in vivo* at the beginning of each expansion were very small, so it was very difficult to obtain accurate measurements. Therefore, the results obtained for the parameters a and b can be considered as an important first step to understanding the behavior of the skin as it is expanded by taking into account differences between the patients in this study in terms of skin site, age, and race. The behavior of the parameters a and b during skin expansion of the scalp as a function of V^* is described by

$$a = 0.088 + 0.006e^{4.25V^*}, \quad b = 27.66 + 0.06e^{5.46V^*}. \tag{4-4}$$

These equations can predict the changes of the parameters for the skin of the scalp as it is stretched. The parameters for skin stretched for the first time $V^* = 0$ were $a = 0.094$ MPa and $b = 27.72$, and increased exponentially as the expansion progressed.

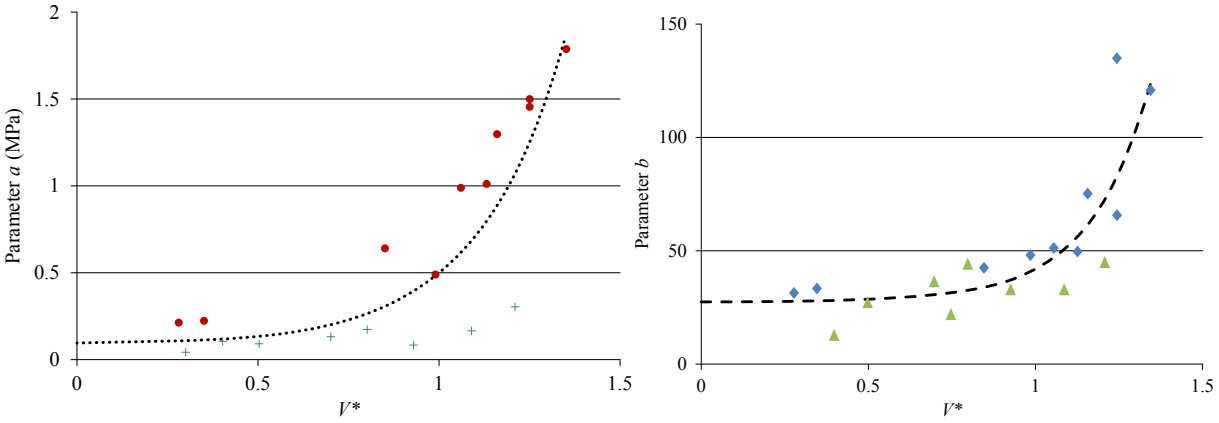

Figure 4. Continuous curves describing the change in parameters a (left) and b (right) with the variable V^* for skin expansion of both the scalp and lower leg. For unstretched skin, a was 0.094 MPa. For unstretched skin of the lower leg, b was 27.72.

4.4. ***Comparison of the thickness ratio between the scalp and skin of the lower leg.*** The results of this study could potentially be useful for plastic surgeons in various cosmetic procedures if the parameters a and b obtained could be connected to the ratio between the original thickness, H, and the thickness after expansion, t [Pitanguy et al. 1998]. When we combined the results in this manner, it became clear that the parameters of the first patient that received skin expansion of the scalp did not fit well with the other three patients, as seen in Figure 5. Specifically, the left half of the figure shows the behavior of a for patient 1 compared to the other 3 patients. When $\lambda_1\lambda_2 = H/t = 1$, there was no deformation, and the value of a for the scalp of patient 1 was 0.12 MPa, as a particular case of the fit

$$a = 0.045e^{0.98\lambda_1\lambda_2}, \tag{4-5}$$

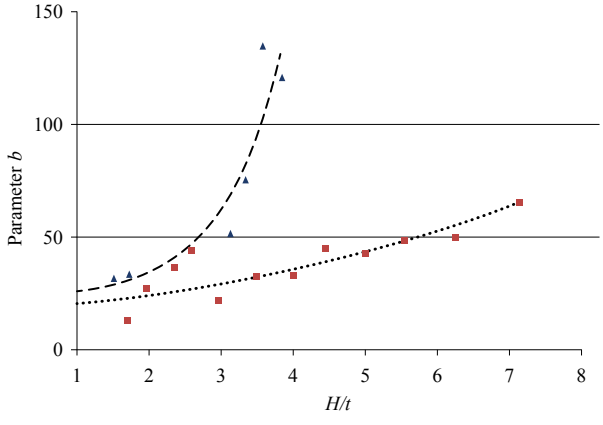

Figure 5. Changes in parameters a (left) and b (right) with the product $\lambda_1\lambda_2$ for patient 1 (dashed lines) and the other three patients combined (dotted line).

while for the other three patients combined the value was 0.04 MPa:

$$a = 0.030e^{0.56\lambda_1\lambda_2} - 0.01. \tag{4-6}$$

Figure 5, right, shows the behavior of parameter b for patient 1 compared to the other three patients. When $\lambda_1\lambda_2 = \frac{H}{t} = 1$, the value of b for the scalp of patient 1 was 26.50, as a particular case of the fit

$$b = 22.97 + e^{1.26\lambda_1\lambda_2}, \tag{4-7}$$

while for the other three patients combined, it was 20.19:

$$b = 16.71e^{0.19\lambda_1\lambda_2}. \tag{4-8}$$

Although the curves for patient 1 were quite different from the other three patients, the results for parameter b (26.5 and 20.2 for patient 1 and the other 3 patients combined, respectively) were similar when the skin was first stretched (i.e., $\lambda_1\lambda_2 = 1$). In contrast, parameter a was three times higher for patient 1 when the skin was first stretched than the other three patients combined (0.12 MPa vs. 0.04 MPa, respectively). Patient 1 being older than the others, with consequent skin flaccidity, is a possible explanation for the results observed. On the other hand, skin expanders used on the scalp are inserted under the galea, which is a tight and inelastic tendon. This procedural difference may also explain the difference in the two curves. The fact that patient 1 had darker skin was not considered as a relevant factor.

5. Conclusions

The study described here has pioneered the approach for modeling human skin over successive skin expansions. Based on these results, we have obtained different parameters for characterizing skin as the expansions proceed and the skin is stretched. The characterization of skin located in the scalp and lower leg was possible through the association of the numerical and *in vivo* analyses. The *in vivo* measurements showed that the skin relaxed after each expansion, since all pressure measurements inside the expanders were reduced to zero within one week after the procedure. Although there are recent proposals supporting that the tensile stress or the control of the expander internal pressure stimulates the cellular growth, in reality the external control parameter is the volume infiltrated. As a result of the viscoelastic property of the skin, the pressure inside the expander, due to relaxation, drops dramatically in the first days and even in the first hours after expansion. This is the principal reason why skin growth was not considered here, relaxation due to viscoelastic properties and not due to structural or molecular changes is used to model the change in the geometry of the skin.

Although the number of patients assessed for each region of the body was low, we measured between four and six expansions for each patient and obtained at least five measurements for each expansion on each patient. Therefore, the total data obtained from this study included more than 100 volume×pressure *in vivo* measurements.

The results presented here are considered reliable, and the parameters of Delfino's exponential function for the skin of three of the patients were a = 40.0 kPa and b = 20.2. It was not possible to compare our results with the work of other studies because the parameters used when characterizing skin are often from the Elasticity Modulus E, Ogden, Fung's, and other constitutive equations. Those equations and

many others were considered for our study but did not fit our *in vivo* data, since the rapid stiffening that occurs when large loads are applied is best described by a constitutive model based on an exponential strain energy formulation. One study used Mooney's equation for the characterization of the nonlinear mechanical behavior of human dermis and found C_{10} to be 9.4 ± 3.6 kPa and C_{11} to be 82 ± 60 kPa [Hendriks et al. 2003]. In another study, an equivalent equation to Delfino's equation for the artery was used, and the parameters were found to be $a = 44.2$ kPa and $b = 16.7$ [Dorfmann et al. 2010].

The results presented here used two different correlations, and parameters were analyzed in relation to the ratios of V^* and H/t. The curves obtained for the ratio of V^* were well behaved and provided considerable insight of human skin under expansion, which is still an unexplored area of study. However, these data are only useful when analyzing expanded skin. On the other hand, the curves that related parameters a and b with the ratio between the initial and maximum deformed thickness provided important and useful clues of the skin for scientists and surgeons. These analyses allow for the estimation of parameters of skin that is already stretched. After reconstructive surgery, the skin is already stretched, and the results presented here would allow the surgeon to predict the elasticity of the skin after two, three, or even four plastic reconstructive surgeries. Stiffening of the skin after several stretches was seen for both parameters. After the difference in the ratio between thicknesses increased to more than 4-fold, pulling the skin more would not eliminate the wrinkling effect, since it becomes more and more inelastic, which is well documented in the field of cosmetic surgery. As seen empirically, the skin showed an almost rigid body translation, so that pulling the skin in the vicinity of important anatomical structures, such as the eyelids or mouth, may indeed cause deformation of these structures. Importantly, this observation is seen in repeated facial plastic surgeries and serial reconstructive procedures.

It is important to note that as skin is extended, such as with expanders or in other procedures that tighten the skin, the collagen fibers are also extended and cause stiffening in the skin, which results in it being more and more resistant to expansion or further stretching. We observed this phenomenon as an increase in parameters a and b of Delfinos's constitutive equation as subsequent expansions continued.

The results presented in this study are very promising in this field and extend our understanding of the expansion of skin and other biological tissues. Additional research will provide the type, number, and volume of skin expanders, as well as frequency of expansions on several anatomic sites, which are factors necessary to obtain a specified amount of skin for the repair of particular medical problems.

List of symbols

V_{exp}	nominal volume	V^*	ratio between V_i and V_{exp}
V_{i-1}	initial volume	V^{**}	ratio between infiltrated volume and V_{exp}
V_i	final volume	H	initial thickness of the skin
		t	final skin thickness

Acknowledgments

We are especially grateful to Professor Ivo Pitanguy, Dr. Henrique N. Radwanski, and his staff, who have supported our projects over the years. Santa Casa da Misericórdia General Hospital of Rio de Janeiro and the Ivo Pitanguy Institute of Plastic Surgery approved this research. Financial support from

Coordination of Improvement for Higher Level Education (CAPES; grant number E: 0567-2006) and the Brazilian Council for Scientific and Technological Research (CNPq; grant number 301832/2009-9) were essential to making this research possible. We also extend special thanks for the agreement, support, and enthusiasm of the patients without whom this work would not have been possible.

References

[Alexander 1971] H. Alexander, "Tensile instability of initially spherical balloons", *Int. J. Eng. Sci.* **9**:1 (1971), 151–160.

[Austad and Rose 1982] E. D. Austad and G. L. Rose, "A self-inflating tissue expander", *Plast. Reconst. Surg.* **70** (1982), 588–594.

[Beauchene et al. 1989] J. G. Beauchene, M. M. Chambers, A. E. Peterson, and P. G. Scott, "Biochemical, biomechanical, and physical changes in the skin in an experimental animal model of therapeutic tissue expansion", *J. Surgical Res.* **47**:6 (1989), 507–514.

[Buganza Tepole et al. 2011] A. Buganza Tepole, C. J. Ploch, J. Wong, A. K. Gosain, and E. Kuhl, "Growing skin: a computational model for skin expansion in reconstructive surgery", *J. Mech. Phys. Solids* **59**:10 (2011), 2177–2190.

[Delalleau et al. 2006] A. Delalleau, J. Gwendal, J.-M. Lagarde, and J.-M. Berghjou, "Characterization of mechanical properties of skin by inverse analysis combined with the indentation test", *J. Biomech.* **39**:9 (2006), 1603–1610.

[Delalleau et al. 2008] G. Delalleau, J.-M. Josse, H. Lagarde, J.-M. Zahouani, and A. Bergheau, "A nonlinear elastic behavior to identify the mechanical parameters of human skin in vivo", *Skin Res. Technol.* **14**:2 (2008), 152–164.

[Delfino et al. 1997] A. Delfino, N. Stergiopulos, J. E. Moore, and J.-J. Meister, "Residual strain effects on the stress field in a thick wall finite element model of the human carotid bifurcation", *J. Biomech.* **30**:8 (1997), 777–786.

[Diridollou et al. 2000] S. Diridollou, F. Patat, F. Gens, L. Vaillant, D. Black, J. M. Lagarde, Y. Gall, and M. Berson, "In vivo model of the mechanical properties of the human skin under suction", *Skin Res. Technol.* **6**:4 (2000), 214–221.

[Dorfmann et al. 2010] A. Dorfmann, C. Wilson, E. S. Edgar, and R. S. Peattie, "Evaluating patient-specific abdominal aortic aneurysm wall stress based on flow-induced loading", *Biomech. Model. Mechanobiol.* **9**:2 (2010), 127–139.

[Duffy and Shuter 1994] J. S. Duffy and M. Shuter, "Evaluation of soft-tissue properties under controlled expansion for reconstructive surgical use", *Medical Eng. Phys.* **16**:4 (1994), 304–309.

[Geerligs et al. 2011] M. Geerligs, L. C. A. van Breemen, G. W. M. Peters, P. A. J. Ackermans, F. P. T. Baaijens, and C. W. J. Oomens, "Skin in vitro indentation to determine the mechanical properties of epidermis", *J. Biomech.* **44**:6 (2011), 1176–1181.

[Gonçalves et al. 2008] P. B. Gonçalves, D. C. Pamplona, and S. R. X. Lopes, "Finite deformations of an initially stressed cylindrical shell under internal pressure", *Int. J. Mech. Sci.* **50**:1 (2008), 92–103.

[Gonçalves et al. 2009] P. B. Gonçalves, R. M. Soares, and D. C. Pamplona, "Nonlinear vibrations of a radially stretched circular hyperelastic membrane", *J. Sound Vib.* **327**:1-2 (2009), 231–248.

[Green and Adkins 1970] A. E. Green and J. E. Adkins, *Large elastic deformations*, Clarendon Press, Oxford, 1970.

[Hendriks et al. 2003] F. M. Hendriks, D. Brokken, J. van Eemeren, and C. W. J. Oomens, "A numerical-experimental method to characterize the non-linear mechanical behaviour of human skin", *Skin Res. Technol.* **9**:3 (2003), 274–283.

[Holzapfel et al. 2000] G. A. Holzapfel, T. C. Gasser, and R. W. Ogden, "A new constitutive framework for arterial wall mechanics and a comparative study of material models", *J. Elasticity* **61**:1-3 (2000), 1–48.

[Lim et al. 2008] K. H. Lim, S. Jeyapalina, H. N. Ho, C. M. Chew, P. C. Y. Chen, C. L. Teo, and B. H. Lim, "Non-invasive prediction of skin flap shrinkage: a new concept based on animal experimental evidence", *J. Biomech.* **41**:8 (2008), 1668–1674.

[Ogden 2003] R. W. Ogden, *Nonlinear elasticity, anisotropy, material stability and residual stresses in soft tissue biomechanics of soft tissue in cardiovascular systems*, pp. 65–108, CISM Courses and Lectures Series **441**, Udine - Italy, 2003.

[Pailler-Mattei et al. 2009] C. Pailler-Mattei, S. Nicoli, F. Pirot, R. Vargiolu, and H. Zahouani, "A new approach to describe the skin surface physical properties *in vivo*", *Colloids Surf. B* **68**:2 (2009), 200–206.

[Pamplona and Bevilacqua 1992] D. C. Pamplona and L. Bevilacqua, "Large deformations under axial force and moment load of initially flat membranes", *Int. J. Non-Linear Mech.* **27**:4 (1992), 639–650.

[Pamplona et al. 2001] D. C. Pamplona, P. B. Gonçalves, M. Davidovich, and H. I. Weber, "Finite axisymmetric deformations of an initially stressed fluid-filled cylindrical membrane", *Int. J. Solids Struct.* **38**:10-13 (2001), 2033–2047.

[Pamplona et al. 2006] D. C. Pamplona, P. B. Gonçalves, and S. Lopes, "Finite deformations of cylindrical membrane under internal pressure", *Int. J. Eng. Sci.* **48**:6 (2006), 683–696.

[Pitanguy et al. 1998] I. Pitanguy, D. C. Pamplona, H. I. Weber, F. Leta, F. Salgado, and H. Radwanski, "Numerical modeling of facial aging", *Plast. Reconst. Surg.* **102**:1 (1998), 200–204.

[Schmidt et al. 1991] S. C. Schmidt, S. E. Logan, J. M. Hayden, S. T. Ahn, and T. A. Mustoe, "Continuous versus conventional tissue expansion: experimental verification of a new technique", *Plast. Reconst. Surg.* **87**:1 (1991), 10–15.

[Silver et al. 2003] F. H. Silver, L. M. Siperko, and G. P. Seehra, "Mechanobiology of force transduction in dermal tissue", *Skin Res. Technol.* **9**:1 (2003), 3–23.

[Socci et al. 2007] L. Socci, G. Pennati, F. Gervaso, and P. Vena, "An axisymmetric computational model of skin expansion and growth", *Biomech. Model. Mechanobiol.* **6**:3 (2007), 177–188.

[Zahouani et al. 2009] H. Zahouani, C. Pailler-Mattei, B. Sohm, R. Vargiolu, V. Cenizo, and R. Debret, "Characterization of the mechanical properties of a dermal equivalent compared with human skin *in vivo* by indentation and static friction tests", *Skin Res. Technol.* **15**:1 (2009), 68–76.

[Zöllner et al. 2012] A. M. Zöllner, A. Buganza Tepole, and E. Kuhl, "On the biomechanics and mechanobiology of growing skin", *J. Theor. Biol.* **297** (2012), 166–175.

Received 26 Dec 2011. Revised 28 Jun 2012. Accepted 30 Jun 2012.

DJENANE C. PAMPLONA: djenane@puc-rio.br
Laboratório de Membranas and Biomembranas, Departamento de Engenharia Civil, Pontífica Universidade Católica, Rua Marquês de São Vicente, 225, Gávea, 22451-900 Rio de Janeiro, RJ, Brazil

CLAUDIO R. CARVALHO: claudio.uff.civil@gmail.com
Departamento de Engenharia Civil, Universidade Federal Fluminense (UFF), Rua Passo da Pátria, 156, 24210-240 Niterói, RJ, Brazil

JOURNAL OF MECHANICS OF MATERIALS AND STRUCTURES
Vol. 7, No. 7, 2012
dx.doi.org/10.2140/jomms.2012.7.657

msp

IN-PLANE DYNAMIC EXCITATION OF AAC MASONRY WALLS PATCHED WITH FRP: DYNAMIC TESTING AND ANALYSIS

DVIR ELMALICH AND ODED RABINOVITCH

The paper studies the dynamic behavior of autoclave aerated concrete (AAC) masonry walls externally strengthened with composite materials and subjected to in-plane dynamic loads. The study combines experimental, analytical and numerical methodologies, presents the results of two types of dynamic tests, and uses them for comparison with a finite element approach that is based on specially tailored high-order finite elements. The first dynamic test focuses on the natural frequencies and vibration modes of the patched wall. The second set of tests focuses on the dynamic response of the wall to in-plane base excitation. The analysis uses the specially tailored finite elements, combines them with conventional elements, and compares the results with the experiments. The discussion supports the validation of the model and throws light on a range of phenomena that characterize the dynamic behavior of the strengthened wall. These phenomena range from the global in-plane to out-of-plane coupling to the localized effects at the strengthened layer level.

1. Introduction

The structural upgrade of existing masonry walls is a challenge that is often faced by the structural engineering community. The presence of masonry walls in the structural assembly can affect the dynamic response of the entire structure, especially in cases where the dynamic excitation is in the wall's plane. In these cases, the strengthening of the existing walls can modify their own dynamic response and can also modify the response of the entire structure. However, in order to use such walls as a part of the lateral load resisting system, their strengthening is often required. The use of externally bonded fiber reinforced plastic (FRP) has gained widespread acceptance as a modern way to address this need.

In order to use FRP bonding in dynamic upgrade applications, the dynamic behavior of the strengthened wall in general and particularly the dynamic interaction between the existing wall and the external strengthening layers, have to be characterized. These aspects are relevant to the strengthening of the wall to resist out-of-plane dynamic loads (e.g. [Hamed and Rabinovitch 2008; Rabinovitch and Madah 2012a; 2012b]) and they become even more important when the wall is strengthened to resist in-plane dynamic loads and to contribute to the general dynamic upgrade of the structure. The strengthening task requires a sound experimental basis and adequate analytical and numerical tools. The experimental basis is essential for characterizing the structural response and for providing experimental benchmarks for the assessment, examination, and validation of analytical and numerical tools. The analytical and numerical tools are then essential for widening the characterization of the structure and for addressing aspects that cannot be detected experimentally.

Keywords: dynamic analysis, dynamic tests, masonry walls, composite materials, finite element method, validation.

The experimental studies that focus on the in-plane loading and response of the FRP strengthened walls are divided into three main groups. The distinction between the groups is based on the type of the loading (static, cyclic, dynamic) and on the scale of the tested sample. The first group aims to assess the shear behavior of masonry panels and includes small scale panels or block triplets subjected to quasistatic loading. For example, Ehsani et al. [1997] and Suriya Prakash and Alagusundaramoorthy [2008] examined masonry triplets strengthened with FRP sheets and pointed at the effect of the orientation of the fibers on the shear resistance. Hamid et al. [2005] examined small scale FRP strengthened masonry panels made of hollow concrete blocks and subjected to different load directions. The results were used for the derivation of strength parameters for simplified models but they also revealed the impact of the direction of the load on the nature of the response. This response varies from splitting of the blocks when the load is perpendicular to the masonry course to shearing of the bed joints when the load is parallel to the masonry course. These observations raise questions regarding the response in the case of realistic, sign reversing, and orientation changing dynamic loads.

The group of experimental works that focus on small scale specimens also reveals some of the local phenomena that govern the FRP strengthened masonry wall. Among these, delamination and rupture of the FRP layer [Valluzzi et al. 2002; Hamid et al. 2005; Ehsani et al. 1997] and delamination due to buckling [Suriya Prakash and Alagusundaramoorthy 2008] are reported. In that sense, the experiments that focused on small scale specimens provide insight into such physical phenomena. The small scale tests also provide a measure of the structural properties of the strengthened panel. However, these experiments do not address some of the critical aspects of the response of the wall and particularly those related to the dynamic effects (cyclic loading, sign reversing loading, inertial effects, velocity-governed effect etc.).

The second group of experimental studies examines larger FRP strengthened panels that are subjected to cyclic loading. This class of experiments focuses on the global behavior of the strengthened wall to the in-plane load and mainly on the impact of the configuration of the strengthening system on the global response. Within this group, a distinction is made between infill walls and load bearing walls. Haroun and Ghoneam [1997] and Saatcioglu et al. [2005] studied infill walls combined with concrete frames under cyclic loading. Almusallam and Al-Salloum [2007] studied the effect of strengthening with strips made of FRP fabrics. The alignment of the fibers of the strengthening layers in the first and third of these papers was along the bed joint, while in the second the fibers were oriented along the diagonal. The comparison between the two indicates that the configuration of the composite materials directly affect the response, which varies from a pseudoductile behavior with a modest contribution to the ultimate strength in the case of horizontal and vertical fibers, to stiffer, stronger, and less ductile behavior in the case of the diagonal fibers. This trend is also reflected by the experimental results reported in [Altin et al. 2008].

The general focus on the global response and on the impact of global parameters such as type, size, and orientation of the strengthening system is also found in experimental studies on FRP strengthened load bearing walls. Stratford et al. [2004] studied the behavior of such walls under a cyclic loading but with loading, unloading, and reloading in one direction only. The role of the sign reversal of the loads and its impact on the response of the wall were not examined. Foster et al. [2005] studied the behavior of FRP strengthened load bearing walls with opening and examined configurations that combine vertical and diagonal strengthened strips. These experiments confirm that the FRP system can postpone the structural degradation observed in the unstrengthened walls. However, they do not directly reflect the response to a fully dynamic load.

The third group of experimental works includes direct dynamic tests of FRP strengthened walls. This class of experiments is essential for providing insight into the dynamic response and for setting experimental benchmarks for analytical and numerical models. In this class, the inertial forces and the damping effects dictate the response of the wall. The coupling effects that evolve due to the combination of realistic boundary conditions, direct dynamic loading, and inevitable imperfections are also taken into account. For example, Al-Chaar and Hasan [2002] examined the behavior of two parallel walls, one was unstrengthened and the other one was strengthened with FRP sheets. The two dynamically tested walls were made of concrete masonry units (CMU) and they supported a concrete slab. The walls were dynamically excited using a shake table in three directions. The response of these walls reveals some phenomena that characterize walls made of CMU and soft mortar. In particular, they reveal web splitting and cracking along the joints. ElGawady et al. [2002; 2003; 2005] examined the dynamic behavior of FRP strengthened walls made of clay bricks. Also here, the unstrengthened walls accumulated damage mainly along mortar joints. The FRP strengthening improved the resistance to cracking and therefore improved the dynamic lateral resistance of the walls. Turek et al. [2007] examined the dynamic response of masonry walls made of high strength concrete blocks. The results of this experimental study further strengthen the observation that the response is strongly affected by the strength ratio dictated by the high strength masonry units and the low strength mortar joints. With the strength ratio examined, and regardless of the configuration of the FRP, the cracking pattern tends to follow the weak mortar joints.

The above survey designates the direct dynamic testing as the most appropriate methodology for studying the dynamic response of the FRP strengthened wall and for providing benchmark results for the assessment and validation of analytical or numerical models. The direct dynamic tests surveyed above contribute to this effort and gain insight into the dynamics of the strengthened wall. However, in order to provide a sound basis for comparison with advanced analytical and numerical models, including ones that take the interfacial interaction between the existing and the bonded layers into account (e.g. [Elmalich and Rabinovitch 2012a]) a more refined class of experimental results is needed. Specifically, results that can be used for comparing the natural frequencies, the mode shapes, the damping mechanisms, and the elastic deformation fields in the dynamically loaded wall and results that can reflect on the interaction between the dynamically loaded wall and the externally bonded FRP layers are needed.

Another aspect of the dynamic behavior of FRP strengthened masonry walls is associated with the range of masonry materials involved. In historic masonry buildings, heavy solid masonry units and weak mortars (if any) are usually found. In other cases, relatively heavy bricks, solid concrete blocks, or hollow concrete blocks are used as the construction material. The experimental efforts discussed above and particularly the direct dynamic tests have focused on such materials (see, for example, [Al-Chaar and Hasan 2002; ElGawady et al. 2002; 2003; 2005; Turek et al. 2007]). In these cases, the combination of relatively stiff and strong blocks with weak joints dictates a cracking pattern that is limited to the joints.

Opposed to the classical heavy block and soft joint masonry, many modern masonry infill walls and, in some cases, even load bearing masonry walls are built using solid autoclave aerated concrete (AAC) blocks. The AAC is lighter than standard masonry materials and the mortar/adhesive that is used for the construction is often stronger and stiffer than the blocks themselves. As a result, the behavior of the wall is less heterogeneous and less orthotropic and the cracking is not limited to the mortar joints. In addition, the relatively low tensile and shear strengths of the AAC may negatively affect the bond of the externally bonded system and the ability of the interfaces to transfer shear and peeling stresses.

The above observations about the nature of the AAC-FRP system and the potential ability to convert existing AAC walls into dynamic load resisting elements, draw the attention to the FRP strengthening of AAC walls to resist in-plane dynamic loads. In spite of that potential, the dynamic strengthening of AAC panels with FRP did not gain much attention in the literature. The number of works that addressed this application mainly focus on the strengthening to resist out-of-plane loads [Hamed and Rabinovitch 2010], strengthening of AAC lintels [Memari et al. 2010], and synergic sandwich panels made of CFRP and AAC and subjected to static [Uddin et al. 2006; 2007] and impact loads [Serrano-Perez et al. 2007]. Reports on the application of FRP patched AAC walls for the dynamic in-plane upgrade and reports on the direct dynamic testing of FRP strengthened AAC masonry walls under dynamic in-plane loads were not found.

The objective of this paper is to gain insight into the dynamic response of FRP strengthened AAC masonry walls to dynamic in-plane loads. The paper also aims to present dynamic experimental results that can be used for the assessment and validation of analytical and numerical models for the dynamic behavior of the strengthened wall. Finally, it aims to use these results for the examination of a high order specially tailored finite element modeling approach [Elmalich and Rabinovitch 2012a; 2012b; 2012c]. To achieve these goals, the paper combines experimental and analytical/numerical methodologies. The experimental program focuses on direct dynamic testing of FRP patched AAC wall panels. The dynamic testing includes free vibration response to impulsive loads and forced dynamic response to base excitations. The combination of the experimental results and the high order FE analysis and the comparison between them are then used for studying additional aspects of the dynamic behavior of the FRP strengthened wall.

2. Experimental program

2.1. ***Test specimens, geometry, and materials.*** The tested AAC masonry specimens are illustrated in Figure 1. The tested panels are 750 mm wide, 900 mm high, and 100 mm deep. Each specimen is constructed of 6 courses of 250/150/100 AAC blocks. The construction of the specimens uses standard techniques, including the use of a special mortar/adhesive for joining the masonry blocks together. The tested panels include an unstrengthened one and a strengthened one. Both sides of the strengthened panel are patched with externally bonded GFRP sheets saturated with epoxy resin. The material properties of the masonry units, the masonry mortar/adhesive, and the GFRP system are listed in Table 1. These values are based on the materials' manufacturers. Some of the elastic and mechanical properties of the

Material	Elastic modulus [GPa]	Shear modulus [GPa]	Poisson ratio	Dry density [kg/m^3]
AAC block	1.550–1.780	0.62–0712	0.25	540–560*
AAC adhesive/mortar	10	3.84	0.25	1300
GFRP sheet	65 (x, y directions)	3.25	—	2600
Epoxy adhesive/resin	3	1.15	0.3	1100

* Measured value = 550 kg/m^3

Table 1. Material properties (reported by the manufacturers).

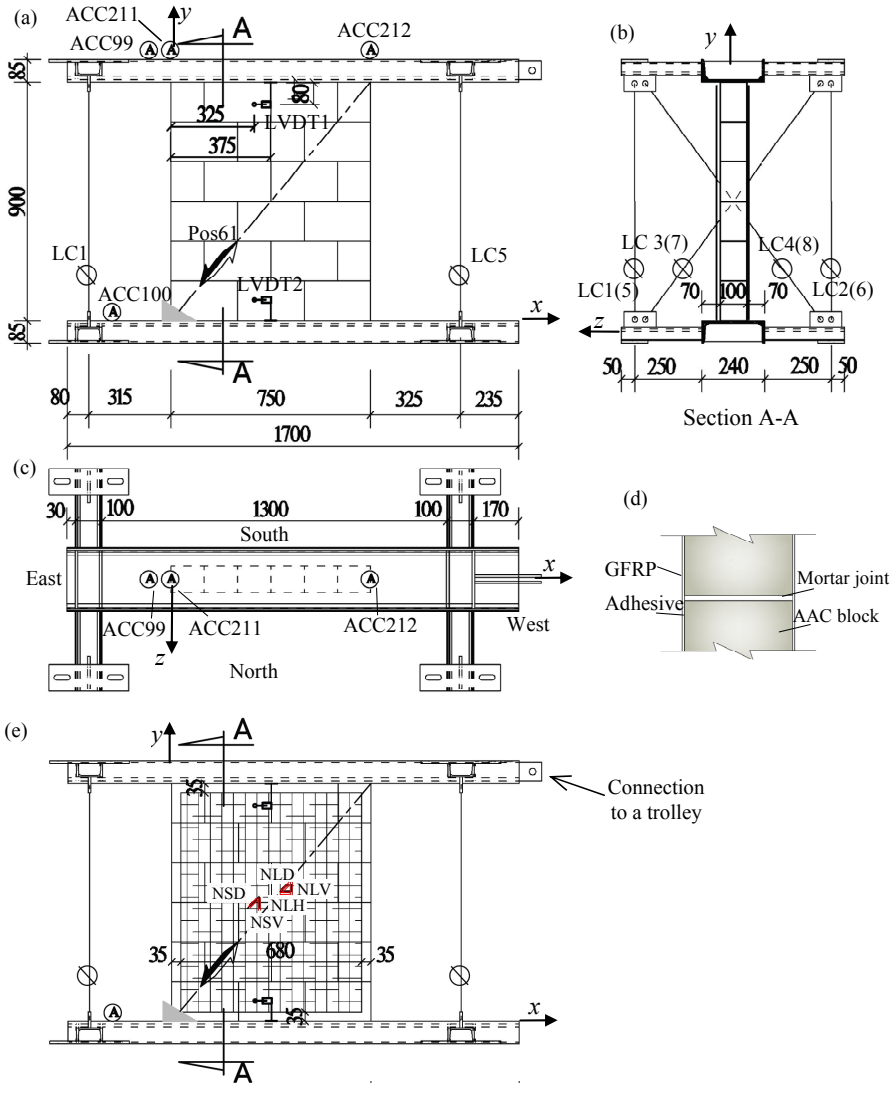

Figure 1. Experimental setup: (a) x-y view; (b) cross section; (c) top view; (d) zoom on a cross section near the joint; (e) x-y view of the FRP patched wall.

assembled AAC panel are further validated through a quasistatic diagonal compression test. Because this process is involved with data reduction through application of the FE model, it is reported later in this section, right after the presentation of the FE model.

2.2. ***Test setup.*** The test setup is also illustrated in Figure 1. A picture of the test setup and the tested specimens appears in Figure 2. For clarity of the discussion, a Cartesian coordinate system is "attached" to the specimen. In this system, x designates the direction of the excitation (east-west), y is the vertical coordinate, and z is perpendicular to the wall's plane (north-south) see Figures 1 and 2. The panels

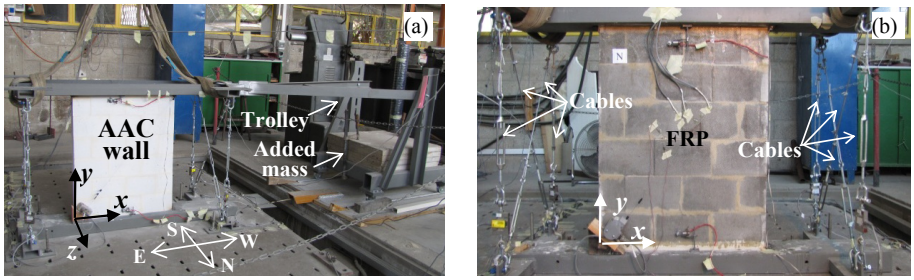

Figure 2. Experimental setup: (a) unstrengthened AAC panel; (b) FRP strengthened AAC panel.

are dynamically excited in the x direction using a shake table. The masonry panels are built on top of a steel beam, which is rigidly mounted on the shake table. In order to apply vertical prestress to the wall, and in order to add mass at the top of the wall, an additional steel beam is mounted on top of the panel (see Figures 1 and 2). The mass of the top beam equals 60 kg. The top and bottom beams are connected by two sets of cables. Each set includes two vertical cables and two diagonal cables. Each cable is pre-tensioned to 1 kN. The tensile forces in all cable are continuously monitored during the pre-tensioning stage and during the dynamic testing stage. The cable systems exert vertical compression on the panel (prestress) and they restrain the out-of-plane displacements (in the z direction) of the top beam by forming two stiffened y-z planes perpendicular to the wall's plane. However, due to the elastic deformability of the cables, the stiffened planes allow for some level of elastic movement of the upper beam in the y and z directions. This allows for the evolution of mode shapes that involve such movement of the top of the wall. The system of cables does not restrain the movement of the upper beam in the direction of the excitation (x). As a result, the dynamic in-plane load is solely carried by the tested wall. In order to simulate the effect of added mass, which represents the contribution of an upper slab, in some of the experiments, the upper steel beam is connected to a trolley. The point where the trolley is connected to the upper beam is shown in Figure 1e. The trolley, which is shown in Figure 2a, is free to move in the x direction on leveled rails. The friction associated with its movement is not significant. The mass of the trolley equals 190 kg and it can carry added mass up to about 800 kg. The added mass takes the form of concrete weights that are mounted on the chassis of the trolley (see Figure 2a). The trolley apparatus introduces the lateral effect of the added mass but it does not increase the vertical dead load on the shake-table.

2.3. ***Sensing and monitoring.*** The monitoring of the dynamic response uses 4 linear transducers (LVDT), 4 uni-axial (single-component) accelerometers, 1 position transducer, and 8 load cells. The location of the sensing devises is illustrated in Figure 1. The in-plane accelerations in the x direction are measured at the level of the bottom beam by the accelerometer designated ACC100 and at the level of top beam by the accelerometer designated ACC99. The out-of-plane accelerations in the z direction are measured using two additional accelerometers (ACC211 and ACC212). These sensors are mounted on the top beam at points that are located above the two upper corners of the wall. ACC211 is located above the east corner and ACC212 is located above the west one. The in-plane diagonal extension/contraction of the specimen is monitored using a position transducer (POS61). One end of this device is connected to

the bottom beam at the lower east corner and the other end is connected to the top beam at the upper west corner. LVDT1 and LVDT2 are used for monitoring relative displacements in the x direction. LVDT1 measures the relative displacement between a point located 80 mm below the upper steel beam and the upper beam itself. LVDT2 measures the relative displacement between a point located 80 mm above the bottom steel beam and the bottom beam itself. LVDT 3 monitors the movement of the shake table in the x direction and LVDT4 monitors the movement of the trolley. Finally, all 8 cables are equipped with load cells (LC1-LC8) that dynamically monitor the level of the tensile forces in each cable.

The FRP strengthening system is monitored using two sets of strain gauges (SG) that are located on both faces of the wall near its center. The strain gages are marked with 3 letters. The first letter refers to the face of the wall (N for north or S for south). The second letter refers to the length of the strain gage (S for 6 mm long strain gauges or L for 30 mm long strain gauges). The third letter refers to the direction of the strain gage (V for vertical, H for horizontal, D for 45°).

The sampling rate of each sensor equals 1200 samples per second. In some tests, this value is reduced to 1000 samples per second. The specific sampling rate in each test is determined depending on the duration of the excitation and on the expected dominant frequencies.

2.4. ***Testing protocol.*** The panels are dynamically tested in two steps. First, the dynamic characteristics of the panels are examined under impulse induced free vibrations. Two methods have been used for the excitation of free vibration of the wall. The first method is based on moving the shake table at constant velocity and then a sudden breaking. The second method is based on hammering the top steel beam in the x direction. Both scenarios yield an impulsive load in the x direction.

The second step of the dynamic testing examines the response of the wall to a cyclic base excitation. In this step, the panels are subjected to a series of cyclic base movement signals. In the present paper, the focus is on excitation signals that are characterized by frequencies of 6 Hz and 4 Hz and on the response of the patched wall.

3. High order FE modeling and analysis

3.1. ***High order finite element.*** The numerical analysis of the FRP patched wall uses the specially tailored FE approach developed in [Elmalich and Rabinovitch 2012a; 2012b]. For completeness and clarity, the main modeling approach and the main modeling assumptions that are used in the derivation of the specially tailored FE are briefly outlined next. Then, the numerical model that implements the specially tailored element in the FE analysis of the entire test setup is outlined. Finally, the assessment of the mechanical properties to be used in the numerical model is discussed.

The specially tailored multilayered FE is presented in Figure 3. The element combines five layers that include the two FRP layers, the two adhesive layers, and the wall. The latter is assumed linear elastic, orthotropic, and geometrically linear. The wall layer is modeled using the first order shear deformation plate theory. Due to the small thickness of the mortar joints used in the AAC masonry assembly and due to the relatively high strength and high modulus of the AAC mortar/adhesive (compared with the AAC blocks), the mechanical properties of the masonry units and the joints are homogenized and the panel is modeled using the equivalent properties.

The FRP layers are assumed geometrically and physically linear, elastic, and symmetrically stacked. These layers are independently modeled using the lamination theory and the first order shear deformation

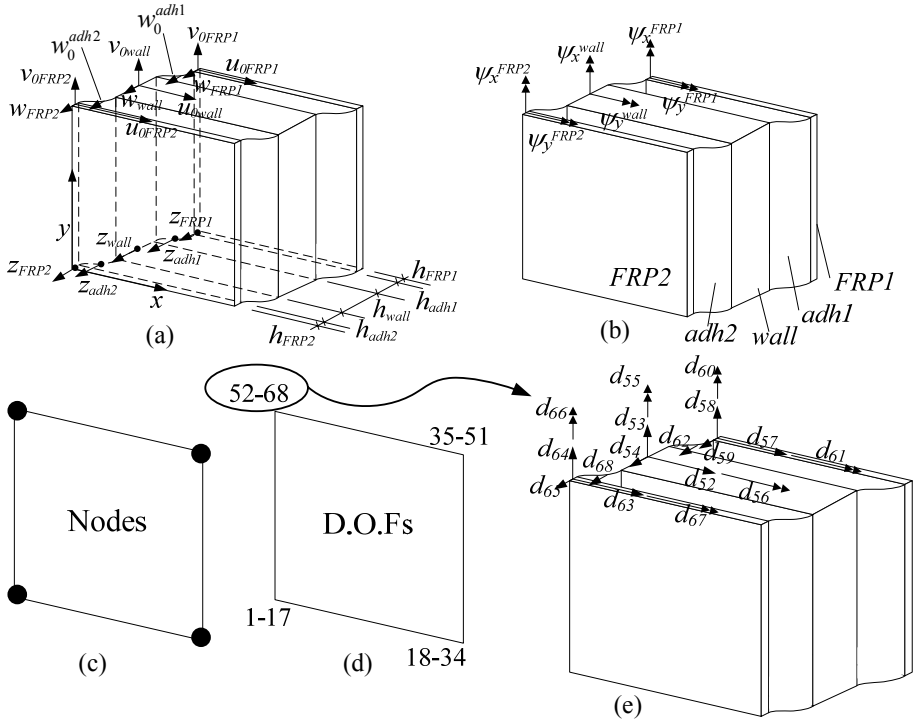

Figure 3. Notation and sign convention for the specially tailored high order element: (a) geometry, coordinate systems, and displacements; (b) rotations; (c) FE nodes; (d) FE degrees of freedom; (e) degrees of freedom in node 4.

plate theory. The adhesive layers are modeled as 3D elastic media. They are assumed physically and geometrically linear. The in-plane normal and in-plane shear rigidities of the adhesive layer are neglected compared with the rigidities of the adjacent components. For all components, the kinematic assumptions used for the dynamic analysis follow the ones used for the static case (see [Elmalich and Rabinovitch 2012a; 2012b] for more details). The various layers are joined together by imposing the conditions of compatible in-plane and out-of-plane displacement at the interfaces. Therefore, it is assumed that all interfaces of the adhesive layers are fully bonded and that they can transfer shear and out-of-plane normal stresses. Finally, the effect of damping is introduced by means of a mass (external) and stiffness (viscous) proportional Rayleigh damping model.

The specially tailored finite element includes 4 nodes and 17 degrees of freedom (DOFs) per node [Elmalich and Rabinovitch 2012a]. The elemental nodes, the DOFs, and the corresponding displacements and rotations are shown in Figure 3. The first 5 DOFs correspond to the nodal displacements of the wall layer ($u_{0\text{wall}}$, $v_{0\text{wall}}$, w_{wall}) in the x, y, and z directions, respectively, and to the rotations (ψ_x^{wall}, ψ_y^{wall}) of the wall's cross sections about the x and y axes, respectively. The following 10 nodal DOFs correspond to the displacements and rotations of the first FRP layer: $u_{0\text{FRP1}}(x, y, t)$, $v_{0\text{FRP1}}(x, y, t)$, $w_{\text{FRP1}}(x, y, t)$, $\psi_x^{\text{FRP1}}(x, y, t)$, $\psi_y^{\text{FRP1}}(x, y, t)$ and to those of the second FRP layer: $u_{0\text{FRP2}}(x, y, t)$, $v_{0\text{FRP2}}(x, y, t)$,

$w_{\mathrm{FRP2}}(x, y, t)$, $\psi_x^{\mathrm{FRP2}}(x, y, t)$, $\psi_y^{\mathrm{FRP2}}(x, y, t)$. The last two nodal DOFs correspond to the out-of-plane displacement at the middle of the adhesive layers: $w_0^{\mathrm{adh1}}(x, y, t)$, $w_0^{\mathrm{adh2}}(x, y, t)$.

The displacements fields in the layered element take the following form [Elmalich and Rabinovitch 2012a]:

$$\begin{Bmatrix} u_i(x, y, z, t) \\ v_i(x, y, z, t) \\ w_i(x, y, z, t) \end{Bmatrix} = \begin{Bmatrix} u_{0i}(x, y, t) \\ v_{0i}(x, y, t) \\ w_i(x, y, t) \end{Bmatrix} + z_i \begin{Bmatrix} \psi_x^i(x, y, t) \\ \psi_y^i(x, y, t) \\ 0 \end{Bmatrix} \qquad (i = \text{wall, FRP1, FRP2}), \tag{1}$$

$$\begin{aligned} w_{\mathrm{adh1}}(x, y, z, t) = {} & \frac{2z_{\mathrm{adh1}}}{h_{\mathrm{adh1}}^2}(z_{\mathrm{adh1}} + \tfrac{1}{2}h_{\mathrm{adh1}})w_{\mathrm{wall}}(x, y, t) + \frac{2z_{\mathrm{adh1}}}{h_{\mathrm{adh1}}^2}(z_{\mathrm{adh1}} + \tfrac{1}{2}h_{\mathrm{adh1}})w_{\mathrm{FRP1}}(x, y, t) \\ & + \frac{1}{h_{\mathrm{adh1}}^2}(h_{\mathrm{adh1}}^2 - 4z_{\mathrm{adh1}}^2)w_0^{\mathrm{adh1}}(x, y, t), \end{aligned} \tag{2}$$

$$\begin{aligned} u_{\mathrm{adh1}}(x, y, z, t) = {} & \frac{1}{24h_{\mathrm{adh1}}^2}\Big((-3h_{\mathrm{adh1}}^3 + 4z_{\mathrm{adh1}}h_{\mathrm{adh1}}^2 + 12z_{\mathrm{adh1}}^2h_{\mathrm{adh1}} - 16z_{\mathrm{adh1}}^3)w_{\mathrm{FRP1}}(x, y, t)_{,x} \\ & + (3h_{\mathrm{adh1}}^3 + 4z_{\mathrm{adh1}}h_{\mathrm{adh1}}^2 - 12z_{\mathrm{adh1}}^2h_{\mathrm{adh1}} - 16z_{\mathrm{adh1}}^3)w_{\mathrm{wall}}(x, y, t)_{,x} \\ & + (32z_{\mathrm{adh1}}^3 - 8z_{\mathrm{adh1}}h_{\mathrm{adh1}}^2)w_0^{\mathrm{adh1}}(x, y, t)_{,x} \\ & - 12h_{\mathrm{adh1}}\big(h_{\mathrm{FRP1}}(z_{\mathrm{adh1}} - \tfrac{1}{2}h_{\mathrm{adh1}})\psi_x^{\mathrm{FRP1}}(x, y, t) + h_{\mathrm{wall}}(z_{\mathrm{adh1}} + \tfrac{1}{2}h_{\mathrm{adh1}})\psi_x^{\mathrm{wall}}(x, y, t) \\ & + (2z_{\mathrm{adh1}} - h_{\mathrm{adh1}})u_{0\mathrm{FRP1}}(x, y, t) - 2(z_{\mathrm{adh1}} + \tfrac{1}{2}h_{\mathrm{adh1}})u_{0\mathrm{wall}}(x, y, t)\big)\Big), \end{aligned} \tag{3}$$

$$\begin{aligned} v_{\mathrm{adh1}}(x, y, z, t) = {} & \frac{1}{24h_{\mathrm{adh1}}^2}\Big((-3h_{\mathrm{adh1}}^3 + 4z_{\mathrm{adh1}}h_{\mathrm{adh1}}^2 + 12z_{\mathrm{adh1}}^2h_{\mathrm{adh1}} - 16z_{\mathrm{adh1}}^3)w_{\mathrm{FRP1}}(x, y, t)_{,y} \\ & + (3h_{\mathrm{adh1}}^3 + 4z_{\mathrm{adh1}}h_{\mathrm{adh1}}^2 - 12z_{\mathrm{adh1}}^2h_{\mathrm{adh1}} - 16z_{\mathrm{adh1}}^3)w_{\mathrm{wall}}(x, y, t)_{,y} \\ & + (-8z_{\mathrm{adh1}}h_{\mathrm{adh1}}^2 + 32z_{\mathrm{adh1}}^3)w_0^{\mathrm{adh1}}(x, y, t)_{,y} \\ & - 12h_{\mathrm{adh1}}\big(h_{\mathrm{FRP1}}(z_{\mathrm{adh1}} - \tfrac{1}{2}h_{\mathrm{adh1}})\psi_y^{\mathrm{FRP1}}(x, y, t) + h_{\mathrm{wall}}(z_{\mathrm{adh1}} + \tfrac{1}{2}h_{\mathrm{adh1}})\psi_y^{\mathrm{wall}}(x, y, t) \\ & + (2z_{\mathrm{adh1}} - h_{\mathrm{adh1}})v_{0\mathrm{FRP1}}(x, y, t) - 2(z_{\mathrm{adh1}} + \tfrac{1}{2}h_{\mathrm{adh1}})v_{0\mathrm{wall}}(x, y, t)\big)\Big), \end{aligned} \tag{4}$$

$$\begin{aligned} w_{\mathrm{adh2}}(x, y, z, t) = {} & \frac{2z_{\mathrm{adh2}}}{h_{\mathrm{adh2}}^2}(z_{\mathrm{adh2}} + \tfrac{1}{2}h_{\mathrm{adh2}})w_{\mathrm{FRP2}}(x, y, t) + \frac{2z_{\mathrm{adh2}}}{h_{\mathrm{adh2}}^2}(z_{\mathrm{adh2}} + \tfrac{1}{2}h_{\mathrm{adh2}})w_{\mathrm{wall}}(x, y, t) \\ & + \frac{1}{h_{\mathrm{adh2}}^2}(h_{\mathrm{adh2}}^2 - 4z_{\mathrm{adh2}}^2)w_0^{\mathrm{adh2}}(x, y, t) \end{aligned} \tag{5}$$

$$\begin{aligned} u_{\mathrm{adh2}}(x, y, z, t) = {} & \frac{1}{24h_{\mathrm{adh2}}^2}\Big((-3h_{\mathrm{adh2}}^3 + 4z_{\mathrm{adh2}}h_{\mathrm{adh2}}^2 + 12z_{\mathrm{adh2}}^2h_{\mathrm{adh2}} - 16z_{\mathrm{adh2}}^3)w_{\mathrm{wall}}(x, y, t)_{,x} \\ & + (3h_{\mathrm{adh2}}^3 + 4z_{\mathrm{adh2}}h_{\mathrm{adh2}}^2 - 12z_{\mathrm{adh2}}^2h_{\mathrm{adh2}} - 16z_{\mathrm{adh2}}^3)w_{\mathrm{FRP2}}(x, y, t)_{,x} \\ & + (-8z_{\mathrm{adh2}}h_{\mathrm{adh2}}^2 + 32z_{\mathrm{adh2}}^3)w_0^{\mathrm{adh2}}{}_{,x}(x, y, t) \\ & - 12h_{\mathrm{adh2}}\big(h_{\mathrm{wall}}(z_{\mathrm{adh2}} - \tfrac{1}{2}h_{\mathrm{adh2}})\psi_x^{\mathrm{wall}}(x, y, t) + \tfrac{1}{2}h_{\mathrm{adh2}})\psi_x^{\mathrm{FRP2}}(x, y, t) \\ & + (2z_{\mathrm{adh2}} - h_{\mathrm{adh2}})u_{0\mathrm{wall}}(x, y, t) + h_{\mathrm{FRP2}}(z_{\mathrm{adh2}} - 2(z_{\mathrm{adh2}} + \tfrac{1}{2}h_{\mathrm{adh2}})u_{0\mathrm{FRP2}}(x, y, t)\big)\Big), \end{aligned} \tag{6}$$

$$
\begin{aligned}
v_{\mathrm{adh2}}(x,y,z,t) = \frac{1}{24h_{\mathrm{adh2}}^2}\Big(& (-3h_{\mathrm{adh2}}^3 + 4z_{\mathrm{adh2}}h_{\mathrm{adh2}}^2 + 12z_{\mathrm{adh2}}^2 h_{\mathrm{adh2}} - 16z_{\mathrm{adh2}}^3) w_{\mathrm{wall}}(x,y,t)_{,y} \\
& + (3h_{\mathrm{adh2}}^3 + 4z_{\mathrm{adh2}}h_{\mathrm{adh2}}^2 - 12z_{\mathrm{adh2}}^2 h_{\mathrm{adh2}} - 16z_{\mathrm{adh2}}^3) w_{\mathrm{FRP2}}(x,y,t)_{,y} \\
& + (-8z_{\mathrm{adh2}}h_{\mathrm{adh2}}^2 + 32z_{\mathrm{adh2}}^3) w_0^{\mathrm{adh2}}(x,y,t)_{,y} \\
& - 12h_{\mathrm{adh2}}\big(h_{\mathrm{FRP1}}(z_{\mathrm{adh2}} - \tfrac{1}{2}h_{\mathrm{adh2}})\psi_y^{\mathrm{wall}}(x,y,t) + \tfrac{1}{2}h_{\mathrm{adh2}})\psi_y^{\mathrm{FRP2}}(x,y,t) \\
& + (2z_{\mathrm{adh2}} - h_{\mathrm{adh2}})v_{0\mathrm{wall}}(x,y,t) + h_{\mathrm{wall}}(z_{\mathrm{adh2}} - 2(z_{\mathrm{adh2}} + \tfrac{1}{2}h_{\mathrm{adh2}})v_{0\mathrm{FRP2}}(x,y,t))\big)\Big), \quad (7)
\end{aligned}
$$

where z_i is measured from the mid-surface of each layer, h_{adh1} and h_{adh2} are the thicknesses of the adhesive layers (Figure 3a). The unknown functions of x, y, and t, which appear on the right hand side of Equations (1)-(7), are approximated by the finite element shape functions $N(x, y)$ and the time dependent nodal displacement $d(t)$. More details on the derivation of the displacement fields, and particularly the displacement fields of the adhesive layers, are found in [Elmalich and Rabinovitch 2012a].

The finite element formulation takes a standard form that reads:

$$\boldsymbol{M}\ddot{\boldsymbol{d}} + \boldsymbol{C}\dot{\boldsymbol{d}} + \boldsymbol{K}\boldsymbol{d} - \boldsymbol{F}(t) = \boldsymbol{0} \quad (8)$$

where $\boldsymbol{M}$ is the mass matrix, $\boldsymbol{K}$ is the stiffness matrix, $\boldsymbol{C}$ is the damping matrix, and $\boldsymbol{F}(t)$ is the vector of external forces. The matrices $\boldsymbol{M}$ and $\boldsymbol{K}$ and the vector $\boldsymbol{F}(t)$ are assembled using the elemental matrices and the standard assembly procedure. The damping matrix $\boldsymbol{C}$ is synthesized following the Rayleigh damping approach:

$$\boldsymbol{C} = a_0\boldsymbol{M} + a_1\boldsymbol{K} \quad (9)$$

where the constants a_0 and a_1 are determined based on prescribed damping ratios that correspond to two of the vibration modes (see, for example, [Chopra 2001]).

3.2. ***FE model of the strengthened AAC wall.*** A schematic illustration of the FE model of the tested wall, its geometry, and the boundary conditions are shown in Figure 4. The thick lines at the top of the wall represent the upper steel beam. This beam is modeled using standard first order shear deformable 3D beam elements. The thin lines in Figure 4 represent the system of cables. Each cable is modeled as a longitudinal bar element with equivalent elastic and mass properties. Since the cables are pre-tensioned,

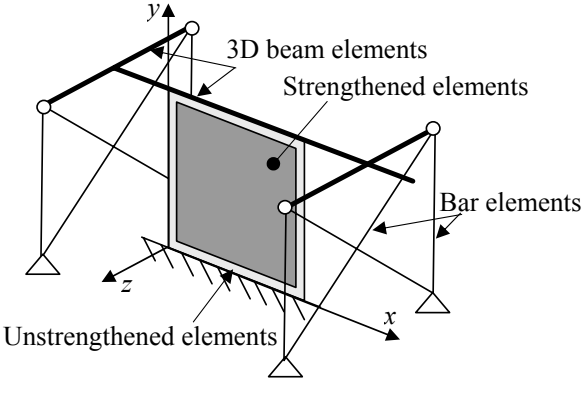

Figure 4. Schematic description of the FE model of the test setup.

the ability of the bar elements to resist compression is attributed to a reduction of the level of pre-tension in the cable and not expected to affect the comparison with the experiments. The diameter of the equivalent cross section is taken as 2.5 mm. This value is estimated based on the measured out-of-plane natural frequencies of the unstrengthened wall and the cables themselves and it reduces the nominal 3.2 mm diameter cross section due to the mass and the softening effects introduced by the tensioning devices, the load cells, and the connectors along the cable.

The dark gray area in Figure 4 represents the FRP strengthened region and the light gray area represents a 35 mm wide unstrengthened region at the perimeter of the patch. The FRP strengthened region is modeled using the specially tailored elements developed in [Elmalich and Rabinovitch 2012a] and briefly discussed above. The 35 mm wide unstrengthened regions at the perimeter are modeled using first order shear deformable shell elements with four nodes. The entire combination of elements (3D beam elements, 3D bar elements, shear deformable shell elements, and specially tailored elements) is assembled together to a unified FE model. In order to reduce the computational load, a substructuring procedure with superelements is adopted (see, for example, [Zienkiewitch 1977]). The application of the superelement substructuring approach to the specially tailored FE formulation of the FRP strengthened wall is discussed in [Elmalich and Rabinovitch 2012c]. In the present work, the substructuring procedure uses the classical Guyan reduction algorithm [Guyan 1965]. The superelement approach is applied to the 2D wall elements and the most refined mesh used here includes 26 by 28 superelements in the x and y directions, respectively. Each superelement is composed of 9 by 9 basic elements of the type derived in [Elmalich and Rabinovitch 2012a]. In the substructure level, each superelement includes 36 boundary nodes that replace a mesh of "regular" elements with 100 nodes. In the global scale, a mesh of superelements with 12,863 nodes replaces a mesh of "regular" basic elements with 59,455 nodes.

The dynamic analysis includes the assessment of natural frequencies and vibration modes as well as time history analysis. The first type of analysis uses the eigenvalue procedure implemented in MATLAB and the second one uses Newmark's method. The time step used in Newmark's method is determined based on the natural frequencies of the unstrengthened wall. If necessary, it is further refined after assessing the stability and the convergence characteristics of the numerical solution (A discussion of the stability and convergence of the high order finite element analysis appears in [Elmalich and Rabinovitch 2012a; 2012b; 2012c]). The time history analysis uses a Rayleigh damping with 10% damping ratio for the first and the third modes evaluated by the eigenvalue analysis of the unstrengthened panel. The relatively high damping ratio reflects the damping of the wall specimen but also the damping involved with the test setup.

3.3. ***Material properties.*** The material properties reported by the manufacturers of the materials are summarized in Table 1. The GFRP layer is assumed orthotropic with a design thickness of 0.065 mm. The thickness of the adhesive layers is estimated as 2 mm. This value also includes the thin resin saturated layer that forms in the outer shell of the AAC blocks.

The homogenized elastic and mechanical properties of the AAC panel play a critical role in the analysis of the dynamic response. Therefore, the elastic properties of the masonry assembly are experimentally evaluated. This is achieved using a diagonal compression test of the AAC unstrengthened panel. The schematic layout of this test is illustrated in Figure 5. The specimen that was used in the dynamic shake table experiments is tested to failure. The corners of the panel are trimmed in order to form a loading

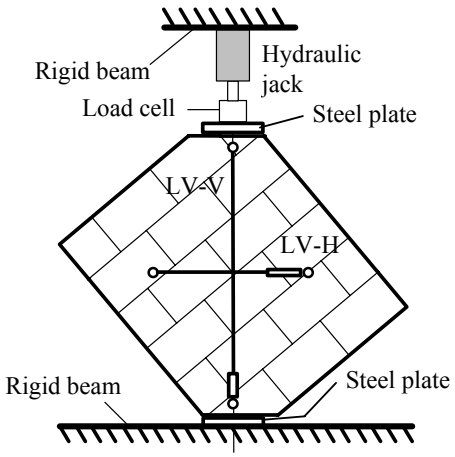

Figure 5. Test setup for the diagonal compression test of the unstrengthened panel.

plane perpendicular to the diagonal of the wall. The specimen is compressed using a hydraulic jack and the response is monitored using LVDTs and a load cell as shown in Figure 5.

A plot of the compressive force versus the averaged vertical strain (the shortening measured by LVDT divided by its length) is shown in Figure 6. The force-strain curve reveals a linear phase up to a strain level of about 0.01%. At this point, a jump in the level of the force is observed. The jump is followed by another linear and much longer phase up to failure. The slope of the second linear phase is almost identical to the slope of the first phase. The slope of this linear phase and the results of numerical simulation of the static compression test are used for the assessment of the homogenized elastic modulus of the masonry assembly. Due to the geometry of the specimen, the testing along the diagonal, and the impact of this layout on the direct conversion of the measured load versus measured shortening (or averaged strain) into a stress-strain curve, the homogenized elastic modulus is calibrated using the FE model. This is achieved by matching the numerically predicted slope of the load-versus average strain curve with the experimental one. Based on this procedure, the homogenized elastic modulus equals

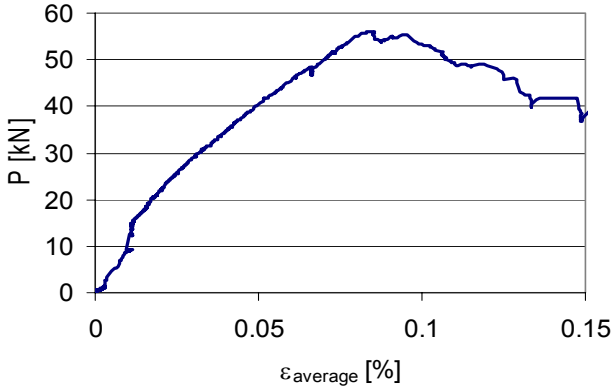

Figure 6. Diagonal compression test of the unstrengthened AAC panel: force versus average strain.

1500 MPa. This value is close to the lower value reported by the manufacturer for the AAC block (see Table 1). The calibrated value is also within the range of elastic moduli reported in the literature for AAC blocks of similar dry densities (see, for example, [Narayanan and Ramamurthy 2000]). The failure of the tested panel was controlled by splitting of the AAC blocks in the walls plane. Failure of the mortar joints was not detected. This observation, which differs from the classical mode of failure of masonry walls built of heavy natural stone or concrete masonry blocks and mortar joints, supports the consideration of the AAC masonry specimen as a homogenized isotropic and elastic medium and the corresponding assumptions used in the formulation.

4. Free vibration response and model validation

In this section, the natural frequencies and vibration modes are experimentally detected and compared with the ones determined by the FE model. The numerical natural frequencies and mode shapes are determined by solving the eigenvalue problem associated with the homogeneous undamped form of (9). In order to verify the convergence of the numerical solution, four meshes are examined. The numerically detected frequencies are listed in Table 2 and the vibration modes are shown in Figure 7. In order to allow a quantitative comparison between the modes, they are normalized to yield the same level of peak potential energy. For clarity of the figure, the displacements in Figure 7 are scaled up by a factor of 100.

The experimental natural frequencies are estimated using a Fast Fourier Transforms (FFT) of the time dependent signals measured by the various sensors in response to the two types of impulse loadings. The FFT plots present the complex result of the transformation multiplied by its complex conjugate. For clarity, the values are normalized with respect to the peak value detected in the figure's frequency range.

The identification of the experimental mode shapes is a more challenging task. The experimental detection of the mode shapes is based on the readings of various sensors and mainly of the readings of the accelerometers mounted on the top beam, the strain gauges mounted on the FRP layer, and the eight load cells mounted on the cables. In some cases, linear combinations of the directly measured signals are also examined. For example, averaging the readings of the z component of accelerations measured above the top east and top west corners of the wall (ACC211 and ACC212) yields a time domain signal that corresponds to the out-of-plane (z direction) movement of the upper beam. This signal is used for identifying mode shapes that are governed by out-of-plane flexure of the wall. The difference between the readings of the same two accelerometers divided by the distance between them defines an angular acceleration of the upper beam. This signal is used for identifying mode shapes that are governed by

Mode	Experiment	Analysis [Hz]			
	[Hz]	Mesh A: 7,956 DOFs	Mesh B: 10,846 DOFs	Mesh C: 14,178 DOFs	Mesh D: 218,671 DOFs
1	20.8	22.415	22.402	22.394	22.366
2	27.2	30.176	30.171	30.168	30.158
3	68.0–69.0	67.089	67.079	67.073	67.046

Table 2. Experimental and numerical results for the first three natural frequencies.

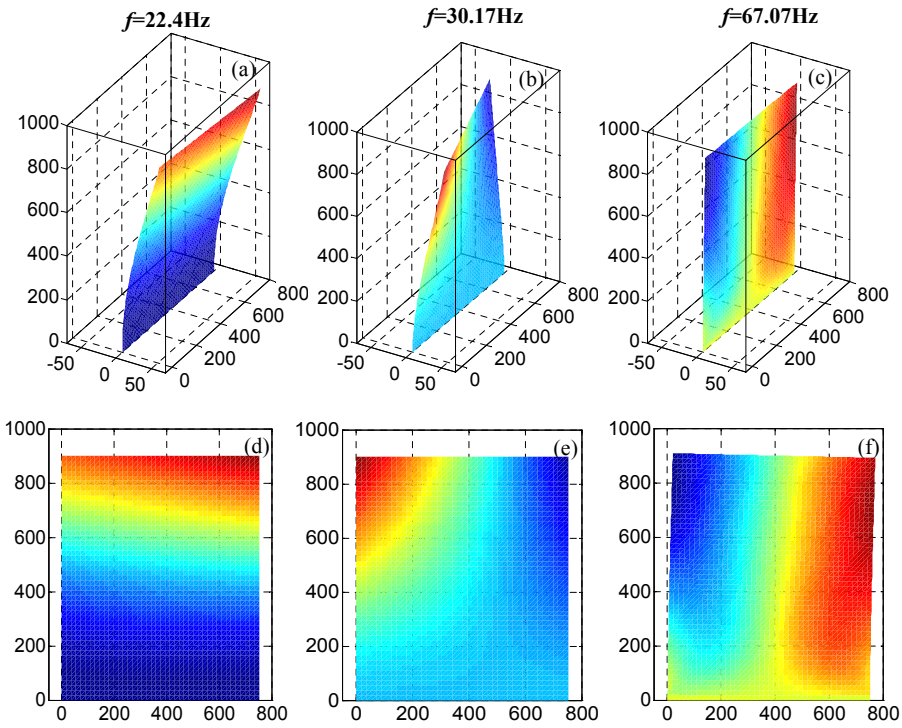

Figure 7. Vibration modes of the strengthened panel detected by the FE analysis and normalized for equal potential energy (the deformed shapes are scaled up by a factor of 100): (a) axonometric view, first mode; (b) axonometric view, second mode; (c) axonometric view, third mode; (d) x-y view, first mode; (e) x-y view, second mode; (f) x-y view, third mode.

twist of the wall and rotation of the top beam about the y axis. More experimental data is extracted by looking into linear combinations of the signals recorded by the load cells mounted on the cables.

The 20.8 Hz frequency detected in the experiment and listed in the first line of Table 2 is attributed to the out-of-plane flexural mode. To support this hypothesis, the average of the out-of-plane accelerations (z direction) at the top corners of the panel (ACC211, ACC212) is examined in Figure 8. The signal is defined by

$$\overline{ACCz(t)} = (ACC211(t) + ACC212(t))/2, \tag{10}$$

where $\overline{ACCz(t)}$ is the averaged signal and $ACC211(t), ACC212(t)$ are the readings of the accelerometers.

The time domain responses of $\overline{ACCz(t)}$ appear in Figure 8a and reveal a cyclic structural response with a slight low frequency beating. The time domain response shows that the differences between one experiment and another and between the two types of impulsive loading (sudden breaking of the shake table and hammering on the top beam) are very small. This indicates good repeatability. The frequency domain results of the averaged accelerations signal $\overline{ACCz(t)}$ appear in Figure 8b and reveal a significant peak at a frequency of 20.8 Hz. The presence of this peak in the averaged signal attributes

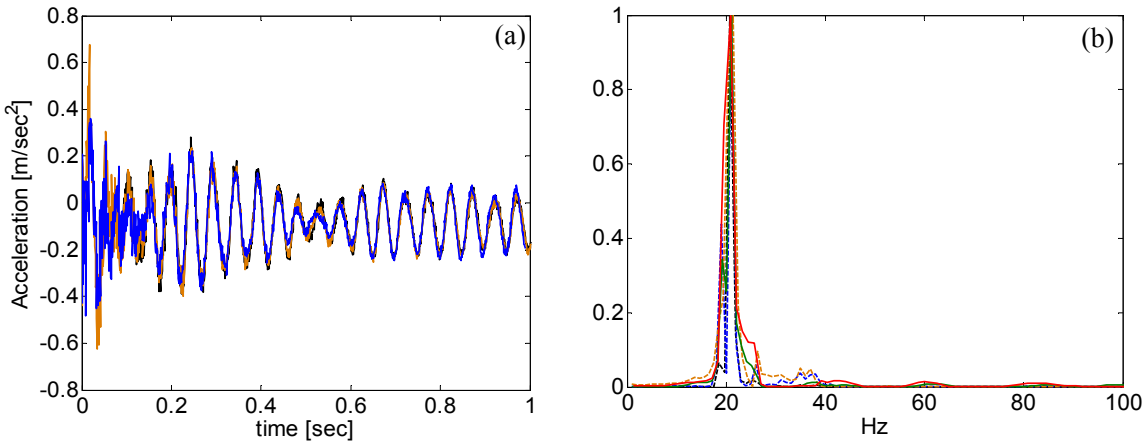

Figure 8. Response of the FRP strengthened masonry wall to in-plane impulse load: (a) time domain response of the averaged out-of-plane acceleration $\overline{ACCz(t)}$; (b) normalized frequency domain response of $\overline{ACCz(t)}$. Legend: — impulse load introduced through the shake table; - - - impulse load introduced through top beam. Each color refers to a different test.

this frequency to an out-of-plane flexure mode. Another observation that supports the hypothesis that the 20.8 Hz frequency corresponds to the out-of-plane flexure mode is found in the average of the lateral components of the variations in the tensile forces in the diagonal cables at the two stiffening planes. This signal is defined by

$$\overline{\Delta F_{z\mathrm{DIAG}}(t)} = (\Delta LC3(t) + \Delta LC4(t) + \Delta LC7(t) + \Delta LC8(t)) \cdot \cos(\alpha)/4, \tag{11}$$

where $\Delta LCi(t) = LCi(t) - LCi(0)$ is the time domain signal of the variation of the force in the i-th load cell, $LCi(t)$ $(i = 1 \ldots 8)$ is the signal measured by the i-th load cell, $LCi(0)$ is the reading of the i-th load cell at $t = 0$, and $\alpha = 0.866$ rad is the inclination angle of the diagonal cables. The frequency domain response of $\overline{\Delta F_{z\mathrm{DIAG}}(t)}$ is shown in Figure 9. This measure, which corresponds to out-of-plane movement of the top of the wall, also reveals one major peak at a frequency of 20.8 Hz. The correlation between the two FFT analyses attributes the 20.8 Hz frequency to the out-of-plane flexure mode.

The first natural frequency predicted by the numerical model equals 22.37 Hz and the corresponding mode, which appears in Figures 7a and 7d, is governed by out-of-plane flexure and out-of-plane movement of the upper beam. The numerically evaluated frequency is in good agreement with the experimental one and the model well captures the first out-of-plane mode (including the slight bending-twist coupling due to the asymmetric mass distribution of the upper beam; see Figures 1 and 7). The numerical values also point at convergence of the numerical solution with refinement of the mesh. This convergence and the agreement with the experiments support the validity of the FE model.

In physical terms, the experimental characterization of the first mode highlights the coupling of the in-plane and out-of-plane responses. The triggering of out-of-plane vibrations due to the in-plane impulsive excitation demonstrates this inevitable coupling. This observation implies that in many cases, the

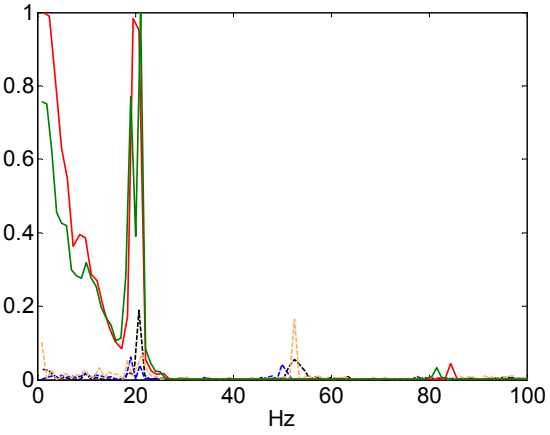

Figure 9. Response of the FRP strengthened masonry wall to in-plane impulse load: normalized frequency domain response of the averaged out-of-plane component in the diagonal cables $\overline{\Delta F_{z\mathrm{DIAG}}(t)}$. Legend: — impulse load introduced through the shake table; - - - impulse load introduced through top beam. Each color refers to a different test.

decoupling of the dynamic handling of the wall to a pure in-plane case and a pure out-of-plane case may be involved with loss of important physical information.

The 27.2 Hz frequency reported in the second line of Table 2 is attributed to the twisting mode of the wall. This mode, which is illustrated based on the analysis in Figure 7b, is governed by rotation of the top beam about the y axis. In the experiment, this mode is reflected by the angular acceleration of the top beam. This signal is defined by

$$ACC_{\theta y}(t) = (ACC211(t) - ACC212(t))/L_{\mathrm{ACC}}, \tag{12}$$

where L_{ACC}=750 mm is the distance between the two accelerometers (see Figure 1). The time history signal of $ACC_{\theta y}(t)$ appears in Figure 10a and reveals a high level of repeatability and minor differences between one test and another and between one testing method and another. The frequency domain transform of the signal appear in Figure 10b and reveals one major peak at a frequency of 27.2 Hz. The presence of this peak implies that this experimentally detected frequency corresponds to the second, twist governed, mode shown in Figures 7b,e. In order to further support this observation, the difference between the lateral components of the forces in the diagonal cables is examined. This signal, which is studied in Figure 11, is defined as by

$$\Delta\Delta F_{z\mathrm{DIAG}}(t) = (\Delta LC3(t) + \Delta LC4(t) - \Delta LC7(t) - \Delta LC8(t)) \cdot \cos(\alpha) \tag{13}$$

Figure 11 indicates that the normalized FFT of the response to the impulse load at the top beam includes a clear peak at a frequency that is close to the one observed in the frequency analysis of the angular acceleration (Figure 10b). The FFT analysis of the response to impulsive base motion and the larger amount of energy input it introduces include this peak. However, it also includes additional and more significant ones at higher frequencies.

The comparison between the FE result (30.17 Hz) and the experimental results (27.2 Hz) reveals a reasonable agreement. The differences, and mainly the fact that the experimental natural frequencies are

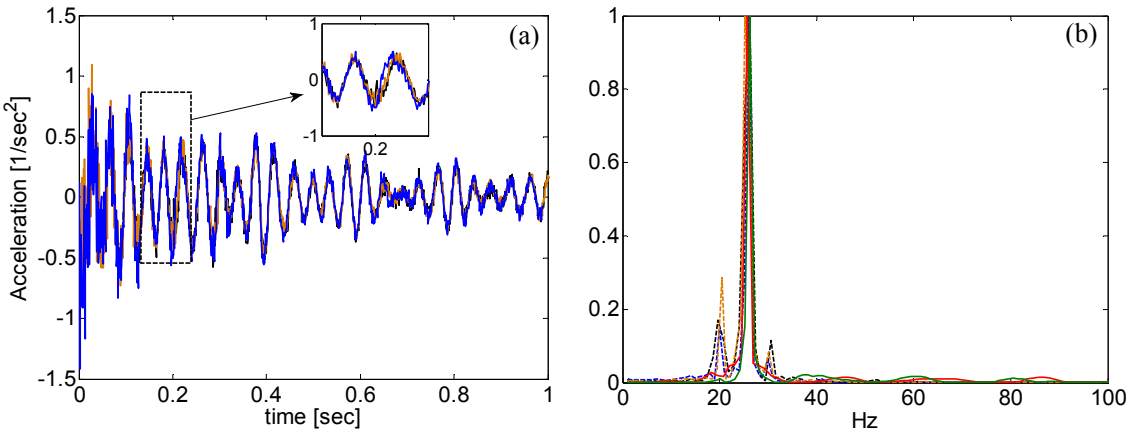

Figure 10. Response of the FRP strengthened masonry wall to in-plane impulse load: (a) time domain response of the angular acceleration $ACC_{\theta y}(t)$; (b) normalized frequency domain response of $ACC_{\theta y}(t)$. Legend: — impulse load introduced through the shake table; - - - impulse load introduced through top beam. Each color refers to a different test.

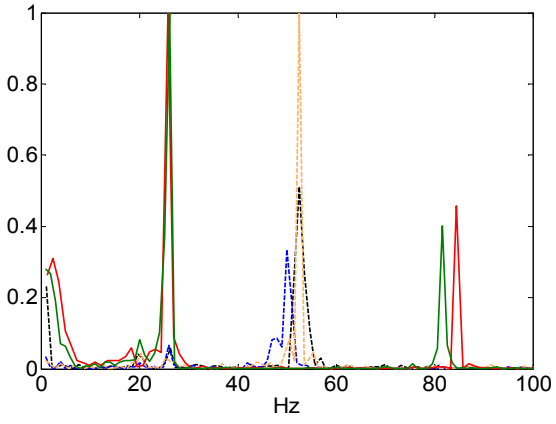

Figure 11. Response of the FRP strengthened masonry wall to in-plane impulse load: normalized frequency domain response of $\Delta\Delta F_{z\mathrm{DIAG}}(t)$. Legend: — impulse load introduced through the shake table; - - - impulse load introduced through top beam. Each color refers to a different test.

lower than the analytical ones, are attributed to the range of inevitable imperfections that are part of the experiment but not accounted for in the "sterile" numerical model. Nevertheless, the agreement between the FE analysis and the experimental results, both in terms of the natural frequency and in terms of the vibration mode, support the validity of the FE model.

The in-plane response of the tested specimen is studied in Figure 12. The time domain and the frequency domain distributions of the in-plane acceleration (x direction) at the top beam (ACC99) are shown in Figures 12a,b, respectively. The major peaks are observed at a frequency of 17 Hz and at a band

that ranges from 35 to 37 Hz. The first value is attributed to interaction with the shake table itself. In order to gain more insight into the source of the second peak (35–37 Hz) and its relation to the in-plane behavior of the panel, the differential forces in the vertical cables are examined. This combination of signals is defined by

$$\Delta\Delta F_{y\mathrm{VERT}}(t) = \Delta LC1(t) + \Delta LC2(t) - \Delta LC5(t) - \Delta LC6(t) \tag{14}$$

This combination aims to examine the rocking behavior of the upper beam, which is part of the in-plane response mode, see Figure 7c and Figure 7f. The time domain response of this combination appears in Figure 12c and reveals a good repeatability. The frequency domain response appears in Figure 12d and reveals peaks at a range of frequencies between 35 to 37 Hz.

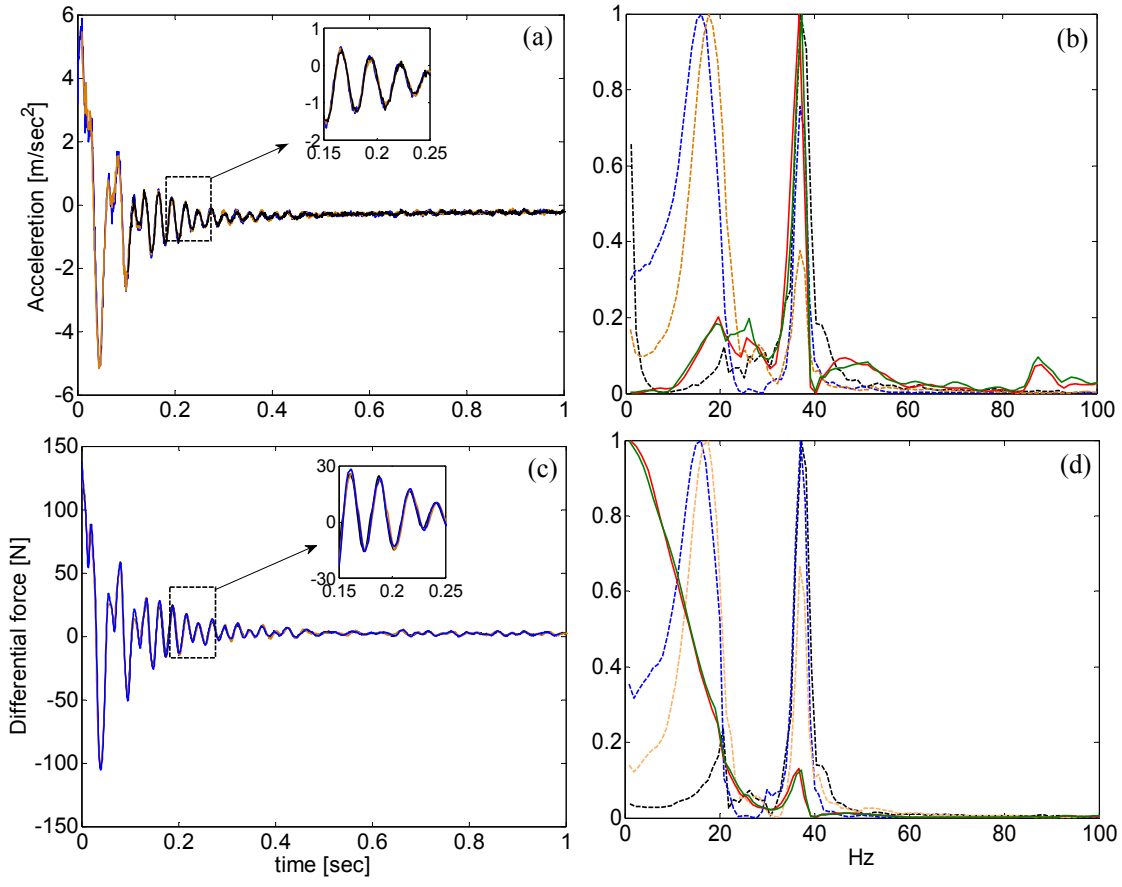

Figure 12. Response of the FRP strengthened masonry wall to in-plane impulse load: (a) time domain response of the in-plane acceleration; (b) normalized frequency domain response of the in-plane acceleration; (c) time domain response of $\Delta\Delta F_{y\mathrm{VERT}}(t)$; (d) normalized frequency domain response of $\Delta\Delta F_{y\mathrm{VERT}}(t)$. Legend: — impulse load introduced through the shake table; - - - impulse load introduced through top beam. Each color refers to a different test.

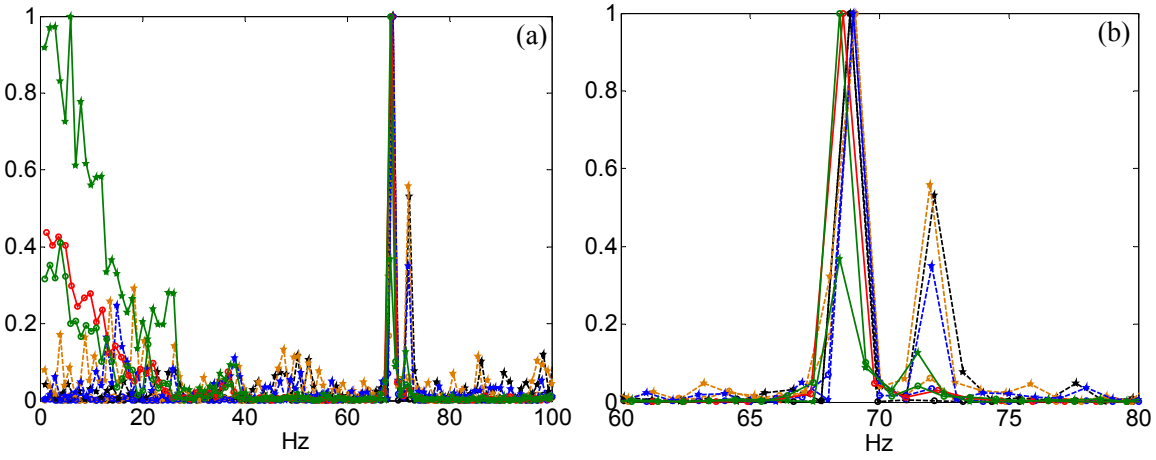

Figure 13. Response of the FRP strengthened masonry wall to in-plane impulse load: normalized frequency domain response of the short strain gages on the north face: (a) full range; (b) zoom on 60–80 Hz. Legend: diagonal strain gage, shake table movement results; vertical strain gage, shake table movement results; diagonal strain gage, top beam loading results; vertical strain gage, top beam loading results. Each color refers to a different test.

Figure 12 points at a clear range of frequencies. This range is, however, way below the results of the FE analysis, or any other estimation of the expected frequency. In order to examine and settle down this contradiction, additional experimental results are looked at. First, the readings of the strain gages that are mounted on the FRP layer are examined. The frequency domain analysis of the readings of the short strain gages is shown in Figure 13a and a zoom plot on the relevant frequencies band appears in Figure 13b. These experimental results reveal clear peaks at 68–69 Hz.

The experimental result of the in-plane natural frequency detected based on the readings of the strain gages is in good agreement with the third eigenfrequency obtained by the FE analysis (see Table 2). That this frequency is not clearly observed in the FFT analysis of the in-plane acceleration and is not observed in the FFT analysis of the forces in the cables suggests that another, much more dominant, local frequency is involved. It is hypothesized that the 35–37 Hz band of frequencies is attributed to the natural frequencies of the cables themselves. This hypothesis is examined and possibly supported by looking into two additional experimental observations. First, a free vibration test of the tensioned vertical and diagonal cables is carried out. In this test, each cable is removed from the setup and tensioned between two rigid supports. Then, it is subjected to an impulse load that yields free vibrations. The time domain response is monitored using two accelerometers (tuned to measure the out-of-plane accelerations of the cable) and a load cell. Then the various signals are transformed to the frequency domain. The results of the free vibration tests of the diagonal cables, for different level of pre-tensioning, appear in Figure 14a. They clarify that for the level of tensile force used in the experiment, the natural frequencies of the cable are in the range of 33–35 Hz.

The second experimental observation takes a closer look at the acceleration signal. With the 33–35 Hz band attributed to the natural frequencies of the cables, the reading of the longitudinal (x direction)

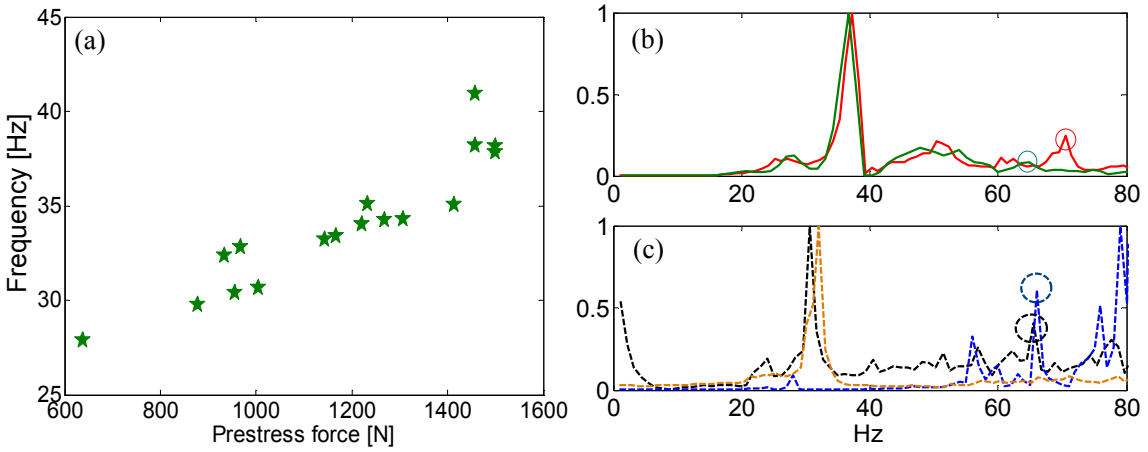

Figure 14. Effect of the localized vibration of the cables: (a) free vibration test of diagonal cable: natural frequency versus tensile force; (b) normalized frequency response of the in-plane acceleration after attenuating the effect the cables — impulse triggered by the shake table; (c) normalized frequency response of the in-plane acceleration after attenuating the effect the cables — impulse triggered through the top beam.

accelerometer $ACC99(t)$ are examined again but in this case, the effect of the cables on the frequency domain is attenuated. For the experiments conducted by moving the shake table at a constant velocity and then breaking, this is achieved by dividing the FFT representation of the accelerometer signal $ACC99(t)$ by the FFT representation of the sum of the vertical components of the tensile forces in the cables of the east stiffening plane (the stiffening plane that is closer to the location of the accelerometer). This signal is defined by

$$\Delta F_{y\text{EAST:ALL}} = \Delta LC1(t) + \Delta LC2(t) + \Delta LC3(t) \cdot \sin(\alpha) + \Delta LC4(t) \cdot \sin(\alpha) \tag{15}$$

The result of this signal appears in Figure 14b. In the experiments conducted by hammering the upper beam in the x direction, the energy input is much smaller than in the case of breaking the shake table and the response detected by the diagonal cables is not sufficiently prominent to yield a meaningful signal. Therefore, for these cases, the last two terms in (15) are omitted and the frequency domain signal of the accelerometer is divided by the frequency domain signal of the vertical cables:

$$\Delta F_{y\text{EAST:VERT}} = \Delta LC1(t) + \Delta LC2(t) \tag{16}$$

The FFT representation of the reading of the accelerometer after attenuating the effect of the cables using the signal given by (16) is studied in Figure 14c. This signal, as well as the one shown in Figure 14b, includes peaks in the range of 30–37 Hz, but they also reveal clear peaks in the range of 65–70 Hz. (The relevant peaks are circled in the figures). The 65–70 Hz frequencies are attributed to the in-plane vibration mode of the FRP strengthened wall. The presence of these peaks indicates that the global in-plane mode is detected by the accelerometer, but it is strongly affected by the localized vibration of the cables. This sensitivity is also affected by the proximity of the accelerometer to the points where the cables connect to the top beam. The strain gages, which are directly mounted on the FRP system, are

not significantly affected by the localized vibration of the cables. Therefore, the natural frequencies of the cables (33–37 Hz) are less prominent in the signal of the strain gauges.

The experimental and numerical results discussed above support the identification of the experimentally detected vibration modes and the validity of the FE model. This allows gaining more insight into the effect of each mode on the response of the strengthened wall. It also allows looking into aspects that cannot be directly detected in the experiment. One of these aspects, which directly reflects the interaction between the wall and the FRP, is the evolution of stresses at the interfaces of the adhesive layers. The distributions of the interfacial out-of-plane normal stresses that correspond to the first three modes are shown in Figure 15. Figures 15a,c,e show the stresses at the adhesive-AAC interface and Figures 15b,d,f

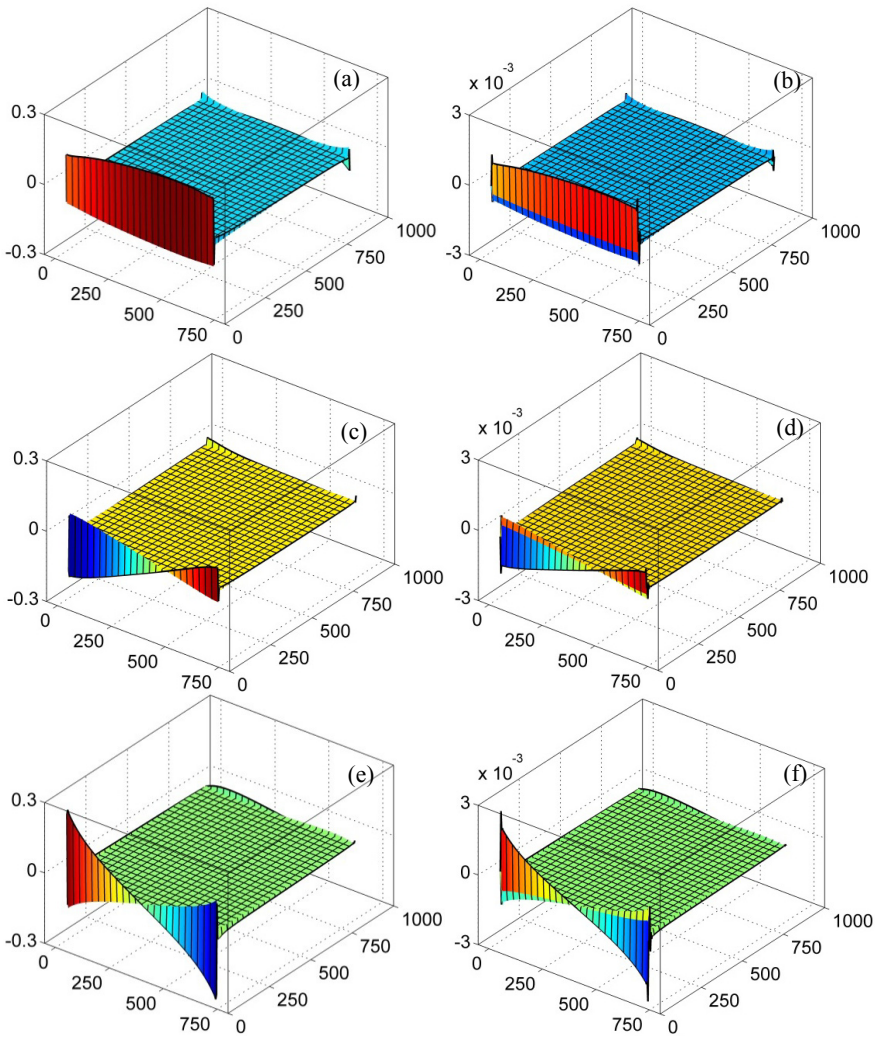

Figure 15. Modal out-of-plane normal stresses at the interfaces of the adhesive layer: (a) first mode, adhesive-wall interface; (b) first mode, adhesive-FRP interface; (c) second mode, adhesive-wall interface; (d) second mode, adhesive-FRP interface; (e) third mode, adhesive-wall interface; (f) third mode, adhesive-FRP interface.

show the stresses at the adhesive-FRP interface. In all cases, the modes are normalized to have the same level of strain energy.

Figure 7 indicates that for the same level of energy input, the largest displacements are observed in the out-of-plane (1st) and in the twisting (2nd) modes. In both cases, these displacements are "out-of-plane" by nature and they are about 4 orders of magnitude larger than the in-plane displacements attributed to the in-plane mode (Figures 7c,f). On the other hand, Figure 15 reveals that the largest peeling stresses are observed in the in-plane (3rd) mode (Figure 15e). This means that although the in-plane modal displacements are significantly smaller than the ones associated with the out-of-plane modes (per the same energy input), the in-plane vibration is associated with significant interfacial stresses. These stresses may trigger accumulation of interfacial damage or even debonding failures. Figure 15 also reveals that in all three modes, the adhesive-wall interface (Figures 15a,c,e) is subjected to a level of stresses that is much higher than the ones observed in the adhesive-FRP interface (Figures 15b,d,f). The negligible levels of peeling stresses detected at the adhesive-FRP interfaces are due to the small thickness of the FRP layer and its negligible bending rigidity. The thin FRP layer cannot resist significant out-of-plane normal tractions and it forces their decay through the depth the adhesive layer. On the other hand, the variation of the shear stresses along the strengthened region (and mainly near its edges) yields prominent out-of-plane normal stresses that evolve at the vulnerable adhesive-AAC interface.

5. Response to base excitation

The second phase of the study examines the response of the strengthened panel to base excitation. This phase aims to gain insight into the response of the strengthened wall to a direct dynamic load and to examine the FE model on a more local level and under a more demanding dynamic scenario. The dynamic load is introduced to the structure through a cyclic base excitation. Two cyclic displacement input signals with frequencies of 4 Hz and 6 Hz are examined. These frequencies fall below the natural frequencies of the studied strengthened panel, however, due to setup limitations, higher frequencies and especially frequencies that are close to the natural ones are not examined. The time history of the base displacement and acceleration records measured in the experiment are shown in Figure 16. The acceleration signals are also used as input for the FE analysis.

The results of the FE analysis are compared with the experimental ones on two scales. On the global scale, the accelerations detected by the analysis at the top of the wall are compared with the ones measured in the experiment. On the more local scale, the numerical and experimental relative displacements between the top beam ($x = 375$ mm, $y = 900$ mm) and a point located at $x = 325$ mm, $y = 820$ mm on the face of the wall (see Figure 1) are compared. In addition, the experimentally and the numerically detected principal strains at $x = 430$ mm and $y = 515$ mm are also compared. This measure is also attributed to the elastic response of the wall to the dynamic load.

The experimental and numerical accelerations of the top beam due to the two input excitations are plotted in Figure 17. Figures 17a,c refer to the 4 Hz signal and Figures 17b,d refer to the 6 Hz signal. The solid lines in Figure 17 stand for the FE results and the dotted lines stand for the experimental values. The comparison between the x component of the accelerations (Figures 17a,b) shows that the numerical results are in reasonable agreement with the experimental ones. Some of the discrepancies that are still observed stem from the effect of the vibrating cables on the accelerometers, an aspect that

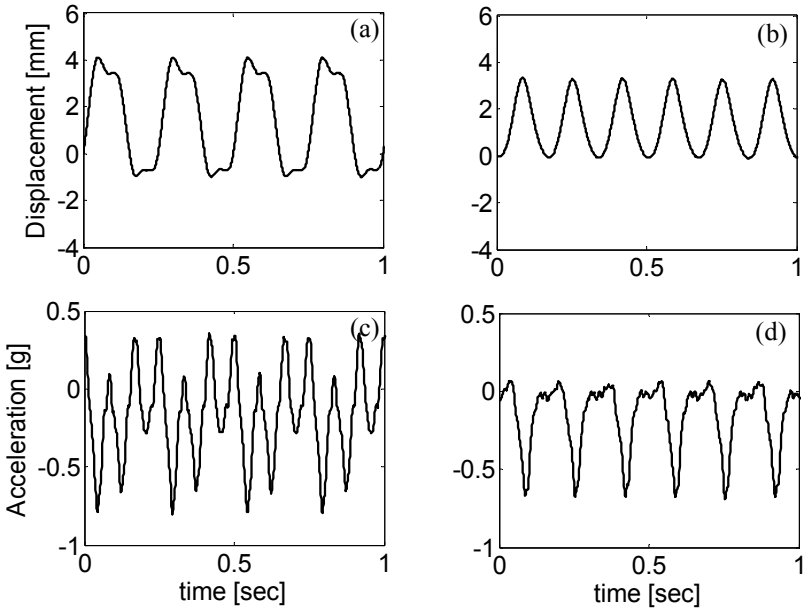

Figure 16. Time history signal of the base excitations: (a) 4 Hz base motion; (b) 6 Hz base motion; (c) 4 Hz base acceleration; (d) 6 Hz base acceleration.

is not taken into account in the analysis. It is also observed that the high frequency components of the acceleration signals (Figures 17a,b) are more significant in the experimental results (dotted lines) than in the numerical ones (solid lines). This discrepancy is attributed to the way damping is considered in the numerical mode. The Rayleigh damping model (9) and the estimated damping ratios tend to overestimate the impact of damping on the high frequency components. This observation designates the effect of damping as an aspect that requires further research into the dynamics of the FRP strengthened wall and further development of the model.

Figures 17c,d, which refer to the out-of-plane accelerations, reveal that the imperfections in the test setup trigger out-of-plane accelerations in response to the in-plane excitation. These effects are not observed in the "sterile" numerical analysis. The out-of-plane accelerations also trigger out-of-plane inertial forces and therefore a general 3D type of response. For example, in the tested cases, the out-of-plane acceleration goes up to 15% of the accelerations in the direction of the main excitation. This observation shades on the ability to decompose the analysis of the strengthened wall into a distinct in-plane and out-of-plane ones. On the contrary, it indicates that the two cases are coupled. The evolution of out-of-plane accelerations under the in-plane excitation also highlights the role that the strengthening system should take in improving the out-of-plane behavior of the masonry wall and in avoiding its collapse due to out-of-plane dynamic loads (see, for example, [Hamed and Rabinovitch 2008; Rabinovitch and Madah 2012a; 2012b] for dynamic out-of-plane strengthening, testing, and analysis).

The relative in-plane displacement between the top steel beam and the wall, and the relative in-plane displacements between the connection points processed by the FE model are plotted in Figure 18. The experimental curves are marked with dots and the FE results are marked with solid lines. The comparison between the two reveals a good agreement. The agreement is both in terms of the time history pattern

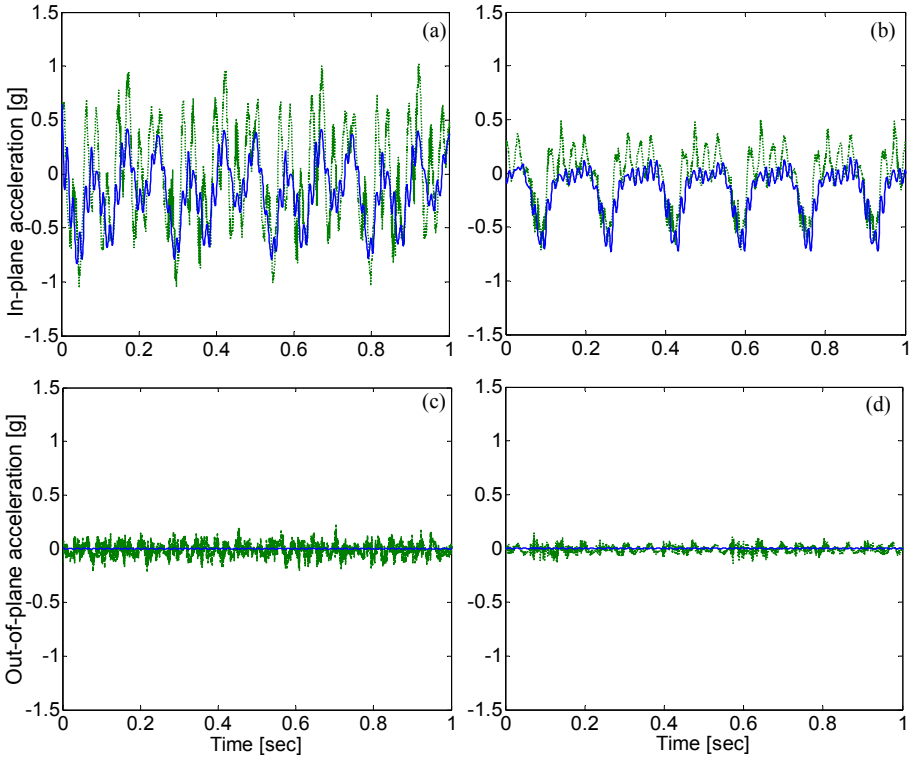

Figure 17. Accelerations of the top beam: (a) in-plane acceleration, 4 Hz signal; (b) in-plane acceleration, 6 Hz signal; (c) out-of-plane acceleration, 4 Hz signal; (d) out-of-plane acceleration 6 Hz signal. Legend: ——— FEA; · · · · · · experimental.

and in terms of amplitude and it is observed under both excitations. Opposed to the aspects studied in the previous sections, which are all linked to the global behavior of the tested wall, this relative displacement directly reflects the elastic response of the FRP patched wall to the dynamic load. The agreement between the numerical and the experimental results points at the ability of the FE model to capture and quantify the time dependent elastic response of the strengthened wall.

Another aspect of the localized elastic response of the dynamic load is the evolution of strains in the bonded layers. The strains on the north FRP patch are compared with the dynamic FE results in Figure 19. This comparison is limited to the 6 Hz signal. For clarity, the measured and the calculated strains are converted into principal ones. The experimental and numerical results reveal that although the excitation with frequencies notably lower than the relevant natural frequency yields a significant rigid body component, it is also involved with an elastic component. The comparison of this dynamic strain signal, which is sufficiently high to be detected by the sensors, with the numerical results reveals good agreement of patterns and magnitudes. The correlation between the numerically determined strains and the experimentally detected ones and the correlation in terms of elastic displacements (Figure 18) demonstrates the ability of the model to detect the dynamic elastic deformation fields.

The magnitude of the deformation component in the dynamic displacement field is amplified when it is tested with the trolley and its added mass. The input acceleration signal and the in-plane acceleration

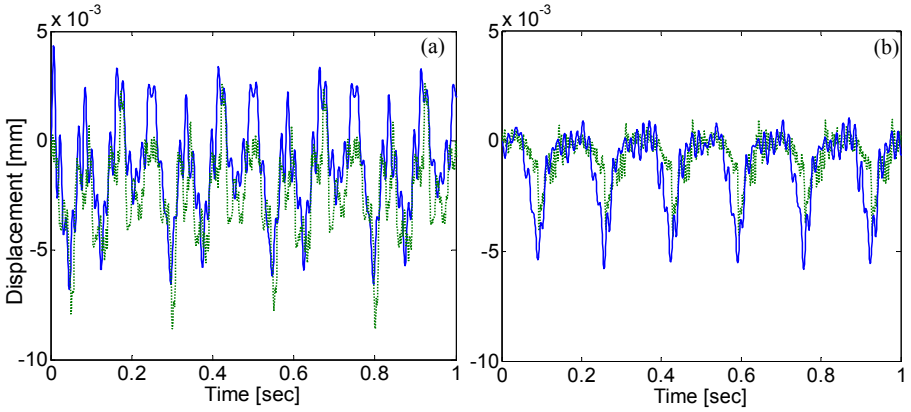

Figure 18. Relative displacement between top steel beam and the FRP patched panel measured by LVDT1: (a) 4 Hz signal; (b) 6 Hz signal load. Legend: ——— FEA; · · · · · · experimental.

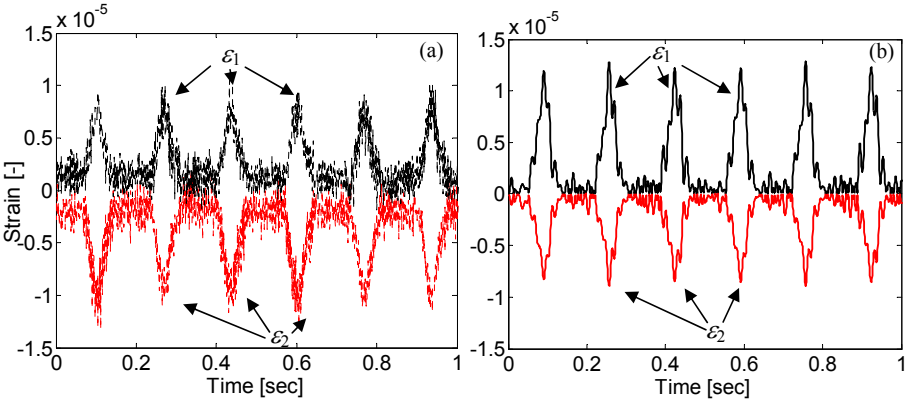

Figure 19. Measured and calculated principal strains at $x = 430$ mm, $y = 515$ mm versus time: (a) experimental results; (b) numerical results.

measured at the top of the wall when tested with added lateral mass of 580 kg appear in Figure 20a. Due to the supplemental lateral mass, the input acceleration signal is amplified and the accelerations at the top of the wall are about twice as large as the input signal at its base. The elastic deformation field reflected by the diagonal strains measured at $x = 430$ mm, $y = 515$ mm and presented in Figure 20b is also more prominent. The levels of strain measured under this dynamic loading condition are about 5 times larger than the ones measured without the added mass. Yet, from a quantitative point of view, the measured strains are still within the capacity limits of the strengthening system and damage to the wall, to the strengthening system, or to the interfaces between them was not observed.

The validation of the FE model and the evolution of an elastodynamic deformation field allow to explore more aspects of the dynamic response of FRP patched wall and to examine ones that cannot be directly detected in the experiment. From a practical point of view, it is interesting to examine the dynamic response of the FRP system and the bond layer. For brevity, this examination focuses on the

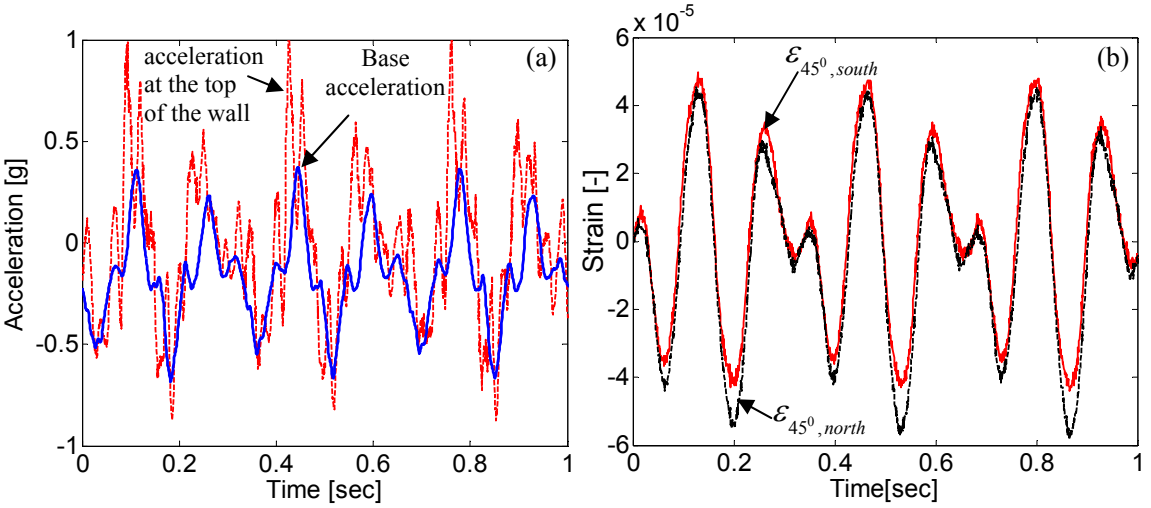

Figure 20. Response to a 6 Hz base excitation with added mass of 580 kg: (a) accelerations; (b) diagonal strains on the FRP layer. Legend: —— Base acceleration; - - - in-plane acceleration at the top of the wall; —— diagonal strain at $x = 430$ mm, $y = 515$ mm on the north face; - - - diagonal strain at $x = 430$ mm, $y = 515$ mm on the south face.

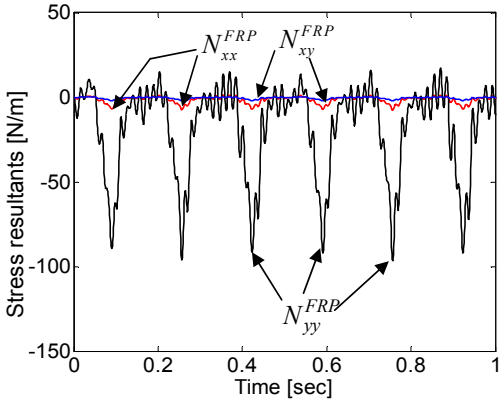

Figure 21. Stress resultants in the south FRP layer due to 6 Hz excitation versus time.

6 Hz cyclic excitation without the added mass. The time history response of the axial and shear resultants in the south FRP layer at $x = 125$ mm and $y = 125$ mm is studied in Figure 21. The curves indicate that the stress resultant N_{yy} is dominant and it attains values that are much higher than the stress resultants in the x direction and shear resultants. It is also observed that at the examined point, the dominant N_{yy} values are negative and reflect compression. Although the magnitudes are rather small (compared, for example, with the tensile strength of the FRP), the cyclic compression of the thin FRP layer may lead to a geometrical instability (buckling) of the patch. Such potential buckling is an inherent aspect of the response of the FRP strengthened wall to dynamic in-plane loads and it should be taken into account in the design of such systems.

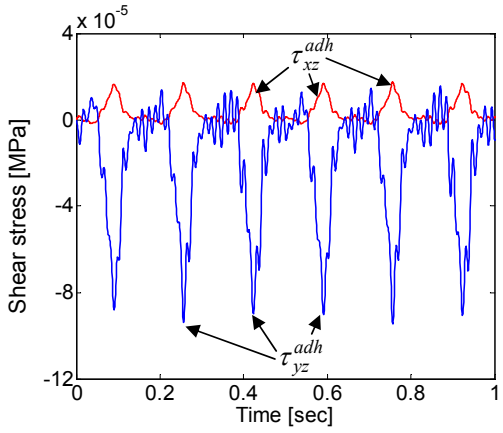

Figure 22. Shear stresses in the south bond layer due to 6 Hz excitation versus time.

The variation of the interfacial shear stresses at $x = 125$ mm and $y = 125$ mm in time appears in Figure 22 and reveals that the shear stresses in the y direction τ_{yz} are higher than τ_{xz}. In addition, they are more affected by the higher frequencies. The pattern of the shear stresses τ_{yz} corresponds to the one of the axial stress resultants in the y direction and the higher frequency component corresponds to the 67 Hz of the in-plane mode. This observation indicates that this unique mode is not solely governed by in-plane shear but also by a rocking response driven by the axial stresses in the y direction (Figure 22) and the accompanying shear stresses in the adhesive layer (Figure 21).

The out-of-plane normal stresses at the interfaces of the adhesive layer at $t = 0.259$ sec are studied in Figure 23. As discussed in the previous section, the interfacial stresses at the adhesive-AAC interface in Figure 23a are much higher than those in the adhesive-FRP interface (Figure 23b). As a result, the brittle adhesive-AAC interface is more susceptible to debonding. The interfacial out-of-plane stresses points at localized effects near the fixed edge of the AAC panel. At this point in time, the distribution of the stresses changes from positive (peeling) stresses to negative stresses along the x axis. Quantitatively, it is observed that the examined excitation, which involve accelerations that go up to about 0.6 g but central

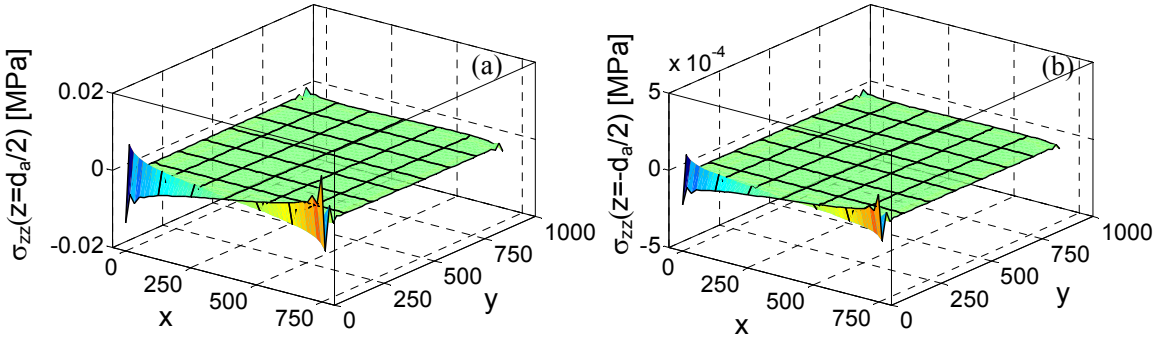

Figure 23. Interfacial out-of-plane normal stresses due to 6 Hz signal at $t = 0.259$ sec: (a) adhesive-wall interface; (b) adhesive-FRP interface. (Note the different scales.)

frequencies that are below the natural frequencies of the wall and relatively small elastic deformations, yields relatively low levels of interfacial stresses. Correspondingly, and in spite of the low tensile strength of the AAC interface, delaminations of the FRP system were not observed in the experiment.

6. Summary and conclusions

Dynamic strengthening of masonry structures using externally bonded fiber reinforced plastics is an attractive structural application with a significant potential in the field of dynamic upgrade of structures. In this paper, the 3D dynamic behavior of FRP strengthened AAC masonry panels has been experimentally and numerically studied. The FRP strengthened AAC panel has been dynamically tested under impulsive load that yields a free vibration response and under dynamic base excitations. The natural frequencies of the strengthened panel have been studied and compared with numerical results obtained using a specially tailored FE model. This model combines high-order multilayered 2D elements that are specially tailored for the patched wall with conventional bar, beam and shell elements that model all other components of the test setup. The correlation between the numerical model and the experimental natural frequencies and vibration modes has supported the validity of the FE model. It has also allowed to expand the free vibration analysis and to look into more localized effects such as the modal distribution of interfacial stresses. Strain energy based normalization has allowed quantitatively comparing between the in-plane and the out-of-plane modes, characterizing their impact on the interfacial stresses, and revealing the significant role that the in-plane dynamic response plays in the evolution of such interfacial stresses. In the second phase of the study, the FRP strengthened AAC panel has been subjected to cyclic base excitations. Also here, the dynamic experimental results have been compared with numerical ones and the numerical model has been used for a more localized analysis of the strengthened AAC panel. In this case, the dynamic analysis has focused on the response of the strengthening system.

From the analytical point of view, the comparison between the experimental results and the numerical ones in term of natural frequencies, vibration modes, and dynamic response to base excitation supports the validity of the FE model. The correlation in terms of the free vibration response demonstrates the ability of the model to quantify the global dynamic behavior of the FRP patched AAC masonry wall. The agreement between the numerical and experimental responses to base excitation, and mainly the local aspects that have been examined, demonstrate its ability to quantify some of the localized aspects of the behavior of the wall. The numerical and comparative studies also highlight the strength of the FE model in terms of integrating the specially tailored FE for the FRP patched wall into a broader and more general FE based analysis framework.

From the practical point of view, the experimental and numerical study has highlighted and quantified a range of physical phenomena that characterize the FRP strengthened panel. Among them, the coupling of the in-plane and the out-of-plane responses to the dynamic excitation, the coupling of shear and rocking effects in the in-plane response, and the modes in which the dynamic structural response effectively activates the strengthening system are listed. It has also been observed that all modes and all aspects of the response to base excitation trigger interfacial effects and particularly out-of-plane normal stresses at the adhesive-wall interface. Due to the low bending stiffness of the FRP sheet, these stresses tend to concentrate at the vulnerable adhesive-AAC interface and to decay through the depth of the adhesive layer.

The experimental observations, the numerical study, and the validation of the numerical model through comparison with experimental benchmarks, throw some light on the dynamic behavior of the FRP strengthened AAC masonry wall. The characterization of some of the local scale results also gains some insight into the dynamic response of the wall. These contributions take another step towards the application of this method for the dynamic strengthening of masonry walls.

Acknowledgement

This research was supported by The Israel Science Foundation (Grant No. 772/06).

References

[Al-Chaar and Hasan 2002] G. K. Al-Chaar and H. A. Hasan, "Dynamic response and seismic testing of CMU walls rehabilitation with composite material applied to only one side", *Proc. Inst. Civ. Eng.* **152**:2 (2002), 135–146.

[Almusallam and Al-Salloum 2007] T. H. Almusallam and Y. A. Al-Salloum, "Behavior of FRP strengthened infill walls under in-plane seismic loading", *J. Compos. Constr.* (*ASCE*) **11**:3 (2007), 308–318.

[Altin et al. 2008] S. Altin, O. Anil, M. E. Kara, and M. Kaya, "An experimental study on strengthening of masonry infilled RC frames using diagonal CFRP strips", *Compos. B Eng.* **39**:4 (2008), 680–693.

[Chopra 2001] A. K. Chopra, *Dynamic of structures*, 2nd ed., Prentice Hall, New Jersey, NJ, 2001.

[Ehsani et al. 1997] M. R. Ehsani, H. Saadatmanesh, and A. Al-Saidy, "Shear behavior of URM retrofitted with FRP overlays", *J. Compos. Constr.* (*ASCE*) **1**:1 (1997), 17–25.

[ElGawady et al. 2002] M. A. ElGawady, P. Lestuzzi, and M. Badoux, "Dynamic in-plane behavior of URM wall upgraded with composites", in *3rd International Conference on Composites in Infrastructure, ICCI '02* (San Francisco, 2002), Omnipress/University of Arizona, Tucson, AZ, 2002. CD-ROM.

[ElGawady et al. 2003] M. A. ElGawady, P. Lestuzzi, and M. Badoux, "In-plane lateral behavior of URM walls upgraded with composites", in *Response of structures to extreme loading, XL-2003* (Toronto, ON, 2003), edited by A. Ghobarah and P. L. Gould, Elsevier, Boston, 2003. CD-ROM.

[ElGawady et al. 2005] M. A. ElGawady, P. Lestuzzi, and M. Badoux, "In-plane seismic response of URM walls upgraded with FRP", *J. Compos. Constr.* (*ASCE*) **9**:6 (2005), 524–535.

[Elmalich and Rabinovitch 2012a] D. Elmalich and O. Rabinovitch, "Dynamic analysis of walls strengthened with composite materials", *Compos. Struct.* **94**:7 (2012), 2157–2173.

[Elmalich and Rabinovitch 2012b] D. Elmalich and O. Rabinovitch, "A high-order finite element for dynamic analysis of soft-core sandwich plates", *J. Sandw. Struct. Mater.* **14**:5 (2012), 525–555.

[Elmalich and Rabinovitch 2012c] D. Elmalich and O. Rabinovitch, "Localized effects in walls strengthened with externally bonded composite materials", *J. Eng. Mech.* (*ASCE*) **138**:9 (2012), 1112–1126.

[Foster et al. 2005] P. B. Foster, J. Gergely, D. T. Young, W. M. McGinley, and A. Corzo, "FRP repair methods for unreinforced masonry buildings subjected to cyclic loading", pp. 289–306 in *7th International Symposium on Fiber-Reinforced* (*FRP*) *Polymer Reinforcement for Concrete Structures* (Kansas City, MO, 2005), edited by C. K. Shield et al., ACI Special Publication **230**, American Concrete Institute, Farmington, MI, 2005.

[Guyan 1965] R. J. Guyan, "Reduction of stiffness and mass matrices", *AIAA J.* **3**:2 (1965), 380.

[Hamed and Rabinovitch 2008] E. Hamed and O. Rabinovitch, "Masonry walls strengthened with composite materials: dynamic out-of-plane behavior", *Eur. J. Mech. A Solids* **27**:6 (2008), 1037–1059.

[Hamed and Rabinovitch 2010] E. Hamed and O. Rabinovitch, "Lateral out-of-plane strengthening of masonry walls with composite materials", *J. Compos. Constr.* (*ASCE*) **14**:4 (2010), 376–387.

[Hamid et al. 2005] A. A. Hamid, W. W. El-Dakhakhni, Z. H. R. Hakam, and M. Elgaaly, "Behavior of composite unreinforced masonry-fiber reinforced polymer wall assemblages under in-plane loading", *J. Compos. Constr.* (*ASCE*) **9**:1 (2005), 73–83.

[Haroun and Ghoneam 1997] M. A. Haroun and E. H. Ghoneam, "Seismic performance testing of masonry-infilled frames retrofitted by fiber composite", pp. 1650–1656 in *Proceedings of the 15th International Modal Analysis Conference, IMAC XV* (Orlando, FL, 1997), edited by A. L. Wicks, SPIE **3089**, Society for Experimental Mechanics, Bethel, CT, 1997.

[Memari et al. 2010] A. M. Memari, A. Lepage, and J. Setthachayanon, "An experimental study of autoclaved aerated concrete lintels strengthened with externally bonded glass FRP", *J. Reinf. Plast. Compos.* **29**:22 (2010), 3322–3337.

[Narayanan and Ramamurthy 2000] N. Narayanan and K. Ramamurthy, "Structure and properties of aerated concrete: a review", *Cem. Concr. Compos.* **22**:5 (2000), 321–329.

[Rabinovitch and Madah 2012a] O. Rabinovitch and H. Madah, "Dynamics of FRP strengthened unidirectional masonry walls, I: A multi-layered finite element", *J. Mech. Mater. Struct.* **7**:1 (2012), 1–28.

[Rabinovitch and Madah 2012b] O. Rabinovitch and H. Madah, "Dynamics of FRP strengthened unidirectional masonry walls, II: Experiments and comparison", *J. Mech. Mater. Struct.* **7**:1 (2012), 29–44.

[Saatcioglu et al. 2005] M. Saatcioglu, F. Serrato, and S. Foo, "Seismic performance of masonry infill walls retrofitted with CFRP sheets", pp. 341–354 in *7th International Symposium on Fiber-Reinforced (FRP) Polymer Reinforcement for Concrete Structures* (Kansas City, MO, 2005), edited by C. K. Shield et al., ACI Special Publication **230**, American Concrete Institute, Farmington, MI, 2005.

[Serrano-Perez et al. 2007] J. C. Serrano-Perez, U. K. Vaidya, and N. Uddin, "Low velocity impact response of autoclaved aerated concrete/CFRP sandwich plates", *Compos. Struct.* **80**:4 (2007), 621–630.

[Stratford et al. 2004] T. Stratford, G. Pascale, O. Manfroni, and B. Bonfiglioli, "Shear strengthening masonry panels with sheet glass-fiber reinforced polymer", *J. Compos. Constr. (ASCE)* **8**:5 (2004), 434–443.

[Suriya Prakash and Alagusundaramoorthy 2008] S. Suriya Prakash and P. Alagusundaramoorthy, "Load resistance of masonry wallettes and shear triplets retrofitted with GFRP composites", *Cem. Concr. Compos.* **30**:8 (2008), 745–761.

[Turek et al. 2007] M. Turek, C. E. Ventura, and S. Kuan, "In-plane shake-table testing of GFRP-strengthened concrete masonry walls", *Earthq. Spectra* **23**:1 (2007), 223–237.

[Uddin et al. 2006] N. Uddin, F. H. Fouad, U. K. Vaidya, A. K. Khotpal, and J. C. Serrano-Perez, "Structural characterization of hybrid fiber reinforced polymer (FRP)-autoclave aerated concrete (AAC) panels", *J. Reinf. Plast. Compos.* **25**:9 (2006), 981–999.

[Uddin et al. 2007] N. Uddin, F. H. Fouad, U. K. Vaidya, A. K. Khotpal, and J. C. Serrano-Perez, "Structural behavior of fiber-reinforced polymer-autoclaved aerated concrete panels", *ACI Struct. J.* **104**:6 (2007), 722–730.

[Valluzzi et al. 2002] M. R. Valluzzi, D. Tinazzi, and C. Modena, "Shear behavior of masonry panels strengthened by FRP laminates", *Constr. Build. Mater.* **16**:7 (2002), 409–416.

[Zienkiewitch 1977] O. C. Zienkiewitch, *The finite element method*, McGraw-Hill, London, 1977.

Received 6 Feb 2012. Revised 24 Jun 2012. Accepted 20 Jul 2012.

DVIR ELMALICH: dvir@tx.technion.ac.il
Faculty of Civil and Environmental Engineering, Technion - Israel Institute of Technology, Technion City, 32000 Haifa, Israel

ODED RABINOVITCH: cvoded@tx.technion.ac.il
Faculty of Civil and Environmental Engineering, Technion - Israel Institute of Technology, Technion City, 32000 Haifa, Israel

JOURNAL OF MECHANICS OF MATERIALS AND STRUCTURES
Vol. 7, No. 7, 2012
dx.doi.org/10.2140/jomms.2012.7.687

msp

HYGROTHERMAL ANALYSIS OF EXPONENTIALLY GRADED RECTANGULAR PLATES

ASHRAF M. ZENKOUR

The static characteristics of an exponentially inhomogeneous plate under a transverse uniform loading and exposed to hygrothermal conditions are studied. The elastic coefficients, thermal coefficient and moisture expansion coefficient of the plate are assumed to be exponentially graded in the thickness direction. The trigonometric shear deformation theory solution is presented. In this solution, the initial terms of a power series through the plate thickness are used for the displacements in addition to other trigonometric terms. The effect due to transverse shear deformations is included. A number of examples will be solved to illustrate the numerical results concerning bending response of homogeneous and exponentially graded rectangular plates subjected to hygrothermomechanical effects. The influences of temperature, moisture concentration, transverse shear deformation, plate aspect ratio, and the exponentially graded parameter on the bending response are investigated.

1. Introduction

The analysis of the rectangular plates subjected to moisture and temperature effects has been the subject of research interest of many investigators. Moisture and temperature may be distributed through the volume of the structure and may induce residual stresses and extensional strains. These residual stresses and extensional strains may also affect the gross performance of the structure. In particular, the bending characteristics, buckling loads and vibration frequencies can be modified by the presence of moisture, temperature or both. Therefore, to utilize the full potential of advanced structures, it will be necessary to analyze the effects of moisture and temperature in composite structural components.

The vibration characteristics of thick isotropic rectangular plates under an arbitrary state of initial stress were investigated in [Herrmann and Armenakas 1962; Brunelle and Robertson 1974; 1976]. Adams and Miller [1977], Ishikawa et al. [1978] and Strife and Prewo [1979] have studied the effect of environment on the material properties of composite materials and observed that it has significant effect on strength and stiffness of the composites. Therefore, there is a need to understand the behavior of composite structures subjected to hygrothermal conditions. Whitney and Ashton [1971] have used the classical laminate plate theory to study the hygrothermal effects on bending, buckling and vibration of composite laminated plates using the Ritz method and neglecting the transverse shear deformation. Pipes et al. [1976] have presented the distribution of in-plane stresses through the thickness of symmetric laminates subjected to moisture absorption and desorption. Yang and Shieh [1987] have considered the free vibration of antisymmetric cross-ply laminates in presence of a non-uniform initial stress, where the effects of transverse shear and rotary inertia were also included. Sai Ram and Sinha [1991; 1992] have studied the hygrothermal effects on the bending and free vibration behavior of laminated composite plates using

Keywords: hygrothermal conditions, rectangular plate, exponentially graded.

the first-order shear deformation theory and employing finite element method. The effects of moisture and temperature on the deflections and stress resultants are presented for simply supported and clamped antisymmetric cross-ply and angle-ply laminates using reduced lamina properties at elevated moisture concentration and temperature. Lee et al. [1992] have studied the influence of hygrothermal effects on the cylindrical bending of symmetric angle-ply laminated plates subjected to uniform transverse load for different boundary conditions via classical laminated plate theory and von Karman's large deflection theory. The material properties of the composite are assumed to be independent of temperature and moisture variation. It has been observed that the classical laminated plate theory may not be adequate for the analysis of composite laminates even in the small deflection range.

Many studies, based on classical plate theory, of thin rectangular plates subjected to mechanical or thermal loading or their combinations as well as the hygrothermal effects are available in the literature [Whitney and Ashton 1971; Sai Ram and Sinha 1992]. However, studies of temperature and moisture effects on the bending of rectangular plates based on the shear deformation theories are limited in number, and all these studies assumed perfectly initial configurations [Pipes et al. 1976; Yang and Shieh 1987; Sai Ram and Sinha 1991; 1992]. The classical laminated plate theory and the first-order shear deformation plate theory are typical deformation theories for the analysis of laminated composite plates. The classical theory neglects the shear stresses while the first order theory assumes a constant transverse shear strain across the thickness direction, and a shear correction factor is generally applied to adjust the transverse shear stiffness for the static and stability analyses. However, some investigations showed that the bending and postbuckling responses of rectangular plates are sensitive to the choice of the shear correction factor.

To avoid the use of shear correction factor, various higher-order theories have been proposed to predict the bending response of rectangular plates. Shen [2001] has investigated the influence of hygrothermal environment on postbuckling behaviors of laminated plates based on Reddy's [1997] higher-order plate theory, considering the effects of temperature and moisture on the material properties. Patel et al. [2002] have studied the static and dynamic response of the thick laminated composite plates under hygrothermal environment based on a higher order theory. Rao and Sinha [2004] have studied the effects of moisture and temperature on the bending characteristics of thick multidirectional fibrous composite plates. The finite element analysis accounts for the hygrothermal strains and reduced elastic properties of multidirectional composites at an elevated moisture concentration and temperature. Deflections and stresses have been evaluated for thick multidirectional composite plates under uniform and linearly varying through-the-thickness moisture concentration and temperature. Results reveal the effects of fiber directionality on deflection and stresses. Wang et al. [2005] have studied the response of dynamic interlaminar stresses in laminated composite plates with piezoelectric layers using an analytical approach. Benkhedda et al. [2008] have proposed an analytical approach to calculate the hygrothermal stresses in laminated composite plates, and took into account the change of mechanical characteristics due to moisture and temperature. In their study, the distribution of the transient in-plane stresses through the thickness of laminates is presented, whereas the transverse stresses were not taken into account. Lo et al. [2010] have developed a global-local higher order theory to study the response of laminated plates exposed to hygrothermal environment. Recently, Zenkour [2010] has presented a hygrothermal bending analysis for a functionally graded material (FGM) plate resting on elastic foundation.

From the literature reviewed, it can be found that research on local hygrothermal stresses of exponentially graded material (EGM) plates subjected to temperature and moisture effects seems to be lacking,

which is the problem to be addressed in this paper. It is to be noted that, moisture and temperature have an adverse effect on the performance of composites. Stiffness and strength are reduced with the increase in moisture concentration and temperature. However, the discussion on the change of global and local response with respect to material variation due to elevated temperatures and moisture concentrations has been less reported in the published literature. In this article, a trigonometric shear deformation plate theory is developed to study the response of exponentially graded rectangular plates exposed to hygrothermal conditions. The present theory satisfies the continuity conditions of transverse shear stresses through the plate thickness. The analysis takes into account the change of material properties and a change in moisture concentrations through the plate thickness. Relationships between displacements/stresses and temperature or moisture concentrations have been studied under different hygrothermal conditions

The objective of this investigation is to present a general hygrothermal formulation for EGM plates using the sinusoidal shear deformation theory [Zenkour 2004a; 2004b; 2006; 2009]. The model has been developed within the phenomenological approach, where the effect of temperature and moisture has been taken into account at constitutive level. The governing partial differential equations are reduced to a set of coupled ordinary differential equations in the thickness direction. Numerical results for displacements and stresses are presented for homogeneous and EGM plates subjected to hygrothermomechanical effects. To make the study reasonably, displacements and stresses are given for different environment parameters and homogenization schemes as well as exponents in the power-law that describes through-the-thickness variation of the plate.

2. Mathematical model

Consider a rectangular plate of length a, width b and thickness h made of an exponentially graded material (EGM). The plate is subjected to a distributed transverse static mechanical load $q(x, y)$ and a temperature field $T(x, y, z)$ as well as a moisture concentration $C(x, y, z)$. The sinusoidal plate theory is presented for the small displacement and the corresponding small strains. The material properties P of the EGM plate, such as Young's modulus and the thermal and moisture expansion coefficients are assumed to be functions of the thickness of the plate. The present plate is supported at four edges defined in the (x, y, z) coordinate system with x- and y-axes located in the middle plane $(z = 0)$ and its origin placed at the corner of the plate as shown in Figure 1. An exponential relationship between the material property $\bar{P}$ and z for the EG plate is assumed as in [Zenkour 2005]:

$$\bar{P} = \bar{P}(z) = \bar{P}_0 e^{-\eta(z/h)^k}, \tag{1}$$

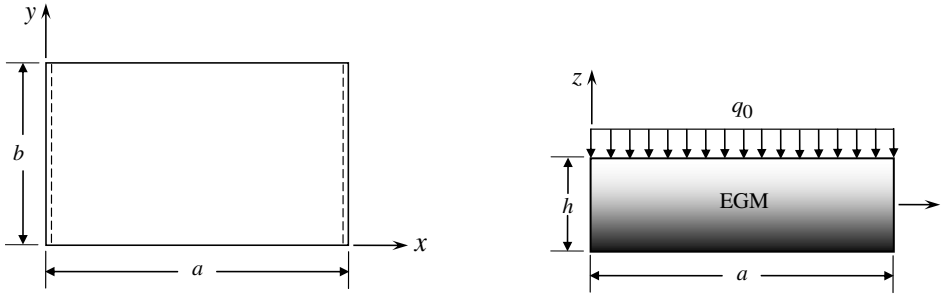

Figure 1. Geometry and coordinate system of the EGM plate under uniform load.

where $\bar{P}_0$ is the corresponding property of the homogeneous plate, and η and k are geometric parameters. The value of η equals to zero represents a fully homogeneous plate. The above exponential law assumption reflects a simple rule of mixtures applies only to the thickness direction. The power law exponents, η and k, may be varied to obtain different distributions of the components materials through the thickness of the plate.

The total potential energy of the present EGM rectangular plate may be expressed as

$$\Pi = U_{\text{str}} - W_{\text{ext}} - W_{\text{int}}, \tag{2}$$

where U_{str} is the strain energy of the EGM plate, W_{ext} is the work of external forces, and W_{int} is the work of internal forces. They are given by

$$U_{\text{str}} = \int_{V_0} \sigma_{ij}\epsilon_{ij}\, dV, \tag{3a}$$

$$W_{\text{ext}} = \int_{S_0} p_i u_i\, dS, \tag{3b}$$

$$W_{\text{int}} = \int_{V_0} X_i u_i\, dV, \tag{3c}$$

where σ_{ij} is the Cauchy stress tensor, ϵ_{ij} is the small strain tensor, p_i are the external applied loads, u_i are the displacements in the spatial frame, and X_i are the body forces per unit initial volume. The general governing equations of equilibrium are obtained by employing the principle of virtual displacements. The stresses and applied loads are assumed to be constants.

The displacements of a material point located at (x, y, z) in the EGM plate may be written as follows [Zenkour 2004a; 2004b; 2006; 2009]:

$$\left.\begin{aligned} u_1(x, y, z) &= u - z\,\partial w/\partial x + \Psi(z)\phi_1, \\ u_2(x, y, z) &= v - z\,\partial w/\partial y + \Psi(z)\phi_2, \\ u_3(x, y, z) &= w, \end{aligned}\right\} \tag{4}$$

where u, v, and w are the displacements of the middle surface along the axes x, y and z, respectively, and ϕ_1 and ϕ_2 are the rotations about the y and x axes and account for the effect of transverse shear. The coefficient of ϕ_1 and ϕ_2 which is given by $\Psi(z)$ should be odd function of z. All of the generalized displacements $(u, v, w, \phi_1, \phi_2)$ are functions of the (x, y). The displacements of the classical thin plate theory (CPT) is obtained easily by setting $\Psi(z) = 0$. The displacements of the first-order shear deformation plate theory (FPT) is obtained by setting $\Psi(z) = z$. In addition, the higher-order shear deformation plate theory (HPT) [Reddy 2000] is obtained by setting

$$\Psi(z) = z\Big[1 - \frac{4}{3}\Big(\frac{z}{h}\Big)^2\Big]. \tag{5}$$

Also, the sinusoidal shear deformation plate theory (SPT) is obtained by setting (see [Zenkour 2004a; 2004b; 2006; 2009])

$$\Psi(z) = \frac{h}{\pi}\sin\frac{\pi z}{h}. \tag{6}$$

Note that the present SPT, as well as HPT, is simplified by enforcing traction-free boundary conditions at the plate faces. The SPT accounts according to a cosine-law distribution of the transverse shear deformation through the thickness of the EGM plate. The SPT, HPT and FPT contain the same number of dependent unknowns. No transversal shear correction factors are needed for both SPT and HPT because a correct representation of the transversal shearing strain is given.

The six strain components ϵ_{ij} compatible with the displacement field in (4) are

$$\begin{Bmatrix}\epsilon_{11}\\ \epsilon_{22}\\ \epsilon_{12}\end{Bmatrix} = \begin{Bmatrix}\epsilon^0_{11}\\ \epsilon^0_{22}\\ \epsilon^0_{12}\end{Bmatrix} + z\begin{Bmatrix}\kappa_{11}\\ \kappa_{22}\\ \kappa_{12}\end{Bmatrix} + \Psi(z)\begin{Bmatrix}\theta_{11}\\ \theta_{22}\\ \theta_{12}\end{Bmatrix}, \quad \epsilon_{33}=0, \quad \begin{Bmatrix}\epsilon_{23}\\ \epsilon_{13}\end{Bmatrix} = \Psi(z)_{,3}\begin{Bmatrix}\epsilon^0_{23}\\ \epsilon^0_{13}\end{Bmatrix}, \tag{7}$$

where

$$\epsilon^0_{11} = u_{,1}, \quad \epsilon^0_{22} = v_{,2}, \quad \epsilon^0_{23} = \phi_2, \quad \epsilon^0_{13} = \phi_1, \quad \epsilon^0_{12} = v_{,1} + u_{,2}, \tag{8}$$

$$\kappa_{11} = -w_{,11}, \quad \kappa_{22} = -w_{,22}, \quad \kappa_{12} = -2w_{,12}, \quad \theta_{11} = \phi_{1,1}, \quad \theta_{22} = \phi_{2,2}, \quad \theta_{12} = \phi_{2,1} + \phi_{1,2}. \tag{9}$$

The stress-strain relations for a linear isotropic elastic plate are given by

$$\begin{Bmatrix}\sigma_{11}\\ \sigma_{22}\end{Bmatrix} = \frac{E(z)}{1-\nu^2}\begin{bmatrix}1 & \nu\\ \nu & 1\end{bmatrix}\begin{Bmatrix}\epsilon_{11}-\alpha\Delta T-\beta\Delta C\\ \epsilon_{22}-\alpha\Delta T-\beta\Delta C\end{Bmatrix}, \quad \{\sigma_{23},\sigma_{13},\sigma_{12}\} = \frac{E(z)}{2(1+\nu)}\{\epsilon_{23},\epsilon_{13},\epsilon_{12}\}, \tag{10}$$

where E is Young's modulus, ν is Poisson's ratio, α and β are the thermal and moisture expansion coefficients, $\Delta T = T - T_0$ in which T is the applied temperature and T_0 is the reference temperature, and $\Delta C = C - C_0$ in which C is the moisture concentration and C_0 is the reference moisture concentration.

The applied temperature distribution $T(x, y, z)$ and the moisture concentration $C(x, y, z)$ through the thickness are assumed, respectively, to be

$$\begin{aligned} T(x,y,z) &= T_1(x,y) + \frac{z}{h}T_2(x,y) + \frac{\Psi(z)}{h}T_3(x,y),\\ C(x,y,z) &= C_1(x,y) + \frac{z}{h}C_2(x,y) + \frac{\Psi(z)}{h}C_3(x,y). \end{aligned} \tag{11}$$

3. Governing equations

The governing equations of equilibrium can be derived by using the principle of virtual displacements. The equilibrium equations associated with the present sinusoidal shear deformation theory are

$$N_{1,1} + N_{12,2} = 0, \tag{12a}$$

$$N_{12,1} + N_{2,2} = 0, \tag{12b}$$

$$M_{1,11} + 2M_{12,12} + M_{2,22} + q = 0, \tag{12c}$$

$$S_{1,1} + S_{12,2} - Q_{13} = 0, \tag{12d}$$

$$S_{12,1} + S_{2,2} - Q_{23} = 0, \tag{12e}$$

where the stress and moment resultants (N_1, N_2, N_{12}, M_1, M_2, M_{12}, S_1, S_2, S_{12}, Q_{13}, Q_{23}) of the FGM

plate can be obtained by integrating (10) over the thickness, and are written as

$$\begin{Bmatrix} N_i \\ M_i \\ S_i \end{Bmatrix} = \frac{1}{1-\nu^2} \begin{bmatrix} A_{11}^1 & A_{12}^1 & A_{13}^1 \\ A_{12}^1 & A_{22}^1 & A_{23}^1 \\ A_{13}^1 & A_{23}^1 & A_{33}^1 \end{bmatrix} \begin{Bmatrix} \bar{\epsilon}_i^0 \\ \bar{\kappa}_i \\ \bar{\theta}_i \end{Bmatrix} + \frac{1}{\nu-1} \begin{bmatrix} A_{11}^\alpha & A_{12}^\alpha & A_{13}^\alpha \\ A_{12}^\alpha & A_{22}^\alpha & A_{23}^\alpha \\ A_{13}^\alpha & A_{23}^\alpha & A_{33}^\alpha \end{bmatrix} \begin{Bmatrix} T_1^* \\ T_2^* \\ T_3^* \end{Bmatrix} + \frac{1}{\nu-1} \begin{bmatrix} A_{11}^\beta & A_{12}^\beta & A_{13}^\beta \\ A_{12}^\beta & A_{22}^\beta & A_{23}^\beta \\ A_{13}^\beta & A_{23}^\beta & A_{33}^\beta \end{bmatrix} \begin{Bmatrix} C_1^* \\ C_2^* \\ C_3^* \end{Bmatrix}, \tag{13a}$$

$$\begin{Bmatrix} N_{12} \\ M_{12} \\ S_{12} \end{Bmatrix} = \frac{1}{2(1+\nu)} \begin{bmatrix} A_{11}^1 & A_{12}^1 & A_{13}^1 \\ A_{12}^1 & A_{22}^1 & A_{23}^1 \\ A_{13}^1 & A_{23}^1 & A_{33}^1 \end{bmatrix} \begin{Bmatrix} \epsilon_{12}^0 \\ \kappa_{12} \\ \eta_{12} \end{Bmatrix}, \tag{13b}$$

and

$$\begin{Bmatrix} Q_{13} \\ Q_{23} \end{Bmatrix} = \frac{B}{2(1+\nu)} \begin{Bmatrix} \epsilon_{13}^0 \\ \epsilon_{23}^0 \end{Bmatrix}, \tag{13c}$$

where $i = 1, 2$ and

$$\begin{aligned} \bar{\epsilon}_1^0 &= \epsilon_{11}^0 + \nu\epsilon_{22}^0, \quad & \bar{\epsilon}_2^0 &= \epsilon_{22}^0 + \nu\epsilon_{11}^0, \\ \bar{\kappa}_1 &= \kappa_{11} + \nu\kappa_{22}, \quad & \bar{\kappa}_2 &= \kappa_{22} + \nu\kappa_{11}, \\ \bar{\theta}_1 &= \theta_{11} + \nu\theta_{22}, \quad & \bar{\theta}_2 &= \theta_{22} + \nu\theta_{11}, \\ T_1^* &= T_1 - T_0, & C_1^* &= C_1 - C_0, \\ T_j^* &= T_j/h, & C_j^* &= C_j/h, \qquad j = 2, 3. \end{aligned} \tag{14}$$

In (13a)–(13c), N_1, N_2, and N_{12} and M_1, M_2, and M_{12} are the basic components of stress resultants and stress couples; S_1, S_2, and S_{12} are additional stress couples associated with the transversal shear effects; and Q_{13} and Q_{23} are transversal shear stress resultants. The coefficients $A_{rs}^\gamma (\gamma = 1, \alpha, \beta; r, s = 1, 2, 3)$ are defined by

$$\begin{gathered} \{A_{11}^\gamma, A_{12}^\gamma, A_{22}^\gamma\} = \int_{-h/2}^{+h/2} \gamma E\{1, z, z^2\}\, dz, \quad \{A_{13}^\gamma, A_{23}^\gamma, A_{33}^\gamma\} = \int_{-h/2}^{+h/2} \gamma \Psi E\{1, z, \Psi\}\, dz, \\ B = \bar{K} \int_{-h/2}^{+h/2} E(\Psi_{,3})^2\, dz, \end{gathered} \tag{15}$$

where $\bar{K}$ is the shear correction factor for FPT, taken to be $\frac{5}{6}$.

4. Exact solutions for EGM plates

The determination of transverse deflections and stresses are of fundamental importance in the design of many structural components. An exact closed-form solution to (12a)–(12e) can be constructed when the plate is of a rectangular geometry (Figure 1) with the following edge conditions, loading and displacements.

4.1. ***Boundary conditions.*** The following set of simply supported boundary conditions along the edges of the plate is considered:

$$\begin{aligned} v = w = \phi_2 = N_1 = M_1 = S_1 = 0 \quad & \text{at } x = 0, a, \\ u = w = \phi_1 = N_2 = M_2 = S_2 = 0 \quad & \text{at } y = 0, b, \end{aligned} \tag{16}$$

4.2. ***Loading and displacements.*** Rectangular plates are generally classified in accordance with the type support used in the absence of the body forces and lateral loads except the external force $q(x, y)$. We are here concerned with the exact solutions of (12a)–(12e) for simply supported FGM plate. To solve this problem, Navier presented the uniform external force and the transverse uniform temperature and moisture concentration loads in the form of a double trigonometric series

$$\begin{Bmatrix} q \\ T_i \\ C_i \end{Bmatrix} = \sum_{m,n=1,3,5,\ldots}^{\infty} \begin{Bmatrix} q_0 \\ t_i \\ c_i \end{Bmatrix} \frac{16}{mn\pi^2} \sin(\lambda x)\sin(\mu y), \quad (i = 1, 2, 3), \tag{17}$$

where $\lambda = m\pi/a$, $\mu = n\pi/b$, m and n are mode numbers, q_0 represents the intensity of the load at the plate center, t_i and c_i are constants.

Following the Navier solution procedure, we assume the following solution form for $(u, v, w, \phi_1, \phi_2)$ that satisfies the simply supported boundary conditions,

$$\begin{Bmatrix} u \\ v \\ w \\ \phi_1 \\ \phi_2 \end{Bmatrix} = \sum_{m,n=1,3,5,\ldots}^{\infty} \begin{Bmatrix} U_{mn}\cos(\lambda x)\sin(\mu y) \\ V_{mn}\sin(\lambda x)\cos(\mu y) \\ W_{mn}\sin(\lambda x)\sin(\mu y) \\ X_{mn}\cos(\lambda x)\sin(\mu y) \\ Y_{mn}\sin(\lambda x)\cos(\mu y) \end{Bmatrix}, \tag{18}$$

where U_{mn}, V_{mn}, W_{mn}, X_{mn}, and Y_{mn} are arbitrary parameters to be determined subjected to the condition that the solution in (18) satisfies the differential equations, (12a)–(12e). Substituting (18) into (12a)–(12e), one obtains

$$[P]\{\underline{\Delta}\} = \{F\}, \tag{19}$$

where $\{\underline{\Delta}\}$ and $\{F\}$ denote the columns given by

$$\{\underline{\Delta}\}^T = \{U_{mn}, V_{mn}, W_{mn}, X_{mn}, Y_{mn}\}, \quad \{F\}^T = \{F_1, F_2, F_3, F_4, F_5\}. \tag{20}$$

The elements P_{ij} of the coefficient matrix $[P]$ and the elements F_i of the load vector $\{F\}$ are given in the Appendix.

Moreover, substituting (7) into (10) with the help of (18), one can obtain the stress components σ_{ij} in terms of Young's modulus and the arbitrary parameters U_{mn}, V_{mn}, W_{mn}, X_{mn}, and Y_{mn} as follows:

$$\begin{aligned}\sigma_{11} = -E(z) \sum_{m,n=1,3,5,\ldots}^{\infty} \Bigg\{ & \frac{1}{1-\nu^2}\left(\lambda U_{mn} + \nu\mu V_{mn} - z(\lambda^2 + \nu\mu^2)W_{mn} + \Psi(z)(\lambda X_{mn} + \nu\mu Y_{mn})\right) \\ & + \frac{\alpha(z)}{(1-\nu)h}\left(h(t_1 - T_0) + zt_2 + \Psi(z)t_3\right) + \frac{\beta(z)}{(1-\nu)h}\left(h(c_1 - C_0) + zc_2 + \Psi(z)c_3\right)\Bigg\} \sin(\lambda x)\sin(\mu y),\end{aligned} \tag{21a}$$

$$\begin{aligned}\sigma_{22} = -E(z) \sum_{m,n=1,3,5,\ldots}^{\infty} \Bigg\{ & \frac{1}{1-\nu^2}\left(\nu\lambda U_{mn} + \mu V_{mn} - z(\nu\lambda^2 + \mu^2)W_{mn} + \Psi(z)(\nu\lambda X_{mn} + \mu Y_{mn})\right) \\ & + \frac{\alpha(z)}{(1-\nu)h}\left(h(t_1 - T_0) + zt_2 + \Psi(z)t_3\right) + \frac{\beta(z)}{(1-\nu)h}\left(h(c_1 - C_0) + zc_2 + \Psi(z)c_3\right)\Bigg\} \sin(\lambda x)\sin(\mu y),\end{aligned} \tag{21b}$$

$$\sigma_{23} = \frac{E(z)}{2(1+\nu)} \sum_{m,n=1,3,5,\ldots}^{\infty} \Psi(z)_{,3} Y_{mn} \sin(\lambda x) \cos(\mu y), \tag{21c}$$

$$\sigma_{13} = \frac{E(z)}{2(1+\nu)} \sum_{m,n=1,3,5,\ldots}^{\infty} \Psi(z)_{,3} X_{mn} \cos(\lambda x) \sin(\mu y), \tag{21d}$$

$$\sigma_{12} = \frac{E(z)}{2(1+\nu)} \sum_{m,n=1,3,5,\ldots}^{\infty} \big(\mu U_{mn} + \lambda V_{mn} - 2z\lambda\mu W_{mn} + \Psi(z)(\mu X_{mn} + \lambda Y_{mn})\big) \cos(\lambda x) \cos(\mu y). \tag{21e}$$

5. Numerical results

The flexural response of EGM plates subjected to uniform transverse pressure in hygrothermal environment is studied and the results are depicted in graphical form in Figures 2–5. The material properties of the composite material are considered to be dependent on temperature and moisture. The material properties are taken in the analysis at the reference temperature $T_0 = 21°\text{C}$ (room temperature) and

η	Theory	$k=1$			$k=2$		
		w^*	σ_1	σ_5	w^*	σ_1	σ_5
0.0	CPT	1.37568	1.13905	—	1.37568	1.13905	—
	FPT	1.41072	1.13905	0.83759	1.41072	1.13905	0.83759
	HPT	1.41071	1.16220	1.03274	1.41071	1.16220	1.03274
	SPT	1.41065	1.16329	1.06316	1.41065	1.16329	1.06316
0.5	CPT	1.39072	1.10461	—	1.42831	1.09636	—
	FPT	1.42540	1.10461	0.82893	1.46481	1.09636	0.87263
	HPT	1.42556	1.12654	1.06057	1.46418	1.11202	1.01562
	SPT	1.42552	1.12785	1.09444	1.46410	1.11235	1.04159
1.0	CPT	1.43690	1.06625	—	1.48857	1.04696	—
	FPT	1.47052	1.06625	0.80368	1.52655	1.04696	0.90790
	HPT	1.47118	1.09251	1.14760	1.52531	1.05738	1.00654
	SPT	1.47116	1.09458	1.19207	1.52519	1.05720	1.02878
1.5	CPT	1.51752	1.03519	—	1.55630	0.99370	—
	FPT	1.54948	1.03519	0.76393	1.59576	0.99370	0.94335
	HPT	1.55089	1.06756	1.30451	1.59391	1.00052	1.00418
	SPT	1.55092	1.07050	1.36763	1.59378	0.99999	1.02332
2.0	CPT	1.63862	1.01769	—	1.63137	0.93864	—
	FPT	1.66843	1.01769	0.71272	1.67232	0.93864	0.97893
	HPT	1.67080	1.05580	1.54971	1.66988	0.94305	1.00744
	SPT	1.67089	1.05943	1.64112	1.66972	0.94231	1.02400

Table 1. Effects of the exponents k and η on the deflection w^* and stresses σ_1 and σ_5 for EGM rectangular plate using various theories ($t_2 = 10$, $c_2 = 1$, $t_3 = c_3 = 0$).

moisture concentration $C_0 = 0\%$ as follows:

$$E = 3.45\,\text{GPa}, \qquad \nu = 0.35, \qquad \alpha = 72.0 \times 10^{-6}/^{\circ}\text{C}, \qquad \beta = 0.33.$$

Many examples have been solved numerically using the following fixed data: (unless otherwise stated) $q_0 = 100$, $a = 10h$, $b = 2a$, $k = 2$, $t_1 = t_2 = 0$, $c_1 = c_2 = 0$. The plate is assumed to be simply supported on all four edges. Numerical results are presented in terms of nondimensional stresses and deflection. The various nondimensional parameters used are

$$w^* = \frac{10^2 D}{a^4 q_0} w\Big(\frac{a}{2}, \frac{b}{2}\Big), \qquad \sigma_1 = \frac{1}{10^2 q_0}\sigma_{11}\Big(\frac{a}{2}, \frac{b}{2}, \frac{z}{h}\Big), \qquad \sigma_5 = -\frac{1}{10 q_0}\sigma_{13}\Big(0, \frac{b}{2}, \frac{z}{h}\Big),$$

$$\sigma_6 = \frac{1}{10^2 q_0}\sigma_{12}\Big(0, 0, \frac{z}{h}\Big), \qquad D = \frac{h^3 E_0}{12(1-\nu^2)}.$$

The longitudinal stress σ_1, the transverse shear stress σ_5 and the in-plane shear stress σ_6 are computed at $z = h/2$, $z = 0$ and $z = -h/2$, respectively. For the sake of completeness, Table 1 on the previous page shows results of the present sinusoidal plate theory (SPT) are compared with those obtained using HPT,

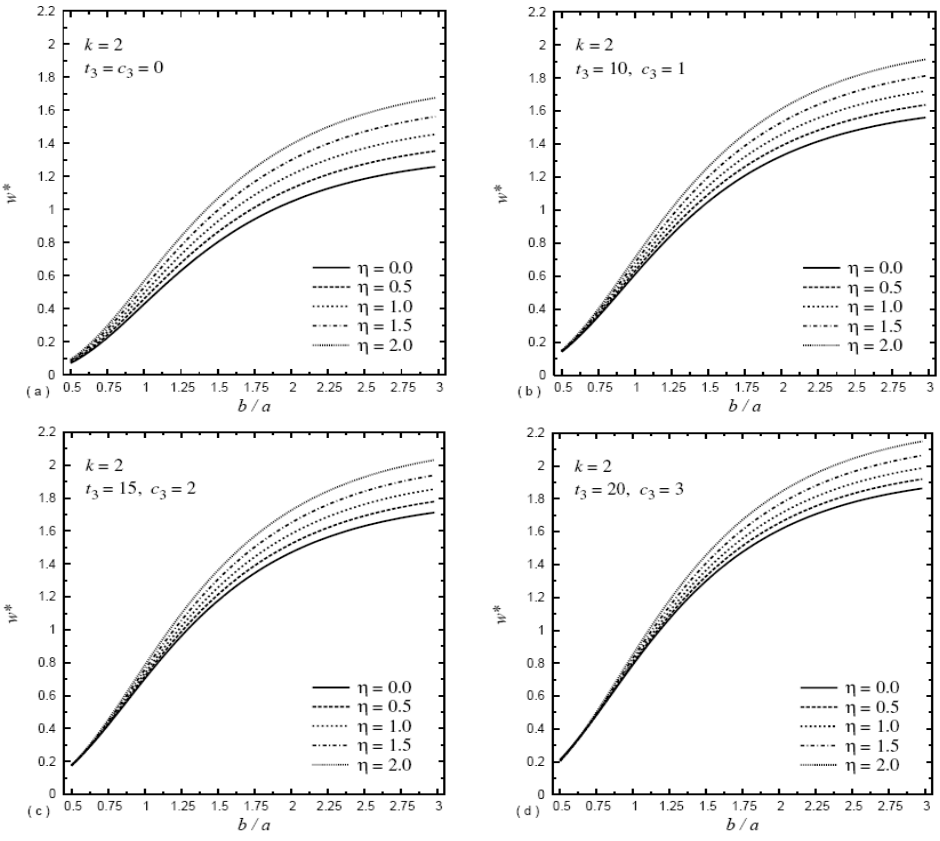

Figure 2. Dimensionless center deflection w^* versus the aspect ratio b/a of an EGM plate for various values of the power-law exponent η: (a) $t_3 = c_3 = 0$; (b) $t_3 = 10$, $c_3 = 1$; (c) $t_3 = 15$, $c_3 = 2$; (d) $t_3 = 20$, $c_3 = 3$.

FPT, and CPT for the deflection w^*, the in-plane longitudinal stress σ_1 and the transverse shear stress σ_5 in bending of EGM plates under uniformly distributed loading. The deflection w^* increases with an increase in the exponent k or in η. The stresses σ_1 and σ_5 increase as k increases, but decrease as η increases. It is to be noted that the CPT gives the same in-plane longitudinal stress σ_1 as that of the FPT.

The effects of temperature, moisture concentration and their combination on the nondimensional bending response of the EGM plate are shown in Figures 2–5. The effect of the EG parameter η on the center deflection and stresses for different values of the thermal and moisture concentration parameters is investigated. The variation of the center deflection versus the aspect ratio b/a for homogeneous ($\eta = 0$) and EGM plates is presented in Figure 2. It is observed that central deflection increases with increase in moisture concentration, temperature and increase in both simultaneously. The increase is highest when hygrothermal condition is taken and it is least when only effect of temperature is considered. It is also noted that the deflection increases with the increase of b/a and η.

The distribution of the in-plane longitudinal stress σ_1 through-the-thickness of the homogeneous ($\eta = 0$) and EGM plates is displayed in Figure 3. The longitudinal stress is no longer linear through-the-thickness of the EGM plates in the absence of the hygrothermal parameters in which the stresses

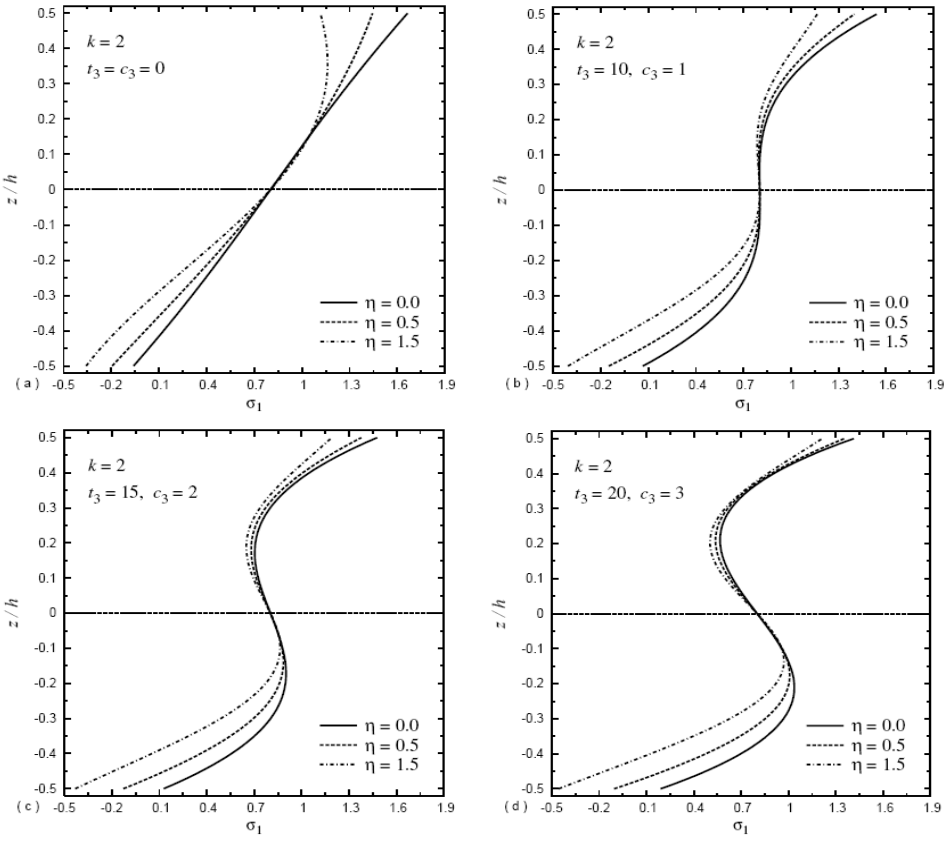

Figure 3. Dimensionless in-plane normal stress σ_1 through-the-thickness of a rectangular plate ($b/a = 2$) for various values of the power-law exponent η: (a) $t_3 = c_3 = 0$; (b) $t_3 = 10$, $c_3 = 1$; (c) $t_3 = 15$, $c_3 = 2$; (d) $t_3 = 20$, $c_3 = 3$.

still tensile through the plate thickness. The longitudinal stress becomes compressive near the bottom base of the plate, especially for $\eta \neq 0$. The behavior of stress is very sensitive to the variation of η. The homogeneous plate yields the maximum longitudinal stress through-the-thickness of the plate and this irrespective of the values of the hygrothermal parameters.

The distribution of the transverse shear stress σ_5 through-the-thickness of the homogeneous ($\eta = 0$) and EGM plates is displayed in Figure 4. The minimum shear stress occurs at the mid-plane of the homogeneous and EGM plates and the stress still symmetric through the plate thickness. In the absence of the hygrothermal parameters the shear stress is maximum for homogeneous plate in the interval $-0.21 \leq z/h \leq 0.21$. This interval is decreased to be $-0.13 \leq z/h \leq 0.13$ when $t_3 = 10$ and $c_3 = 1$. For other cases ($t_3 = 15$, $c_3 = 2$ and $t_3 = 20$, $c_3 = 3$), the shear stress of the homogeneous plate is the smallest one.

Figure 5 show that the in-plane shear stress σ_6 is linearly distributed through-the-thickness of the homogeneous plate irrespective of the thermal or moisture concentration parameters. Otherwise, σ_6 is very sensitive to the variation of η, t_3 and c_3. This stress is tensile near the bottom surface of the plate while it is compressive near the top surface of the plate. It is symmetric through-the-thickness of the

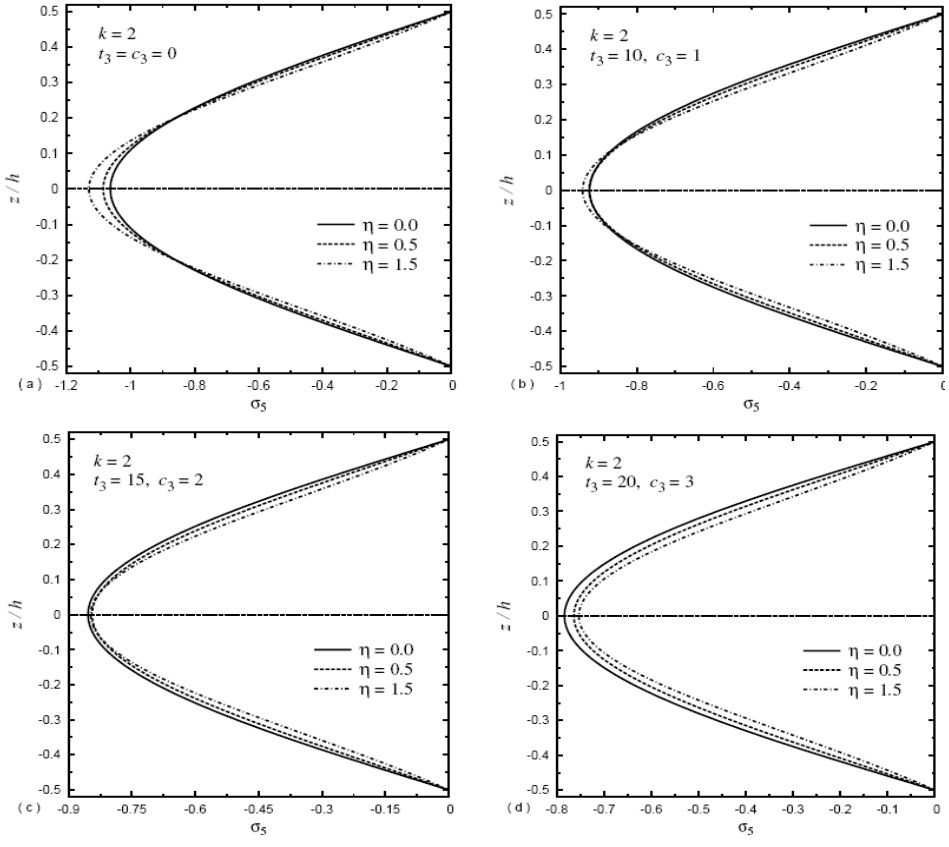

Figure 4. Dimensionless transverse shear stress σ_5 through-the-thickness of a rectangular plate ($b/a = 2$) for various values of the power-law exponent η: (a) $t_3 = c_3 = 0$; (b) $t_3 = 10$, $c_3 = 1$; (c) $t_3 = 15$, $c_3 = 2$; (d) $t_3 = 20$, $c_3 = 3$.

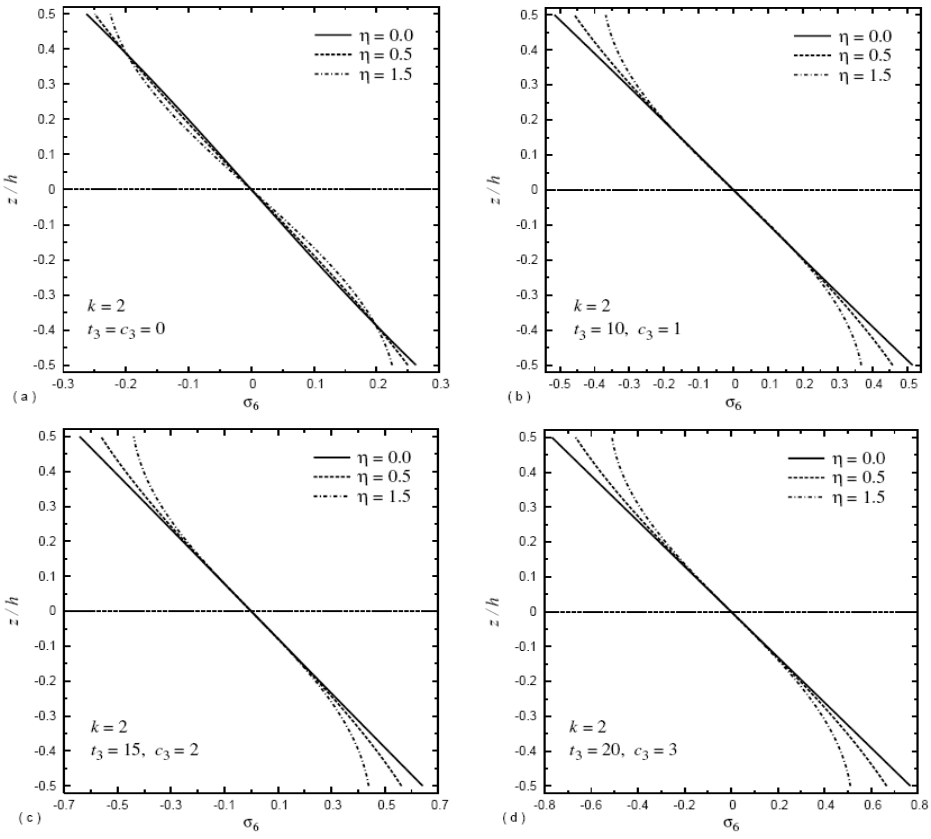

Figure 5. Dimensionless in-plane shear stress σ_6 through-the-thickness of a rectangular plate $(b/a = 2)$ for various values of the power-law exponent η: (a) $t_3 = c_3 = 0$; (b) $t_3 = 10$, $c_3 = 1$; (c) $t_3 = 15$, $c_3 = 2$; (d) $t_3 = 20$, $c_3 = 3$.

plate and vanished at its mid-plane. It is observed that this stress increases with increase in moisture concentration, temperature and increase in both simultaneously.

6. Conclusion

The hygrothermal effects of homogeneous and EGM plates under uniformly distributed load are presented based on the sinusoidal shear deformation theory. The present analysis includes the effects of temperature and moisture concentration on the material properties. Numerical results show that due to the change in material properties caused by a rise of temperature and a change of moisture concentration, the relationship between the hygrothermal response of homogeneous and EGM plates and the rise of temperature and/or moisture concentrations is no longer linear. The results presented herein show that the deflection and stresses will degrade with increasing moisture concentrations and temperatures. They also confirm that the characteristics of stresses and deflection are significantly influenced by temperature rise, the degree of moisture concentration, plate aspect ratio, as well as the EGM coefficient.

Appendix

The elements $P_{ij} = P_{ji}$ of the coefficient matrix $[P]$ in (19) are given by

$$
\begin{aligned}
P_{11} &= A^1_{11}[2\lambda^2 + (1-\nu)\mu^2], & P_{12} &= \lambda\mu A^1_{11}(1+\nu),\\
P_{13} &= -2\lambda A^1_{12}(\lambda^2+\mu^2), & P_{14} &= A^1_{13}[2\lambda^2 + (1-\nu)\mu^2],\\
P_{15} &= P_{24} = \lambda\mu A^1_{13}(1+\nu), & P_{22} &= A^1_{11}[(1-\nu)\lambda^2 + 2\mu^2],\\
P_{23} &= -2\mu A^1_{12}(\lambda^2+\mu^2), & P_{25} &= A^1_{13}[(1-\nu)\lambda^2 + 2\mu^2],\\
P_{33} &= 2A^1_{22}(\lambda^2+\mu^2)^2, & P_{34} &= -2\lambda A^1_{23}(\lambda^2+\mu^2),\\
P_{35} &= -2\mu A^1_{23}(\lambda^2+\mu^2), & P_{44} &= A^1_{33}[2\lambda^2 + (1-\nu)\mu^2] + B(1-\nu),\\
P_{45} &= \lambda\mu A^1_{33}(1+\nu), & P_{55} &= A^1_{33}[(1-\nu)\lambda^2 + 2\mu^2] + B(1-\nu).
\end{aligned}
$$

The elements F_i of the load vector $\{F\}$ in (19) are given by

$$
\begin{aligned}
F_1 &= -2\lambda(1+\nu)\Big(A^\alpha_{11}t_1 + A^\beta_{11}c_1 + \frac{1}{h}(A^\alpha_{12}t_2 + A^\alpha_{13}t_3 + A^\beta_{12}c_2 + A^\beta_{13}c_3)\Big),\\
F_2 &= -2\mu(1+\nu)\Big(A^\alpha_{11}t_1 + A^\beta_{11}c_1 + \frac{1}{h}(A^\alpha_{12}t_2 + A^\alpha_{13}t_3 + A^\beta_{12}c_2 + A^\beta_{13}c_3)\Big),\\
F_3 &= \quad 2(1+\nu)\Big\{\Big(A^\alpha_{12}t_1 + A^\beta_{12}t_1 + \frac{1}{h}(A^\alpha_{22}t_2 + A^\alpha_{23}t_3 + A^\beta_{22}c_2 + A^\beta_{23}c_3)\Big)(\lambda^2+\mu^2) + q_{mn}(1-\nu)\Big\},\\
F_4 &= -2\lambda(1+\nu)\Big(A^\alpha_{13}t_1 + A^\beta_{13}c_1 + \frac{1}{h}(A^\alpha_{23}t_2 + A^\alpha_{33}t_3 + A^\beta_{23}c_2 + A^\beta_{33}t_3)\Big),\\
F_5 &= -2\mu(1+\nu)\Big(A^\alpha_{13}t_1 + A^\beta_{13}c_1 + \frac{1}{h}(A^\alpha_{23}t_2 + A^\alpha_{33}t_3 + A^\beta_{23}c_2 + A^\beta_{33}c_3)\Big).
\end{aligned}
$$

Acknowledgement

This paper was funded by the Deanship of Scientific Research (DSR), King Abdulaziz University, Jeddah, under grant no. 360/130/1431. The author, therefore, acknowledges with thanks DSR technical and financial support.

References

[Adams and Miller 1977] D. F. Adams and A. K. Miller, "Hygrothermal micro stress in a unidirectional composite exhibiting inelastic materials behavior", *J. Compos. Mater.* **11** (1977), 285–299.

[Benkhedda et al. 2008] A. Benkhedda, A. Tounsi, and E. A. Adda Bedia, "Effect of temperature and humidity on transient hygrothermal stresses during moisture desorption in laminated composite plates", *Compos. Struct.* **82**:4 (2008), 629–635.

[Brunelle and Robertson 1974] E. J. Brunelle and S. R. Robertson, "Initially stressed Mindlin plates", *AIAA J.* **12** (1974), 1036–1045.

[Brunelle and Robertson 1976] E. J. Brunelle and S. R. Robertson, "Vibrations of an initially stressed thick plate", *J. Sound Vib.* **45**:3 (1976), 405–416.

[Herrmann and Armenakas 1962] G. Herrmann and A. E. Armenakas, "Vibrations and stability of plates under initial stress", *Trans. ASCE* **127**:1 (1962), 458–491.

[Ishikawa et al. 1978] T. Ishikawa, K. Koyama, and S. Kobayayaski, "Thermal expansion coefficients of unidirectional composites", *J. Compos. Mater.* **12** (1978), 153–168.

[Lee et al. 1992] S. Y. Lee, C. J. Chou, J. L. Jang, and J. S. Lim, "Hygrothermal effects on the linear and nonlinear analysis of symmetric angle-ply laminated plates", *Compos. Struct.* **21** (1992), 41–48.

[Lo et al. 2010] S. H. Lo, W. Zhen, Y. K. Cheung, and C. Wanji, "Hygrothermal effects on multilayered composite plates using a refined higher order theory", *Compos. Struct.* **92** (2010), 633–646.

[Patel et al. 2002] B. P. Patel, M. Ganapathi, and D. P. Makhecha, "Hygrothermal effects on the structural behaviour of thick composite laminates using higher-order theory", *Compos. Struct.* **56** (2002), 25–34.

[Pipes et al. 1976] R. B. Pipes, J. R. Vinson, and T. W. Chou, "On the hygrothermal response of laminated composite systems", *J. Compos. Mater.* **10** (1976), 129–148.

[Rao and Sinha 2004] V. V. S. Rao and P. K. Sinha, "Bending characteristic of thick multidirectional composite plates under hygrothermal environment", *J. Reinf. Plast. Compos.* **23** (2004), 1481–1495.

[Reddy 1997] J. N. Reddy, *Mechanics of laminated composite plates*, CRC Press, Boca Raton, FL, 1997.

[Reddy 2000] J. N. Reddy, "Analysis of functionally graded plates", *Int. J. Numer. Methods Eng.* **47** (2000), 663–684.

[Sai Ram and Sinha 1991] K. S. Sai Ram and P. K. Sinha, "Hygrothermal effects on the bending characteristics on laminated composite plates", *Comput. Struct.* **40** (1991), 1009–1015.

[Sai Ram and Sinha 1992] K. S. Sai Ram and P. K. Sinha, "Hygrothermal effects on the free vibration of laminated composite plates", *J. Sound Vib.* **158** (1992), 133–148.

[Shen 2001] H. S. Shen, "Hygrothermal effects on the postbuckling of shear deformable laminated plates", *Int. J. Mech. Sci.* **43** (2001), 1259–1281.

[Strife and Prewo 1979] J. R. Strife and K. M. Prewo, "The thermal expansion behavior of unidirectional and bidirectional Kevlar/epoxy composites", *J. Compos. Mater.* **13** (1979), 264–267.

[Wang et al. 2005] X. Wang, K. Dong, and X. Y. Wang, "Hygrothermal effect on dynamic interlaminar stresses in laminated plates with piezoelectric actuators", *Compos. Struct.* **71** (2005), 220–228.

[Whitney and Ashton 1971] J. M. Whitney and J. E. Ashton, "Effect of environment on the elastic response of layered composite plates", *AIAA J.* **9** (1971), 1708–1713.

[Yang and Shieh 1987] I. H. Yang and J. A. Shieh, "Vibrations of initially stressed thick, rectangular, orthotropic plates", *J. Sound Vib.* **119** (1987), 545–558.

[Zenkour 2004a] A. M. Zenkour, "Buckling of fiber-reinforced viscoelastic composite plates using various plate theories", *J. Eng. Math.* **50** (2004), 75–93.

[Zenkour 2004b] A. M. Zenkour, "Thermal effects on the bending response of fiber-reinforced viscoelastic composite plates using a sinusoidal shear deformation theory", *Acta Mech.* **171** (2004), 171–187.

[Zenkour 2005] A. M. Zenkour, "Analytical solutions for rotating exponentially-graded annular disks with various boundary conditions", *Int. J. Struct. Stab. Dyn.* **5**:4 (2005), 557–577.

[Zenkour 2006] A. M. Zenkour, "Generalized shear deformation theory for bending analysis of functionally graded plates", *Appl. Math. Model.* **30** (2006), 67–84.

[Zenkour 2009] A. M. Zenkour, "The refined sinusoidal theory for FGM plates on elastic foundations", *Int. J. Mech. Sci.* **51** (2009), 869–880.

[Zenkour 2010] A. M. Zenkour, "Hygro-thermo-mechanical effects on FGM plates resting on elastic foundations", *Compos. Struct.* **93** (2010), 234–238.

Received 16 Mar 2012. Revised 9 Jul 2012. Accepted 10 Jul 2012.

ASHRAF M. ZENKOUR: zenkour@gmail.com
Mathematics Department, King Abdulaziz University, Faculty of Science, P.O. Box 80203, Jeddah 21589, Saudi Arabia
and
Department of Mathematics, Faculty of Science, Kafrelsheikh University, Kafr El-Sheikh 33516, Egypt

JOURNAL OF MECHANICS OF MATERIALS AND STRUCTURES
Vol. 7, No. 7, 2012
dx.doi.org/10.2140/jomms.2012.7.701

msp

GREEN'S FUNCTION FOR SYMMETRIC LOADING OF AN ELASTIC SPHERE WITH APPLICATION TO CONTACT PROBLEMS

ALEXEY S. TITOVICH AND ANDREW N. NORRIS

A compact form for the static Green's function for symmetric loading of an elastic sphere is derived. The expression captures the singularity in closed form using standard functions and quickly convergent series. Applications to problems involving contact between elastic spheres are discussed. An exact solution for a point load on a sphere is presented and subsequently generalized for distributed loads. Examples for constant and Hertzian-type distributed loads are provided, where the latter is also compared to the Hertz contact theory for identical spheres. The results show that the form of the loading assumed in Hertz contact theory is valid for contact angles up to about ten degrees. For larger angles, the actual displacement is smaller and the contact surface is no longer flat.

1. Introduction

Contact between spheres has intrigued researchers for more than a century, and still no simple closed-form analytical solution exists. One of the first and most important developments in the field, due to Heinrich Hertz [1881], is an approximate solution for the normal, frictionless contact of linear elastic spheres. The major assumption in Hertz's model was that the contact area is small compared to the radii of curvature, which has served as a useful engineering approximation in many applications. Ever since then many have tried to relax this assumption while maintaining a compact, workable solution. The Green's function for symmetric loading on a sphere provides the means to find the exact response for arbitrary loading, a first step towards improving on Hertz's classic solution. Existing forms of the Green's function are however not suitable for fast and ready computation, either due to slow convergence of series or analytically cumbersome expressions. The goal of the present paper is to provide an alternative form of the Green's function suitable for fast computation of solutions under arbitrary loading.

Sternberg and Rosenthal [1952] present an in-depth study of the nature of the singularities on an elastic sphere loaded by two opposing concentrated point forces. As expected, the dominant inverse square singularity in the stress components can be removed by subtraction of an appropriate multiple of Boussinesq's solution for a point load at the surface of a half space. Sternberg and Rosenthal showed that the quickly convergent residual field retains a weaker singularity of logarithmic form, a result that is also evident in the solution developed here. The singular solutions obtained by Sternberg and Rosenthal were extended to arbitrarily oriented point forces in [Guerrero and Turteltaub 1972]. Our interest here is in developing an analogous separation of the Green's function (circular ring loading). In this regard, a relatively compact form of the Green's function for the sphere was derived by Bondareva [1969] who used it to solve the problem of the weighted sphere. In [Bondareva 1971], she formulates an example with a sphere contacting a rigid surface. This has been used to solve for the rebound of a sphere from a

Keywords: Green's function, sphere, contact.

surface [Villaggio 1996]. Bondareva's solution starts with the known series expansion [Lur'e 1955] for the solution of the elasticity problem of a sphere, and replaces it with finite integrals of known functions.

In this paper we introduce an alternative form for the Green's function for a sphere, comprised of analytical functions and a quickly convergent series. No direct integration is required. The methodology for determining the analytical functions is motivated by the simple example of a point load on a sphere, for which we derive a solution similar in spirit to that of [Sternberg and Rosenthal 1952], but using a fundamentally different approach: partial summation of infinite series as compared with a functional ansatz. The present methods allows us to readily generalize the point-load solution to arbitrary symmetric normal loading. A typical contact problem involves solving a complicated integral equation for the contact stress once a displacement is specified. Instead, we will use the derived Green's function in the direct sense, solving for the displacements for a given load. This is used to check the validity of Hertz contact theory through the assumed form of the stress distribution.

The outline of the paper is as follows. The known series solution for symmetric loading on a sphere is reviewed in Section 2. The proposed method for simplification is first illustrated in Section 3 by deriving a quickly convergent form of the solution for a point force. The Green's function for symmetric loading is then developed in Section 4, and is illustrated by application to different loadings. Conclusions are given in Section 5.

2. Series solution

Consider a solid sphere of radius R, with surface $r = R$, $0 \le \theta \le \pi$, in spherical polar coordinates (r, θ, ϕ). The sphere is linear elastic with shear modulus G and Poisson's ratio ν. The surface is subject to tractions

$$\sigma_{r\theta} = 0, \quad \sigma_{r\phi} = 0, \quad \sigma_{rr} = \sigma(\theta) \quad \text{for } r = R,\ 0 \le \theta \le \pi,\ 0 \le \phi < 2\pi. \tag{1}$$

Using the known properties of Legendre functions, see (45), allows us to express the normal stress as

$$\sigma(\theta) = \frac{1}{2}\sum_{n=0}^{\infty}(2n+1)\sigma_n P_n(\cos\theta), \tag{2}$$

where the Legendre series coefficients are

$$\sigma_n = \int_0^{\pi} \sigma(\phi) P_n(\cos\phi)\sin\phi\, d\phi. \tag{3}$$

The displacements and tractions for the sphere can also be represented in series form [Zhupanska 2011, Equation (5)]:

$$2Gu_r = \sum_{n=0}^{\infty}[(n-2+4\nu)A_n r + B_n r^{-1}]r^n P_n(\cos\theta),$$

$$2Gu_\theta = \sum_{n=1}^{\infty}[n(n+5-4\nu)A_n r + (n+1)B_n r^{-1}]r^n \frac{P_n^1(\cos\theta)}{n(n+1)},$$

$$\begin{aligned}\sigma_{rr} &= \sum_{n=0}^{\infty}\big[[n(n-1)-2(1+\nu)]A_n + (n-1)B_n r^{-2}\big]r^n P_n(\cos\theta),\\ \sigma_{r\theta} &= \sum_{n=1}^{\infty}\big[n[(n-1)(n+3)+2(1+\nu)]A_n + (n^2-1)B_n r^{-2}\big]r^n \frac{P_n^1(\cos\theta)}{n(n+1)},\end{aligned} \tag{4}$$

with $B_0 \equiv 0$, and where B_1 corresponds to a rigid body translation via $2G\boldsymbol{u}(0,\,\cdot\,) = B_1\boldsymbol{e}_z$. It follows from (1) that

$$\begin{aligned}A_0 &= \frac{-\sigma_0}{2(1+\nu)}, \qquad A_1 = 0,\\ A_n &= -\frac{\sigma_n}{4R^n}\frac{(n+1)(2n+1)}{[n(n-1)+(2n+1)(1+\nu)]}, \quad n \ge 2,\\ B_n &= \frac{-n}{n^2-1}[(n-1)(n+3)+2(1+\nu)]R^2 A_n, \quad n \ge 2.\end{aligned} \tag{5}$$

Thus, noting that $P_n^1(\cos\theta) = \dfrac{d}{d\theta}P_n(\cos\theta)$, we have

$$\begin{aligned}u_r(R,\theta) &= \frac{R}{4G}\left(\frac{2(1-2\nu)}{1+\nu}\sigma_0 + \sum_{n=2}^{\infty}\sigma_n\Big(\frac{2n+1}{n-1}\Big)\left(\frac{2(1-\nu)n^2+\nu n-1+2\nu}{n^2+(1+2\nu)n+1+\nu}\right)P_n(\cos\theta)\right),\\ u_\theta(R,\theta) &= \frac{R}{4G}\frac{d}{d\theta}\sum_{n=2}^{\infty}\sigma_n\Big(\frac{2n+1}{n-1}\Big)\left(\frac{(-1+2\nu)n+2-\nu}{n^2+(1+2\nu)n+1+\nu}\right)P_n(\cos\theta).\end{aligned} \tag{6}$$

Bondareva [1969], using a different representation, replaced the infinite summation of Legendre functions by a combination of closed form expressions and an integral, each dependent on ν. The integral term contains a logarithmic singularity which, together with the complex-valued nature of its coefficients, makes its evaluation indirect. Here we propose an alternative form for the Green's function in a combination of closed-form expressions and a standard summation of Legendre functions that is, by design, quickly convergent.

3. Point force

3.1. ***Exact solution.*** In order to illustrate the method, we first consider the simpler problem of the point force of magnitude F applied at $\theta = 0$ defined by

$$\sigma(\theta) = \frac{-F}{2\pi R^2}\lim_{\psi\downarrow 0}\frac{\delta(\theta-\psi)}{\sin\psi} \quad\Longleftrightarrow\quad \sigma_n = \frac{-F}{2\pi R^2}, \tag{7}$$

where we have used the property $P_n(1) = 1$. The difficulty with the infinite summations (6) is twofold: first, this is not a suitable form to reproduce the singular nature of the Green's function; secondly, they do not converge quickly as a function of the truncated value for n. The idea here is to replace the summation by closed form expressions plus a summation that is both regular and quickly convergent.

The fundamental idea behind the present method is to write u_r and u_θ of (6) in the form

$$u_r(R,\theta) = \frac{-F}{8\pi GR}\Big(4(1-\nu)S(\theta) + \sum_{j=0}^{M} a_j(\nu)S_j(\theta) + f(\theta)\Big), \tag{8a}$$

$$u_\theta(R,\theta) = \frac{-F}{8\pi GR}\frac{d}{d\theta}\Big(\sum_{j=0}^{M} b_j(\nu)S_j(\theta) + g(\theta)\Big), \tag{8b}$$

where the functions $S(\theta)$ and $S_j(\theta)$ ($j = 1, \dots M$), are closed-form expressions, in this case:

$$S(\theta) = \sum_{n=0}^{\infty} P_n(\cos\theta) = \frac{1}{2}\csc\frac{\theta}{2}, \tag{9a}$$

$$S_j(\theta) = \sum_{n=0}^{\infty} \frac{P_{n+j}(\cos\theta)}{n+1}, \quad j = 0, 1, \dots, \tag{9b}$$

and $f(\theta)$, $g(\theta)$ are regular functions of θ defined by quickly convergent series in n,

$$f(\theta) = \sum_{n=0}^{\infty} C_n P_n(\cos\theta), \qquad g(\theta) = \sum_{n=0}^{\infty} D_n P_n(\cos\theta). \tag{10}$$

The coefficients $a_0, a_1, \dots, a_M$ are defined so that $C_n = \mathrm{O}\big(n^{-(M+2)}\big)$ as $n \to \infty$. This criterion uniquely provides the constants $a_0, a_1, \dots, a_M$ as solutions of a system of linear equations. Similarly, $b_0, b_1, \dots, b_M$ are uniquely defined by $D_n = \mathrm{O}\big(n^{-(M+2)}\big)$ as $n \to \infty$.

Here we consider the specific case of $M = 2$. Other values of M could be treated in the same manner; however, we will show that $M = 2$ is adequate for the purpose of improving convergence. In this case (8) becomes

$$\begin{aligned} u_r(R,\theta) &= \frac{-F}{8\pi GR}[4(1-\nu)S(\theta) + a_0S_0(\theta) + a_1S_1(\theta) + a_2S_2(\theta) + f(\theta)] \\ &= \frac{-F}{8\pi GR}\Big[\sum_{n=2}^{\infty}\Big(4(1-\nu) + \frac{a_0}{n+1} + \frac{a_1}{n} + \frac{a_2}{n-1} + C_n\Big)P_n(\theta) + C_0P_0(\theta) + C_1P_1(\theta) \\ &\qquad + 4(1-\nu)\big(P_0(\theta) + P_1(\theta)\big) + a_0\big(P_0(\theta) + \tfrac{1}{2}P_1(\theta)\big) + a_1P_1(\theta)\Big], \end{aligned} \tag{11a}$$

$$\begin{aligned} u_\theta(R,\theta) &= \frac{-F}{8\pi GR}\frac{d}{d\theta}\Big[b_0S_0(\theta) + b_1S_1(\theta) + b_2S_2(\theta) + g(\theta)\Big] \\ &= \frac{-F}{8\pi GR}\frac{d}{d\theta}\Big[\sum_{n=2}^{\infty}\Big(\frac{b_0}{n+1} + \frac{b_1}{n} + \frac{b_2}{n-1} + D_n\Big)P_n(\theta) \\ &\qquad + b_0\big(P_0(\theta) + \tfrac{1}{2}P_1(\theta)\big) + b_1P_1(\theta) + D_0P_0(\theta) + D_1P_1(\theta)\Big], \end{aligned} \tag{11b}$$

where the associated functions $S_j(\theta)$, $j = 0, 1, 2$, are (see Appendix B)

$$S_0(\theta) = \log\Big(1 + \csc\frac{\theta}{2}\Big), \tag{12a}$$

$$S_1(\theta) = -S_0(\theta) - 2\log\sin\frac{\theta}{2}, \tag{12b}$$

$$S_2(\theta) = S_1(\theta)\cos\theta - 2\sin\frac{\theta}{2}\Big(1 - \sin\frac{\theta}{2}\Big). \tag{12c}$$

Equations (8), (9a), and (12) indicate the expected Boussinesq-like θ^{-1} singularity as well as the weaker $\log\theta$ singularity first described in [Sternberg and Rosenthal 1952]. The logarithmic singularities in $S_j(\theta)$, $j = 0, 1, 2$, can be compared to the potential functions $[D_1]$, $[D_2]$, and $[D_3]$ in Equation (17) of that reference, which provide a logarithmic singularity. In the present notation these are, respectively (using capital Φ so as not to be confused with the angle ϕ, and making the substitution $\theta \to \pi - \theta$),

$$\begin{aligned} &\Phi_1(\theta) = 2\log\sin\frac{\theta}{2}, \qquad \Phi_2(\theta) = -R\Big(1 + 2\cos\theta\log\sin\frac{\theta}{2}\Big), \\ &\Phi_3(\theta) = R^2\Big(2(1 - 3\cos^2\theta)\log\sin\frac{\theta}{2} + \cos^2\theta - 3\cos\theta - 1\Big). \end{aligned} \tag{13}$$

These clearly display the same form of the singularity as in equations (12), but are otherwise different.

Define the first two coefficients of $f(\theta)$ and $g(\theta)$ from (10) as

$$C_0 = \frac{2(1-2\nu)}{1+\nu} - 4(1-\nu) - a_0, \quad C_1 = -4(1-\nu) - \tfrac{1}{2}a_0 - a_1, \tag{14a}$$

$$D_0 = -b_0, \qquad D_1 = -\tfrac{1}{2}b_0 - b_1. \tag{14b}$$

The coefficients a_n and b_n are then found by comparing expression (11) to the series solution in (6), expanding both expressions for large n, and equating the coefficients of the same order terms. Thus, the original assumed form of the solution (8) implies

$$\begin{aligned} \sum_{n=2}^{\infty} \frac{P_n(\theta)}{n^2 + (1+2\nu)n + 1 + \nu}\Big(\frac{2n+1}{n-1}\Big) \times \begin{cases} \big(2(1-\nu)n^2 + \nu n - 1 + 2\nu\big) \\ \big((-1+2\nu)n + 2 - \nu\big) \end{cases} \\ = \sum_{n=2}^{\infty} P_n(\theta) \times \begin{cases} \Big(4(1-\nu) + \dfrac{a_0}{n+1} + \dfrac{a_1}{n} + \dfrac{a_2}{n-1} + C_n\Big), \\ \Big(\dfrac{b_0}{n+1} + \dfrac{b_1}{n} + \dfrac{b_2}{n-1} + D_n\Big), \end{cases} \end{aligned} \tag{15}$$

where

$$\begin{aligned} a_0 &= \tfrac{1}{2}(1+\nu)(1-2\nu)(-16\nu^2 + 8\nu + 5), \\ a_1 &= -32\nu^4 + 16\nu^3 + 30\nu^2 - 16\nu - 1, \\ a_2 &= 16\nu^4 - 16\nu^3 - 5\nu^2 + \tfrac{13}{2}\nu + \tfrac{1}{2}, \\ b_0 &= \tfrac{1}{2}(1+\nu)(16\nu^2 - 12\nu - 1), \\ b_1 &= -16\nu^3 + 4\nu^2 + 13\nu - 4, \\ b_2 &= 8\nu^3 - 6\nu^2 - \tfrac{5}{2}\nu + \tfrac{5}{2}. \end{aligned} \tag{16}$$

The remaining coefficients C_n and D_n are then determined directly from (15):

$$C_n = \frac{(1+\nu)}{L_n}\big((6-a_1-6a_2)n+a_1\big)$$
$$= -\frac{(1+\nu)}{L_n}\big((64\nu^4-80\nu^3+23\nu-4)n+(32\nu^4-16\nu^3-30\nu^2+16\nu+1)\big), \tag{17a}$$
$$D_n = \frac{(1+\nu)}{L_n}\big((6-b_1-6b_2)n+b_1\big)$$
$$= -\frac{(1+\nu)}{L_n}\big((32\nu^3-32\nu^2-2\nu+5)n+(16\nu^3-4\nu^2-13\nu+4)\big), \tag{17b}$$

where

$$L_n \equiv n(n^2-1)\big(n^2+(1+2\nu)n+1+\nu\big). \tag{18}$$

In summary, the new form of the point force solution is given by the displacements in (11) where the functions and coefficients are given in (12)–(14) and (16)–(18).

3.2. ***Numerical examples.*** In the following examples we introduce the integer N as the truncation value of the series in (10). The Poisson's ratio was taken to be 0.4. Displacements have been normalized by the constant coefficient of the series as $U_i = -8\pi GRF^{-1}u_i$, where $i = r, \theta$. Figure 1 shows the rate of convergence of the displacements given by (11), whereas Figures 2 and 3 compare the displacements in (6) with (11).

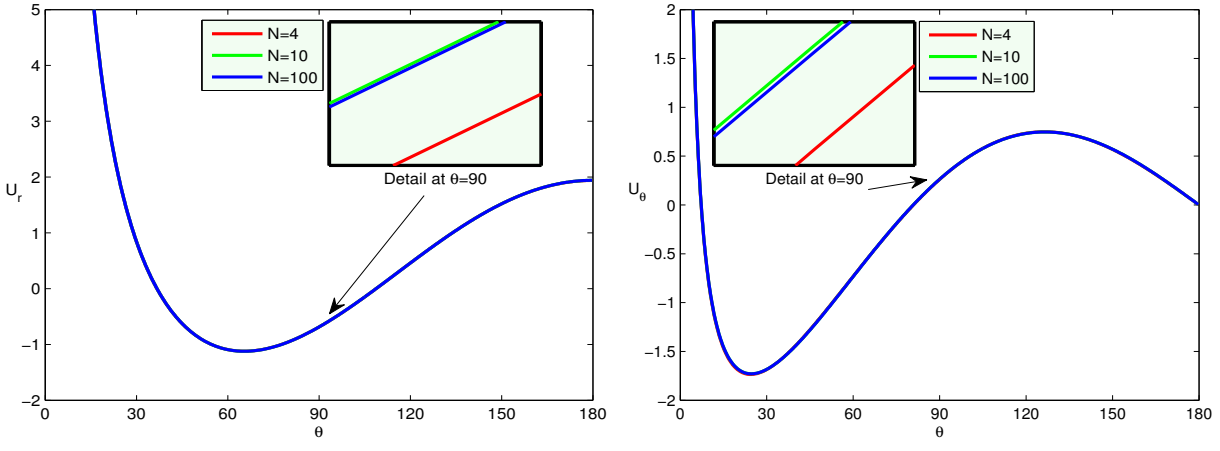

Figure 1. Convergence of the proposed expression for U_r (left) and U_θ (right), which equal $(-8\pi GR/F)$ times the functions u_r and u_θ in (11). The inset on the left shows the U_r graphs around $\theta = \pi/2$ magnified 11250 times: the difference in the value of U_r from $N = 4$ to $N = 10$ is $4.5259 \cdot 10^{-4}$, and from $N = 10$ to $N = 100$ it is $-1.7059 \cdot 10^{-5}$. The inset on the right shows the U_θ graphs around $\theta = \pi/2$ magnified 1200 times: the difference in the value of U_θ from $N = 4$ to $N = 10$ is $2.4097 \cdot 10^{-3}$, and from $N = 10$ to $N = 100$ it is $-1.5040 \cdot 10^{-4}$.

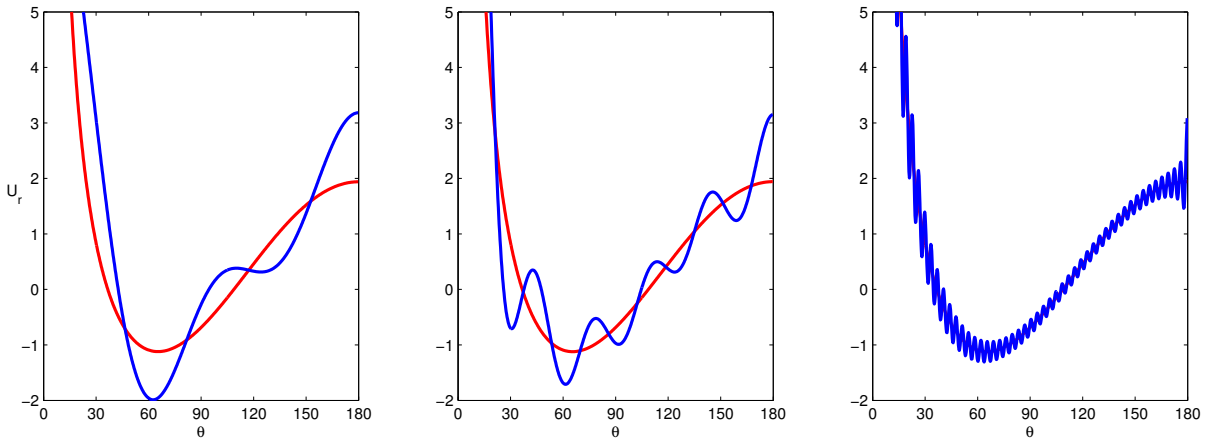

Figure 2. Comparison of the convergence of $U_r = (-8\pi GR/F)u_r$ with the truncation value N for the existing expression ((6), shown in blue) and the expression proposed herein ((11), shown in red). From left to right: $N = 4$, 10, 100.

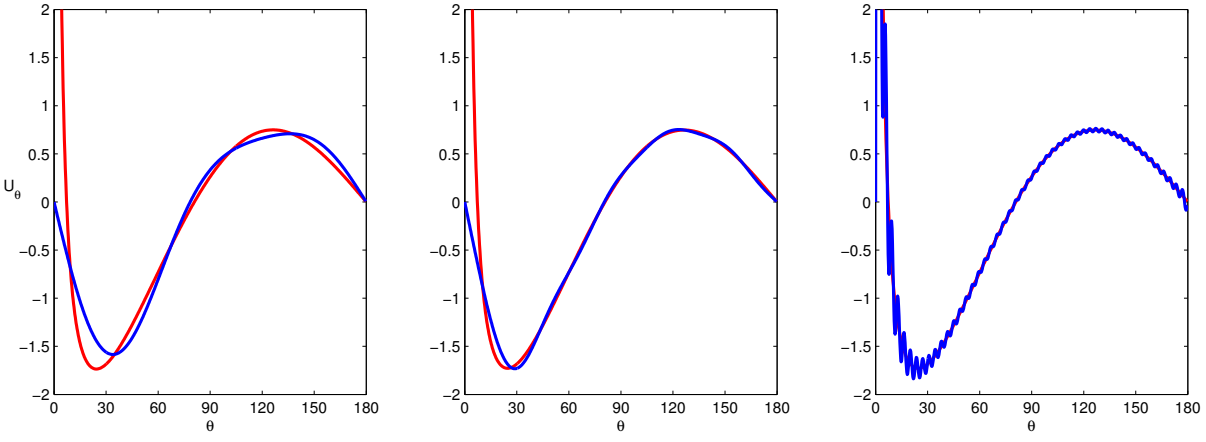

Figure 3. Comparison of the convergence of $U_\theta = (-8\pi GR/F)u_\theta$ with the truncation value N for the existing expression ((6), shown in blue) and the expression proposed herein ((11), shown in red). From left to right: $N = 4$, 10, 100.

By design, the proposed expression, (11), converges much faster than the existing expression, (6), as seen in Figures 2 and 3. Looking at the convergence of the proposed expressions with the truncation value N, Figure 1, we can suggest that the analytic portion of the expression alone gives close results. However, it should be noted that one cannot get rid of the first two terms in the series for $f(\theta)$ and $g(\theta)$ because of their large magnitudes. As far as the general behavior of the normalized displacements with θ, we see that they increase asymptotically approaching $\theta = 0$, change sign between 36.7° and 108.7° for U_r (7.27° and 80.83° for U_θ), and have a minimum at 65.5° for U_r (24.6° for U_θ). This is difficult to see in the figures, but due to the symmetry of the loading, the displacement U_θ must have a value of 0 at $\theta = 0$.

4. Green's function

4.1. ***A fast convergent form for the Green's function.*** The surface displacements for arbitrary loading may be written, by analogy with the ansatz (8) for the point force, and generalizing the latter,

$$u_r(R,\theta) = \frac{R}{4G}\int_0^\pi \Big(4(1-\nu)S(\theta,\phi) + \sum_{j=0}^{M} a_j(\nu)S_j(\theta,\phi) + f(\theta,\phi)\Big)\sigma(\phi)\sin\phi\, d\phi, \tag{19a}$$

$$u_\theta(R,\theta) = \frac{R}{4G}\frac{d}{d\theta}\int_0^\pi \Big(\sum_{j=0}^{M} b_j(\nu)S_j(\theta,\phi) + g(\theta,\phi)\Big)\sigma(\phi)\sin\phi\, d\phi, \tag{19b}$$

where $S(\theta,\phi)$ and $S_j(\theta,\phi)$ $(j = 1,\dots M)$ are

$$S(\theta,\phi) = \sum_{n=0}^{\infty} P_n(\cos\theta)P_n(\cos\phi), \tag{20a}$$

$$S_j(\theta,\phi) = \sum_{n=0}^{\infty} \frac{1}{n+1}P_{n+j}(\cos\theta)P_{n+j}(\cos\phi), \quad j = 0, 1, \dots, \tag{20b}$$

and $f(\theta,\phi)$ and $g(\theta,\phi)$ are regular functions of θ defined by quickly convergent series in n:

$$f(\theta,\phi) = \sum_{n=0}^{\infty} C_n P_n(\cos\theta)P_n(\cos\phi), \quad g(\theta,\phi) = \sum_{n=0}^{\infty} D_n P_n(\cos\theta)P_n(\cos\phi). \tag{21}$$

The coefficients $a_0, a_1, \dots, a_M$ are the same as before. The main complication is to find the functions (20). Thus, $S(\theta,\phi)$ follows from (52) as

$$S(\theta,\phi) = \begin{cases} \dfrac{1}{\pi}\csc\dfrac{\theta}{2}\sec\dfrac{\phi}{2}K\left(\left(\cot\dfrac{\theta}{2}\tan\dfrac{\phi}{2}\right)^2\right), & \theta > \phi, \\ \dfrac{1}{\pi}\sec\dfrac{\theta}{2}\csc\dfrac{\phi}{2}K\left(\left(\tan\dfrac{\theta}{2}\cot\dfrac{\phi}{2}\right)^2\right), & \theta < \phi, \end{cases} \tag{22}$$

where $K(m)$ is the complete elliptic integral of the first kind [Abramowitz and Stegun 1964, 17.3.1], while (50a) implies

$$S_{01}(\theta,\phi) \equiv S_0(\theta,\phi) + S_1(\theta,\phi) = \begin{cases} -2\log\sin\dfrac{\theta}{2}\cos\dfrac{\phi}{2}, & \theta > \phi, \\ -2\log\cos\dfrac{\theta}{2}\sin\dfrac{\phi}{2}, & \theta < \phi. \end{cases} \tag{23}$$

The functions $S_j(\theta,\phi)$ can be determined, but their form is overly complicated, and defeats our objective of simplifying the Green's function. We therefore restrict the solution to the use of the above two series: $S(\theta,\phi)$ and $S_{01}(\theta,\phi)$.

We therefore consider the following form of the ansatz (19) using the series S and S_{01} of (22) and (23), respectively. Substituting them into (19) yields the identities

$$\begin{aligned}u_r(R,\theta) &= \frac{R}{4G}\int_0^\pi \big(4(1-\nu)S(\theta,\phi)+a_{01}(\nu)S_{01}(\theta,\phi)+f(\theta,\phi)\big)\sigma(\phi)\sin\phi\,d\phi\\ &= \frac{R}{4G}\int_0^\pi \Bigg[\sum_{n=2}^{\infty}\Big(4(1-\nu)+a_{01}\Big(\frac{2n+1}{n(n+1)}\Big)+C_n\Big)P_n(\cos\theta)P_n(\cos\phi)\\ &\quad +4(1-\nu)\big(P_0(\cos\theta)P_0(\cos\phi)+P_1(\cos\theta)P_1(\cos\phi)\big)+a_{01}\big(P_0(\cos\theta)P_0(\cos\phi)\\ &\quad +\tfrac{3}{2}P_1(\cos\theta)P_1(\cos\phi)\big)+C_0P_0(\cos\theta)P_0(\cos\phi)+C_1P_1(\cos\theta)P_1(\cos\phi)\Bigg]\sigma(\phi)\sin\phi\,d\phi, \qquad (24a)\\ u_\theta(R,\theta) &= \frac{R}{4G}\frac{d}{d\theta}\int_0^\pi \big(b_{01}(\nu)S_{01}(\theta,\phi)+g(\theta,\phi)\big)\sigma(\phi)\sin\phi\,d\phi\\ &= \frac{R}{4G}\frac{d}{d\theta}\int_0^\pi \Bigg[\sum_{n=2}^{\infty}\Big(b_{01}\Big(\frac{2n+1}{n(n+1)}\Big)+D_n\Big)P_n(\cos\theta)P_n(\cos\phi)\\ &\quad +b_{01}\big(P_0(\cos\theta)P_0(\cos\phi)+\tfrac{3}{2}P_1(\cos\theta)P_1(\cos\phi)\big)\\ &\quad +D_0P_0(\cos\theta)P_0(\cos\phi)+D_1P_1(\cos\theta)P_1(\cos\phi)\Bigg]\sigma(\phi)\sin\phi\,d\phi. \qquad (24b)\end{aligned}$$

Once again we define the first two coefficients of $f(\theta,\phi)$ and $g(\theta,\phi)$ as

$$C_0=\frac{2(1-2\nu)}{1+\nu}-4(1-\nu)-a_{01}, \qquad C_1=-4(1-\nu)-\tfrac{3}{2}a_{01}, \qquad (25a)$$

$$D_0=-b_{01}, \qquad D_1=-\tfrac{3}{2}b_{01}, \qquad (25b)$$

which allows us to solve the following expressions for the coefficients a_{01} and b_{01}:

$$\begin{aligned}&\sum_{n=2}^{\infty}\Big(\frac{2n+1}{n-1}\Big)\Big(\frac{2(1-\nu)n^2+\nu n-1+2\nu}{n^2+(1+2\nu)n+1+\nu}\Big)P_n(\cos\theta)P_n(\cos\phi)\\ &\qquad =\sum_{n=2}^{\infty}\Big(4(1-\nu)+\frac{(2n+1)}{n(n+1)}a_{01}+C_n\Big)P_n(\cos\theta)P_n(\cos\phi), \qquad (26a)\\ &\sum_{n=2}^{\infty}\Big(\frac{2n+1}{n-1}\Big)\Big(\frac{(-1+2\nu)n+2-\nu}{n^2+(1+2\nu)n+1+\nu}\Big)P_n(\cos\theta)P_n(\cos\phi)\\ &\qquad =\sum_{n=2}^{\infty}\Big(\frac{(2n+1)}{n(n+1)}b_{01}+D_n\Big)P_n(\cos\theta)P_n(\cos\phi). \qquad (26b)\end{aligned}$$

This is done by expanding (26) for large n and equating same order terms yielding

$$a_{01}=(2\nu-1)^2, \qquad b_{01}=2\nu-1. \qquad (27)$$

Using (27), C_n and D_n are found directly from (26) (see also (18)):

$$\begin{aligned}C_n=-\frac{1}{L_n}[&(\nu-1)(4\nu-1)(4\nu+1)n^3+(8\nu^2-11\nu-1)n^2\\ &+(-12\nu^3+8\nu^2+3\nu-5)n-(\nu+1)(2\nu-1)^2], \qquad (28a)\end{aligned}$$

$$D_n = -\frac{(2n+1)}{L_n}[(\nu-1)(4\nu+1)n^2 + 2(-\nu^2+\nu-1)n - (\nu+1)(2\nu-1)]. \tag{28b}$$

In summary,

$$u_i(R,\theta) = \frac{R}{4G}\int_0^\pi H_i(\theta,\phi)\sigma(\phi)\sin\phi\, d\phi, \quad i = r,\theta, \tag{29a}$$

$$H_r(\theta,\phi) = 4(1-\nu)S(\theta,\phi) + (1-2\nu)^2 S_{01}(\theta,\phi) + \sum_{n=0}^{\infty} C_n P_n(\cos\theta)P_n(\cos\phi), \tag{29b}$$

$$H_\theta(\theta,\phi) = \frac{d}{d\theta}\Big((2\nu-1)S_{01}(\theta,\phi) + \sum_{n=0}^{\infty} D_n P_n(\cos\theta)P_n(\cos\phi)\Big), \tag{29c}$$

where the coefficients C_n and D_n are given in (28). Note that C_n, $D_n = \mathrm{O}(n^{-2})$ as $n \to \infty$, ensuring rapidly convergent series. The Green's functions of (29) are generally valid for $\theta \in [0,\pi]$. The integrands $H_i(\theta,\phi)$ are smooth and bounded functions of ϕ for $\phi \neq \theta$, which is always the case if the displacements are evaluated at points outside the region of the loading $\sigma(\phi)$. However, for points under the load, the integration of $H_r(\theta,\phi)$ involves a logarithmic singularity at $\phi = \theta$. A simple means of dealing with this is described next.

4.1.1. *Removing the singularity under the load.* The function $S(\theta,\phi)$ exhibits a logarithmic singularity by virtue of the asymptotic behavior:

$$K(m) = \log\frac{4}{\sqrt{1-m}} + \mathrm{O}(1-m), \quad m \uparrow 1. \tag{30}$$

The integral in (24a) is evaluated by rewriting (24a) in the equivalent form

$$u_r(R,\theta) = \frac{R}{4G}\Bigg\{\int_0^{\phi_0}\big[\big(a_{01}(\nu)S_{01}(\theta,\phi) + f(\theta,\phi)\big)\sigma(\phi) + 4(1-\nu)\big(S(\theta,\phi)\sigma(\phi) - \hat{S}(\theta,\phi)\sigma(\theta)\big)\big]\sin\phi\, d\phi$$
$$+ 4(1-\nu)\sigma(\theta)\int_0^{\phi_0}\hat{S}(\theta,\phi)\sin\phi\, d\phi\Bigg\}, \quad 0 \le \theta \le \phi_0, \tag{31}$$

where the angle ϕ_0 defines the domain of the loading, which is normally for contact problems, much less that π. The function $\hat{S}(\theta,\phi)$ has the same singularity as $S(\theta,\phi)$ and has a relatively simple integral. We choose

$$\hat{S}(\theta,\phi) = \begin{cases} -\dfrac{1}{2\pi}\csc\dfrac{\theta}{2}\sec\dfrac{\phi}{2}\log\Big(\cos^2\dfrac{\phi}{2} - \cos^2\dfrac{\theta}{2}\Big), & \theta > \phi, \\ -\dfrac{1}{2\pi}\sec\dfrac{\theta}{2}\csc\dfrac{\phi}{2}\log\Big(\sin^2\dfrac{\phi}{2} - \sin^2\dfrac{\theta}{2}\Big), & \theta < \phi. \end{cases} \tag{32}$$

The integrand of the first integral in (31) is now a smoothly varying function with no singularity, and the second integral is, explicitly,

$$\int_0^{\phi_0} \hat{S}(\theta,\phi)\sin\phi\,d\phi = -\frac{2}{\pi\sin(\theta/2)}\int_{\cos(\theta/2)}^{1}\log\Big(x^2-\cos^2\frac{\theta}{2}\Big)dx - \frac{2}{\pi\cos(\theta/2)}\int_{\sin(\theta/2)}^{\sin(\phi_0/2)}\log\Big(x^2-\sin^2\frac{\theta}{2}\Big)dx \quad (33)$$

$$= \frac{G(\cos(\theta/2),1)}{\sin(\theta/2)} + \frac{G(\sin(\theta/2),\sin(\phi_0/2))}{\cos(\theta/2)}, \quad 0\le\theta\le\phi_0,$$

where

$$G(x,y) = -\frac{2}{\pi}\big((y-x)\log(y-x)+(y+x)\log(y+x)-2(y-x+x\log 2x)\big). \quad (34)$$

In summary, the solution for u_r with the singularity removed has the following form (see also (29a) for $H_r(\theta,\phi)$ and (33) for $G(x,y)$)

$$\begin{aligned} u_r(R,\theta) &= \frac{R}{4G}\left\{\int_0^{\phi_0}[H_r(\theta,\phi)\sigma(\phi)-\hat{H}_r(\theta,\phi)\sigma(\theta)]\sin\phi\,d\phi + h(\theta)\right\},\\ \hat{H}_r(\theta,\phi) &= 4(1-\nu)\hat{S}(\theta,\phi), \quad (35)\\ h(\theta) &= 4(1-\nu)\left[\frac{G(\cos(\theta/2),1)}{\sin(\theta/2)} + \frac{G(\sin(\theta/2),\sin(\phi_0/2))}{\cos(\theta/2)}\right]\sigma(\theta). \end{aligned}$$

4.2. ***Examples of distributed loads.*** To check the convergence of the expressions in (24) we will consider a symmetric constant distributed load $\sigma(\phi)$ of the form

$$\sigma(\phi) = \frac{-F}{\pi R^2}\frac{1}{\sin^2\phi_0}, \quad 0\le\phi\le\phi_0, \quad (36)$$

and a symmetric Hertzian-type load of the form

$$\sigma(\phi) = \frac{-3F}{2\pi R^2}\frac{\sqrt{\sin^2\phi_0-\sin^2\phi}}{\sin^3\phi_0}, \quad 0\le\phi\le\phi_0. \quad (37)$$

Both loads have been normalized such that their resultant forces are $-F$ for all ranges of the angle ϕ_0, which is equivalent to the point force given by (7). The solution on the interval $0\le\theta\le\phi_0$ is obtained using (35) and for $\phi_0<\theta\le\pi$ we apply (29) directly.

Firstly, the convergence of the proposed solution, (35), is compared to the series solution for a Hertzian-type load in Figures 4 and 5. These curves indicate that the convergence of the radial displacement U_r in the proposed solution is substantially superior to the series solution. Figures 6 and 7 show the convergence of the displacements with the truncation limit N under both types of loading. Subsequently, Figures 8 and 9 demonstrate that in the limit as $\phi_0\to 0$ the displacements due to the distributed loads approach those obtained for the point load. Moreover, the normalized radial displacement, U_r, is almost indistinguishable from the point load for a ϕ_0 as large as ten degrees. A Poisson's ratio of $\nu=0.4$ has been used throughout.

We would also like to investigate how the displacement due to a Hertzian-type load compares with that from Hertzian contact theory. The dimensionless vertical displacement that we obtain by the methods

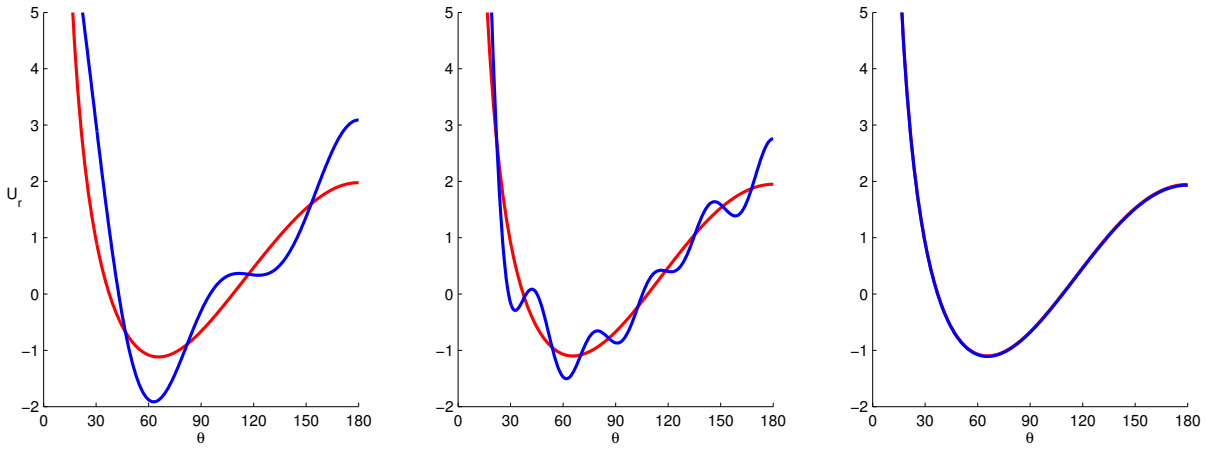

Figure 4. Comparison of the proposed solution ((35), shown in red) and existing series solutions ((6), shown in blue) for $U_r = (-8\pi GR/F)u_r$ under a Hertzian-type load distributed up to $\phi = 10°$. From left to right: $N = 4$, 10, 100.

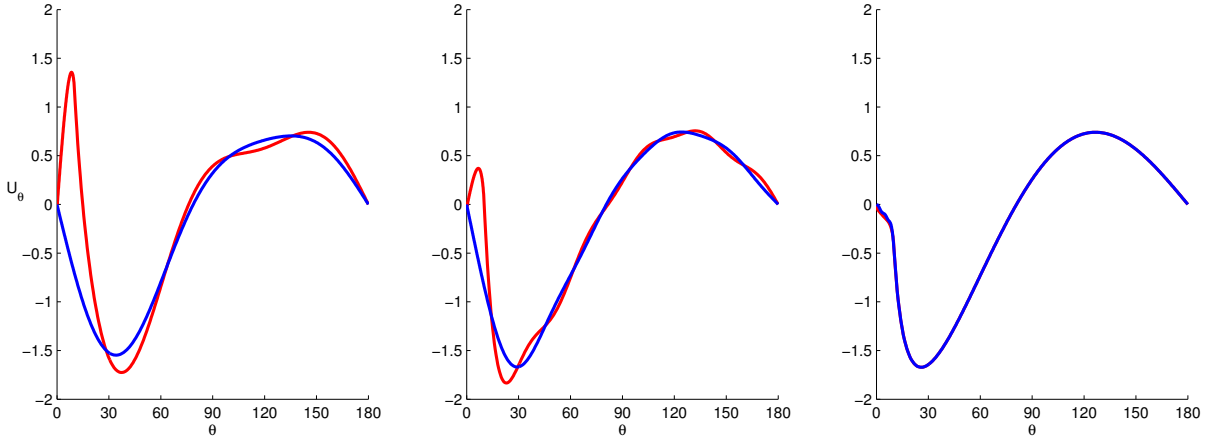

Figure 5. Comparison of the proposed solution ((35), shown in red) and existing series solutions ((6), shown in blue) for $U_\theta = (-8\pi GR/F)u_\theta$ under a Hertzian-type load distributed up to $\phi = 10°$. From left to right: $N = 4$, 10, 100.

outlined in this paper has the form

$$U_z = U_r \cos\theta - U_\theta \sin\theta = (8\pi GR)\frac{u_z}{F}, \tag{38}$$

where u_z is the physical vertical displacement.

Hertz contact theory [Johnson 1985] is formulated in terms of the radius of the contact area a, the displacements directly under the load δ, and the magnitude of the applied load F. We need to reformulate these quantities in terms of the contact angle ϕ_0. The radius of the contact area is simply

$$a = R \sin\phi_0. \tag{39}$$

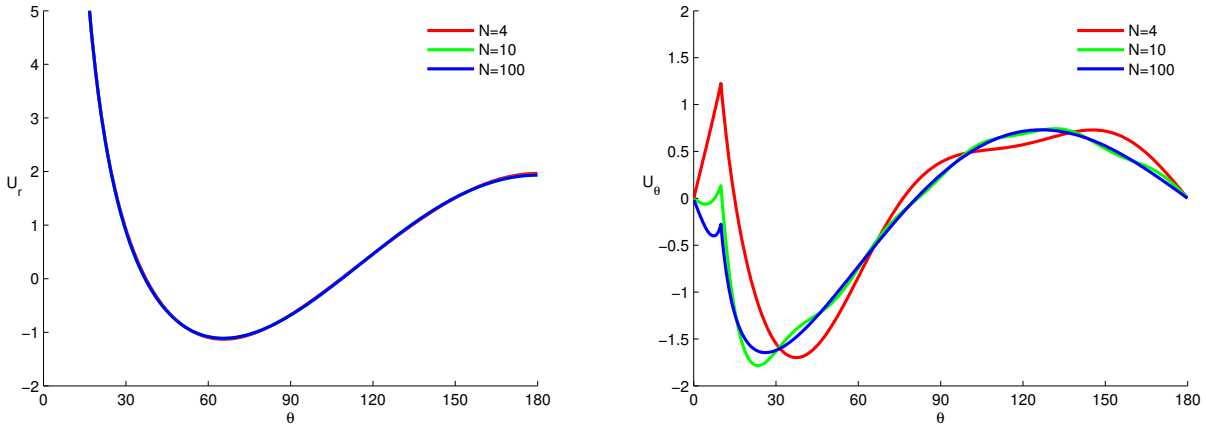

Figure 6. Convergence of the expressions for $U_r = (-8\pi GR/F)u_r$ and $U_\theta = (-8\pi GR/F)u_\theta$ given in (24) with N for a constant distributed load given by (36). The load was distributed up to $\phi_0 = 10°$.

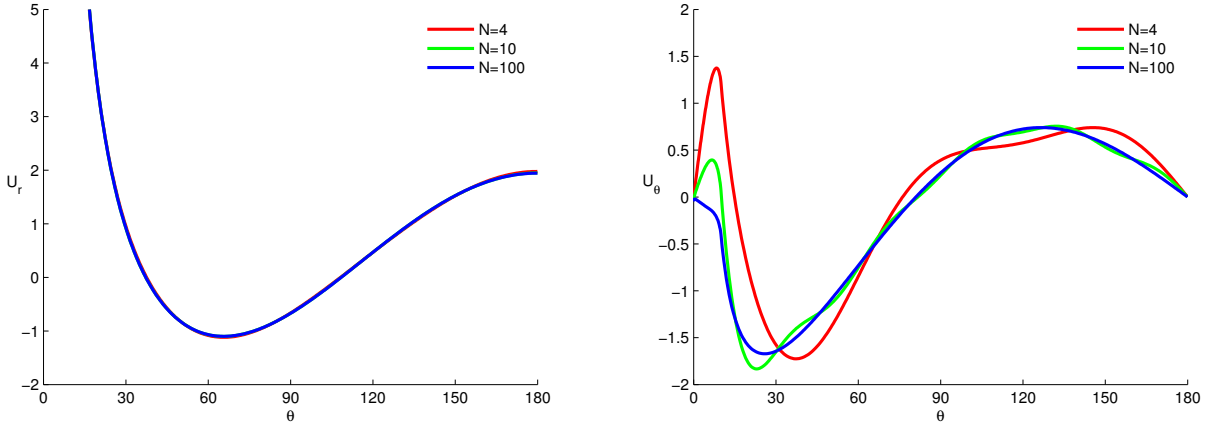

Figure 7. Convergence of the expressions for $U_r = (-8\pi GR/F)u_r$ and $U_\theta = (-8\pi GR/F)u_\theta$ given in (24) with N for a Hertzian-type distributed load given by (37). The load was distributed up to $\phi_0 = 10°$.

The maximum vertical displacement is related to a in the following manner:

$$\delta = \frac{a^2}{R} = R\sin^2\phi_0 = 2u_z(0), \tag{40}$$

where (39) was used and the last equality arises from the fact that the Hertzian solution presented here is for the contact of two spheres hence we need to halve the total displacement. Furthermore, Hertz contact theory tells us that the resultant force F is proportional to a^3, or, more accurately,

$$F = \frac{4}{3}\left(\frac{G}{1-\nu}\right)\frac{a^3}{R} = \frac{4}{3}\left(\frac{G}{1-\nu}\right)R^2\sin^3\phi_0. \tag{41}$$

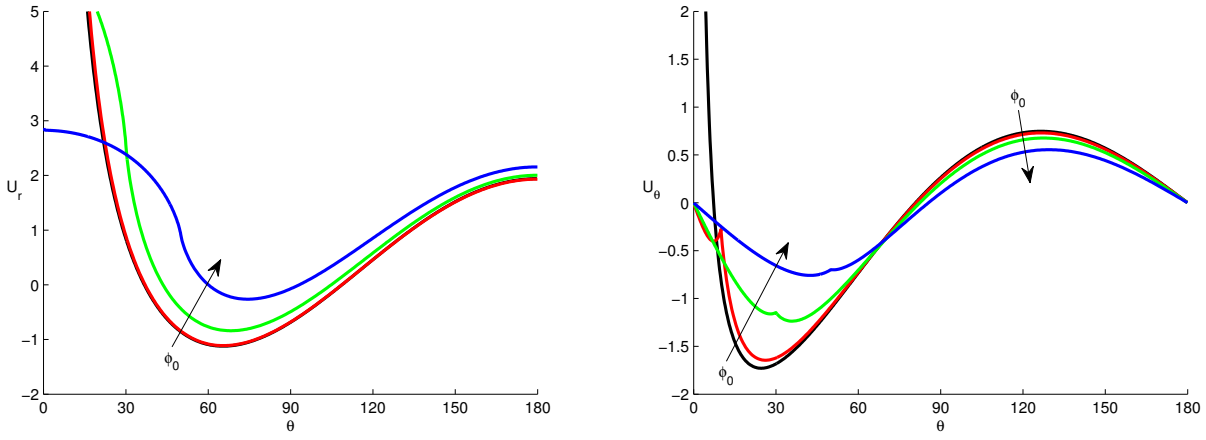

Figure 8. Comparison of the displacement due to a constant distributed load to the displacement due to a point force of the same magnitude (black). The solution was truncated at $N = 300$. The loads were distributed over $\phi_0 = 10°$ (red), 30° (green), and 50° (blue).

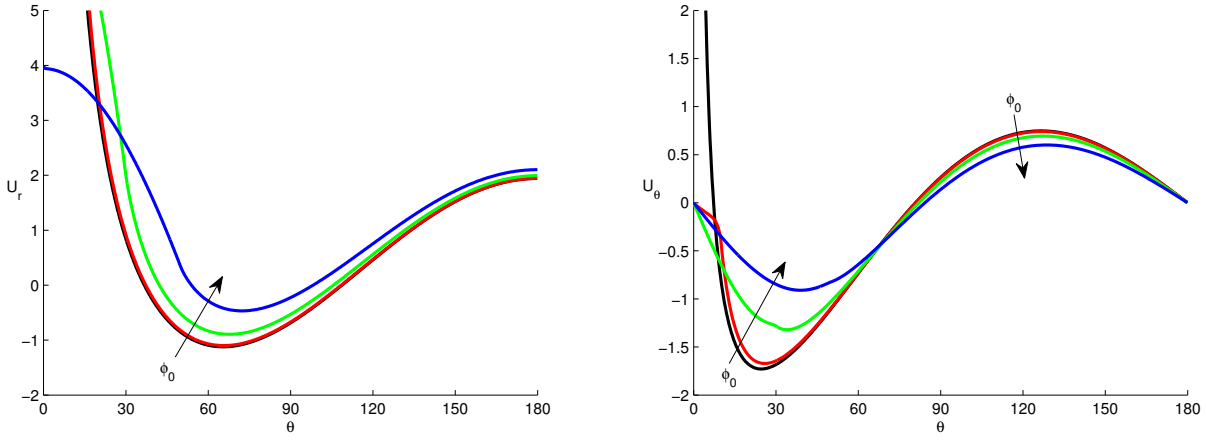

Figure 9. Convergence of the displacement due to a Hertzian-type distributed load to the displacement due to a point force of the same magnitude (black). The solution was truncated at $N = 300$. The loads were distributed over $\phi_0 = 10°$ (red), 30° (green), and 50° (blue).

This allows us to rewrite (38) for the dimensionless vertical displacement via Hertz contact theory, denoted as $U_z^H(0)$. Substituting (40) and (41) into (38) yields

$$U_z^H(0) = (8\pi GR)\frac{(R/2)\sin^2\phi_0}{(4/3)(G/(1-\nu))R^2\sin^3\phi_0} = \frac{3\pi(1-\nu)}{\sin\phi_0}. \tag{42}$$

Equation (42) gives us a way to compare the presented solution for the Hertzian-type load to the solution from Hertz contact theory. The numerical results are presented in Figure 10, which compares

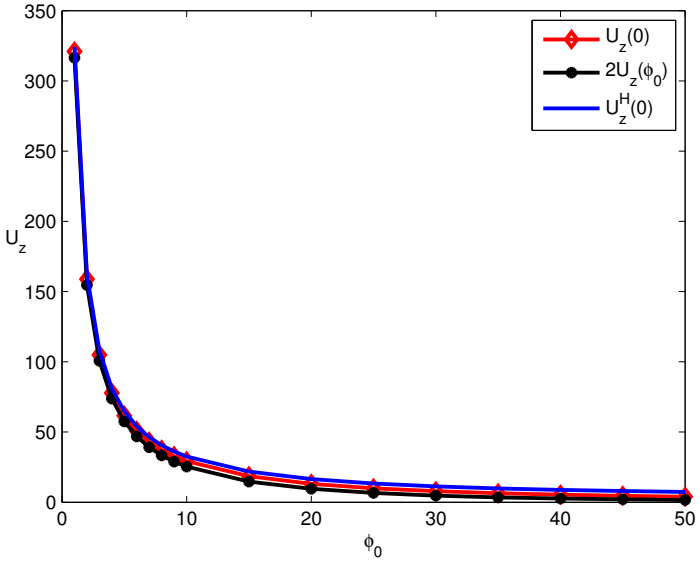

Figure 10. Comparison of the dimensionless vertical displacement $U_z = (8\pi GR)u_z/F$ as obtained by the methods in this paper for a Hertzian-type load and that obtained from Hertz contact theory U_z^H defined in (42), as a function of the contact angle ϕ_0.

the vertical displacements ((38) with (42)) as a function of the contact angle ϕ_0. Note that along with $U_z(0)$ and $U_z^H(0)$ we also plot $2U_z(\phi_0)$, which according to Hertz theory should be equal to $U_z(0)$. The normalized difference between the displacements is shown in Figure 11. As expected, the solutions are close for small contact areas and diverge as this area increases. The same can be said about the relationship between the displacements $U_z(0)$ and $2U_z(\phi_0)$.

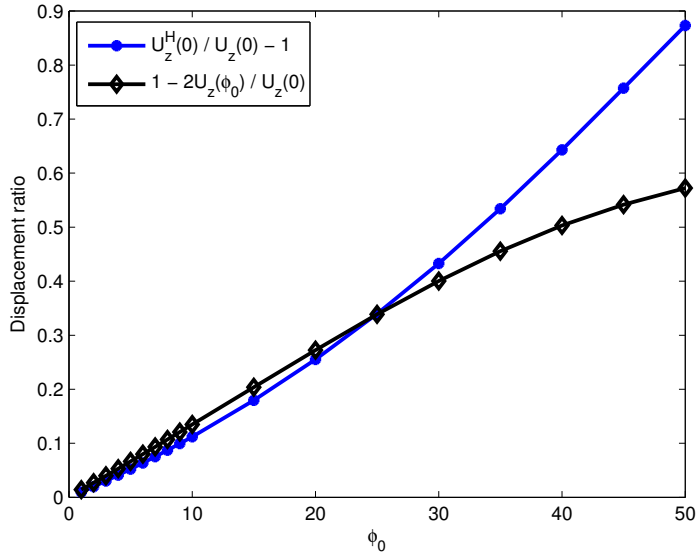

Figure 11. Normalized difference between the displacements in Figure 10 as a function of the contact angle ϕ_0.

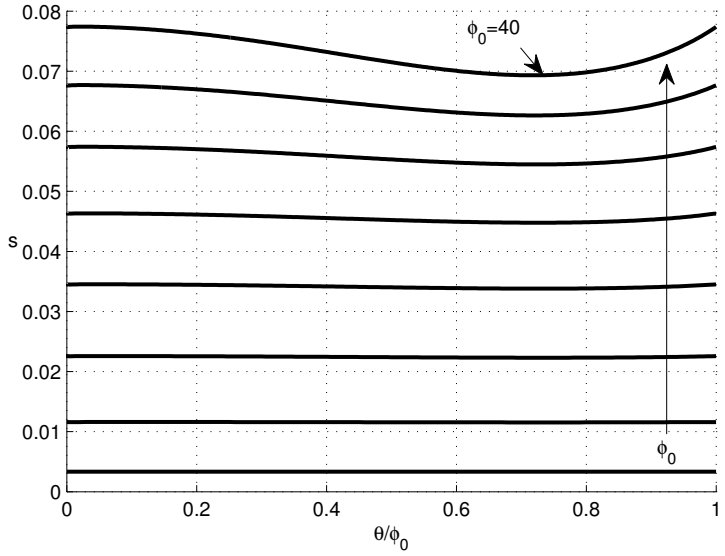

Figure 12. The flatness of the area under the load as defined in (44) as a function of the normalized angle θ/ϕ_0. Each curve corresponds to a different contact angle ranging from $\phi_0 = 5^\circ$ to 40° in 5° increments.

Comparing the maximum displacements $U_z(0)$ with $U_z^H(0)$ does not tell us anything about the shape of the contact area for a sphere loaded by a Hertzian-type load. Hertz contact theory states that the contact area between two identical spheres is flat, and thus we can describe it using $R(\cos\theta - \cos\phi_0)$. Therefore we define a function $s(\theta)$ to determine how close is our calculated displacement to the Hertzian solution as

$$s(\theta) = kU_z(\theta) - (\cos\theta - \cos\phi_0), \tag{43}$$

where k is a constant determined by enforcing $s(0) = s(\phi_0)$, which results in

$$s(\theta) = \frac{U_z(\theta)}{U_z(0) - U_z(\phi_0)}(1 - \cos\phi_0) - (\cos\theta - \cos\phi_0). \tag{44}$$

The function $s(\theta)$ is plotted in Figure 12 for several angles ϕ_0. These results show that the contact area is flat for small contact angles, but gains curvature for larger angles. According to Hertz theory, for small contact angles ϕ_0, the function $s(\theta)$ behaves as a constant $s(\theta) \approx \phi_0^2/2$. The angles shown in Figure 12 are too large to see this behavior, however, at $\phi_0 = 5^\circ$ the values are close with $s(\theta) = 0.00334$ and $\phi_0^2/2 = 0.00381$.

5. Conclusions

A compact Green's function for a sphere is presented which uses the fundamental idea of expressing a slowly convergent series with analytical functions and a quickly convergent series. The increased speed of convergence is demonstrated for the point force solution, which is also shown to be consistent with the more general distributed loading in the limit as the contact angle approaches zero. Since the general Green's function contains elliptical integrals, an easy method for dealing with the singularity in the

integrand is presented. Comparing the exact displacement due to a Hertzian-type distributed load to the displacement given by Hertz contact theory we conclude that Hertz contact theory gives accurate results for contact angles up to about ten degrees, with a steadily increasing error. For larger contact angles, Hertz theory overestimates the displacements and cannot account for the shape of the contact area. This is to say that the stress distribution assumed in Hertz theory results in a curved contact surface for larger contact angles.

Appendix A: Legendre polynomial formulas

The orthogonality and completeness relations for the Legendre functions are

$$\frac{1}{2}(2n+1)\int_0^\pi P_m(\cos\theta)\,P_n(\cos\theta)\sin\theta\,d\theta = \delta_{mn}, \tag{45a}$$

$$\sum_{n=0}^{\infty}\frac{1}{2}(2n+1)\,P_n(\cos\theta)\,P_n(\cos\phi) = \frac{\delta(\theta-\phi)}{\sin\phi}, \tag{45b}$$

Starting with the definition for $P_n(x)$,

$$P_n(\cos\theta) = \frac{1}{\pi}\int_0^\pi (\cos\theta + i\sin\theta\cos\alpha)^n\,d\alpha, \tag{46}$$

and using $\displaystyle\sum_{n=0}^{\infty} z^n = \frac{1}{1-z}$, $|z|<1$, the well-known generating function follows:

$$\sum_{n=0}^{\infty} t^n P_n(\cos\theta) = \frac{1}{\sqrt{1+t^2-2t\cos\theta}}, \quad |t|\le 1. \tag{47}$$

Integrating the identity (47) with respect to t implies

$$\begin{aligned}\sum_{n=0}^{\infty} t^{n+1}\frac{P_n(\cos\theta)}{n+1} &= \sinh^{-1}(\cot\theta) + \sinh^{-1}\Big(\frac{t-\cos\theta}{\sin\theta}\Big)\\ &= \log\Big(1+\csc\frac{\theta}{2}\Big) - \sinh^{-1}\Big(\tan\frac{\theta}{2}\Big) + \sinh^{-1}\Big(\frac{t-\cos\theta}{\sin\theta}\Big),\ |t|\le 1,\ 0\le\theta\le\pi.\end{aligned} \tag{48}$$

Taking the limit as $t\to 1$ yields (12a). $S_1(\theta)$ of (12b) follows from a similar result [Prudnikov et al. 1986, Equation 5.10.1.4], while $S_2(\theta)$ of (12c) follows from the recurrence relation

$$(n+1)P_{n+1}(x) - (2n+1)x\,P_n(x) + n\,P_{n-1}(x) = 0, \tag{49}$$

after dividing by n and summing from $n=1$ to ∞ (S_2 agrees with [Prudnikov et al. 1986, Equation 5.10.1.6]). The recurrence relation can be used to then find $S_j(\theta)$ for $j=3,4,\ldots$.

A series of products of Legendre functions is given by Equations 6.11.3.1 and 6.11.3.2 of [Brychkov 2008]:

$$\sum_{n=1}^{\infty} \frac{2n+1}{n(n+1)} P_n(x) P_n(y) = -1 - \log \frac{(1-x)(1+y)}{4}, \tag{50a}$$

$$\sum_{n=1}^{\infty} \frac{2n+1}{n^2(n+1)^2} P_n(x) P_n(y) = 1 - \log \frac{1+y}{2} \log \frac{(1-x)(1+y)}{4} + Li_2\Big(\frac{1+x}{2}\Big) - Li_2\Big(\frac{1+y}{2}\Big), \tag{50b}$$

for $-1 \le x < y \le 1$. Equation (50a) can be derived by operating on both sides by the Legendre differential operator

$$L_x = \frac{d}{dx}(1-x^2)\frac{d}{dx},$$

and using the eigenvalue property $L_x P_n(x) = -n(n+1) P_n(x)$ to arrive at (8b) (for $x < y$). At the same time, the constants in the right member of (50a) follow by considering the formula for $x = 0$, $y = 1$, in which case the sum on the left can be found. Equation (50a) gives $S_0(\theta, \phi) + S_1(\theta, \phi)$ by noting that

$$\frac{1}{n} + \frac{1}{n+1} = \frac{2n+1}{n(n+1)}.$$

The following is a simple consequence of Legendre's addition formula [Martin 2006, Equation 3.19]:

$$P_n(\cos\theta) P_n(\cos\phi) = \frac{1}{\pi} \int_0^{\pi} P_n(\cos\theta\cos\phi - \sin\theta\sin\phi\cos\alpha)\, d\alpha. \tag{51}$$

Multiplying both sides of (51) by t^n and summing implies, using (47), the identity [Prudnikov et al. 1986, Equation 5.10.2.1], for $|t| < 1$,

$$\sum_{n=0}^{\infty} t^n P_n(\cos\theta) P_n(\cos\phi) = \frac{4}{\pi(u_+ + u_-)} K\left(\frac{u_+ - u_-}{u_+ + u_-}\right), \quad u_\pm = \sqrt{1 - 2t\cos(\theta \pm \phi) + t^2}. \tag{52}$$

Appendix B: Analytical functions and their derivatives

We require the derivatives with respect to θ of the functions defined in (12). They are

$$\begin{aligned} \frac{dS_0(\theta)}{d\theta} &= \frac{\sin(\theta/2) - 1}{\sin\theta}, \\ \frac{dS_1(\theta)}{d\theta} &= -\frac{dS_0(\theta)}{d\theta} - \cot\frac{\theta}{2}, \\ \frac{dS_2(\theta)}{d\theta} &= \frac{dS_1(\theta)}{d\theta}\cos\theta - S_1(\theta)\sin\theta + \cos\frac{\theta}{2}\Big(2\sin\frac{\theta}{2} - 1\Big). \end{aligned} \tag{53}$$

Similarly, the analytical function used to find u_θ, (29), in Section 4 is

$$S_{01}(\theta, \phi) = S_0(\theta, \phi) + S_1(\theta, \phi) = \begin{cases} -2\log\sin\dfrac{\theta}{2}\cos\dfrac{\phi}{2}, & \theta > \phi, \\ -2\log\cos\dfrac{\theta}{2}\sin\dfrac{\phi}{2}, & \theta < \phi. \end{cases} \tag{54}$$

The derivative of $S_{01}(\theta, \phi)$ is

$$\frac{\partial S_{01}(\theta,\phi)}{\partial\theta} = \begin{cases} -\cot\theta/2, & \theta > \phi, \\ \tan\theta/2, & \theta < \phi. \end{cases} \tag{55}$$

References

[Abramowitz and Stegun 1964] M. Abramowitz and I. A. Stegun, *Handbook of mathematical functions with formulas, graphs, and mathematical tables*, National Bureau of Standards Applied Mathematics Series **55**, U.S. Government Printing Office, Washington, DC, 1964. Reprinted by Dover, New York, 1974.

[Bondareva 1969] V. Bondareva, "On the effect of an axisymmetric normal loading on an elastic sphere", *Prikl. Mat. Mekh.* **33**:6 (1969), 1029–1033. In Russian; translated in *J. Appl. Math. Mech.* **33**:6 (1969), 1001–1005.

[Bondareva 1971] V. Bondareva, "Contact problems for an elastic sphere", *Prikl. Mat. Mekh.* **35**:1 (1971), 61–70. In Russian; translated in *J. Appl. Math. Mech.* **35**:1 (1971), 37–45.

[Brychkov 2008] Y. A. Brychkov, *Handbook of special functions: derivatives, integrals, series and other formulas*, CRC Press, Boca Raton, FL, 2008.

[Guerrero and Turteltaub 1972] I. Guerrero and M. J. Turteltaub, "The elastic sphere under arbitrary concentrated surface loads", *J. Elasticity* **2**:1 (1972), 21–33.

[Hertz 1881] H. Hertz, "Ueber die Berührung fester elastischer Körper", *J. Reine Angew. Math.* **92** (1881), 156–171.

[Johnson 1985] K. L. Johnson, *Contact mechanics*, Cambridge University Press, Cambridge, 1985.

[Lur'e 1955] A. I. Lur'e, *Three-dimensional problems of the theory of elasticity*, Gostekhizdat, Moscow, 1955.

[Martin 2006] P. A. Martin, *Multiple scattering: interaction of time-harmonic waves with N obstacles*, Encyclopedia of Mathematics and its Applications **107**, Cambridge University Press, Cambridge, 2006.

[Prudnikov et al. 1986] A. P. Prudnikov, Y. A. Brychkov, O. I. Marichev, and N. M. Queen, *Integrals and series, 2: Special functions*, Gordon & Breach, New York, 1986.

[Sternberg and Rosenthal 1952] E. Sternberg and F. Rosenthal, "The elastic sphere under concentrated loads", *J. Appl. Mech.* (*ASME*) **19** (1952), 413–421.

[Villaggio 1996] P. Villaggio, "The rebound of an elastic sphere against a rigid wall", *J. Appl. Mech.* (*ASME*) **63**:2 (1996), 259–263.

[Zhupanska 2011] O. I. Zhupanska, "Contact problem for elastic spheres: applicability of the Hertz theory to non-small contact areas", *Int. J. Eng. Sci.* **49**:7 (2011), 576–588.

Received 18 Apr 2012. Revised 4 Aug 2012. Accepted 11 Aug 2012.

ALEXEY S. TITOVICH: alexey17@eden.rutgers.edu
Department of Mechanical and Aerospace Engineering, Rutgers University, 98 Brett Road, Piscataway, NJ 08854-8058, United States

ANDREW N. NORRIS: norris@rutgers.edu
Department of Mechanical and Aerospace Engineering, Rutgers University, 98 Brett Road, Piscataway, NJ 08854-8058, United States

JOURNAL OF MECHANICS OF MATERIALS AND STRUCTURES
Vol. 7, No. 7, 2012
dx.doi.org/10.2140/jomms.2012.7.721

msp

MULTI-HIT ARMOUR CHARACTERISATION OF METAL-COMPOSITE BI-LAYERS

KANDAN KARTHIKEYAN, BENJAMIN P. RUSSELL,
VIKRAM S. DESHPANDE AND NORMAN A. FLECK

The ballistic performance of equi-mass plates made from (i) stainless steel (SS); (ii) carbon fibre/epoxy (CF) laminate and (iii) a hybrid plate of both materials has been characterised for a spherical steel projectile. The hybrid plate was orientated with steel on the impact face (SSCF) and on the distal face (CFSS). The penetration velocity (V_{50}) was highest for the SS plate and lowest for the CF plate. A series of double impact tests were performed, with an initial velocity V_I and a subsequent velocity V_{II} at the same impact site. An interaction diagram in (V_I, V_{II}) space was constructed to delineate penetration from survival under both impacts. The degree of interaction between the two impact events was greater for the CFSS plate than for the SSCF plate, implying that the distal face has the major effect upon the degree of interaction.

1. Introduction

Composite materials are increasingly used in transportation and protection systems as they can give significant weight savings over their metallic counterparts. In a number of these applications there is a need for high impact resistance. For example, military vehicles are required to resist projectile impacts while in civilian aerospace applications the gas turbine (and airframe) needs to resist impacts from birds and other foreign objects. In most cases, the structure needs to be able to maintain its integrity under multiple impacts. The primary aim of this paper is to characterise the multi-impact ballistic performance of composite and metal/composite hybrid plates and to compare their performance with the reference case of a metallic plate of equal areal mass.

1.1. ***Ballistic damage characterisation.*** The residual strength of continuous fibre reinforced composite panels has been extensively investigated in the literature. A plethora of characterisation techniques assessing composite damage have been developed. All can be classified as either *visual techniques* or *residual performance tests*. Visual techniques include laser shearography [Hung 1982], X-ray tomography, thermography, digital image strain mapping, ultra-sound and both visual and electron microscopy. They are used to identify damage with a view to informing and validating computational modelling techniques. Residual performance tests are designed to ascertain the ability of a component to maintain function without necessarily developing an understanding of the mechanisms at play. Examples include post-impact compression tests (PICS) and tension after impact (TAI). Cantwell and Morton [1991], and Richardson and Wisheart [1996] have written reviews and detail these techniques for damage assessment. For example, Kazemahvazi et al. [2010] assessed the residual strength of composite panels with the TAI

Keywords: composite, damage, ballistic loading, multi-impact, bi-layers.

technique. While most studies focus on damage characterisation after a single impact, Appleby-Thomas et al. [2011] have recently investigated the damage mechanisms in carbon fibre composites subject to multiple impacts using both PICS and CT-scan techniques.

1.2. ***Hybridisation of materials.*** Polymer-matrix composites are increasingly used in light-weight transport due to their high specific strength and stiffness. However, their impact resistance is often inferior to their metallic counterparts. Recently, hybrid material systems, combining composite and metal, have been developed in order to combine high specific stiffness, strength and impact resistance. For example, Fibre Metal Laminates (FMLs) such as GLARE (Glass Laminate Aluminium Reinforced Epoxy) are finding application in the latest generation of commercial aircraft due to their superior performance under service and blast/impact loads [Vlot 1993; Young et al. 1994; Lambert 1995], when compared with equivalent mass metallic structures. The multi-impact performance of such hybrid panels has not been reported to-date.

1.3. ***Objectives of study.*** The objectives of this study are two-fold. First, this paper proposes a methodology to assess ballistic performance of plates under multi-hit. The focus here is restricted to two consecutive impacts at the same location although the scheme developed can be extended to more complex situations. Secondly, we use this methodology to assess the performance of metallic, composite and hybrid plates subject to projectile loadings.

2. Experimental protocol

Three types of clamped circular plates were impacted normally (zero obliquity) and centrally with spherical steel balls. The three plate types were (i) monolithic 304 stainless steel; (ii) 0–90° carbon fibre/epoxy laminate and (iii) a hybrid plate comprising a steel plate bonded to a carbon fibre/epoxy laminate. All had an areal mass of approximately $5.7\,\mathrm{kg\,m^{-2}}$. The aims of the experimental investigation were as follows.

(1) To develop a methodology to characterise ballistic performance of plates subjected to two impacts at the same location.

(2) To compare the ballistic performance of the three plate types for both a single impact as well as two impacts at the same location.

(3) To determine the sensitivity of the ballistic performance of the hybrid plates to the orientation of the plate; i.e., whether the impacted face is the steel or composite face of the plate.

2.1. ***Materials and manufacture.*** Square plates measuring $150\,\mathrm{mm} \times 150\,\mathrm{mm}$ were manufactured to the following specification:

(1) *Monolithic steel plates*: Cold-rolled 304 stainless steel plates of thickness 0.70 mm were water jet cut from as-received stainless steel sheets of the same thickness.

(2) *Monolithic composite plates*: The composite plates comprised 0–90° laminates with IM7-12k carbon fibres embedded within a HexPly® 8552 resin. Alternating 0° and 90° plies (each of thickness 0.25 mm) were stacked to construct a plate with lay-up $[(0°/90°)_7/0°]$, overall thickness 3.75 mm and density $1570\,\mathrm{kg\,m^{-3}}$. Large composite plates were manufactured via a standard lay-up and autoclaving procedure, and cut to the requisite size with a diamond saw.

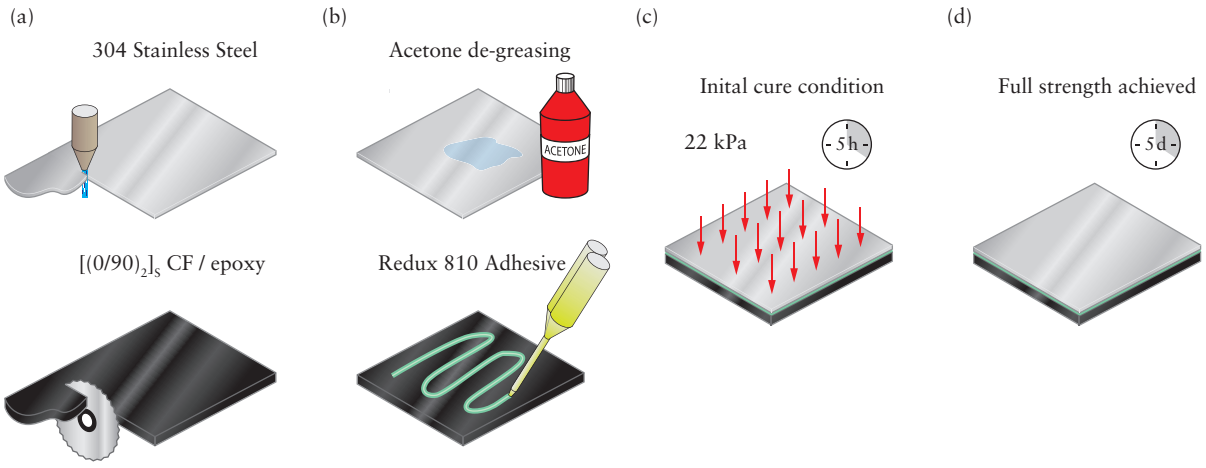

Figure 1. Manufacturing route for the hybrid bi-layer plates: (a) metal plates are cut to the required size by water jet and the composite plates cut by a diamond saw; (b) acetone is used to clean the metal surfaces before Redux 810 adhesive is applied to both the metal and composite surfaces; (c) over the initial 5 hours of the cure cycle, the specimen is held under pressure after which (d) the adhesive is allowed a further 5 days to harden to full strength.

(3) *Hybrid plates*: The hybrid plates comprised a 0.3 mm cold-rolled stainless steel plate bonded to a 2 mm thick composite plate with lay-up $[0°/90°]_4$, i.e., 60% by mass composite. The hybrid plates were manufactured as follows. The cold-rolled steel and cured composites plates (manufactured from the same materials and using the same procedure as for the monolithic composite plates) were bonded together with a chemical cure epoxy resin system, Redux 810[1] as shown schematically in Figure 1. First the bonding surfaces were cleaned thoroughly and then the epoxy applied to both surfaces. Both these surfaces were then bonded under a pressure of 22 kPa for a period of 5 hours. This procedure ensured a thin bond thickness and eliminated air gaps. The plates were allowed to cure for a further 120 hours to achieve full strength before testing. Note that the use of a room temperature chemically curing adhesive ensured that we minimised the build up of interfacial stresses due to the differences in thermal expansion coefficients between the two materials.

Table 1 presents the geometric details of all the plates used in this study along with the designations by which each of these plates will be referred to subsequently. Note that the hybrid plates are used in two configurations: (i) SSCF where the stainless steel (SS) surface is the impacted face while the carbon fibre (CF) plate is the rear surface and (ii) CFSS where the CF plate is the impacted face.

2.2. ***Material properties.*** The quasi-static uniaxial compressive and tensile responses of the carbon fibre laminates with lay-up $[(0°/90°)_7/0°]$, was measured at an applied nominal strain rate $10^{-3}\,s^{-1}$ using the procedure detailed in [Russell et al. 2008]. In brief, dogbone-shaped specimens were cut from the composite sheets. The tensile responses in the 0–90° and ±45° orientation (where the angles refer to the angles between the fibre direction and the loading axis) were measured by friction gripping of

[1]Manufactured by Hexcel Composites.

Designation	Thickness, t (mm)	Impact Face	Distal Face	Areal mass (kg m^{-2})
SS	0.71	304 Stainless steel		5.55
CF	3.75	CF/epoxy $[(0°/90°)_7/0°]$		5.85
SSCF	0.3 / 2	304 Stainless steel	CF/epoxy $[0°/90°]_4$	5.65*
CFSS	2 / 0.3	CF/epoxy $[0°/90°]_4$	304 Stainless steel	5.65*

*Inclusive of adhesive layer (0.19 kg m^{-2})

Table 1. Materials and geometry of the four plate configurations investigated here.

these specimens and then conducting tensile tests in a screw-driven test machine. The applied load was measured via the load cell of the test machine and was used to define the applied stress while a $0/90°$ strain gauge rosette was used to measure the axial and transverse strain components. In order to perform compression tests that do not lead to premature failure by Euler buckling of the specimens, a sandwich column comprising an aluminium hexagonal honeycomb core and the face sheets made from the test composite material were constructed. The compression tests were also performed in the screw driven test machine with the loads and strain measured in a similar manner to that described for the tensile tests. Tensile tests on the 0.3 mm thick 304 stainless steel sheets were also conducted on dogbone-shaped specimens in a manner similar to the composite specimens. One key difference in the experimental methodology is that due to the larger strains in the stainless steel, a laser extensometer rather than strain gauges was used to measure strain in the tensile tests on the stainless steel.

The measured tensile responses of the 0–90° and ±45° CFRP laminates is plotted in Figure 2, left. While the 0–90° is elastic-brittle with a tensile strength of about 1 GPa, the ±45° has a non-linear response that can be approximated as elastic perfectly plastic with a yield strength of about 80 MPa and a tensile

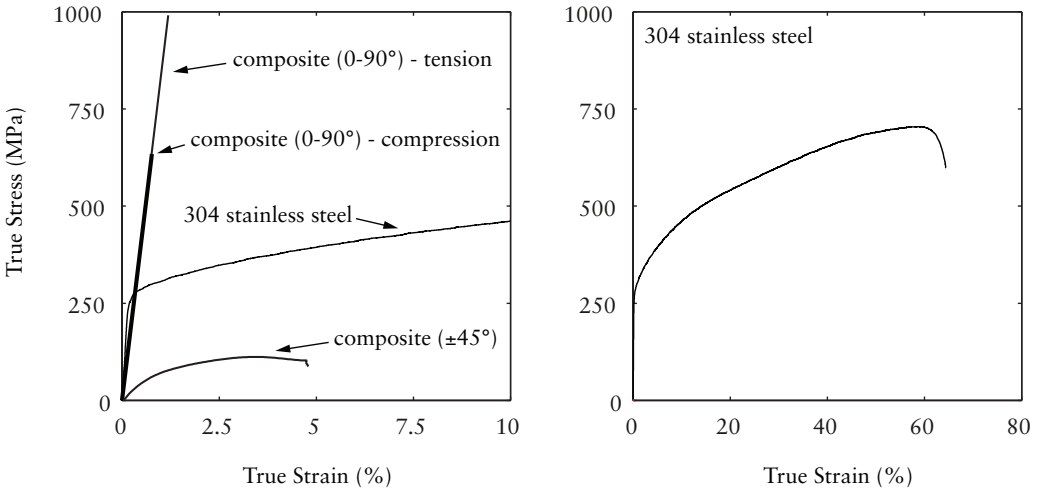

Figure 2. Left: the measured tensile and compressive stress versus strain responses of the materials used in the plate construction. Right: the full tensile stress versus strain response of the stainless steel beyond the onset of necking.

ductility of 5%. This difference is due to the fact that while the 0–90° laminate response of governed by the tensile response of the 0° carbon fibres the response of the ±45° laminate is governed by the shear response of the matrix. The compressive strength of the laminate is approximately 630 MPa and set by the micro-buckling strength of the 0° plies. The 304 stainless steel has an elastic-plastic response with approximately linear work hardening after initial yield. It has a significantly higher ductility compared to the CFRP with a true necking strain of about 60% (Figure 2, right).

2.3. ***Ballistic measurement set-up and test methodology.*** A schematic of the experimental set-up is shown in Figure 3. A gas-gun with a barrel length of 4.5 m and a bore of diameter 13 mm was used to accelerate steel spheres of diameter 12.7 mm and mass $M = 8.3 \times 10^{-3}$ kg at velocities V_0 ranging 25 ms^{-1} to 210 ms^{-1}. These projectiles impacted the test plates normally and centrally. A set of laser gates situated at the end of the barrel were used to measure the velocity of the projectile as it exits the barrel and prior to impact. The test plates were clamped between two annular steel plates of inner diameter 100 mm. Twelve equi-spaced holes of 6 mm diameter were drilled through the test plates on a pitch radius 62.5 mm, such that the specimens could be sandwiched been the clamping rings to ensure a clamped boundary condition. High speed photography was used to observe the impacted face of the plates during the experiments. A grid pattern was marked onto the face to clarify the deformation resultant from

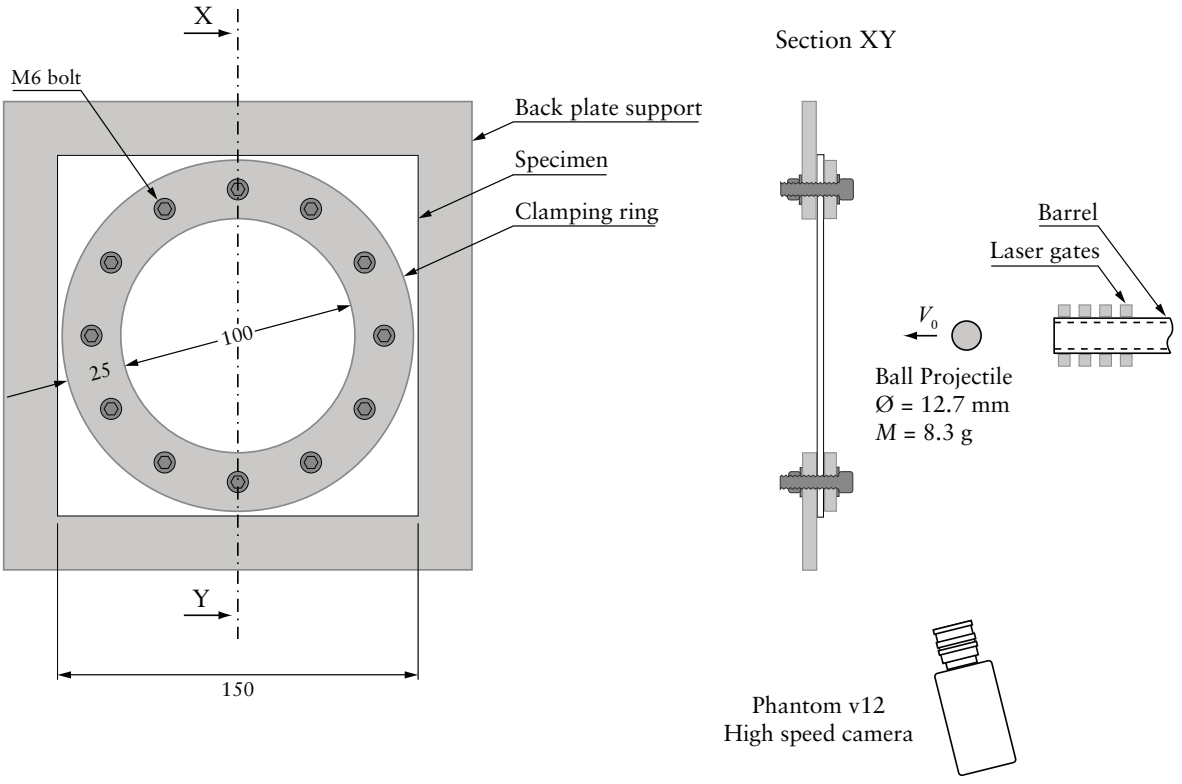

Figure 3. Left: plan view of the plate test fixture showing the plate geometry and the clamping arrangement. Right: a side view of the test set-up showing the showing end of the barrel of the gas gun and the clamped plate. All dimensions are in mm.

the impact. A Phantom V12 Camera[2] was used to visualise the dynamic deformation with an inter-frame time of 15 μs and an exposure time of 1 μs. In some cases the camera was used to view the impacted surface so as to be able to measure the rebound velocity of the projectile while in other cases the camera viewed the distal surface in order to visualise the dynamic deformation of the rear of the plate and the penetration of the projectile.

For each plate configuration, there exists a limiting projectile velocity V_L at which the plate is on the cusp of failure, i.e., a fractional increase in the impact velocity V_0 will result in the penetration of the plate. This limiting velocity was determined to an accuracy of 1–5 ms^{-1} by performing a series of tests at impact velocities V_0 in the vicinity of V_L. In the case of the stainless steel plates, the failure/penetration of the plates was clearly seen after the test. However, in the case of the composite specimens, there was a large degree of spring-back resulting in closure of the hole created by the penetrated projected. This could result in an erroneous conclusion that the plate had survived the impact event, if the judgement was made by inspection of the plate after the test. Further, the high degree of spallation from the back of the composite plates also made it difficult to judge via high speed photography whether the projectile had penetrated the composite plates. Thus, a corrugated cardboard "witness" plate was placed 20 cm behind the composite plate: penetration of this witness plate by the projectile is clearly seen after the impact event and was used to confirm the penetration of the composite plates.

2.4. ***Ballistic characterisation technique.*** The ballistic performance of the targets is characterised via two metrics in this study:

(1) The *ballistic limit* V_L. It denotes the critical velocity at which a given projectile just penetrates the target, and is often referred to as V_{50} in the literature.

(2) A *limit surface* in velocity space, to delineate penetration from survival due to an initial velocity V_I and a subsequent velocity V_{II}. Both impacts on the plate occur normally and centrally. A series of double impact tests, with an initial velocity V_I and a subsequent velocity V_{II} at the same impact site allow for the construction of an interaction diagram in (V_I, V_{II}) space.

The limit surface in V_I-V_{II} space is depicted in Figure 4, left. The interpretation of this limit surface is as follows. For any combination of V_I and V_{II} that lies inside this limit surface, the projectile does not penetrate the target after the second impact while the target is penetrated if the combination of these velocities lies on or outside this limit surface. By definition, when $V_I = V_L$, $V_{II} = 0$ and conversely $V_{II} = V_L$ when $V_I = 0$. The form of the limit surface at intermediate values of V_I and V_{II} depends strongly upon the material properties of the target. For example, we anticipate that an elastic-brittle target will undergo negligible damage for impacts at a velocity less than V_L resulting in no interaction between V_I and V_{II}. Thus, the limit surface for an elastic-brittle target is expected to be square such that $\max(V_I, V_{II}) = V_L$ as depicted in Figure 4, right: this square surface represents an 'upper bound' for the limit surface. On the other hand, a more ductile target that undergoes progressive damage will have significant interaction between V_I and V_{II} resulting in a limit surface that lies inside the square limit surface of the elastic-brittle target; see Figure 4, right. In this study we shall determine the forms of these limit surfaces of the 4 plate configurations detailed in Section 3.

[2]Vision Research, 100 Dey Rd. Wayne, NJ 07470, USA

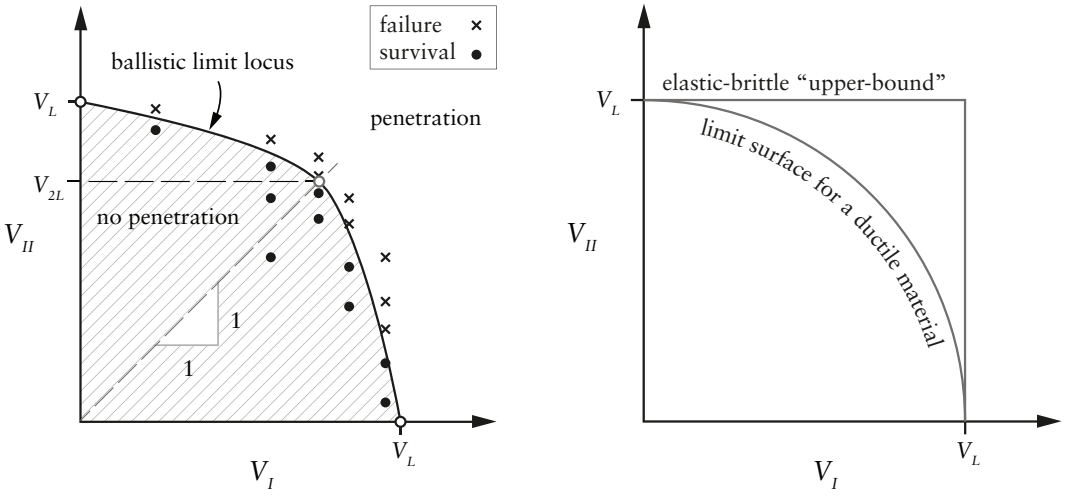

Figure 4. Left: sketch illustrating the measurement of the ballistic limit surface in V_I-V_{II} space. For a given $V_I < V_L$ tests are done for increasing values of V_{II} to locate the limiting penetration velocity as indicated by the circles and crosses. The definition of the equivelocity penetration limit V_{2L} is also included. Rigth: sketch of the upper bound ballistic limit surface defined by $\max(V_I, V_{II}) = V_L$ for an elastic-brittle material. An illustrative limit surface for a more ductile material is also included.

In addition to the ballistic limit surfaces in V_I-V_{II} space we will also report the performance of the plates in terms of two additional metrics:

(1) The *rebound velocity* V_R: The rebound velocity of the steel ball for first impacts at a velocity $V_I < V_L$ was measured via high speed photography. We report this rebound velocity in terms of a co-efficient of restitution $e \equiv -V_R/V_I$, where e is a positive number as V_R and V_I have opposite signs.

(2) The *equivelocity ballistic limit* V_{2L}: The limit surfaces in V_I-V_{II} space provide a detailed view of the double impact ballistic performance of the plates. It is useful to define a simple scalar measure that quantifies this double hit ballistic performance. The equivelocity ballistic limit V_{2L} is the penetration velocity along the trajectory $V_I = V_{II}$; see Figure 4, left. We report it in the normalised form $\bar{V}_{2L} \equiv V_{2L}/V_L$ in order to quantify the reduction in the penetration velocity over the single hit ballistic limit V_L.

3. Ballistic performance of plates

The measured ballistic limit surfaces of the four types of plates investigated here are plotted in Figure 5 with the first impact velocity V_I plotted in the x-axis and the second impact velocity V_{II} plotted on the y-axis. Data points corresponding to no penetration (marked by circles) and penetration (marked by crosses) are plotted in Figure 5 while the ballistic limit boundary in V_I-V_{II} is space sketched by interpolating between the circles and the crosses. Figure 6 shows these same limit surfaces plotted together. We shall first describe the key measurements and then proceed to discuss the observed penetration mechanisms.

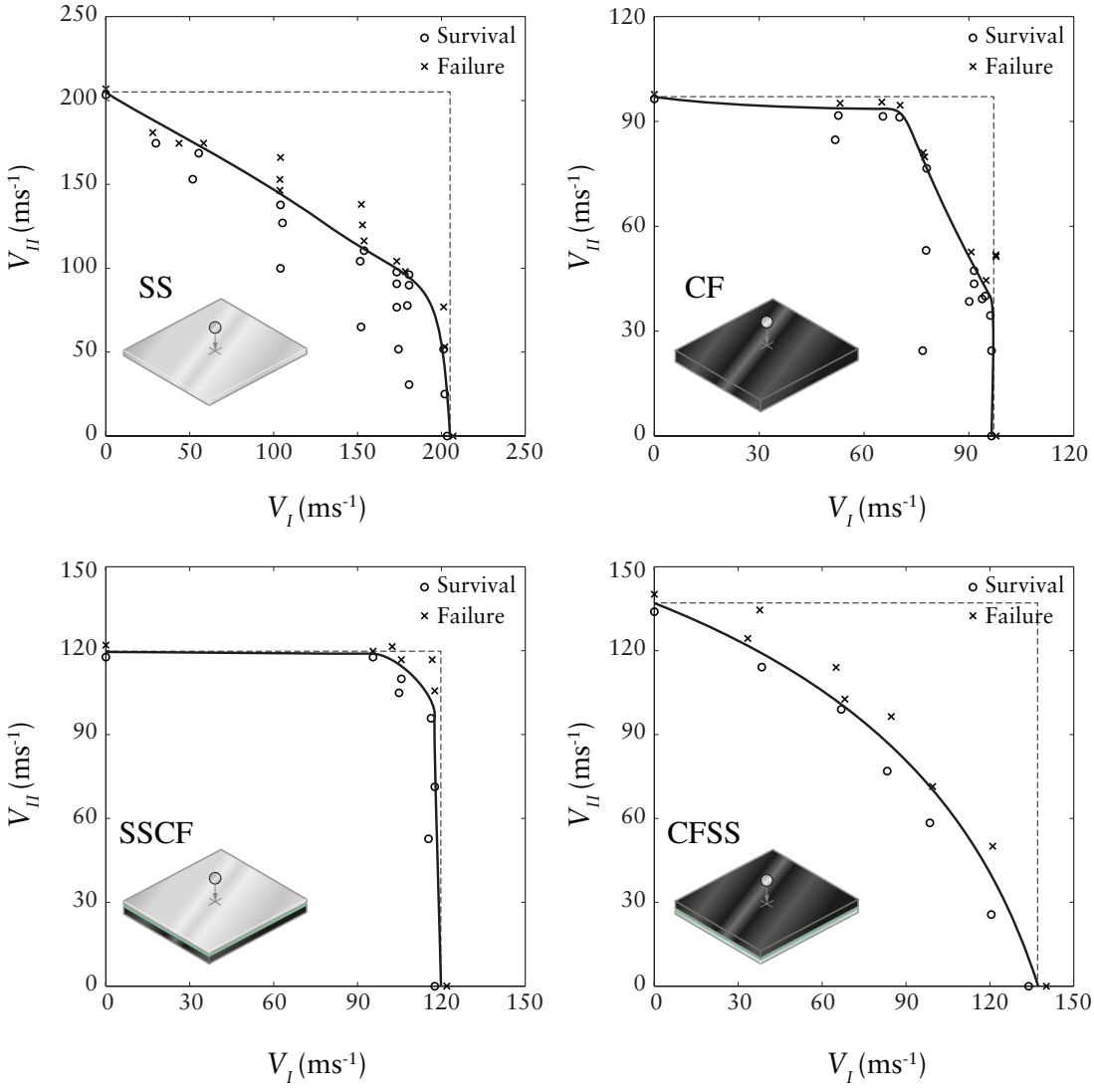

Figure 5. The measured ballistic limit surfaces in V_I-V_{II} space for monolithic stainless steel (SS), monolithic carbon fibre/epoxy (CF), steel fronted hybrid (SSCF), and composite fronted hybrid (CFSS). The crosses mark experiments corresponding to penetration while the circles are experiments where the plates survived. The "upper-bound" limit surface is sketched in via a dashed line in each case.

Single hit performance: For the given areal mass and projectile the ballistic limit V_L or V_{50} increases in the following order: (i) carbon fibre plates (CF); (ii) hybrid plate with steel front (SSCF); (iii) hybrid plate with carbon fibre front (CFSS) and (iv) monolithic steel plate (SS); see Figure 7.

The ballistic limit surfaces: The measured limit surfaces in Figure 6, left, show the comparative performance of all plates. The CF plate and both hybrid plates lie nested within the no penetration region of the SS plate. The hybrid plates display an interesting regime where the multi-hit performance

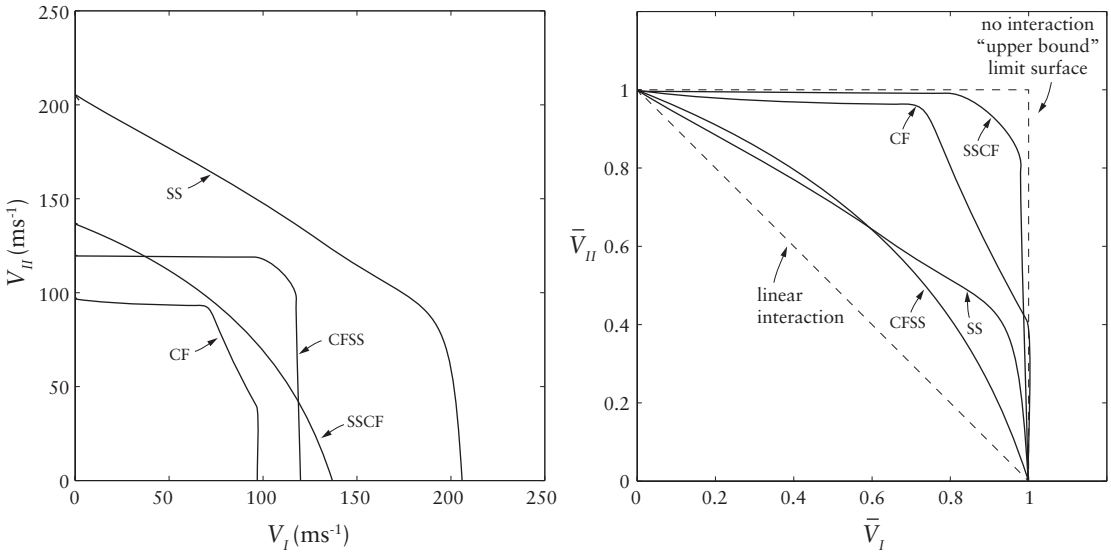

Figure 6. Ballistic limit surfaces for all plates in V_I-V_{II} space (left) and $\overline{V}_I$-$\overline{V}_{II}$ space (right).

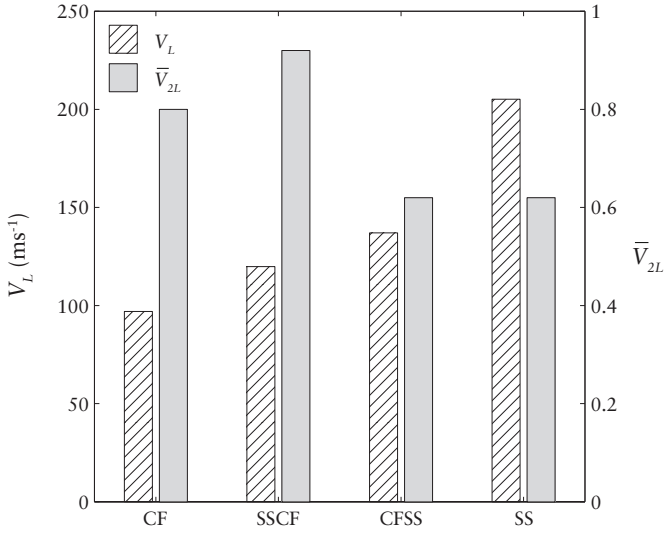

Figure 7. Bar chart plotting the measured ballistic limit (V_L or V_{50}) and the normalised equivelocity ballistic limit ($\bar{V}_{2L}$) for the four plate configurations investigated here.

of the SSCF give superior performance where $V_I \approx V_{II}$, and the CFSS plate superior at the extremes where $V_I \ll V_{II}$ and $V_{II} \ll V_I$. The normalised limit surfaces in Figure 6, right, indicate that the ballistic limits of the monolithic steel (SS) and carbon fronted hybrid plate (CFSS) degrades due to a first impact at a velocity $\overline{V}_I < 1$ with the measured limit surface lying well within the "upper bound limit surface" described by $\max(\overline{V}_I, \overline{V}_{II}) = 1$ and sketched by the dashed lines in Figure 6, right. On the other hand, the ballistic limit the carbon fibre plates (CF) and the steel front hybrid plates (SSCF) indicate that there is little interaction between the two impacts for these plates with the measured limit surfaces are close

to the "upper bound". A lower limit — the linear interaction dashed line — is the maximum interaction of the two impacts assuming that the ballistic limit surface is convex.

The equivelocity ballistic limit: The normalised equivelocity ballistic limit $\bar{V}_{2L}$ for the four plates investigated here are included in the bar chart in Figure 7. Both the SS and CFSS plates have approximately a 40% reduction in their penetration velocities due to the first impact with $\bar{V}_{2L} = 0.62$. The reductions in the penetration velocities of the SSCF and CF plates is much less with $\bar{V}_{2L} = 0.92$ and 0.8, respectively.

3.1. ***Discussion on the penetration mechanisms.*** Photographs of the front and back surfaces of the penetrated plates are included in Figure 8 for the SS and CF plates and in Figure 9 for the CFSS and SSCF plates. These failed specimens were penetrated after two impacts such that $V_I = V_{II} = V_{2L}$. Penetration of the monolithic steel plate occurs by ductile tearing around periphery of a circle whose diameter is approximately equal to the diameter of the projectile as seen in Figures 8a and 8b. By contrast, the

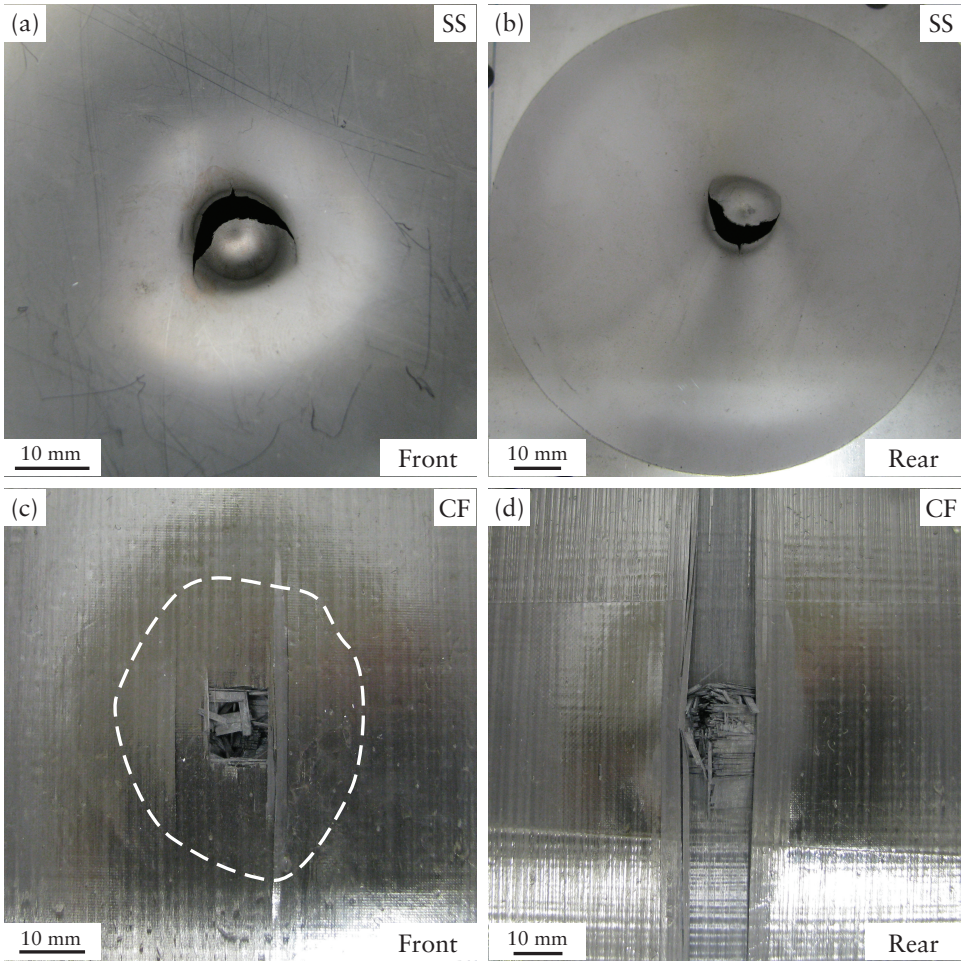

Figure 8. Post-test images of the steel (SS) and carbon fibre/epoxy (CF) plates impacted at velocities $V_I = V_{II} = V_{2L}$. The front and rear faces of the SS plate are shown in (a) and (b), while (c) and (d) show images of the front and rear of the CF plate.

carbon fibre plate fails by fibre breakage of both the 0° and 90° fibres resulting in the square holes seen in Figure 8c. Also, a strip of a single ply delaminates and is removed by the exiting projectile on the rear surface of the CF plate; see Figure 8d. Clearly, the failure mechanism of the steel plate is ductile while the carbon fibre plate fails in a quasi-brittle mode.

In order to quantify the degree of inelasticity involved in the impact of the steel projectile against these plates we plot in Figure 10 the effective co-efficient of restitution e as a function of the normalised impact velocity $\bar{V}_I \equiv V_I / V_L$. The rebound of the projectile off the composite plate is shown via a series of high speed photographs, for an impact velocity $\bar{V}_I = 0.77$. Time $t = 0$ in these images corresponds to the instant of impact and hence we have shown images with both negative t (i.e., before impact with the projectile approaching the plate) and positive t corresponding to the time when the projectile has

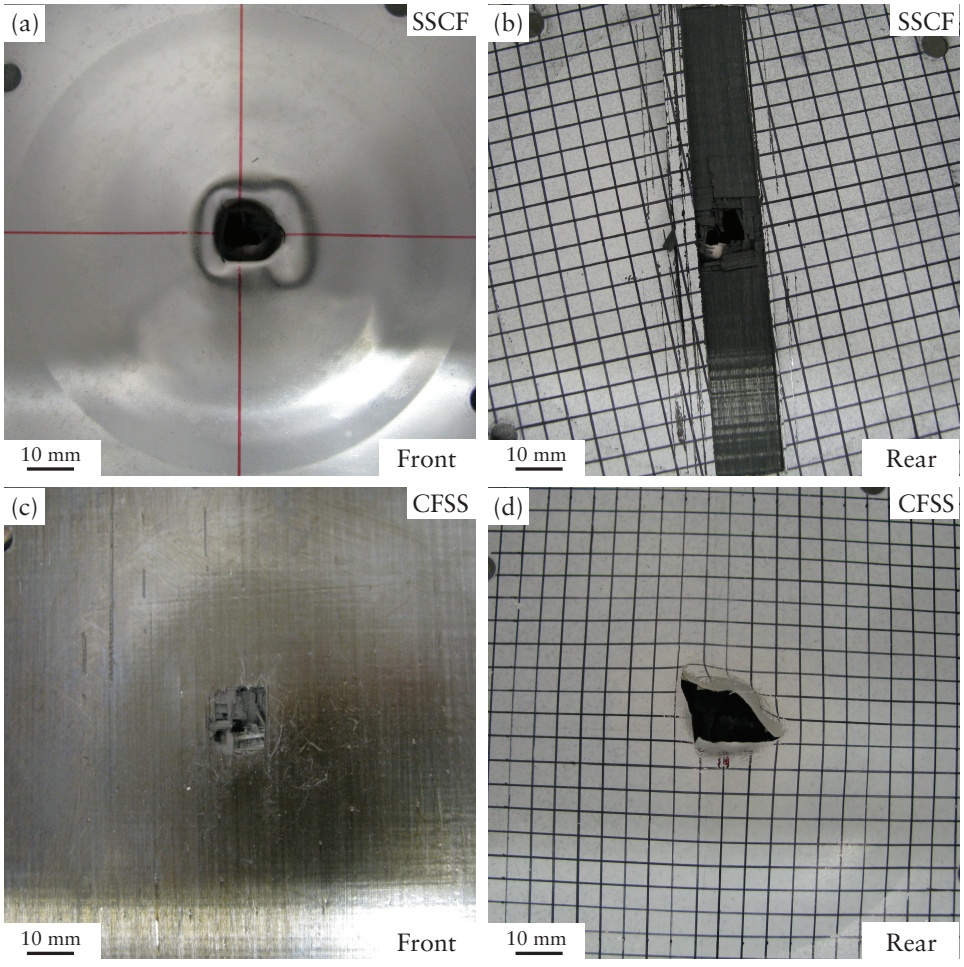

Figure 9. Post-test images of the steel fronted hybrid (SSCF) and carbon fibre/epoxy front hybrid (CFSS) plates impacted at velocities $V_I = V_{II} = V_{2L}$. The front and rear faces of the SSCF plate are shown in (a) and (b), while (c) and (d) show images of the front and rear of the CFSS plate.

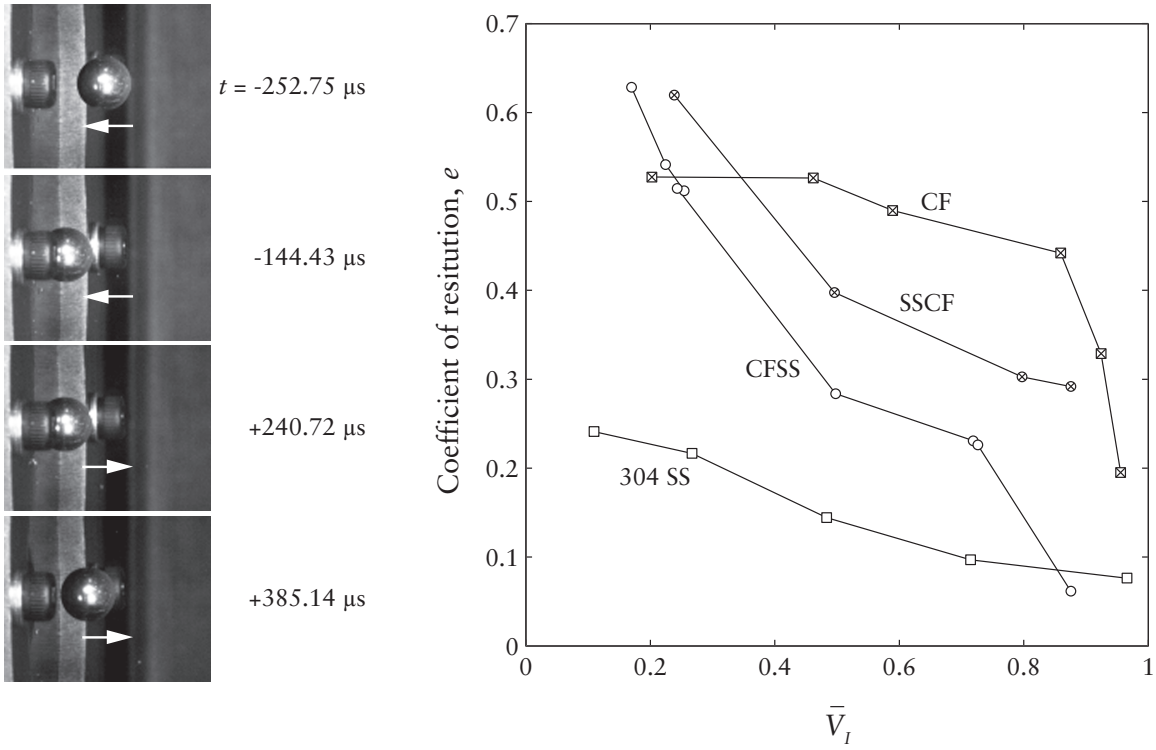

Figure 10. Left: high-speed photographs showing the rebound of the projectile impacting the carbon fibre/epoxy (CF) plate at $\bar{V}_I = 0.77$. In these images time $t = 0$ corresponds to the instant of impact. Right: measured effective co-efficient of restitution e of the projectile as a function of the normalised impact velocity $\bar{V}_I$ for the four plate configurations investigated here.

rebounded off the plate. The measured co-efficient of restitution plotted in Figure 10, right, decreases from approximately 0.25 to less than 0.1 for the steel plate as the impact velocity increases from about $\bar{V}_I = 0.1$ to the ballistic limit, i.e., the impacts can be viewed as significantly inelastic. By contrast, $e \approx 0.5$ at low values of $\bar{V}_I$ for the carbon fibre plates but decreases as V_I approaches the ballistic limit when we anticipate significant inelastic processes to occur in the impacted carbon fibre plate. We note in passing that the hardened steel projectiles (which are ball bearings) undergo negligible plastic deformation in any of the impacts investigated here. Thus, e can be directly related to the energy absorbed ΔE by the target plate via the relation

$$\Delta E = \tfrac{1}{2} M V_I^2 (1 - e^2), \tag{1}$$

where M is the mass the projectile.

Photographs of the failed SSCF and CFSS hybrid plates are shown in Figure 9. There is clear ductile deformation of the rear steel plate with brittle failure of the front carbon plate for the CFSS plate as seen in Figures 9c and 9d, respectively. However, in the case of the SSCF plate the stiff rear carbon plate prevents ductile deformation of the front steel plate. This results in a plugging type failure of the front

steel plate followed by the usual brittle failure of the carbon rear plate. We thus anticipate that overall deformation/failure processes in the SSCF plates involve significantly less inelastic processes compared to the CFSS plates. This is borne out further by two observations:

(1) The co-efficient of restitution plotted in Figure 10 is higher for the SSCF plates compared to the CFSS plates.

(2) The ballistic limit surface of the SSCF plate (Figure 5) shows that there is little interaction between V_I and V_{II} resulting in a failure surface that is well approximated by "upper bound" $\max(V_I, V_{II}) = V_L$. By contrast, in the CFSS plates, the initial impact results in a significant reduction in the ballistic limit for the second impact and the ballistic failure surface lies well inside the upper bound; see Figure 5, bottom right.

4. Concluding remarks

The ballistic performance of three types of plates, all with the same areal mass was investigated for both single and two impacts at the same location by a steel ball bearing of diameter 12.7 mm. The three types of plates were (i) monolithic stainless steel; (ii) monolithic carbon fibre/epoxy (CFRP) laminates with equal number of 0° and 90° plies and (iii) a hybrid laminate plate comprising a stainless steel plate glued on to a 0°/90° carbon fibre plate. This hybrid plate had 60% by mass CFRP. The hybrid plates were tested in two orientations: the steel facing on the impact side and vice versa.

The single impact ballistic resistance was characterised in terms of the usual metric: the V_{50}, defined as the limiting projectile velocity at which the plate is just penetrated. In terms of the V_{50}, the ballistic limit is the highest for the stainless steel plate, followed by the hybrid plate with the CFRP on the impacted side. The ballistic limit of the same hybrid plate is slightly lower when the stainless steel is on the impacted side. Monolithic CFRP has the lowest ballistic limit. The double impact ballistic performance was characterised by measuring the ballistic limit surfaces that give the limiting velocity V_{II} required to penetrate the plate after an initial impact at a velocity $V_I < V_{50}$. While the steel plate has the highest ballistic limit, it undergoes significant damage after an initial impact which means that the second hit ballistic limit V_{II} decreases significantly with increasing V_I. The same is true for the hybrid plate with the steel on the rear face as the steel delaminates from the CFRP and responds independently. By contrast, the ballistic performance of the monolithic CFRP plate and the hybrid plate with steel on the impacted face is not significantly affected by the initial impact as the CFRP responds in an elastic-brittle manner; i.e., it either breaks and allows the projectile to penetrate or responds elastically which results in the projectile rebounding off the plate.

This study has demonstrated that while the ballistic performance of CFRP plates is lower than that of a steel plate on an equal mass basis, CFRP and CFRP hybrid plates might be considered for ballistic applications especially if the application requires the plate to withstand multiple impacts. The study has also demonstrated the sensitivity of the ballistic performance to the orientation of the hybrid plates, viz. while the ballistic limit surface of the hybrid plate with CFRP facing the impact is qualitatively similar to the steel plate, the hybrid plate with steel on the impacted surface behaves more like the monolithic CFRP plate.

Acknowledgements

The authors are grateful for financial support from the US Office of Naval Research (contract N62909-10-1-7122). Dr B. P. Russell was supported by a Ministry of Defence / Royal Academy of Engineering Research Fellowship.

References

[Appleby-Thomas et al. 2011] G. J. Appleby-Thomas, P. J. Hazell, and G. Dahini, "On the response of two commercially-important CFRP structures to multiple ice impacts", *Compos. Struct.* **93**:10 (2011), 2619–2627.

[Cantwell and Morton 1991] W. Cantwell and J. Morton, "The impact resistance of composite materials: a review", *Composites* **22**:5 (1991), 347–362.

[Hung 1982] Y. Hung, "Shearography: a new optical method for strain-measurement and non-destructive testing", *Opt. Eng.* **21**:3 (1982), 391–395.

[Kazemahvazi et al. 2010] S. Kazemahvazi, J. Kiele, and D. Zenkert, "Tensile strength of UD-composite laminates with multiple holes", *Compos. Sci. Technol.* **70**:8 (2010), 1280–1287.

[Lambert 1995] M. Lambert, "Shielding against space debris. A comparison between different shields: the effect of materials on their performances", *Int. J. Impact Eng.* **17**:4–6 (1995), 477–485.

[Richardson and Wisheart 1996] M. Richardson and M. Wisheart, "Review of low-velocity impact properties of composite materials", *Compos. A Appl. Sci. Manuf.* **27**:12 (1996), 1123–1131.

[Russell et al. 2008] B. P. Russell, V. S. Deshpande, and H. N. G. Wadley, "Quasistatic deformation and failure modes of composite square honeycombs", *J. Mech. Mater. Struct.* **3**:7 (2008), 1315–1340.

[Vlot 1993] A. Vlot, "Impact properties of fibre metal laminates", *Compos. Eng.* **3**:10 (1993), 911–927.

[Young et al. 1994] J. B. Young, J. G. N. Landry, and V. N. Cavoulacos, "Crack growth and residual strength characteristics of two grades of glass-reinforced aluminium glare", *Compos. Struct.* **27**:4 (1994), 457–469.

Received 7 Aug 2012. Accepted 4 Oct 2012.

KANDAN KARTHIKEYAN: kk412@cam.ac.uk
Department of Engineering, Cambridge University, Cambridge, CB2 1PZ, United Kingdom

BENJAMIN P. RUSSELL: bpr23@cam.ac.uk
Department of Engineering, Cambridge University, Cambridge, CB2 1PZ, United Kingdom

VIKRAM S. DESHPANDE: vsd20@cam.ac.uk
Department of Engineering, Cambridge University, Cambridge, CB2 1PZ, United Kingdom

NORMAN A. FLECK: naf1@cam.ac.uk
Department of Engineering, Cambridge University, Cambridge, CB2 1PZ, United Kingdom

SUBMISSION GUIDELINES

ORIGINALITY

Authors may submit manuscripts in PDF format online at the Submissions page. Submission of a manuscript acknowledges that the manuscript is original and has neither previously, nor simultaneously, in whole or in part, been submitted elsewhere. Information regarding the preparation of manuscripts is provided below. Correspondence by email is requested for convenience and speed. For further information, write to one of the Chief Editors:

Davide Bigoni	bigoni@ing.unitn.it
Iwona Jasiuk	ijasiuk@me.concordia.ca
Yasuhide Shindo	shindo@material.tohoku.ac.jp

LANGUAGE

Manuscripts must be in English. A brief abstract of about 150 words or less must be included. The abstract should be self-contained and not make any reference to the bibliography. Also required are keywords and subject classification for the article, and, for each author, postal address, affiliation (if appropriate), and email address if available. A home-page URL is optional.

FORMAT

Authors can use their preferred manuscript-preparation software, including for example Microsoft Word or any variant of TEX. The journal itself is produced in LATEX, so accepted articles prepared using other software will be converted to LATEX at production time. Authors wishing to prepare their document in LATEX can follow the example file at www.jomms.net (but the use of other class files is acceptable). At submission time only a PDF file is required. After acceptance, authors must submit all source material (see especially Figures below).

REFERENCES

Bibliographical references should be complete, including article titles and page ranges. All references in the bibliography should be cited in the text. The use of BibTEX is preferred but not required. Tags will be converted to the house format (see a current issue for examples); however, for submission you may use the format of your choice. Links will be provided to all literature with known web locations; authors can supply their own links in addition to those provided by the editorial process.

FIGURES

Figures must be of publication quality. After acceptance, you will need to submit the original source files in vector format for all diagrams and graphs in your manuscript: vector EPS or vector PDF files are the most useful. (EPS stands for Encapsulated PostScript.)

Most drawing and graphing packages—Mathematica, Adobe Illustrator, Corel Draw, MATLAB, etc.—allow the user to save files in one of these formats. Make sure that what you're saving is vector graphics and not a bitmap. If you need help, please write to graphics@msp.org with as many details as you can about how your graphics were generated.

Please also include the original data for any plots. This is particularly important if you are unable to save Excel-generated plots in vector format. Saving them as bitmaps is not useful; please send the Excel (.xls) spreadsheets instead. Bundle your figure files into a single archive (using zip, tar, rar or other format of your choice) and upload on the link you been given at acceptance time.

Each figure should be captioned and numbered so that it can float. Small figures occupying no more than three lines of vertical space can be kept in the text ("the curve looks like this:"). It is acceptable to submit a manuscript with all figures at the end, if their placement is specified in the text by means of comments such as "Place Figure 1 here". The same considerations apply to tables.

WHITE SPACE

Forced line breaks or page breaks should not be inserted in the document. There is no point in your trying to optimize line and page breaks in the original manuscript. The manuscript will be reformatted to use the journal's preferred fonts and layout.

PROOFS

Page proofs will be made available to authors (or to the designated corresponding author) at a Web site in PDF format. Failure to acknowledge the receipt of proofs or to return corrections within the requested deadline may cause publication to be postponed.

Journal of Mechanics of Materials and Structures

Volume 7, No. 7 September 2012

Molecular dynamics-based continuum models for the linear elasticity of nanofilms and nanowires with anisotropic surface effects
WONBAE KIM, SEUNG YUN RHEE and MAENGHYO CHO 613

Characterization of human skin through skin expansion
DJENANE C. PAMPLONA and CLAUDIO R. CARVALHO 641

In-plane dynamic excitation of AAC masonry walls patched with FRP: dynamic testing and analysis
DVIR ELMALICH and ODED RABINOVITCH 657

Hygrothermal analysis of exponentially graded rectangular plates
ASHRAF M. ZENKOUR 687

Green's function for symmetric loading of an elastic sphere with application to contact problems
ALEXEY S. TITOVICH and ANDREW N. NORRIS 701

Multi-hit armour characterisation of metal-composite bi-layers
K. KARTHIKEYAN, B. P. RUSSELL, V. S. DESHPANDE and N. A. FLECK 721

1559-3959(2012)7:7;1-7